



**HAL**  
open science

## New antenna for millimetre wave radar

Muhammad Nazrol Bin Zawawi

► **To cite this version:**

Muhammad Nazrol Bin Zawawi. New antenna for millimetre wave radar. Other. Université Nice Sophia Antipolis, 2015. English. NNT: 2015NICE4017 . tel-01198671

**HAL Id: tel-01198671**

**<https://theses.hal.science/tel-01198671v1>**

Submitted on 14 Sep 2015

**HAL** is a multi-disciplinary open access archive for the deposit and dissemination of scientific research documents, whether they are published or not. The documents may come from teaching and research institutions in France or abroad, or from public or private research centers.

L'archive ouverte pluridisciplinaire **HAL**, est destinée au dépôt et à la diffusion de documents scientifiques de niveau recherche, publiés ou non, émanant des établissements d'enseignement et de recherche français ou étrangers, des laboratoires publics ou privés.

UNIVERSITE NICE SOPHIA ANTIPOLIS

**ECOLE DOCTORALE STIC**  
SCIENCES ET TECHNOLOGIES DE L'INFORMATION ET DE LA COMMUNICATION

# **T H E S E**

pour l'obtention du grade de

**Docteur en Sciences**

de l'Université Nice Sophia Antipolis

Mention : Électronique

présentée et soutenue par

*Muhammad Nazrol BIN ZAWAWI*

**New Antenna for Millimetre Wave Radar**

Thèse dirigée par *Claire MIGLIACCIO*

**Jury :**

Mauro ETTORRE	HDR, CR1-CNRS, IETR UMR 6164, Université de Rennes 1	Rapporteur
Thierry MONEDIERE	Professeur, Université de Limoges	Rapporteur
Claire MIGLIACCIO	Professeur, Univ. Nice Sophia Antipolis	Directeur de thèse
Jérôme LANTERI	MCF, Univ. Nice Sophia Antipolis	Encadrant



Keep moving forward



# Acknowledgments

Foremost, I would like to express my sincere gratitude to my supervisor, Claire Migliaccio for her continuous support in my study and research. Her patience, motivation, enthusiasm and immense knowledge had greatly influenced me. Her guidance helped me in all the time of research and writing of this study. I could not have imagined having a better supervisor for my electronic path study and my academic career progress.

Besides my supervisor, I would like to thank my assistant supervisor Jerome Lanteri for his idea, views and technical knowledge in RF field. Not to forget my classmate and officemate Philippe Perissol for his great help. My sincere thanks also go to all lecturers in Electronic Department of University Nice Sophia Antipolis, Christian Pichot, Jean Yves Dauvignac, Geoges Kossiavas and Jean Marc Ribero for their professional support and knowledge during my academic studies.

I am greatly indebted to Lutfi Arif Bin Ngah and Raja Fazliza Binti Raja Suleiman for their stimulating discussions, great opinions, insightful comments and guidance in writing. I also would like to thank my fellow batch mates and the rest of colleagues in LEAT.

Last but not least, I am eternally indebted to my beloved mother and the rest of my family members for their spiritually endless support.



# Contents

<b>1. Introduction</b>	<b>1</b>
<b>2. Bibliography</b>	<b>3</b>
2.1. Overview . . . . .	3
2.2. Introduction to reflectarray . . . . .	4
2.2.1. History . . . . .	4
2.2.2. Main components . . . . .	4
2.2.3. Working principle . . . . .	7
2.2.4. Phase-shift distribution . . . . .	10
2.2.5. Beam scanning . . . . .	13
2.2.5.1. 2x2 antenna array using Butler matrix . . . . .	13
2.2.5.2. Focal plane array based on microfluid . . . . .	16
2.2.5.3. Reflectarray with single bit phase shifter . . . . .	18
2.2.6. Advantages & Disadvantages . . . . .	20
2.3. Elementary cell . . . . .	21
2.3.1. Single layer . . . . .	21
2.3.2. Multi layer . . . . .	22
2.4. Active Reflectarray . . . . .	24
2.4.1. Active elementary cell . . . . .	24
2.4.2. RF MEMS . . . . .	25
2.4.3. Varicap diode . . . . .	27
2.4.4. Liquid Crystal . . . . .	30
2.4.5. Ferroelectric . . . . .	33
2.4.6. PIN diode . . . . .	35
2.5. Fresnel Reflectarray . . . . .	37
2.6. Application . . . . .	39
2.7. Conclusion . . . . .	39
<b>3. Reflectarray modelisation</b>	<b>41</b>
3.1. Theoretical analysis . . . . .	42
3.2. Parameters definitions . . . . .	45
3.3. Directivity calculation . . . . .	48
3.3.1. Power received at the elementary cell . . . . .	48
3.3.2. Incident wave at the elementary cell . . . . .	48
3.3.3. Reflected wave at the elementary cell . . . . .	49
3.3.4. Total radiated wave . . . . .	52



3.3.5.	Power density and directivity . . . . .	54
3.4.	Simulation program . . . . .	55
3.4.1.	Functionalities . . . . .	56
3.4.1.1.	Feed gain radiation pattern file . . . . .	57
3.4.1.2.	Reflection coefficient ( $S_{11}$ ) file for passive reflectarray . . . . .	57
3.4.2.	Ansoft HFSS elementary cell simulation model . . . . .	58
3.4.3.	Environment and structure . . . . .	61
3.5.	Simulation analysis . . . . .	62
3.5.1.	Results comparison . . . . .	64
3.5.2.	Order of the phase correction . . . . .	68
3.6.	Conclusion . . . . .	72
<b>4.</b>	<b>Active fresnel reflectarray (AFR)</b>	<b>73</b>
4.1.	Elementary cell design . . . . .	73
4.1.1.	Passive cell . . . . .	74
4.1.2.	Frequency adaptation . . . . .	76
4.1.3.	Diode integration . . . . .	82
4.1.4.	The diode DC polarization circuit . . . . .	87
4.1.5.	Dielectric standardization using RT/duroid® 6002 . . . . .	94
4.1.6.	Dielectric standardization using Meteorwave™ 2000 . . . . .	107
4.2.	Reflectarray simulations . . . . .	122
4.2.1.	Optimal frequency of the AFR . . . . .	122
4.2.2.	Beam scanning capability . . . . .	130
4.2.3.	Result comparison against CST . . . . .	133
4.2.4.	Improvement using optimized elementary cell design . . . . .	135
4.3.	Conclusion . . . . .	138
<b>5.</b>	<b>Diode controller</b>	<b>139</b>
5.1.	Circuit conception . . . . .	139
5.2.	Working mechanism . . . . .	142
5.3.	Components . . . . .	143
5.3.1.	Micro-controller (Arduino board) . . . . .	145
5.3.2.	Matrix sub-circuit . . . . .	146
5.3.2.1.	Serial to parallel output circuit . . . . .	149
5.3.2.2.	Digital to analog switch circuit . . . . .	153
5.4.	Test and validation . . . . .	156
5.5.	Conclusion . . . . .	161
<b>6.</b>	<b>General conclusion</b>	<b>163</b>
<b>7.</b>	<b>Resume (French)</b>	<b>165</b>
<b>A.</b>	<b>Object oriented programming in Matlab</b>	<b>167</b>
<b>References</b>		<b>173</b>

<b>Publications</b>	<b>181</b>
<b>Curriculum Vitae</b>	<b>183</b>



# 1. Introduction

This project has been conducted in Laboratoire d'Electronique, Antennes et Télécommunications (LEAT) in Sophia Antipolis and is funded by Universiti Malaysia Pahang (UMP) under the doctorate grant awarded by the Ministry of Education Malaysia (MOE). The supervisor for this project is Claire Migliaccio (Professor at University Nice Sophia Antipolis) and assisted by Jerome Lanteri (Associate professor at University Nice Sophia Antipolis).

The objective of this project is to design and fabricate a reconfigurable reflectarray with beam scanning capability at 20 GHz for unmanned aerial system (UAS) communication link where this antenna will be used to transfer the radar measurements to the satellite in real time. Reflectarray is a type of antenna that shares similar functionality to parabolic reflector antenna. The main difference is the physical and geometry appearance of the antenna where reflectarray has flat reflecting panel instead of parabolic reflector. The reflecting panel consists of elementary cell which is used to control the reflected phase of the incident wave. By controlling the reflected phase on each elementary cell, the radiation pattern of the antenna can be focused to any desired direction.

The integration of the phase control mechanism in the elementary cell is the main challenge that needs to be solved and studied. This consists of understanding the theory of the reflectarray, designing the reconfigurable elementary cell with optimum performance and cost effective material, evaluating the reflectarray performance and integrating the phase control system.

This manuscript is written in 4 main chapters. The first chapter discusses the introduction of the reflectarray, the beam scanning working principle and the latest technologies existing to create a reconfigurable reflectarray. This chapter also presents the chosen technology and discusses the main reason behind the choice.

The second chapter is about the reflectarray theory and the different calculations to produce radiation pattern of the reflectarray. These calculations are used to create in house reflectarray simulator in order to help and to accelerate the design process of the active reflectarray.

In third chapter the process of designing a reconfigurable elementary cell is discussed and explained. Material comparison is made to evaluate the improvement over the reflectarray performance. Simulation results are shown in order to demonstrate the beam scanning capability achieved using the active cell.

The final chapter shows the work realized for the diode controller part which is used to steer the focused beam direction. This includes the simulation, fabrication and validation of the diode controller circuit using LED panel matrix that represented the phase distribution of the reflectarray.

General conclusion is made in in the end of the fourth chapter. The overview of the project completion and the possible improvement for the future work are discussed in this section.

## 2. Bibliography

### 2.1. Overview

Antenna is the critical part in any wireless communication system, where antenna is functioning as the main entrance or departure point in signal reception and transmission. This main point needs to be optimized and carefully designed in order to ensure the functionality of the communication system. There are many types of antennas in different physical forms and technologies for different types of applications. Recently, radar application has been identified as an important application in security and imaging fields, especially in aviation industry.

Radar application requires antenna with high directivity and low secondary lobes. In this application, antenna array is among of the good candidates. By combining small unit of antenna into arrays, the directivity of the antenna can be increased and there is possibility to control the focused beam direction. Antenna array uses microstrip lines to feed the antenna unit. As the size of the array increases, the design of the feed lines will be more complicated and this will increase the loss in the feed transmission lines. To overcome these problems, the transmission lines can be replaced by optical transmission. This is similar to parabolic reflector antenna, which uses optical feed as the primary source. In this category, antenna is able to function based either on transmission or reflection method. When the method chosen is based on the transmission, the antenna is known as “transmitarray” and when the method is based on the reflection, the antenna is known as “reflectarray”.

Both methods share the same designs complexities, which reside in the design of the unit cell or known as the elementary cell. To create a large antenna, the same unit cells designs are combined together. This simplifies the process to create and design passive or active antenna because the same units cell design is repeated for the whole structure. [1] is the recent examples of the reflectarray designed for radar application. The reflectarray functions at 120 GHz and has been designed to enable active phase shifter integration to achieve electronic beam scanning capability.

Beside radar application, there are recent applications which function above 100 GHz and at sub-millimeter wavelengths, such as earth observation, imaging system, and molecular spectroscopy [2, 3, 4, 5] that require reconfigurable reflectarray. Such requirements have created interest among researchers and engineers to design active reflectarray and create new different technologies for controllable reflectarray. This includes MEMS [6], non-linear material such as Ferroelectric films [7] and liquid crystals [8].

## 2.2. Introduction to reflectarray

The reflectarray antenna consists of a flat reflecting surface and an illuminating feed antenna called primary source, which is usually placed in the center of the reflecting surface.

### 2.2.1. History

The concept of the reflectarray was realized by Berry, Malech, and Kennedy [9] in early 1960s. At that time, the design of the reflectarray was bulky and heavy due to the use of low frequencies for most of wireless operations. There was no reflecting panel and short-ended waveguide elements with variable-length were used to compensate the incident wave delay. By determining the appropriate length of the individual waveguide elements, the desired radiation pattern could be formed in the far field region.

In the end of 1970s, the printable microstrip antennas technology was introduced. This encouraged researchers to study the possibility of combining reflectarray concept with the microstrip technology which had produced the first reflectarray based on microstrip elements in 1978 by Malagisi [10]. As the printable microstrip became more accessible in the end of 1980s, many microstrip based reflectarrays had been developed with the purpose to have lighter and smaller reflectarrays. Starting from 1990s, attempts had been made to produce active reflectarray and in 1996, 94 GHz 1-bit monolithic reflectarray fabricated on a single wafer was introduced in Phased Array Conference and was capable to do wide-angle ( $\pm 45^\circ$ ) electronic beam scanning [11].

### 2.2.2. Main components

In Fig. 2.1, the image on the left shows the side view of the reflectarray configuration while image on the right shows the real configuration of the fabricated reflectarray using microstrip rectangle patches as the radiating elements. The feed is positioned in the center of the reflecting panel with a fixed distance from the panel. This distance is noted as  $f$  in the side view image and is known as focal distance. The distance is usually expressed in the ratio of  $f/D$  where  $D$  is the dimension of the reflecting panel.

It is possible to place the feed in a different position than the middle as shown as in Fig. 2.2. The reflectarray [12] uses an offset feed to avoid the aperture blockage problem and a special prolate feed to improve the maximum gain level and to have very low side lobe level. Another alternative to minimize the aperture blockage effect is by using dipole arrays to replace conventional horn antenna as demonstrated in [13]. In the paper, a broadband printed log-periodic dipole arrays (PLPDA) is used to replace the horn antenna.

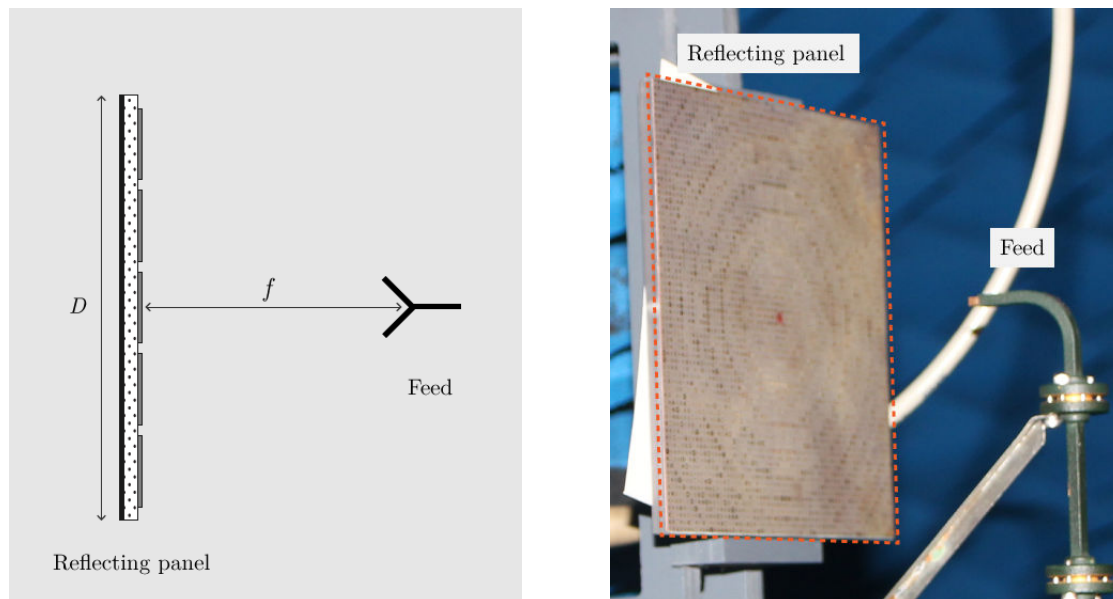


**Figure 2.1.:** Reflectarray components configuration

To form a reflecting surface, there are many types of radiating elements that can be used such as printed micro strip patches [14, 15], open-ended waveguide, dipole [16] or rings [17]. These elements are known as elementary cells. The most common element found in literature is the radiating element based on micro strip patches. There are many shapes [18, 19] and structure variations for the micro strip based elementary cell. Fig. 2.3 and Fig. 2.4 show two different shapes of the radiating element based on fractal and dual split-loop shape respectively. The design of the elementary cell plays very important role in order to optimize the reflectarray performance. More information on the elementary cell will be discussed in sec. 2.3.

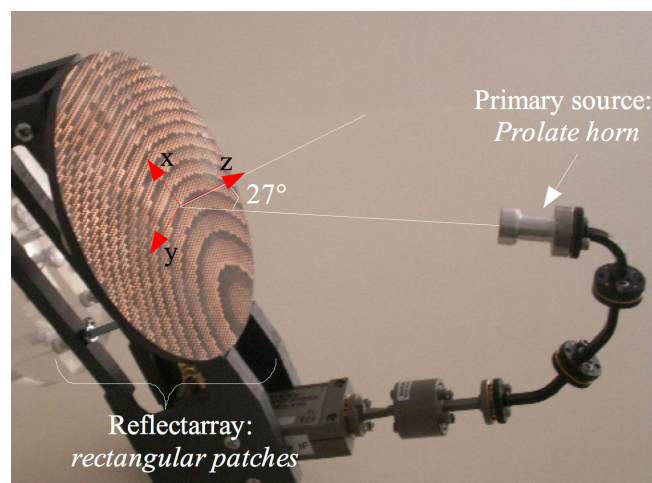


**Figure 2.2.:** Reflectarray with offset feed configuration (From [12], © 2008 IEEE.)



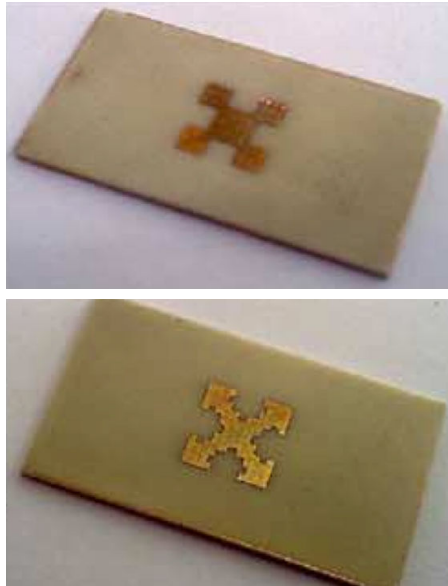


**Figure 2.3.:** Fractal shape elementary cell (From [18], © 2012 IEEE.)

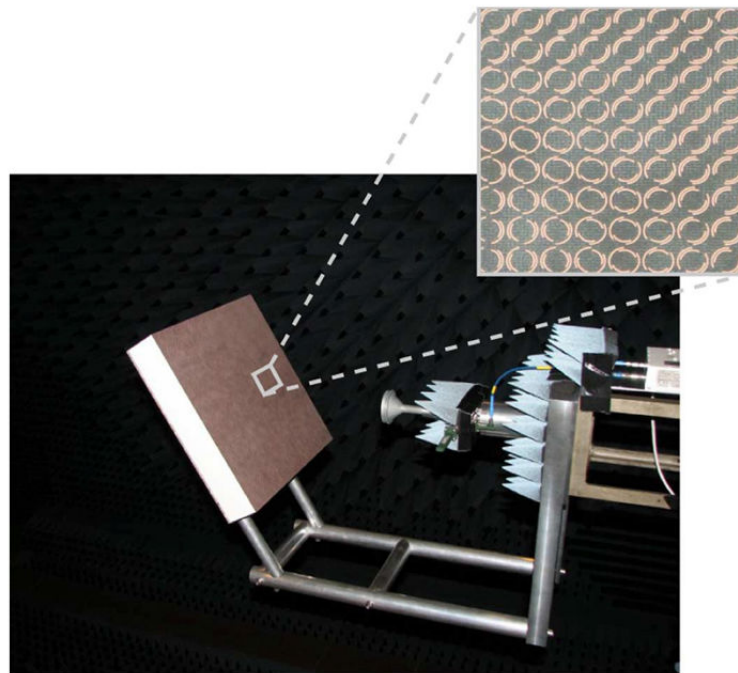


**Figure 2.4.:** Dual split-loop element cell (From [19], © 2014 IEEE.)

### 2.2.3. Working principle

Reflectarray is designed to produce a planar phase front in the far-field region when the feed is positioned at its focal point. It uses the same working principle as the parabolic reflector. In case of the parabolic reflector, it is its unique parabola geometry which forms and reflects the planar phase front as illustrated in Fig. 2.5. The total paths of the rays are represented by the blue and the red lines and show that both of them are parallel and have the same length from the feed. In this case, the rays are said to be collimated. This enables the field on the focal plane to be in phase and travel in the same direction which results in a high directional radiation pattern in the far-field region. Example of parabolic reflector antenna or also known as dish antenna is shown in Fig. 2.6.

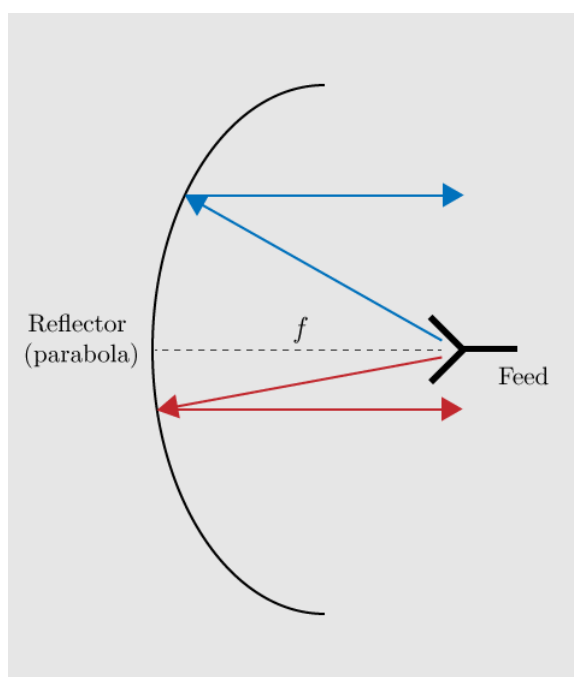


**Figure 2.5.:** Parabolic reflector configuration

In case of reflectarray, the parabola reflector is replaced with the reflecting panel composed with elementary cells as in Fig. 2.7. Due to the absence of parabola reflector, the rays will reach the reflecting panel with some delays and without any correction applied, the reflected rays are not anymore parallel and in phase. To overcome the problem, the phase of each elementary cell on the reflecting surface is adjusted to compensate the delays.

In Fig. 2.7, the elementary cell  $EC_1$  phase ( $\varphi_1$ ) is adjusted to correct the delay for trajectory  $d_1$  and the elementary cell  $EC_2$  phase ( $\varphi_2$ ) is adjusted to compensate the delay for trajectory  $d_2$ . By assigning the correct phase values for each elementary



**Figure 2.6.:** Parabolic reflector antennas used as part of Atacama Large Millimeter Array (ALMA) antennas (© ALMA (ESO/NAOJ/NRAO), W. Garnier (ALMA))

cell, the delay of the incident field can be corrected so that the reflected field will be able to form a planar phase front in the far-field region.

Each elementary cell needs to have different phase values to correctly compensate the delay. The phase value is directly related to the cell position on the reflecting panel, its distance from the feed and the reflected focused beam direction. Typical reflectarray is designed to collimate the main beam at  $\varphi = 0^\circ$  and  $\theta = 0^\circ$  in spherical coordinates as shown in Fig. 2.8. At this direction, the phase for each elementary cell can be obtained using 2.1.

$$\varphi_n = \frac{360}{c} \times f \times d_n \quad (2.1)$$

$c$  : speed of light

$f$  : working frequency

$d_n$  : distance between the elementary cell and the feed

The farthest elementary cell will have the biggest phase compared to the elementary cell located in the center of the reflecting panel.

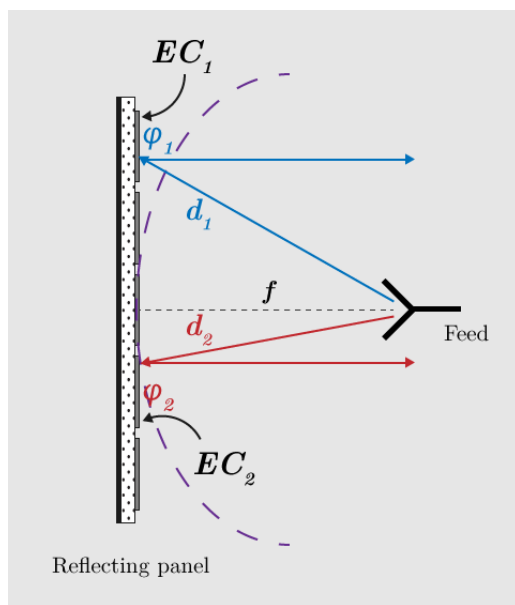


Figure 2.7.: Reflectarray phase compensation

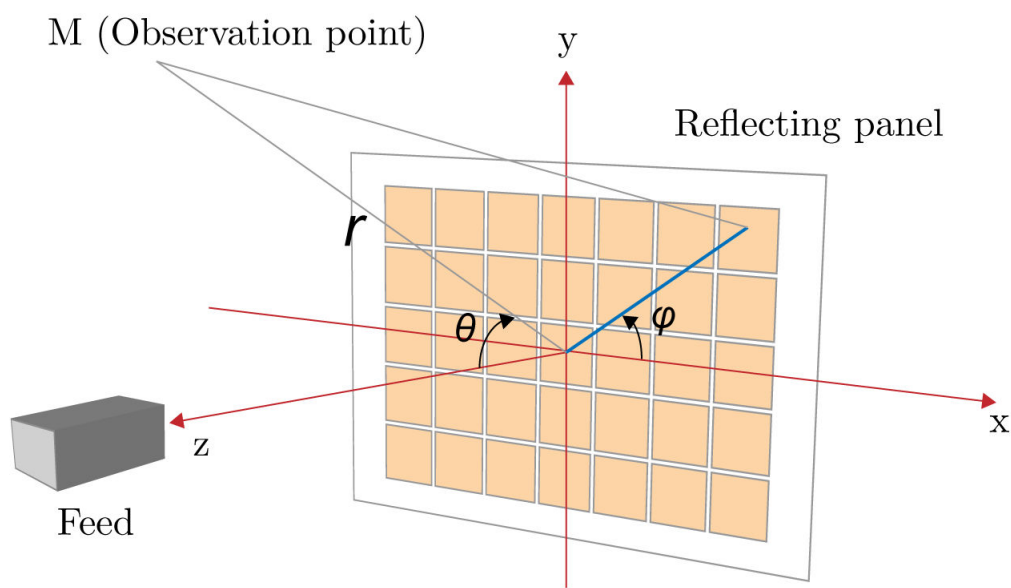


Figure 2.8.: Reflectarray beam direction coordinates

### 2.2.4. Phase-shift distribution

Equation 2.1 assumes that the elementary cell arrangement is in one dimension (1D) as illustrated in Fig. 2.7. In reality, the arrangement of the elementary cell on the reflecting panel is in two dimensions (2D) where  $m$  represents cell column and  $n$  represents cell row. The equation can be rewritten as :

$$\varphi_{mn} = \frac{360}{c} \times f \times d_{mn} \quad (2.2)$$

The two dimensions phase values arrangement will create a phase pattern known as phase-shift distribution for certain reflectarray's size in terms of elementary cell's column (x axis) and row (y axis). Fig. 2.9 shows the phase-shift distribution for  $21 \times 21$  elementary cells when the main beam is collimated at  $\varphi = 0^\circ$  and  $\theta = 0^\circ$  at 20 GHz. This phase-shift distribution will produce a radiation as shown in Fig. 2.10.

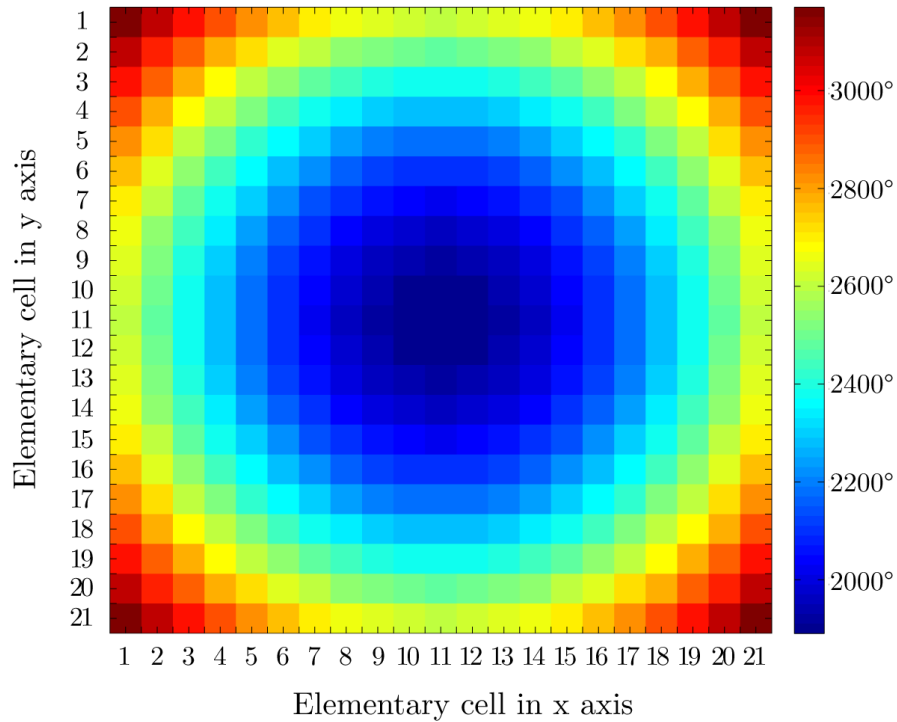


**Figure 2.9.:** Phase-shift distribution for  $21 \times 21$  elementary cells reflectarray at 20 GHz,  $f/D = 0.5$

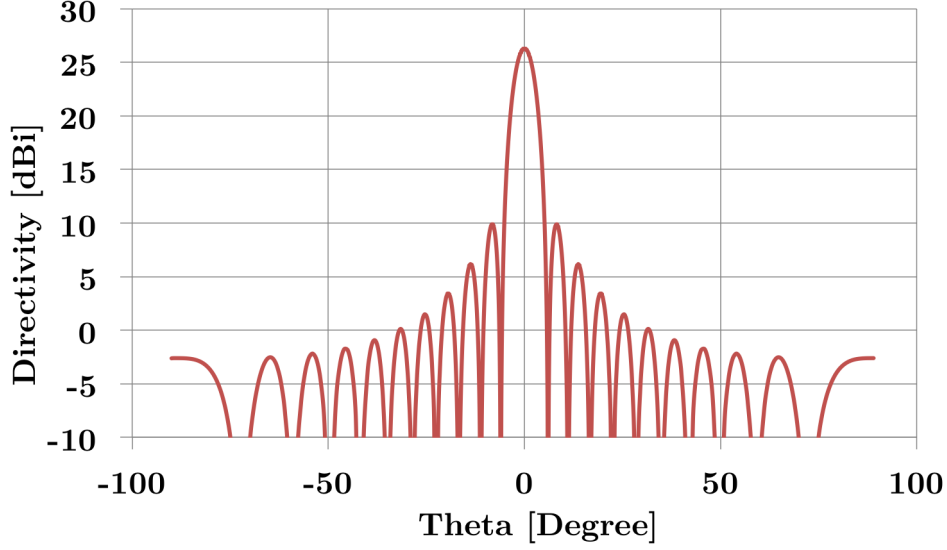


**Figure 2.10.:** Reflectarray's radiation pattern when using phase-shift distribution shown in Fig. 2.9

The equation 2.2 has been simplified from its original equation 2.3 [20] to show that the compensated phase varies linearly with the elementary cell's distance from the feed. This observation is important in order to understand the phase correction influence on the reflectarray performance such as the bandwidth and maximum directivity level.

$$\varphi_{mn} = k_0(d_{mn} - (x_{mn} \cos \varphi_b + y_{mn} \sin \varphi_b) \sin \theta_b) \quad (2.3)$$

In equation 2.3, the direction of the collimated beam is represented by  $\varphi_b$  and  $\theta_b$ . The position of the elementary cells in cartesian coordinate is specified with  $x_{mn}$  and  $y_{mn}$ .  $k_0$  is the propagation constant in vacuum. When modifying the focused beam direction, the phase values for each cell will be also changed. This will generate a new phase distribution pattern as shown in Fig. 2.11. The new pattern shows some phase value offset in x axis direction which indicates that the main beam is not anymore at  $0^\circ$  but has changed to a new direction. This also can be seen on the new radiation pattern in Fig. 2.12 where the main beam direction is now focused at  $20^\circ$ .

This concludes that the radiation pattern can be changed by modifying the phase-shift distribution. In this case, the main beam direction can be varied by using some specific phase distribution patterns such as shown in Fig. 2.11. This can be directly applied to the reflectarray in order to achieve electronic beam-scanning capability.

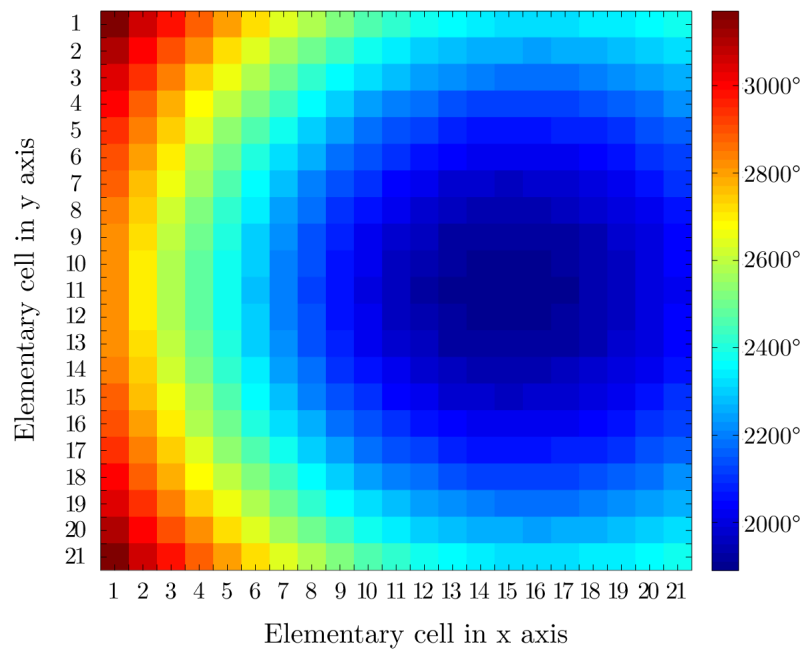


**Figure 2.11.:** Phase-shift distribution for  $21 \times 21$  elementary cells reflectarray functions at 20 GHz with  $f/D = 0.5$  and main beam direction is focused at  $\varphi_b = 0^\circ$  and  $\theta_b = 20^\circ$

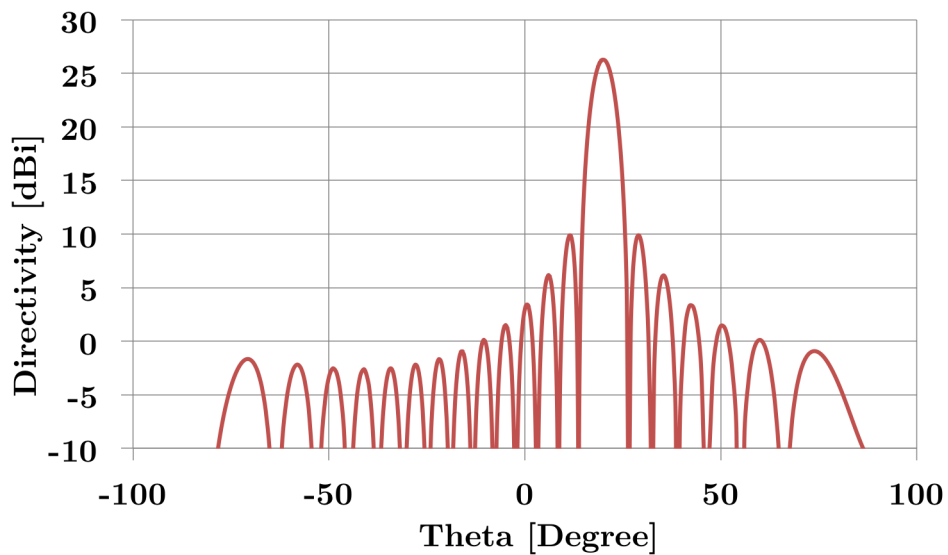


**Figure 2.12.:** Reflectarray radiation pattern when using phase-shift distribution focused at  $\varphi_b = 0^\circ$  and  $\theta_b = 20^\circ$ . Working frequency is 20 GHz and  $f/D = 0.5$

### 2.2.5. Beam scanning

Beam scanning is the capability to change the focused beam direction in a specified range of angles. This capability is essential in radar application and in imaging system such as in medical field in order to detect and determine objects. Beam scanning can be achieved either mechanically or electronically. This section will describe 3 examples of antenna designs with beam scanning capability. The first example uses integrated waveguide phase shifter. The second example is focal plane array (FPA) based on microfluid [21]. The third example will show reflectarray functioning at 60 GHz and uses p-i-n diode as electronic phase shifter. These 3 examples are chosen to show different techniques can be used to do beam scanning.

#### 2.2.5.1. 2x2 antenna array using Butler matrix

In [22], the beam scanning is achieved by using substrate integrated waveguide (SIW) phase shifter. The antenna is designed for Ka-Band application and it is capable to do two-dimensional beam scanning. The physical design of this antenna consists of  $2 \times 2$  antenna array. The single antenna element has 3 layers as shown in Fig. 2.13. The main feed (SIW) is implemented directly into the layer 1 which uses high permittivity Rogers RT/Duroid 6010 ( $\epsilon_r = 10.5$ ,  $\tan \delta = 0.0023@10GHz$ ) as substrate material. Chosen material for layer 2 is Rohacell 31 IG/A ( $\epsilon_r = 1.05$ ,  $\tan \delta = 0.0034@26.5GHz$ ) and the layer 3 material is Rogers ULTRALAM 3850 ( $\epsilon_r = 2.9$ ,  $\tan \delta = 0.0025@10GHz$ ). The radiating element which is the annular ring is printed on the top layer (layer 3).

4 single antenna elements are combined together to represent the Butler matrix which will be used to calculate the focused beam direction. The rectangular waveguide equivalent model for the proposed Butler matrix is shown in Fig. 2.14. Port P1, P2, P3 and P4 are the input feed ports while P5, P6, P7 and P8 are the output ports to feed the circular radiating element on the top layer via coupling. The beam scanning mechanism for this antenna can be analysed using the phase profile equation of the Butler matrix as shown in 2.4 and 2.5.

In these equations,  $\phi_0$  and  $\theta_0$  are the focused beam direction.  $\phi_x$  and  $\phi_y$  are the progressive phase shift in  $x$  and  $y$  direction.  $k$  is the propagation constant in the free space.  $d_x$  and  $d_y$  are the distances between two neighboring antenna element in  $x$  and  $y$  directions. The theoretical progressive phase between ports values are calculated using formula 2.4 and 2.5. Then the theoretical beam directions are obtained. The respective values are shown in the Tab. 2.1 and there are 4 possible focused beam directions.

Fig. 2.15 shows the fabricated antenna with 4 feed ports indicated by P1, P2, P3 and P4. To obtain one beam which focused at one of the four beam directions, only one respective feed port will be used. By changing the feed port, the antenna pattern radiation can be changed and focused to 4 different directions.



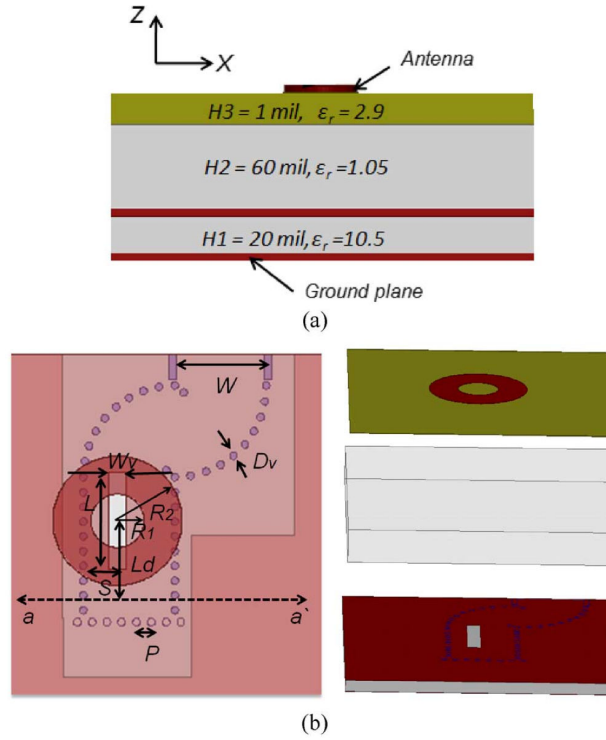


**Figure 2.13.:** Single antenna element with integrated waveguide phase shifter (From [22], © 2014 IEEE.)

$$\phi_x = -kd_x \sin(\theta_0) \cos(\phi_0) \quad \phi_y = -kd_y \sin(\theta_0) \sin(\phi_0) \quad (2.4)$$

$$\phi_0 = \tan^{-1}\left(\frac{\phi_y d_x}{\phi_x d_y}\right) \quad \theta_0 = \sin^{-1} \sqrt{\left(\frac{\phi_x}{kd_x}\right)^2 + \left(\frac{\phi_y}{kd_y}\right)^2} \quad (2.5)$$

Port	$\phi_0, \varphi_0$
1	(21°, 61°)
2	(-38°, -31°)
3	(-21°, 61°)
4	(38°, -31°)

**Table 2.1.:** Theoretical beam directions

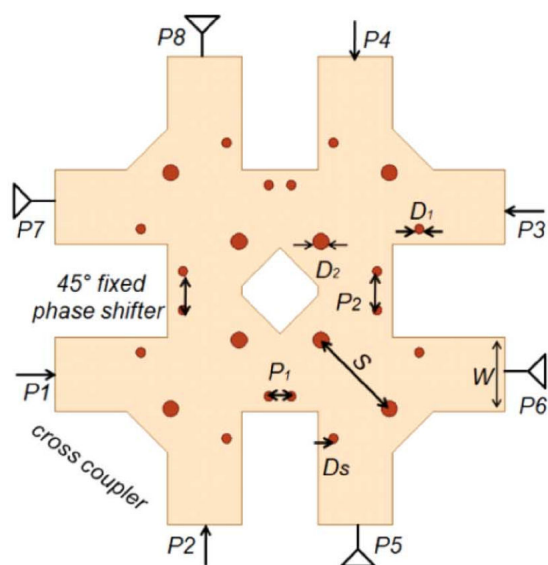


**Figure 2.14.:** Rectangular waveguide equivalent model for 4x4 Butler matrix (From [22], © 2014 IEEE.)

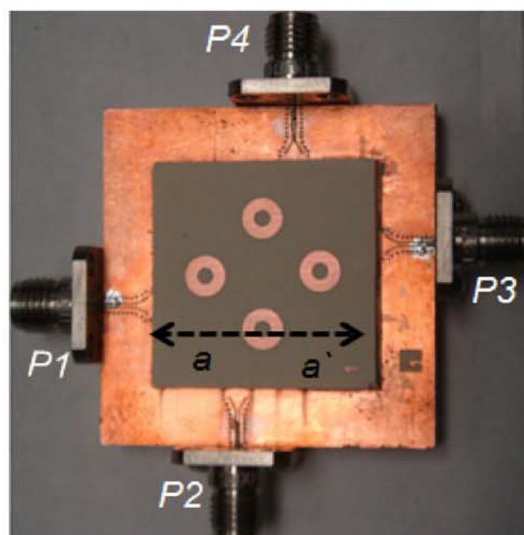


**Figure 2.15.:** Fabricated 2x2 antenna array (From [22], © 2014 IEEE.)

### 2.2.5.2. Focal plane array based on microfluid

In [21], the antenna structure is a multilayer structure that consists of 4 layers and is designed to function at Ka-Band (30 GHz) as shown in Fig. 2.16. This antenna is capable to do 1-D beam scanning by using metal liquid. The top layer has an 8 cm diameter extended hemispherical Rexolite ( $\epsilon_r = 2.56$ ,  $\tan \delta = 0.0026$ ) lens. On layers 2 and 3, there are interconnected microfluid reservoirs and channels fabricated by bonding polydimethyl-siloxane (PDMS) ( $\epsilon_r = 2.8$ ,  $\tan \delta = 0.02$ ) and liquid crystal polymer (LCP) ( $\epsilon_r = 2.9$ ,  $\tan \delta = 0.0025$ ) substrates. There is only a single antenna element in this structure which is a small volume of liquid-metal mercury ( $2.5\mu L$ ,  $\sigma = 1 \times 10^6$  S/m) residing inside a low-loss Fluorinert FC-77 solution ( $\epsilon_r = 1.9$ ,  $\tan \delta = 0.0005$ ). The combination of liquid-metal and Fluorinert solution is filled into microfluid reservoirs and channels. The feeding network is placed on the layer 4 which uses Rogers RT5880 ( $\epsilon_r = 2.2$ ,  $\tan \delta = 0.0007$ ).

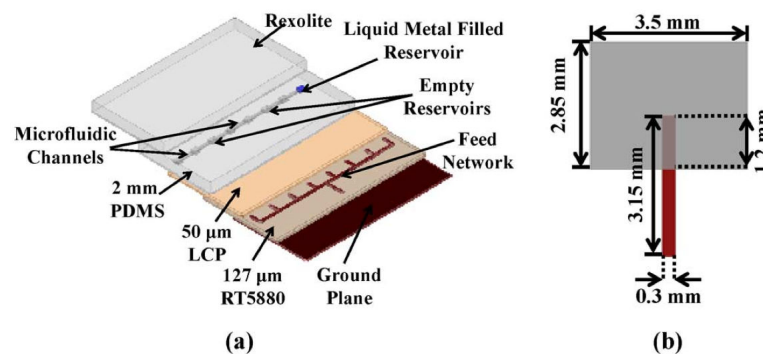


**Figure 2.16.:** Focal plane array structure (From [21], © 2013 IEEE.)

Patch antenna is realized when the reservoir is filled with the liquid-metal and it will radiate using the coupling source coming from the feed network which is located below of the microfluid reservoir. Using this concept, the single patch antenna can be moved into any microfluid reservoir which will result in the changes of the pattern radiation direction. To move the liquid-metal into different reservoirs, a bi-directional micro pump is used as shown in Fig. 2.17. In total, there are 8 liquid reservoirs which will produce 8 different beam directions. These patches act as the feed to the lens and by changing the position of the feed (moving the liquid-metal), the direction of the beam is changed.

Fig. 2.18 shows the fabricated prototype in 3 different views. (a) shows the printed feed network, (b) shows the upper layer with hemispherical Rexolite 8-cm diameter lens and (c) shows the back view of the fabricated antenna. The measured performance of this antenna can be viewed in Fig. 2.19. From the result, the beam scanning capability is achieved by moving liquid-metal into different reservoirs, in this case, the liquid-metal is moved into reservoir #1, #2, #3 and #4.

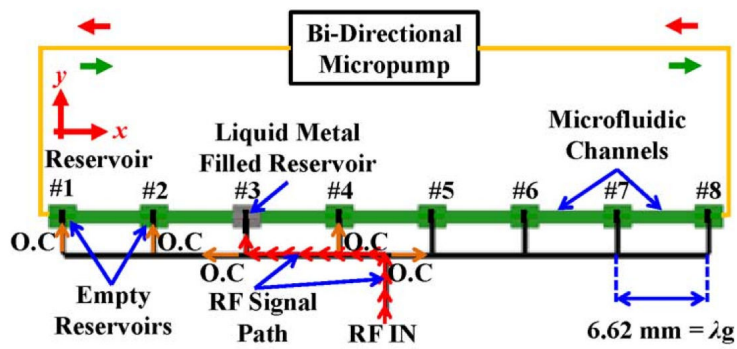


Figure 2.17.: Liquid-metal direction and movement concept (From [21], © 2013 IEEE.)

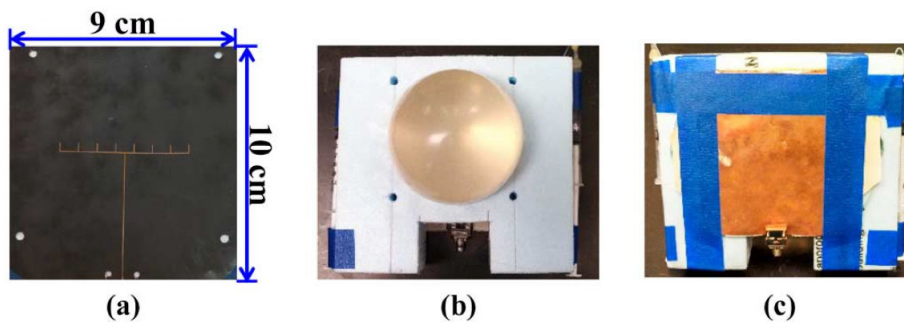


Figure 2.18.: Fabricated prototype of FPA (From [21], © 2013 IEEE.)

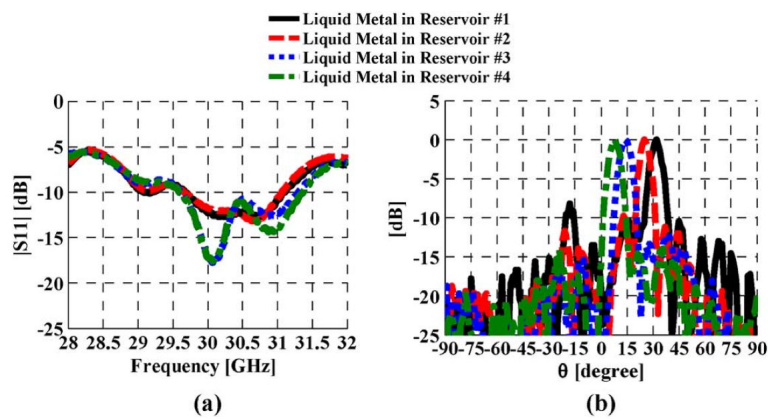
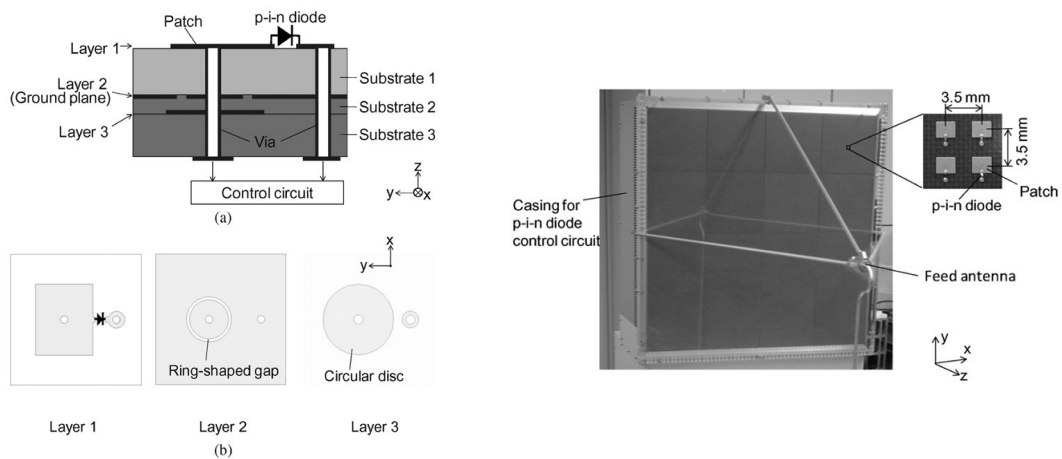


Figure 2.19.: Measured performance : (a)  $|S_{11}|$  and (b) normalized gain (From [21], © 2013 IEEE.)

### 2.2.5.3. Reflectarray with single bit phase shifter

In [23], the beam scanning capability is achieved by modifying the phase distribution of the reflectarray as discussed in sec.2.2.4. The elementary cell is a multilayer structure cell as shown in Fig.2.20. The main radiating element (patch) is printed on the top layer (Layer 1) and this patch is connected to the segmented stub using p-i-n diode. The effective stub length depends on the diode state (ON or OFF) which produces 2 possible stub lengths.



**Figure 2.20.:** (left) Active multilayer elementary cell for 60 GHz single-bit reflectarray; (right) Fabricated reflectarray (From [23], © 2011 IEEE.)

This enables the elementary cell to have 2 different phase values with  $180^\circ$  of difference between them. These values can be controlled electronically using dedicated digital circuit in order to obtain the desired phase value as shown in Fig.2.21.

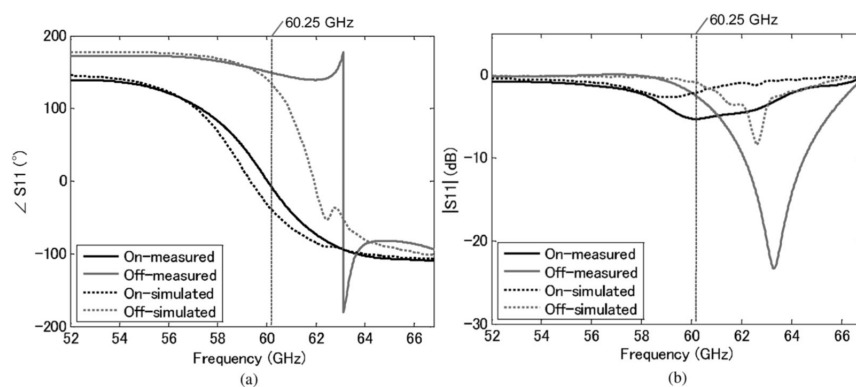


**Figure 2.21.:** Reflection coefficient of the elementary cell using single bit phase shifter (From [23], © 2011 IEEE.)

The cell is limited to correct only 2 phase values and this degrades the reflectarray performance because there is an increase of phase compensation error compared to passive reflectarray. In addition, the reflected power of the cell is decreased due to the high loss in PIN diode. The loss when the diode is biased (ON state) is high which is 5.3 dB and for OFF state the loss is 2.7 dB.

Therefore the size of the reflectarray needs to be increased which results in a total number of 160x160 (25600) elementary cells. The fabricated antenna is shown in Fig. 2.20 on the right side.

Fig. 2.22 shows the measured and simulated radiation patterns with the beam scanning capability for every 5 degrees. From this results, it shows that the simulation and measurement radiation patterns are in good agreement.

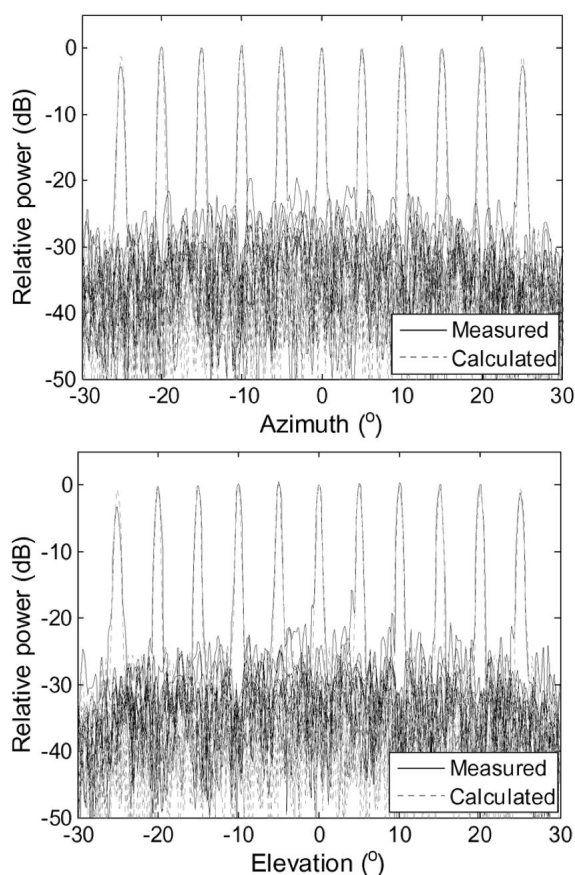


**Figure 2.22.:** Radiation patterns for beam scanned every five degrees in (a) azimuth and (b) elevation (From [23], © 2011 IEEE.)

This active reflectarray will be used as main primary reference and example in this work. More detail and information about this antenna will be discussed in the next following chapters, especially when discussing the active elementary cell's design.

### 2.2.6. Advantages & Disadvantages

Because reflectarray is the combination of reflector antenna and array antenna, it inherits its ancestor advantages such as a very good efficiency. This is true for a very large dimension of reflecting surface or aperture and since no power divider is used thus very little resistive insertion loss is encountered.

Another advantage of reflectarray is that the main beam can be tilted at large angle ( $>50^\circ$ ) from its broadside direction. It's possible to integrate the electronic phase shifter into the elementary cells for wide-angle electronic beam scanning. With this capability, the complicated high-loss beam forming network and high-cost transmit/receive (T/R) amplifier modules of a conventional phased array are no longer needed.

The reflectarray technology can be applied throughout the microwave spectrum, as well as at the millimeter - wave frequencies. So, when working in the millimeter wave spectrum, the size of the antenna could be reduced to a smaller size while maintaining the gain.

On the other hand, working in this spectrum will also allow us to have a larger bandwidth, because there are more spectrum available at the high frequencies compared to lower frequencies ( $< 5$  GHz).

The reflecting surface is usually fabricated using micro strip patches technology. Using this technology, the process is simpler and inexpensive especially when produced in large quantities. Thus, the fabrication cost can be reduced while compromising its quality.

One disadvantage of reflectarray is its bandwidth's limitation. Generally, the bandwidth can't exceed 10% and it depends on its elementary cells design, focal length and aperture size. Compared to parabolic reflector, which is theoretically having an infinite bandwidth, reflectarray has a narrow bandwidth. Many researches have been conducted to tackle this limitation.

## 2.3. Elementary cell

Elementary cell is the primary component in a reflectarray and plays an important role to correct the incident wave delay. As discussed previously in sec. 2.2.5, there are many types of elementary cell designs and the main objective of these designs is to produce the correct or the desired reflected wave phase value. The designs can be categorized into a single layer design elementary cell or multi layer elementary cell.[20]

### 2.3.1. Single layer

Single layer elementary cell is a simple design which consists of a printed radiating elements and a ground metal on a single piece of substrate as shown in Fig. 2.23. This type of design is easy to be fabricated using microstrip technology and inexpensive in term of fabrication's cost. In this design, the phase of reflected wave depends on the radiating element shape design, position and rotation angle. By varying these three characteristics, the desire phase value can be obtained. An inconvenient of this design is that the various combinations are limited to the elementary cell space, which will result in limited number of possible phase values.

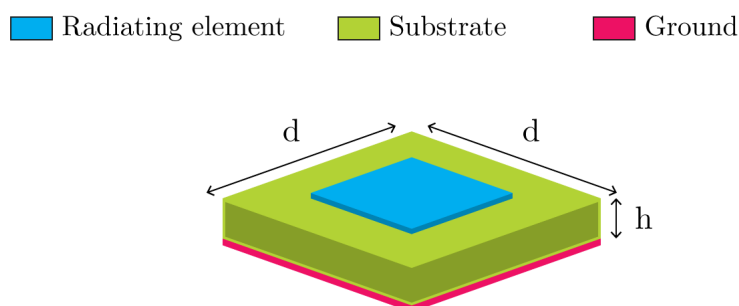


**Figure 2.23.:** Single layer elementary cell design structure

For rectangular shape radiating element or rectangular patch, the reflected phase can be varied by changing the width and height of the patch [24, 25, 26]. Without changing the patch dimension, it is possible to control the reflected phase by attaching the stub with different lengths to the main patch [27]. In this case, the phase value will depend on the length of the stub. There is also elementary cell design which manipulates radiating element rotation angle to control the phase such as in [28]. Using these techniques, the maximum range of phase variation can not exceed  $360^\circ$ . The phase variation versus the variable length or width is strongly non-linear due to the narrow band nature of microstrip patch which is in general about 3%. The phase variations are very sensitive to the frequency or patch dimension variations which will limit the working bandwidth of the reflectarray. To



overcome and improve the reflectarray bandwidth, techniques such as using thicker substrates, stacking multiples patches and using rotated subarray elements have proven to work and 15% of bandwidth improvement has been reported [29].

### 2.3.2. Multi layer

Multi layer elementary cells consists of multiple layers of substrates stack together and is able to produce larger phase variations than single layer elementary cell which is in several times of  $360^\circ$ . In [30], two layers are stacked together as a single unit elementary cell as shown in Fig. 2.24. This design allows the phase variation to be smoother and cover phase values larger than  $360^\circ$ . The thickness of the substrates for each layer can be increased to obtain smooth and more linear phase variation without reducing the phase range values to be less than  $300^\circ$ .

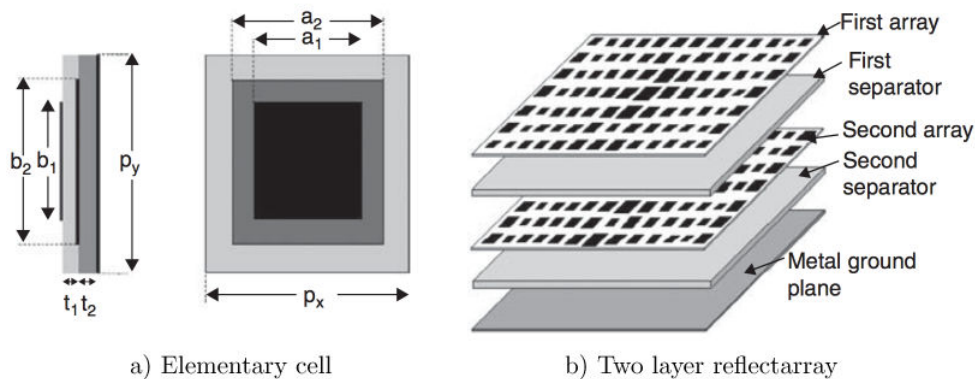


**Figure 2.24.:** Two layer elementary cell design (From [30], © 2001 IEEE.)

The second multi layer design uses elements separations in the structure and works based on the coupling effect between each element [31, 32, 30, 33]. Fig. 2.25 shows the aperture-coupled patches elementary cell design. In this design, there is a clear separation between radiating element and the phase tuning stubs which controls the reflected phase values. The radiating element which is the rectangular patch is separated from the stub by the aperture layer. The phase value can be controlled by adjusting the stubs length and can be folded to obtain very large value of phase variation. To obtain smoother phase variation, the thickness of  $d(1)$  can be increased and the size of rectangle aperture can be adjusted.

The multi layer elementary cell design is more complex. This will increase the fabrication complexity and cost. However, this type of structure is more interesting as many possibilities exist to extend the elementary cell behaviour such as the integration of active and electronic components to produce active elementary cell. The separation of the elements in aperture-coupled patches elementary cell design has some clear advantages over the single layer design. The phase tuning stub is placed

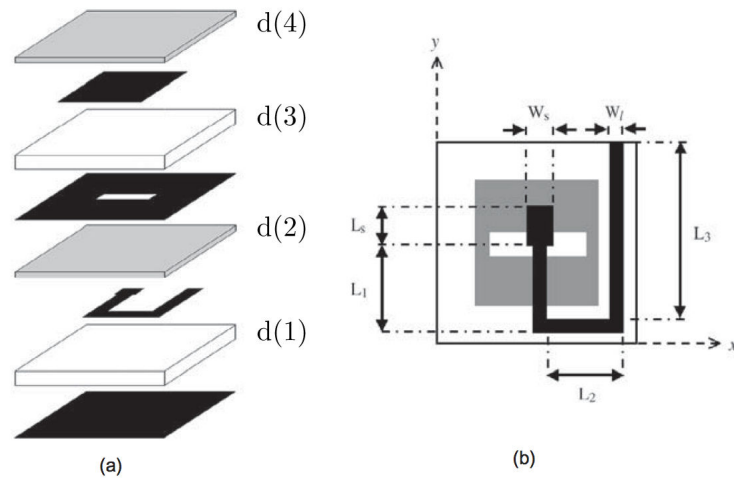


**Figure 2.25.:** Elementary cell based on a U-shaped aperture-coupled delay line (a) Expanded view, (b) top view (From [31], © 2006 IEEE.)

on a separate layer and this will ensure plenty of space left for increasing the stub length, plus the stub length can be folded to fill up the space. Electronic element like diode can be integrated on the phase tuning stub layer without affecting the radiating layer on the top of the cell. The radiating layer itself is very sensitive to any fabrication error or any presence of unwanted physical object which contributes to reflected phase value error.

## 2.4. Active Reflectarray

Passive reflectarray has been proven working well and has been widely used in telecommunication and RADAR applications due to its nature of having high gain and good efficiency. There is a significant growth of RADAR application in security field especially in car safety systems in order to prevent and avoid collisions. This requires an intelligent detection system to ensure that the passengers are well protected and safe. One of the most important part in the system is the antenna which emits and receives signals. Passive reflectarray is the suitable candidate for this type of application because its physical design is compact and small at higher frequencies and has been used as the antenna for such system [34, 35, 36].

To improve modern detection systems, the reflectarray needs to evolve to become intelligent and reconfigurable from passive to active reflectarray. Because of this, the demands for electronic beam scanning capability and radiation pattern configurability are identified as an important challenge for on-going applications and they can be defined as important capabilities for an active reflectarray.

### 2.4.1. Active elementary cell

Active reflectarray uses the same components as the passive reflectarray, but new components are added to the passive's structure. In the elementary cell, electronic phase-shifter is integrated inside the cell design to have the total control of the reflected phase. Additional controller circuit is required to handle a large quantity of electronic phase-shifter inside the elementary cells.

There are variety of technologies that can be used as the phase-shifter in active elementary cell. Each of these technologies has its own benefits and disadvantages especially in term of cost, fabrication complexity, control complexity, losses and power consumption.

### 2.4.2. RF MEMS

MEMS stands for Microelectromechanical systems and in terms of the phase-shifter it can be considered as mechanical switch at a small scale. MEMS switch operates using mechanical structure thus offering some benefits to have null current consumption, good power efficiency, high isolation and low losses. Demonstration and proof of concept using MEMS switch have been made in [37, 38]. In [37], the elementary cell is made of two patches coupled through slots to microstrip-lines, which are connected to a common stubs as shown in Fig. 2.26. This cell is designed to function between 9.40 GHz and 11.40 GHz. The proposed elementary cell design is similar to the passive design discussed previously in sec. 2.3.2. Depending on the MEMS actuation voltage, the switch is either in ON or OFF state, and the phase tuning stub length varies producing two possible values of reflected phase.

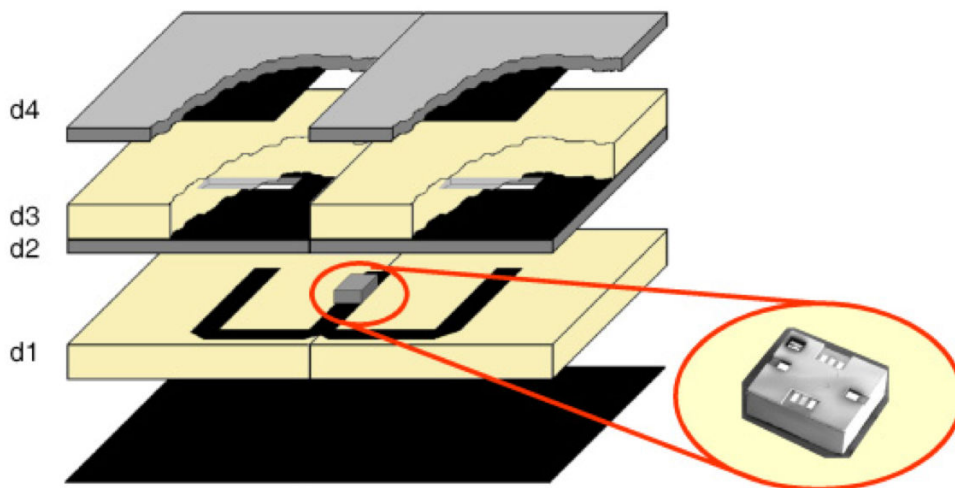


**Figure 2.26.:** Reconfigurable double aperture-coupled delay line elementary cell based on MEMS switch (From [37], © 2011 IEEE.)

Fig. 2.27 shows the MEMS switch schematic. The switch will either join or disconnect the two segments of the phase tuning stub. This can be achieved when a biasing voltage of 25 V is applied between the electrodes and the ground plane. The silicon nitride membrane will be pulled down and touches the signal metal connector which is located between two ground connectors. This produces a short circuit that will join the two segments of the phase tuning stub. The simulated and measured reflected phase values are shown in Fig. 2.28 with phase difference between ON and OFF states is about 300°.

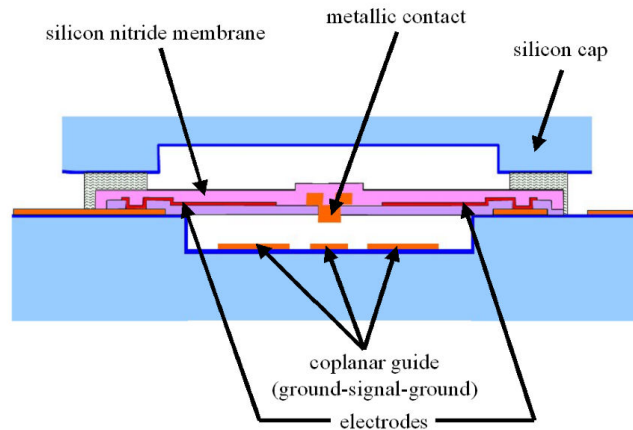


**Figure 2.27.:** Schematic stack of the ohmic electrostatic MEMS switch (From [37], © 2011 IEEE.)

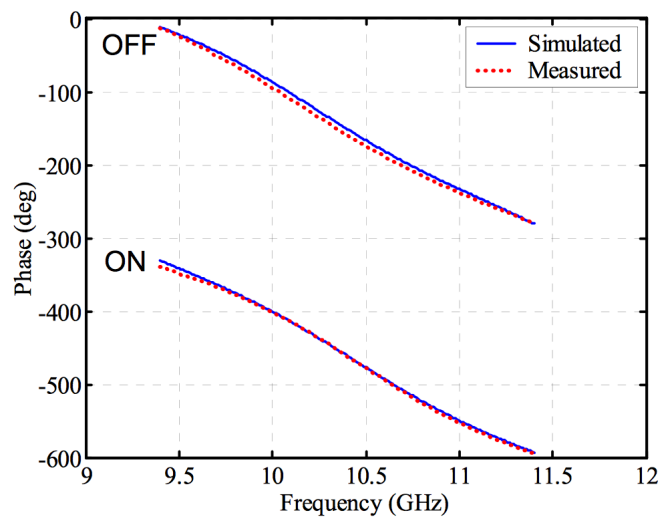


**Figure 2.28.:** Comparison between the measured and simulated reflected phase in the waveguide simulator for both states: OFF and ON (From [37], © 2011 IEEE.)

In total, a MEMS switch in this design requires 8 wires to be functional. They are 2 wires for the DC voltage biasing, 4 wires for the via holes connected to the ground of the coplanar line and 2 wires for the RF signal between each segment of the phase tuning stub. Although MEMS switch can provide low losses of reflected wave, the process to integrate this switch is complex because of multiples connectors are required for each switch. In term of fabrication cost, this will be expensive because there are many switches need to be integrated for a complete reflectarray. In [6], difficulties to fabricate large MEMS array with independent voltage control has been reported.

### 2.4.3. Varicap diode

Varicap diode is a type of diode whose capacitance varies as a function of the voltage applied across its anode and cathode terminals. In case of active elementary cell, varicap diode can be used as active element to control and modify the reflected phase electronically by varying the bias voltage. Delft University of Technology [39] has designed an electronic steerable reflectarray with integrates varicap diode and functions at 6 GHz. The elementary cell structure is a single layer structure with ground plane at the bottom layer. The radiating patch on the top is similar to rectangular patch but with some holes in the center of the patch (Hollow patch) as shown in Fig. 2.29.

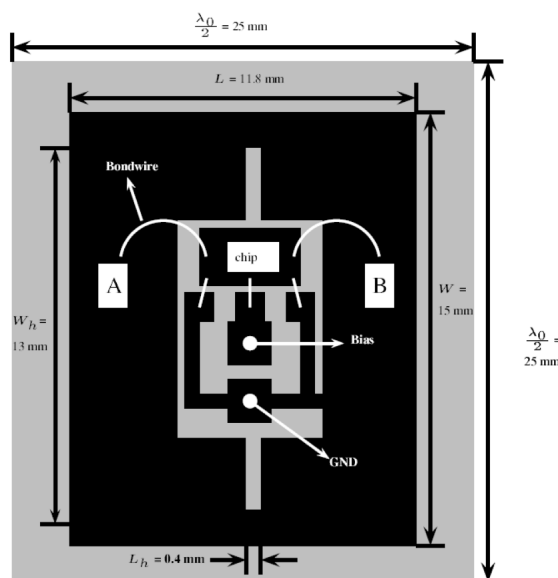


**Figure 2.29.:** Geometry of a hollow patch loaded with varicap diode (From [39], © 2009 IEEE.)

The center part of the hollow patch primarily consists of varactor chip connected to the bias and ground signal microstrips lines. The varactor chip has been designed and developed at DIMES (Delft Institute for Micro-Electronics and Sub-microntechnology) and acts as tunable capacitive device [40, 41]. The chip has 5 connections and it is connected to the patch laminate using bondwires. The connection signal of bias and ground are brought from the bottom layer. This requires two additional vias (white circle) to bring those connectors to the top layer. Points A and B are the connections for the RF path and this path will have capacitance variation which depends on the varactor chip applied bias voltage.

To modify the reflected phase value, the capacitance value of the varactor is varied using a bias voltage between -12 V and 0 V. The reflected phase values versus capacitance values are shown in Fig. 2.30. Maximum phase variation obtained using

the varactor chip is about  $250^\circ$ . At  $f = 5.8$  GHz the phase variation are small and at  $f = 6.2$  GHz the variation is too steep. This shows that the reflectarray has a narrow bandwidth.

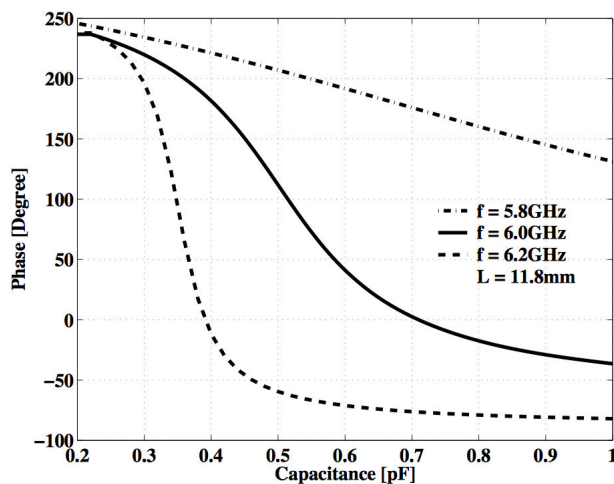


**Figure 2.30.:** Phase diagram of a hollow patch loaded with tunable varactor as function of capacitance (From [39], © 2009 IEEE.)

The fabricated reflectarray is shown in Fig. 2.31 with  $6 \times 6$  elementary cells. The substrate used is Taconic TLX-0-0620-C1/C1 with a thickness of 1.57 mm and dielectric permittivity of  $\epsilon_r = 2.45$ . The connections to control the varactor chips are made from the bottom layer (back view) where each elementary cell can be controlled individually. In total there are 36 wires for biasing voltage purpose (yellow wire) and 6 wires as ground connector. Each column of the reflectarray requires one wire for grounding.

The biasing control is realized via PC and PCI-766 DAC (Digital-to-Analog converter). The DAC chosen has 16 channels with 16-bit resolution. Because there are only 16 channels available as output, the total 36 elementary cells biasing control is not possible to be done individually. The measured E-plane radiation patterns are shown in Fig. 2.32 and shows the reflectarray beam scanning capability between  $-15^\circ$  and  $15^\circ$  at  $f = 6.15$  GHz.

Using varicap diode is an interesting solution to have an active elementary cell but in term of the losses of reflected wave magnitude, varicap diode contributes to high losses of reflected wave magnitude which can degrades the overall reflectarray performance. In addition, the cost to fabricate reflectarray using this diode is expensive.

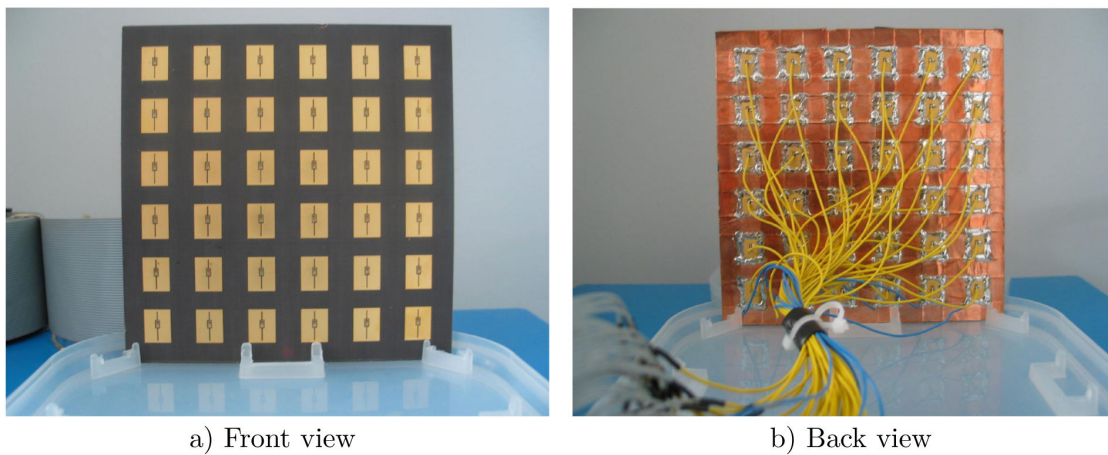


**Figure 2.31.:** Manufactured active antennas: (a) front view; (b) back view. (From [39], © 2009 IEEE.)

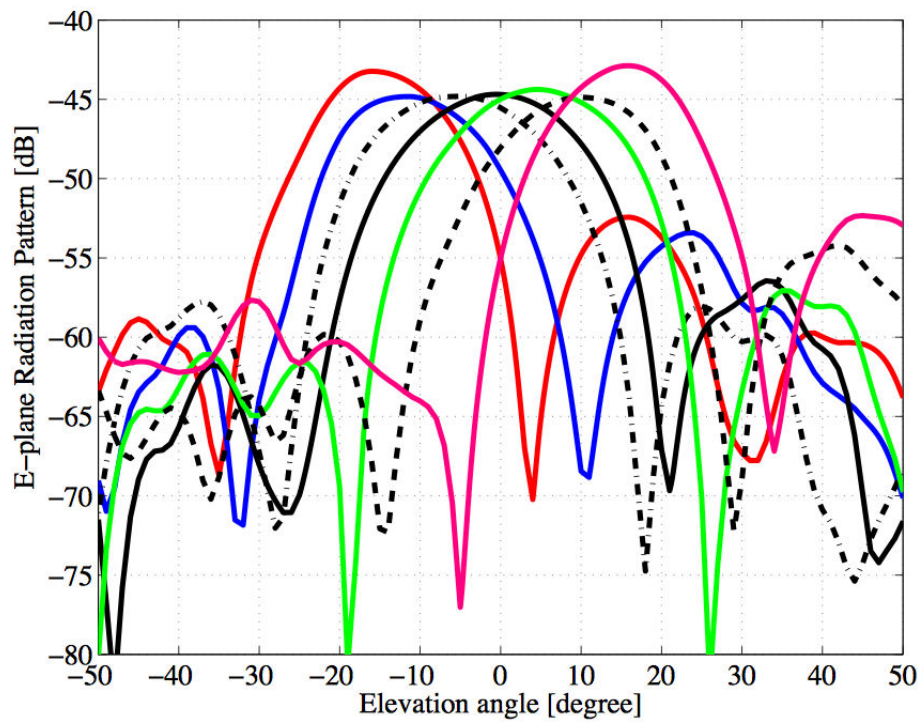


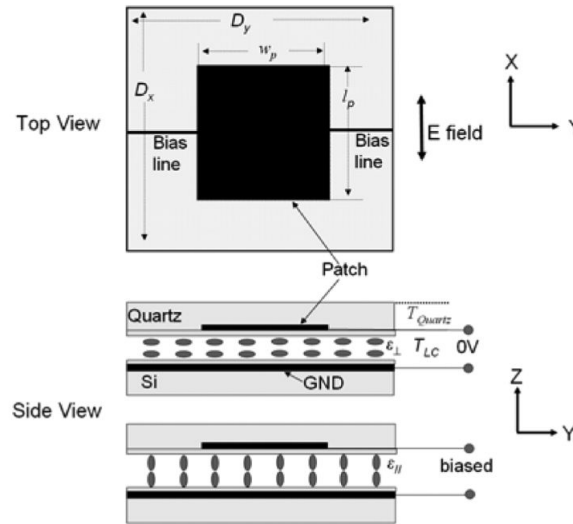
**Figure 2.32.:** Measured radiation pattern of the active hollow MRA at 6.15 GHz (From [39], © 2009 IEEE.)



### 2.4.4. Liquid Crystal

One interesting property of liquid crystal is the ability to change its material permittivity when quasi-static electric field is applied. This property can be exploited to produce a reconfigurable reflectarray. Several active elementary cell examples based on the liquid crystal have been demonstrated in [42, 43, 44].

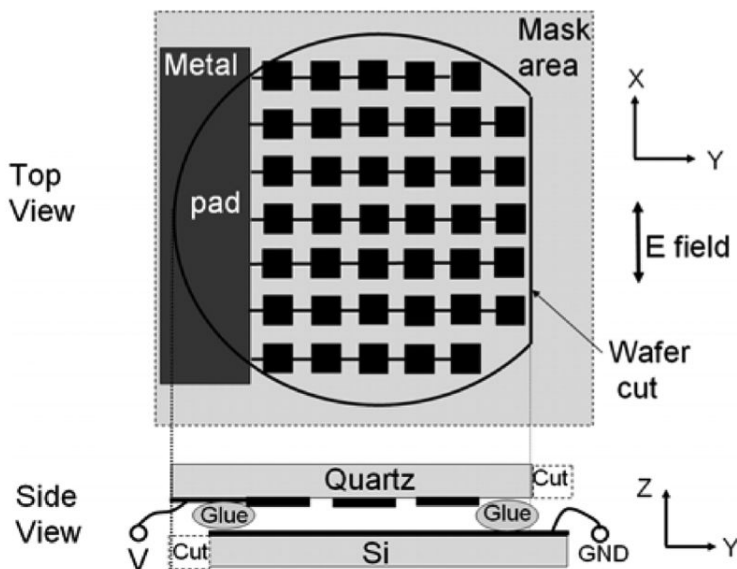
In [44], the elementary cell structure is similar to single layer structure as shown in Fig. 2.33 and designed to function at 102 GHz. The radiating element is a rectangular patch with bias line in the middle. The substrate between the patch and ground is a liquid crystal film with the thickness of  $15 \mu\text{m}$ . The size of the patch is  $w_p = l_p = 0.77 \text{ mm}$  and dimension of the elementary cell is  $D_x = D_y = 0.9 \text{ mm}$ . The ground material chosen is copper coated with Si to satisfy mechanical requirement. The selected wafer surface [45] which is Quartz material ( $\epsilon_r = 2.56$ ,  $\tan\delta = 0.0026$ ) is placed on the top, above the patch to align the director of the liquid crystal molecules in the direction of the wafer surface as shown in the Fig. 2.33 in case of  $0 \text{ V}$ . Without this surface, the director of a liquid crystal is free to point in any direction.



**Figure 2.33.:** Structure of an elementary cell based on liquid crystal in [44] (From [44], © 2008 IEEE.)

Without any voltage applied between the bias line and ground ( $0 \text{ V}$ ), the director of the liquid crystal molecules are aligned in the same direction of the quartz surface. In this case the permittivity is considered as  $\epsilon_{\perp}$ . When  $10 \text{ V}$  of bias voltage is applied, the director of the liquid crystal molecules are oriented perpendicular to the wafer surface which results in a new permittivity value noted as  $\epsilon_{\parallel}$ . This permittivity difference will affect the reflected phase values [46] and in this case, there are 2 possible of phase values, one corresponds for  $0 \text{ V}$  (Normal state) and the another one corresponds to  $10 \text{ V}$  (Biased state).

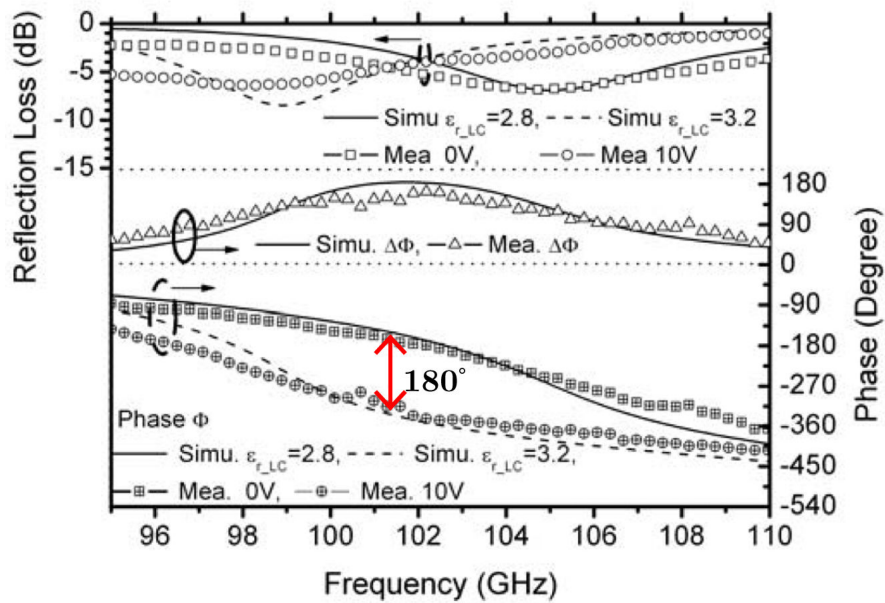
Using the elementary cell design discussed previously, a reflectarray with geometry shown in Fig. 2.34 is fabricated. The bias lines with the width of  $50\ \mu\text{m}$  are connected in columns to the metal pad which means the elementary cell in this design cannot be controlled individually. To do the measurement of the elementary cell in periodic environment, the same bias voltage is applied to all elementary cells simultaneously.



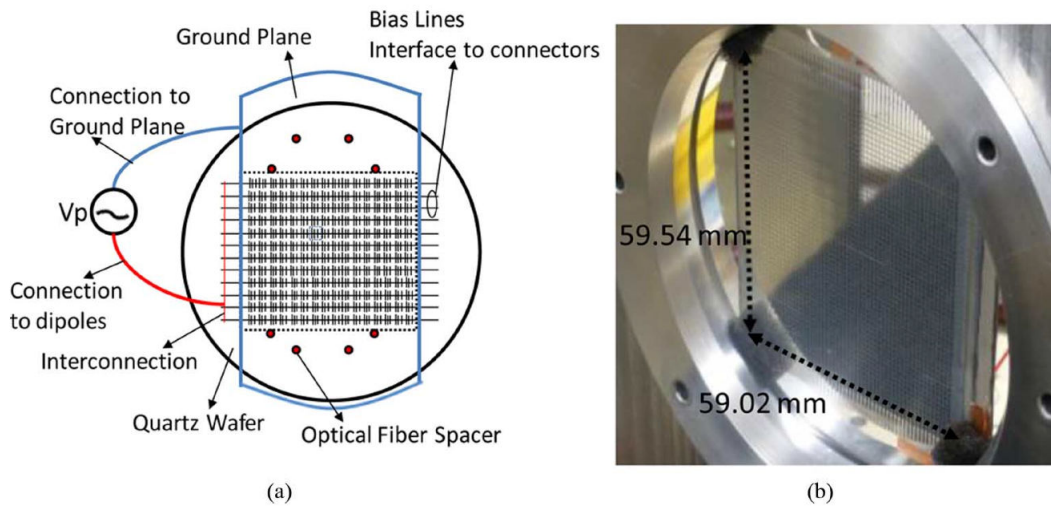
**Figure 2.34.:** Schematic plot of the reflectarray geometry (From [44], © 2008 IEEE.)

Fig. 2.35 shows the simulated and measured reflected magnitude and phase of the elementary cell. At  $f = 101.72\ \text{GHz}$ , the phase difference between normal and biased state is  $180^\circ$ , therefore this frequency is chosen as the center design frequency for the reflectarray. The results show good agreement between the simulated and the measured one.

Designing and fabricating reconfigurable reflectarray using liquid crystal is still considered new and experimental. The cost to use the wafer as the director surface is considered to be expensive and not suitable for large reflectarrays. The difficulty to implement control system for each elementary cell is a challenging process with this technology. In recent work [47] shown in Fig. 2.36, the measurement of the reflectarray is performed at the elementary cell level without the measurement of the reconfigurable radiation patterns. To obtain the gain of the reflectarray, simulation using data from the measured elementary cell is mandatory.



**Figure 2.35.:** Simulated and measured of reflection loss (upper), phase (lower) and phase agility (center) of liquid crystal based elementary cell (From [44], © 2008 IEEE.)



**Figure 2.36.:** Manufactured reconfigurable reflectarray in F-Band (From [47], © 2013 IEEE.)

### 2.4.5. Ferroelectric

Ferroelectric based material is a type of material where the electrical polarization can be changed by application of an external electric field [48, 49]. In microwave applications, ferroelectric material have been extensively studied as tuning elements such as tunable filters [50, 51], phase shifters [52] and matching networks. Barium-Strontium-Titanate or known as BST is the common ferroelectric material used and is commonly found in the literature.

In [53], the single layer structure is used as the elementary cell and is designed to function at 10 GHz. The size of the cell is 4.75 mm. The metallic patch is printed on the BST thick film and sintered on  $Al_2O_3$  substrate ( $\epsilon_r = 9.80$ ) with the thickness of  $650 \mu m$ . The rectangular patch on the top acts as radiating element which is divided into two parts as shown in Fig. 2.37. The gap between the 2 parts is  $13 \mu m$ . Fig. 2.38 shows the cross-section (from A and B) of elementary cell.

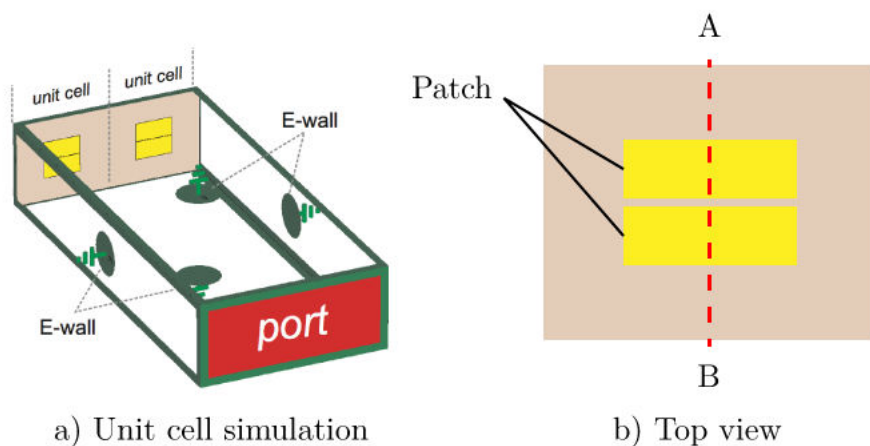


**Figure 2.37.:** Reconfigurable elementary cell with BST based varactor (From [53], © 2009 IEEE.)

The separation of the rectangular into 2 parts produces in a capacitively coupling between those parts. By applying an electrostatic field between the 2 rectangular patches, the effective capacitance between them can be changed. This structure represents a BST varactor and it is implemented directly on the microstrip patch without any off-chip varactor.

The result of the elementary cell measurement is shown in Fig. 2.39. With a tuning field of  $11.5 V/\mu m$ , a phase difference of  $250^\circ$  is obtained at 10.5 GHz. The introduction of the bias lines for the electric field has a considerable influence on the reflected wave, with additional 6 dB of losses and shifted resonance frequency.

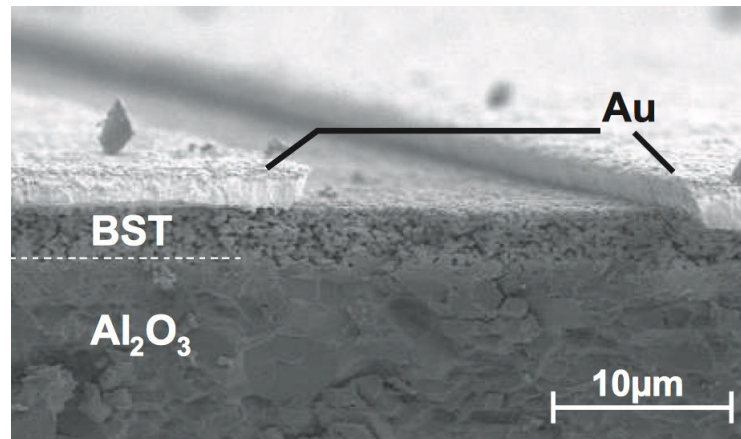


**Figure 2.38.:** Microscopic cross-section of a BST thick-film screen printed on top of  $Al_2O_3$  substrate (From [53], © 2009 IEEE.)

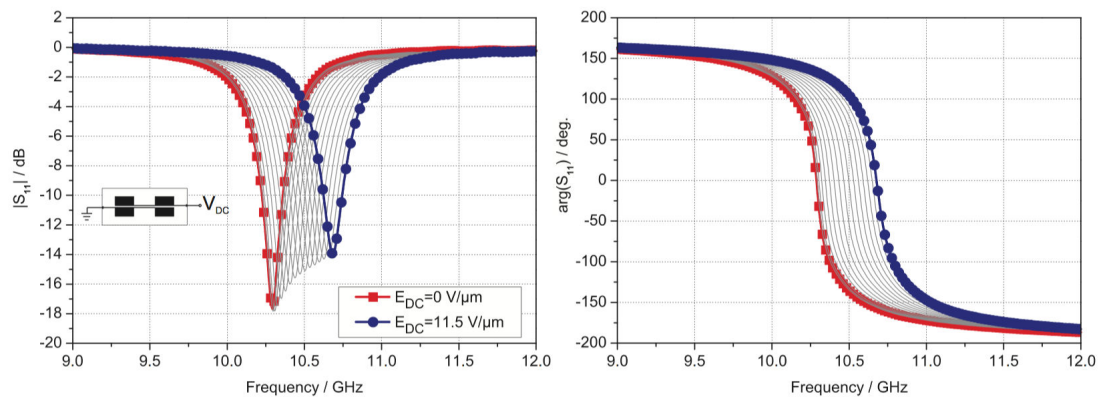


**Figure 2.39.:** Reflected magnitude and phase for applied electrical field between 0 to  $11.5V/\mu m$  (From [53], © 2009 IEEE.)

Utilizing BST thick-film as solution to achieve tunable elementary cell is interesting from the point of view cost and fabrication process. By using screen printing technique, an active elementary cell could be manufactured at a low cost. Plus, the ferroelectric based tunable components have higher tuning speed in picoseconds range [54]. Despite all these advantages, the ferroelectric based elementary cell needs high DC biased fields to obtain large phase-shift range and this will impose an inconvenient for a large size reflectarray. Plus, the process to design and implement complete bias lines is also difficult and will result in poor performance of the elementary cell.

### 2.4.6. PIN diode

PIN diode has been widely used as an electronic switch and it is often associated with phase tuning stub or delay line length variations [55, 56, 57, 58, 59]. In [59], the elementary structure is very similar to the one discussed in sec. 2.4.2 and functions between 10.1 GHz and 10.7 GHz. In this case, the RF MEMS switch is replaced by PIN diode and the bias lines are modified to fit in the diode switch. The expanded view of the elementary cell design is shown in Fig. 2.40.

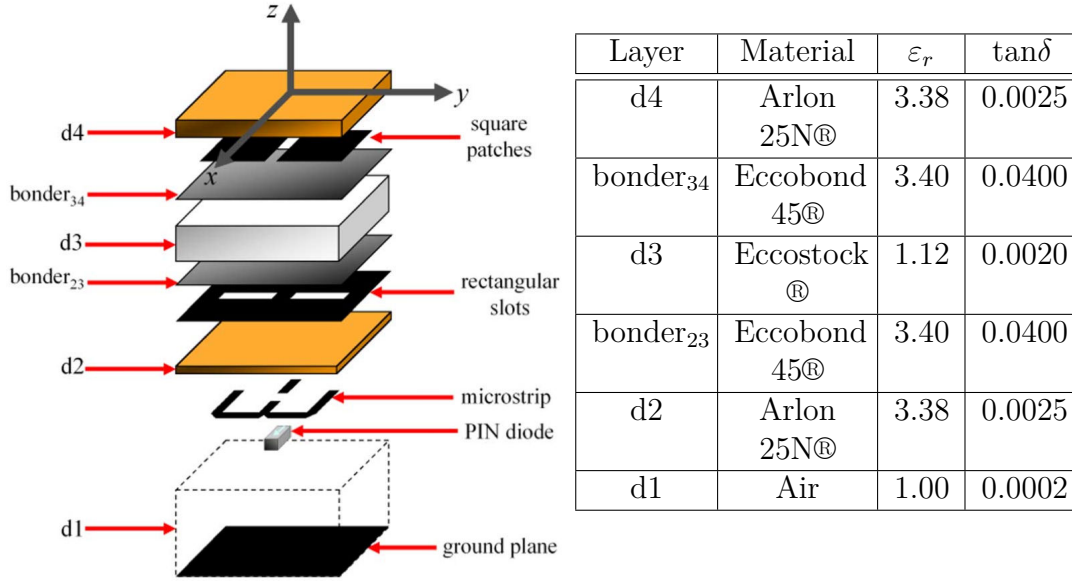


**Figure 2.40.:** Expanded view of a reflectarray elementary cell based on aperture-coupled patches to a common tuning stub, using a PIN diode as electronic switch (From [59], © 2012 IEEE.)

The elementary cell concept is based on gathering two patches together as a single unit elementary cell. This enables the control of the two radiating patches to be done via a single PIN diode, thus reducing the diode usage and their associated DC biasing lines. The size of the unit is  $36 \text{ mm} \times 18 \text{ mm}$  and the size of the square patches as the radiating elements are  $9 \text{ mm} \times 9 \text{ mm}$ . The diode is modeled as capacitance in OFF state (reverse biasing) and as a resistance in ON state (forward biasing). The length of the phase tuning stub will be different and depends on the diode state. This will produce 2 different reflected phase values that will be used to change the phase-shift distribution.

The chosen PIN diode for this design is a GaAs MA4GP907 diode manufactured by MACOM and the diode characteristics are shown in Tab. 2.2. The simulated and measured results for the elementary cell are shown in Fig. 2.41. The required phase variations between 10.1 GHz and 10.7 GHz are about  $150^\circ$  to  $200^\circ$  and the loss is

around 4 dB. The loss by using PIN diode is higher than using RF MEMS switch.

Parameter	Value
Capacitance, $C_T$	0.025 pF
Series resistance, $R_S$	4.2 $\Omega$
Forward voltage, $V_F$	1.33 V
Reverse voltage current, $I_R$	Max 10 $\mu$ A

**Table 2.2.:** MA4GP907 diode electrical characteristics (From [59], © 2012 IEEE.)

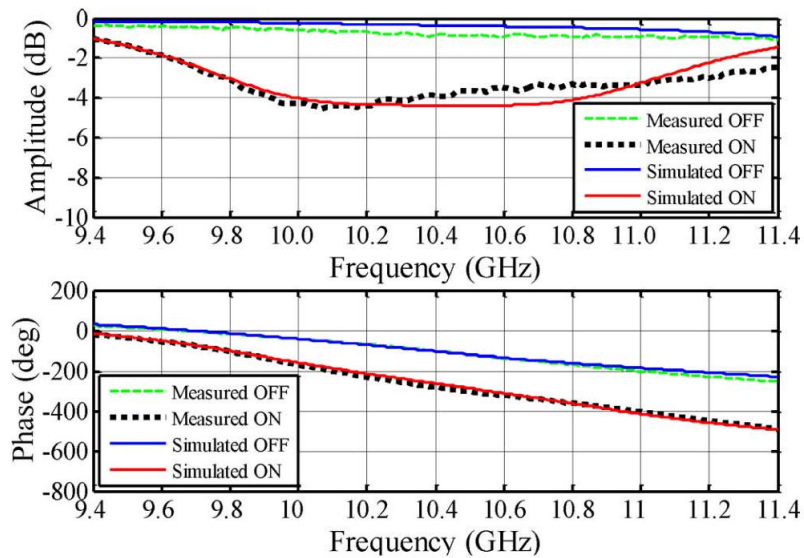


**Figure 2.41.:** Measured and simulated reconfigurable elementary cell based on PIN diode reflected phase and magnitude (From [59], © 2012 IEEE.)

The reflectarray is designed to do 3 states beam scanning which are  $-5^\circ$ ,  $0^\circ$  and  $5^\circ$  and because of this, there is no need to control each individual elementary cell. Instead, they are controlled per row and this reduces the bias line design complexity.

PIN diode technology is quite matured at the industry level. This means that diodes costs are not expensive and they have been extensively tested for various type of applications and conditions. The disadvantages of the PIN diode is that the loss is high especially when it is used at high frequencies and it will consume a lot of energy for large reflectarrays.

## 2.5. Fresnel Reflectarray

Reflectarray works by converting the spherical incident wave coming from the feed to a plane wave in the far-field region. Each of the elementary cell on the reflecting surface needs to have a correct phase value to compensate the incident wave delay associated to its travel's distance, noted  $D_{mn}$  in Fig. 2.42.  $F$  is the focal length.

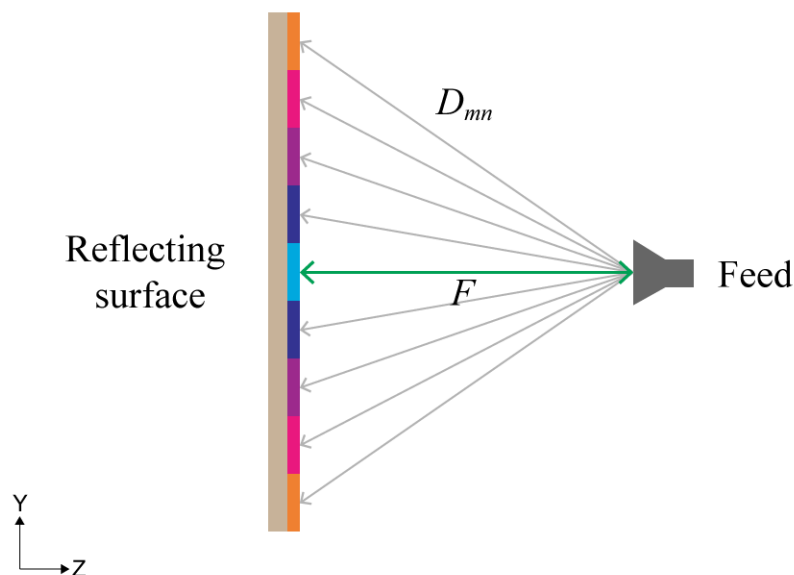


Figure 2.42.: Reflectarray side view

For Fresnel reflectarray, instead of correcting per elementary cell, the incident wave delay is compensated by zones known as Fresnel zone [60, 61]. The zone is defined by using the following equation 2.6.

$$r_n = \sqrt{2nF \frac{\lambda}{P} + \left(\frac{n\lambda}{P}\right)^2} \quad (2.6)$$

The zone radius noted as  $r_n$  is defined from the center of the reflectarray.  $n$  is the index of the zone and this value starts from 1.  $F$  is the focal length and  $\lambda$  is the free-space wavelength.  $P$  is the order of correction desired. The phase correction of the zone is obtained from the equation 2.7.

$$\varphi_n = \frac{(n-1)2\pi}{P} \quad \text{mod } 2\pi \quad (2.7)$$



Theoretically, a large number of  $P$  will ensure better phase correction thus giving better reflectarray's performance in term of maximum gain and lower side lobes levels. In reality, the chosen  $P$  value needs to reflect certain criterions such as the ease of manufacturing, design complexity and acceptable performance. The number of bit required depends on the  $P$  value and it determines the elementary cell design complexity.

Taking the example of  $P = 4$ , there are 4 possible phase values and this requires 2-bits phase resolution of active elementary cell [62, 63]. Study and comparison of the order of correction value has been discussed in [64, 65] and reveals that 1-bit phase resolution ( $P = 2$ ) elementary cell is able to produce acceptable performance. Several large reconfigurable beam steering reflectarrays [66, 64, 67] have been fabricated by using only 1-bit phase shifter and have been reported with only 3dB of loss on directivity and accurate pointing angle. In [68], the 1-bit reflectarray performance can be improved by optimizing the phase compensation value.

In this work, the chosen  $P$  value is 2, which requires 1-bit phase resolution. In this case, the reflectarray is known as half-wavelength Fresnel Reflector and by using equation 2.7, the phase values are either  $0^\circ$  or  $180^\circ$ . To associate these phase values with the elementary cells on the reflecting surface, comparisons between the position of the cells and the zones radius are made. If the cells are located within the zones radius, then the phase associated to the zone will be applied to them. For  $n > 1$ , the zones are defined as ring circle where  $r_n - r_{n-1}$ .

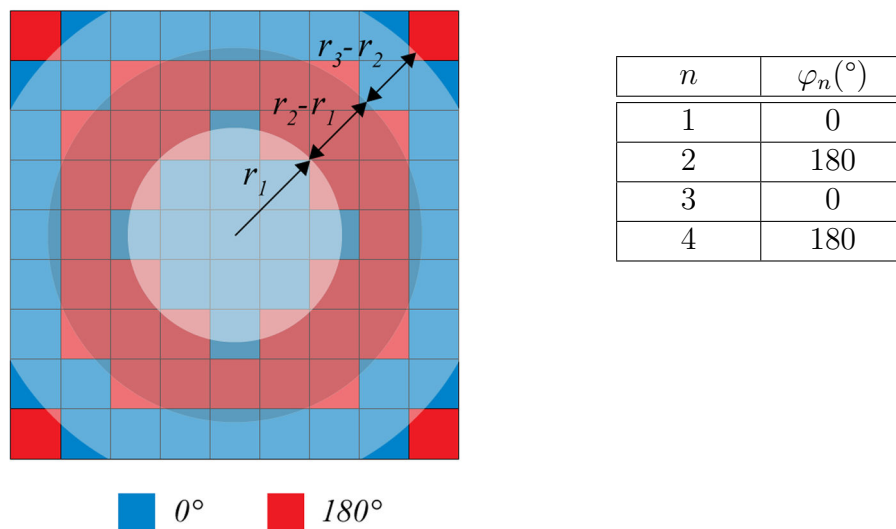


**Figure 2.43.:** Fresnel zone association for 9x9 elementary cells reflectarray

Fig. 2.43 shows the example of zones association with the corresponding phase values in table on the right side. Using Fresnel reflectarray simplifies the reflectarray

design because less phase values are needed. This reflectarray also is less sensitive to fabrication error and for active reflectarray application, the complexity of the circuit control for active element such as diode can be reduced.

The fact that Fresnel reflectarray degrades the antenna's performances is inevitable of the rough discretization used to correct the incident wave's delay. But some compromises need to be made especially when designing active reflectarray where there is loss of energy in the active element itself that has to be considered.

## 2.6. Application

In this project, the envisaged reflectarray application is to integrate the active reflectarray on unmanned aerial system (UAS) as communication link between UAS and satellite in Ka-band. For this purpose, the antenna needs to follow the satellite and maintain the communication link by using electronic beam sweep. Due to the size and weight constraints limited by the UAS's payload, the size and weight of antenna requires to lightweight and compact.

Printed solution such as active Fresnel reflectarray antenna is suitable for this type application because of its small and lightweight geometry. In addition, by using Fresnel reflectarray, the number of phase-shifter can be reduced to minimize the power consumption without compromising the link connection quality. Using electronic beam scanning gives the possibility to increase the link connection quality by eliminating any error coming from the mechanical system. This will reduce the occupied space and at the same time increase the communication speed.

## 2.7. Conclusion

In this chapter, general information on the reflectarray was discussed including history, working mechanism, and the theory behind the electronic beam scanning. Several examples of antenna with beam scanning capability have been discussed with different technologies (integrated waveguide phase shifter, micro-fluid system and electronic phase shifter using p-i-n diode). Advantages and disadvantages of the reflectarray have been identified and having small and lightweight form factor is a plus for this type of antenna within the context of the project's application. Plus, there is possibility to extend the elementary cell design to have reconfigurable reflected phase values.

Multiplés types of elementary cell have been presented and this includes the different technologies to achieve reconfigurable unit cell. The mentioned technologies are by using RF MEMS switch, varicap diode, liquid crystal, ferroelectric material and PIN diode. There is no perfect solution because each of them has their

own strength and weakness. Comprises need to be made when choosing the implemented solution especially in term of fabrication cost, design complexity and having acceptable reflectarray performance.

At the moment, technologies using RF MEMS and PIN diode are considered being the best solutions and the most reliable to produce a working prototype. PIN diode technology is chosen as the preferred solution in the context of this project because it is already proven working in the industry and research fields.

The next chapter will discuss the theory and the calculation of the reflectarray model. This part is important in order to ensure a good of understanding when designing reflectarray especially when dealing with different reflectarrays parameters.

### 3. Reflectarray modelisation

In this chapter, the radiation pattern model of the reflectarray will be discussed. This model is used to create a reflectarray simulator program that can quickly simulate reflectarray design in order to determine its performance. Full 3D electromagnetic simulation is very useful to obtain accurate results, but the time taken to complete the simulation can be long especially for a large size reflectarray. For very large reflectarrays, it is even impossible to have a simulation result. To accelerate the simulation, a high-end workstation is required or another possible solution is by distributing the simulation across high performance computing (HPC) network.

Those solutions will definitely give accurate results, but the cost to implement and setup the system will be expensive. For example, in Ansoft HFSS simulator program, to use the HPC with multiple machines, a separate license needs to be paid to activate that feature. In addition, the hardware costs also need to be taken into account when dealing with computer simulation.

In this project, the reflectarray simulations are not completely relying on the 3D electromagnetic software. Instead, a mixed approach has been used by combining in-house simulator program called HRS which is an acronym for Hybrid Reflectarray Simulator and Ansoft HFSS by Ansys. HRS uses the data generated by Ansoft HFSS to do the calculation in an analytical manner and in simpler ways. This helps to accelerate the elementary cell and reflectarray design process.

The model described in this chapter is based on the transmitarray antenna [69, 70] research [71]. It works using the same mechanism as optical lens. The incident wave coming from the feed is transmitted and collimated to the desired direction as a planar wave. Before transmitting, the incident wave phase is adjusted by using the phase-shift distribution in the elementary cells of the transmission network. The concept is similar to reflectarray but instead of reflecting the incident wave, the transmitarray transmits the wave to the other side of the panel. In this case, some adaptations are required in order to use the transmitarray model.

### 3.1. Theoretical analysis

In [71], the author explains several formulas and steps, which are required to obtain the power density of the transmitarray. Fig. 3.1 shows the summary of the calculations taken in order to determine the transmitarray gain and directivity. This diagram is important because it will help to ease the modeling process and at the same time to have better understanding of the different formulas and steps. By analyzing these formulas and steps, and with a proper adjustment, the model of the reflectarray can be determined and calculated.

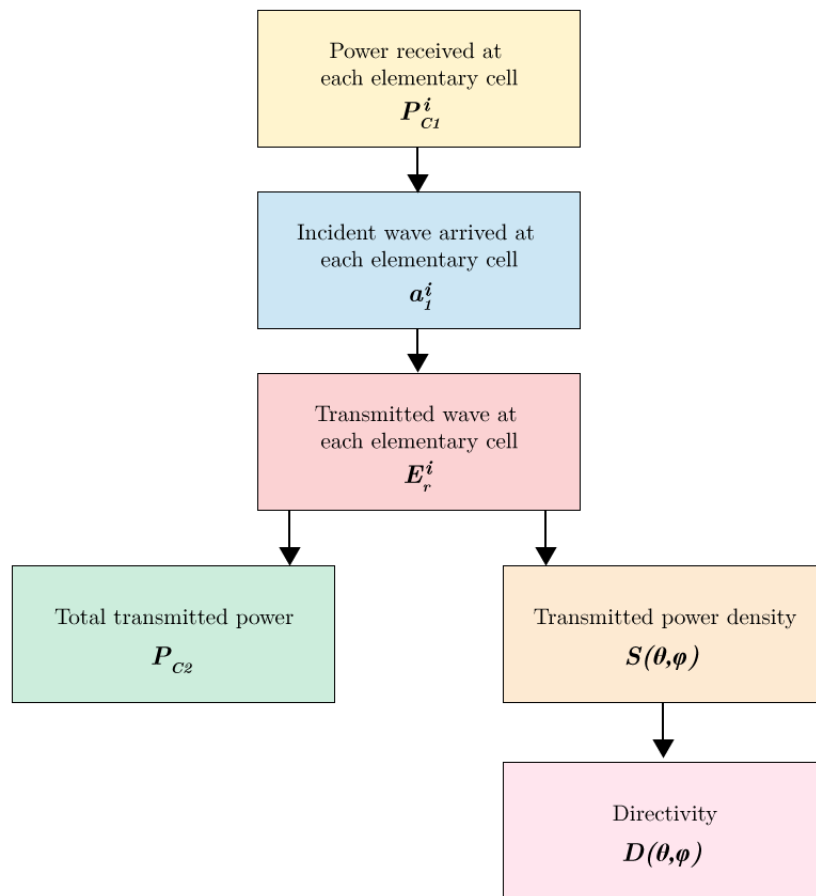


**Figure 3.1.:** Summary of the calculation steps (From [71])

The calculation starts from the top and ends in the bottom with the final results of obtaining gain and directivity. An alternative way to represent the calculations steps is by referring the different power received and power radiated such as illustrated in Fig. 3.2. There are 3 different types of power used in the calculations and their descriptions are shown in Tab. 3.1.

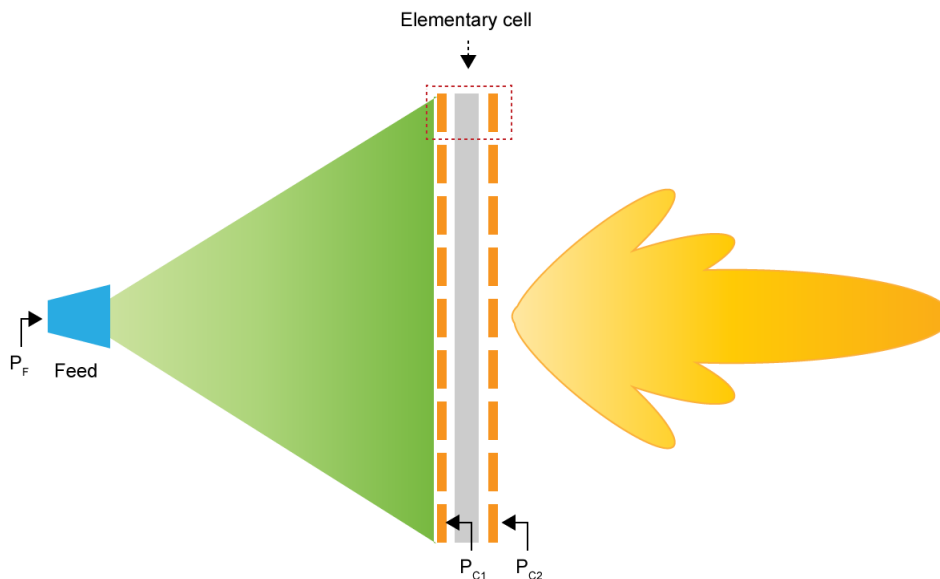


**Figure 3.2.:** Different types of power in transmitarray

Power	Description
$P_F$	Power injected to the feed
$P_{C1}$	Power received by the elementary cells at the feed side
$P_{C2}$	Power radiated by the elementary cells at free space side

**Table 3.1.:** Transmitarray power descriptions

The first power is the  $P_F$  which is defined as the power injected to the feed. The value for this power can be in any values except 0 and for normalization purpose  $P_F = 1$ . The second power is the power received at each elementary cell noted as  $P_{C1}$ . This power can be calculated by using Friis formula [72] and the equation is as indicated in 3.1.

$$P_{C1}^i = \left(\frac{\lambda}{4\pi r_i}\right)^2 \times G_F(\theta_F^i, \varphi_F^i) \times G_{EC}(\theta_{EC}^i, \varphi_{EC}^i) \times P_F \quad (3.1)$$

- $\lambda$  : Wavelength of the working frequency
- $r_i$  : Distance from the feed to  $i$  elementary cell
- $G_F$  : Feed gain
- $G_{EC}$  : Elementary cell gain
- $P_F$  : Input power at the feed. This value is set as 1

When  $P_{C1}$  is obtained, the value of the incident wave noted as  $a_1^i$  can be calculated using the incident wave equation 3.2.

$$a_1^i = \sqrt{P_{C1}^i} \times \exp(-j\frac{2\pi r_i}{\lambda}) \times \exp(j\phi_F^i) \quad (3.2)$$

$\phi_F^i$  : The angle of the feed's phase radiation pattern direct to cell

The third power is the power radiated by the elementary cell on the free space side noted as  $P_{C2}$  and is considered as total radiated power for the transmitarray. The radiated electric field at the  $i$ th elementary cell is defined as the multiplication of the elementary cell transmission coefficient  $S_{21}^i$  with the incident wave  $a_1^i$  calculated previously and can be written as in 3.3.

$$E_r^i = S_{21}^i(\omega) \times a_1^i \quad (3.3)$$

In this case, an adjustment is required to adapt this model for the reflectarray. The equation 3.3 is valid for the transmitarray, whereas for reflectarray, instead of using transmission coefficient  $S_{21}^i$ , reflection coefficient  $S_{11}^i$  is used to calculate the electric field. Both coefficients can be obtained by simulating elementary cell unit design in electromagnetic software simulation in periodic elementary cell environment. To obtain the total radiated power  $P_{C2}$ , the electric field on each elementary cell needs to be added together as written in 3.4.

$$P_{C2} = \sum |E_r^i|^2 \quad (3.4)$$

Finally, the transmitted power density and directivity can be derived from the equations 3.3 and 3.4. More details on the directivity calculation will be discussed in sec. 3.3. Only small adjustment is needed in order to adapt the transmitarray model to fit into reflectarray model. This is by changing the transmission coefficient to reflection coefficient when defining the radiated electrical field on each elementary cell.

The model and calculations concept discussed previously use simplification by ignoring certain electromagnetic properties, thus the obtained results are considered as approximations values. For the coupling effect between elementary cells, it is only taken account via the reflection phase with the consideration that the environment is in infinite periodic array. From the conducted simulations results, the difference between the calculated ones and the taken measurements are coherent with each other.

## 3.2. Parameters definitions

Fig. 3.3 shows the reflectarray modelisation drawing with the parameters notations. This drawing is important as it shows clearly how the angles for the feed and the patches are defined as well as the axis used to position both of them.

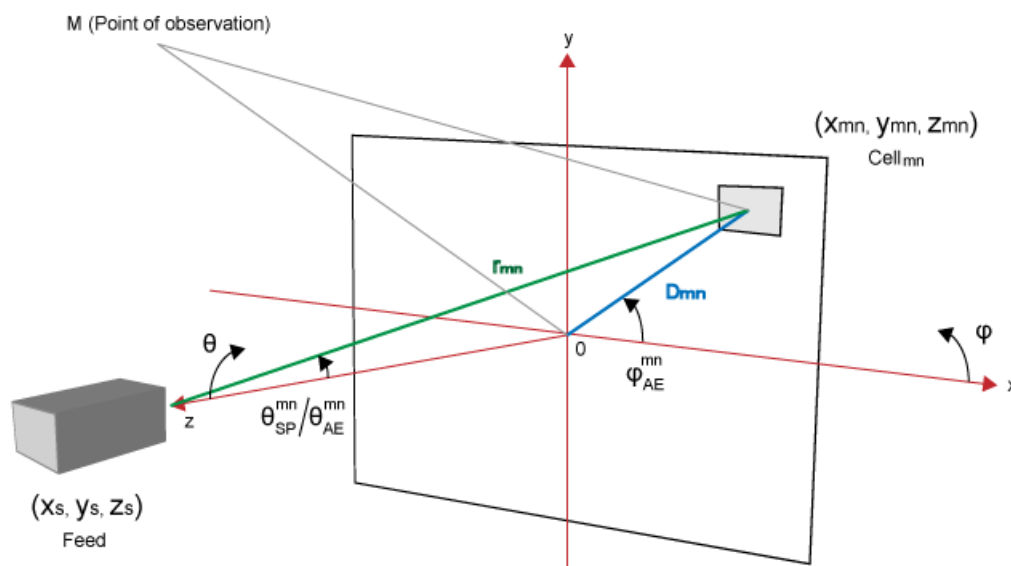


**Figure 3.3.:** Reflectarray modelisation drawing

Fig. 3.3, the point of origin is located on the reflectarray surface (reflecting panel) and the feed is aligned on the center of the reflectarray. The reflectarray is represented by a single patch which is also known as the elementary cell while the feed is represented by a rectangle box.

The feed chosen for this antenna is an open-ended waveguide manufactured by Flann Microwave and it is primarily characterized by its width ( $a$ ), height ( $b$ ) and length ( $l$ ) as shown in Fig. 3.4.  $l$  equals  $\lambda$  (wavelength of the working frequency). When running the reflectarray simulation in HRS, the feed is taken into account into the simulation by including its gain radiation pattern. In this case, the feed is simulated separately in HFSS around the desired working frequency and the gain is included in HRS.



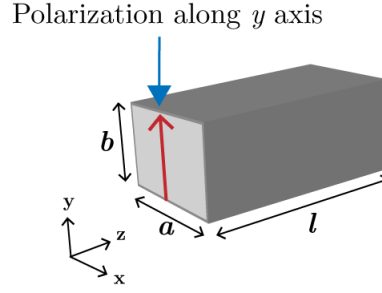


**Figure 3.4.:** Feed parameters

The feed is polarized along y-axis and in this configuration, only a single vector component of  $\vec{u}_y$  exists. Thus, the field equation of the feed can be simplified as in 3.5. This configuration is mainly used in all simulations discussed in this document (chapter 4 and chapter 5). Tab. 3.2 shows the feed dimensions for 2 main working frequencies used in this project.

$$\vec{E}_{SP} = E_{SP}(\theta, \varphi)\vec{u}_y \quad (3.5)$$

Frequency (GHz)	$a$ (mm)	$b$ (mm)	$l$ (mm)
20	10.668	4.318	15
76	2.540	1.270	3.95

**Table 3.2.:** Feed dimensions

The cell's position is noted as  $(x_{mn}, y_{mn}, z_{mn})$  and it indicates the index of the cell within the reflectarray. This also will be used later on as the index of the cell's matrix. The position of the feed is represented by  $(x_s, y_s, z_s)$  and the focal distance noted as  $F$  is equal to  $z_s$ . Each elementary cell on the reflecting panel has  $z_{mn} = 0$  value as they are positioned on the origin.

The distance between feed and elementary cell is noted as  $r_{mn}$ . In the drawing, this distance is represented by the green line. While the blue line, also known as  $D_{mn}$ , is the distance of the elementary cell from the origin (in  $xOy$  plane). All distances are defined in meter.

There are 3 angles defined in the drawing and they are  $\theta_{SP}^{mn}, \theta_{AE}^{mn}, \varphi_{AE}^{mn}$ . In this case  $\theta_{SP}^{mn} = \theta_{AE}^{mn}$  and these angles are defined between the line  $r_{mn}$  and focal distance. Another angle is  $\varphi_{AE}^{mn}$  which is used to indicate the position of the elementary cell on the  $xOy$  plane. Tab. 3.3 shows the summary of the parameters used in the drawing.

Some of the parameters need to be calculated in order to use them in the directivity's calculation. They are  $D_{mn}, r_{mn}, \theta_{AE}^{mn}$  and  $\varphi_{AE}^{mn}$ .  $D_{mn}$  and  $r_{mn}$  are obtained

### 3.2 Parameters definitions

Parameters	Description
$x_{mn}, y_{mn}, z_{mn}$	The coordinate of the elementary cell. $z_{mn} = 0$
$x_s, y_s, z_s$	The coordinate of the feed
$F$	Focal distance. $F = z_s$ in case the feed is centered to the reflectarray
$r_{mn}$	The distance between feed and elementary cell
$D_{mn}$	The distance of the elementary cell from the origin ( $O$ )
$\theta_{SP}^{mn}, \theta_{AE}^{mn}$	Angles which define the elementary cell from the feed's point of view. Note that $\theta_{SP}^{mn} = \theta_{AE}^{mn}$ .
$\varphi_{AE}^{mn}$	Angle which define the position of the elementary cell on $xOy$ plane

**Table 3.3.:** Parameters summary

using the equations 3.6 and 3.7. Because the feed is centered these parameters are set to  $x_s = y_s = 0$ .

$$D_{mn} = \sqrt{x_{mn}^2 + y_{mn}^2} \quad (3.6)$$

$$r_{mn} = \sqrt{x_{mn}^2 + y_{mn}^2 + z_s^2} \quad (3.7)$$

The coordinates for each cell will be calculated automatically by the program, and for that, the inter-element spacing distance which separates each cell from each other need to be specified. In this case, the distance is taken equal to  $\lambda/2$  in order to avoid the appearance of the grating beam.  $\lambda$  is the wave length of the working frequency of the antenna and in this project, the working frequency is 20 GHz which equals to  $\lambda = 15$  mm. For the angles,  $\theta_{AE}^{mn}$  and  $\varphi_{AE}^{mn}$  can be calculated using the equations 3.8 and 3.9.

$$\theta_{AE}^{mn} = \tan^{-1} \sqrt{\frac{x_{mn}^2 - y_{mn}^2}{z_s^2}} \quad (3.8)$$

$$\varphi_{AE}^{mn} = \text{sign}(y_{mn} - y_s) \times \cos^{-1} \frac{\sqrt{x_{mn}^2}}{\sqrt{x_{mn}^2 + y_{mn}^2}} \quad (3.9)$$

### 3.3. Directivity calculation

As being discussed in sec. 3.1, to obtain the directivity of the reflectarray, the calculation is not a straight forward process. The steps are illustrated in Fig. 3.1 but an adjustment is needed in case of reflectarray, where the coefficient of transmission will be replaced by the reflection coefficient when calculating elementary cell's radiated electrical field. In this section, the steps and the calculations adapted for reflectarray will be discussed.

#### 3.3.1. Power received at the elementary cell

The first step is to calculate the power received at each elementary cell using 3.10. The parameters notations are different from the formula used in 3.1 as the notations used are renamed base on the Fig. 3.3.

$$P_R^{mn} = \left(\frac{\lambda}{4\pi r_{mn}}\right)^2 \times G_{SP}(\theta_{SP}^i, \varphi_{SP}^i) \times D_C^{mn}(\theta_{AE}^{mn}, \varphi_{AE}^{mn}) \times P_F \quad (3.10)$$

$G_{SP}$  represents the gain for the feed. This parameter value can be obtained from the simulation value obtained with HFSS or it can be approximated by using  $\cos^n \theta$  function. In this case, the focal to diameter ratio is 0.5, which means that the subtended angle is equals to  $45^\circ$ . According to [14] the aperture efficiency is related directly to the subtended angle and for  $45^\circ$ ,  $n = 5$ , will give the maximum aperture efficiency. Another possible value is to set the gain to a constant value which is 1. This might be useful for validation purpose of the directivity equation.

$D_C^{mn}$  is the directivity for each elementary cell. In this case, the values are assumed to be identical for all elementary cells. The value can be either set to be a constant value which is equals to 1 or using cos approximation.

#### 3.3.2. Incident wave at the elementary cell

From 3.10, the arrived incident wave on each elementary cell can be obtained using 3.11 and it is noted as  $a_1^{mn}$ .

$$a_1^{mn} = \sqrt{P_R^{mn}} \times \exp(-j \frac{2\pi r_{mn}}{\lambda}) \times \exp(j \phi_F^{mn}) \quad (3.11)$$

In 3.11,  $\phi_F^{mn}$  represents primary feed phase distribution in the far field region on the  $mn$  elementary cell. In the first step,  $\phi_F^{mn} = 0$  because it is assumed to be a constant over the antenna aperture. When working with the equations for

this simulator, the preferred angle unit is degrees instead of radians and the main reason is because in this context, the phase-shift distribution values as discussed sec. 2.2.4 in are expressed in degrees. After applying the conversion and substitution of  $k_0 = \frac{2\pi r_{mn}}{\lambda}$ , the equation for the incident wave can be written as in 3.12.

$$a_1^{mn} = \sqrt{P_R^{mn}} \times \exp(-jk_0 r_{mn}) \quad (3.12)$$

#### 3.3.3. Reflected wave at the elementary cell

After determining the incident wave, from that point the reflected wave for a single elementary cell can be obtained. In this step, an adjustment is required where the reflection coefficient  $S_{11}$  is used instead of transmission coefficient  $S_{21}$ . Because of this the term ‘‘Transmitted wave’’ in sec. 3.1 is changed to ‘‘Reflected wave’’ in this section. This coefficient plays an important role in this simulator because it links the analytic formula to a real electromagnetic software simulator. In this case the software chosen is Ansoft HFSS. This will help the simulator to calculate more accurate simulation results as the elementary cell  $S_{11}$  values simulated with Ansoft HFSS are considered to reflect the real life environment and condition.

The  $S_{11}$  coefficient is a complex number where its argument  $Arg(S_{11})$  is the phase required to compensate the incident wave travel’s distance. Each elementary cell has its own  $S_{11}$  value and the argument is called  $\varphi_R$  which equals to the phase-shift distribution values. The equation to calculate this value has been introduced in sec. 2.2.4 and is recalled in 3.13 with the adapted notations.  $\varphi_b$  and  $\theta_b$  are the direction of the desired focused beam.

In normal case where the focused beam is directed perpendicular to the reflecting panel, the values for these angles are  $\varphi_b = 0, \theta_b = 0$ , and this will give  $\varphi_R^{mn} = k_0 r_{mn}$  in radians or  $\varphi_R^{mn} = k_0 r_{mn} \times \frac{180}{\pi}$  in degrees. In this case, the phase values depend uniquely from the distance of the cell to the feed which is  $r_{mn}$ . In the ideal case, the  $|S_{11}| = 1$ . This means that no loss is encountered at the elementary cell level and the reflection coefficient can be written as in 3.15.

$$\varphi_R^{mn} = k_0(r_{mn} - (x_{mn} \cos \varphi_b + y_{mn} \sin \varphi_b) \sin \theta_b) \quad (3.13)$$

$$S_{11}^{mn} = |S_{11}^{mn}| \times \exp(j\varphi_R^{mn}) \quad (3.14)$$

$$S_{11[ideal]}^{mn} = \exp(j\varphi_R^{mn}) \quad (3.15)$$

The radiated field for a single elementary cell is a multiplication between  $S_{11}$  coefficient and the incident wave and is shown in 3.18. This is where the compensation of the incident wave delay takes place and this is the most crucial part in the simulator calculation. The general equation of the radiated field can be written as in 3.16 and it can be simplified into a single component of  $\vec{u}_y$  (Equation 3.17) because the feed is polarized along y-axis ( $\vec{u}_y$ ) and the elementary cell reflected wave's polarization is assumed to be identical.

$$\vec{E}_r^{mn} = E_{rx}^{mn} \vec{u}_x + E_{ry}^{mn} \vec{u}_y \quad (3.16)$$

$$\vec{E}_r^{mn} = E_{ry}^{mn} \vec{u}_y \quad (3.17)$$

To simplify the notations,  $E_{ry}^{mn}$  is written as  $E_r^{mn}$ .

$$E_r^{mn} = S_{11}^{mn} \times a_1^{mn} \times \frac{\exp(-jkr)}{kr} \quad (3.18)$$

Equation 3.18 can be substituted with the expression of  $S_{11}$  and  $a_1^{mn}$  which will result 3.19. In case  $\varphi_b = 0, \theta_b = 0$ , the  $Arg(S_{11}) = \varphi_R^{mn} = k_0 r_{mn}$ . Using this condition, the equation 3.19 can be simplified to be 3.20. In this equation, if  $\varphi_R^{mn} = k_0 r_{mn}$ , then *Compensation* term will be equal to 1. In this case, the incident wave delay due to the travel distance of  $r_{mn}$  is considered to be perfectly compensated by  $\varphi_R^{mn}$  and is categorized as the ideal case.

$$E_r^{mn} = |S_{11}^{mn}| \times \exp(j\varphi_R^{mn}) \times \sqrt{P_R^{mn}} \times \exp(-jk_0 r_{mn}) \times \frac{\exp(-jkr)}{kr} \quad (3.19)$$

$$E_r^{mn} = |S_{11}^{mn}| \times \sqrt{P_R^{mn}} \times \underbrace{\exp(j(\varphi_R^{mn} - k_0 r_{mn}))}_{\text{Compensation}} \times \frac{\exp(-jkr)}{kr} \quad (3.20)$$

In real life condition, the  $S_{11}$  coefficient value comes from the reflection coefficient of the elementary cell and the produced value is not fully identical to the desired phase value. It is impossible to obtain an identical value to  $\varphi_R^{mn}$  when designing elementary cell. This is set by the physical and the geometry of the design and this depends on the fabrication technology, for example using microstrip technology, the smallest size of the printing capability is  $\pm 0.1$  mm.

Some tolerances are required when designing elementary cell so that the phase value produced by the cell is around  $\varphi_R^{mn}$  in order to minimize the difference especially for small reflectarray. The ideal case is useful when comparing the reflectarray performance especially when evaluating phase errors and the order of correction applied as discussed in sec. 2.5.

$E_r^{mn}$  is only for a single elementary cell which is represented by its index  $mn$  and to get the total radiated field, the  $E_r^{mn}$  on each cell needs to be summed up and it is explained on the next section.

### 3.3.4. Total radiated wave

After determining the radiated electrical field on each elementary cell, the total radiated wave by the reflectarray aperture can be calculated using 2D array factor.

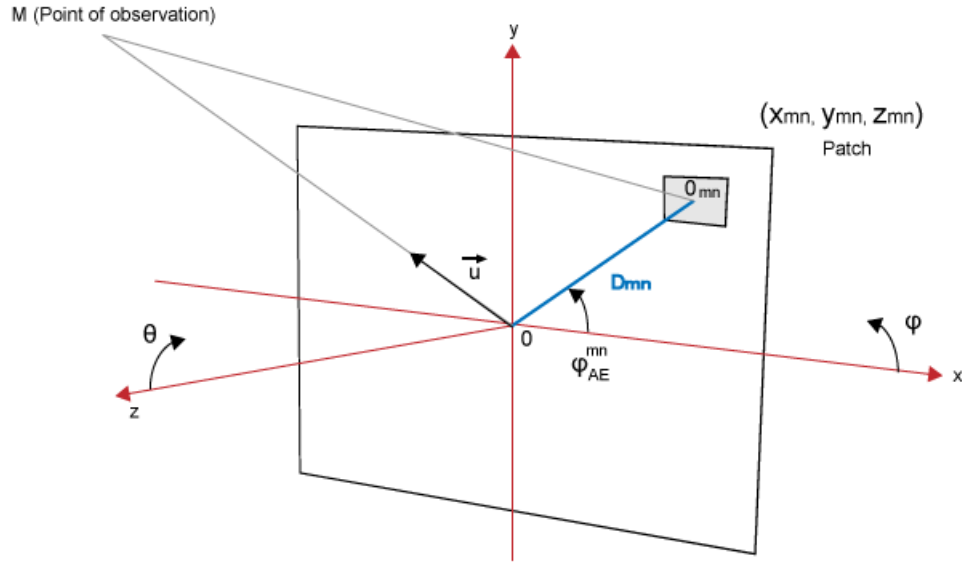


**Figure 3.5.:** Calculation of total radiated drawing

Fig. 3.5 is used to help and to understand the calculation. From this figure, the total radiated wave can be written as in 3.21.  $D_C^{mn}$  is the directivity for each cell, this value can be approximated by the function  $\cos$  over the cell area or can be set to a constant (equals to 1).  $\vec{u}$  is the elementary vector, where  $\vec{u} = \vec{u}_r$  of spherical coordinate.

$$E_T(\vec{u}) = \sum_m \sum_n E_r^{mn} \times \sqrt{D_C^{mn}} \times \exp(j\vec{k} \cdot \overrightarrow{O_{mn}M}) \quad (3.21)$$

In 3.21, the values of  $E_r^{mn}$  and  $D_C^{mn}$  are already known and the expression of  $\vec{k} \cdot \overrightarrow{O_{mn}M}$  is to be determined in the next calculations. This expression can be rewritten as in 3.22.  $\vec{k} \cdot \overrightarrow{OM}$  can be calculated directly as in 3.23.

$$\vec{k} \cdot \overrightarrow{O_{mn}M} = \vec{k} \cdot \overrightarrow{OM} + \vec{k} \cdot \overrightarrow{O_{mn}O} \quad (3.22)$$

$$\vec{k} \cdot \overrightarrow{OM} = \frac{2\pi}{\lambda} \vec{u} \cdot (r\vec{u}) = \frac{2\pi}{\lambda} r \quad (3.23)$$

The calculation of  $\vec{k} \cdot \overrightarrow{O_{mn}\hat{O}}$  requires additional steps. First, the expression of  $\overrightarrow{O_{mn}\hat{O}}$  needs to be determined.  $\overrightarrow{O_{mn}\hat{O}}$  has 2 components on  $x$  and  $y$  and can be expressed as  $\overrightarrow{O_{mn}\hat{O}} = X\vec{u}_x + Y\vec{u}_y$ . This expression multiplied by  $k$  will give the equation 3.24.

$$\vec{k} \cdot \overrightarrow{O_{mn}\hat{O}} = \frac{2\pi}{\lambda} x_{mn} \vec{u} \cdot \vec{u}_x + \frac{2\pi}{\lambda} y_{mn} \vec{u} \cdot \vec{u}_y \quad (3.24)$$

The scalar product for  $\vec{u} \cdot \vec{u}_x$  is  $\sin \theta \cos \varphi$  and for  $\vec{u} \cdot \vec{u}_y$  is  $\sin \theta \sin \varphi$ . Substituting these products into 3.24 will produce 3.25.

$$\vec{k} \cdot \overrightarrow{O_{mn}\hat{O}} = \frac{2\pi}{\lambda} \sin \theta \{x_{mn} \cos \varphi + y_{mn} \sin \varphi\} \quad (3.25)$$

The distance of the elementary cell from the feed in  $x$  and  $y$  axis can be rewritten using angle  $\varphi_{AE}^{mn}$  and  $D_{mn}$  as in 3.26 and 3.27. This will reduce the number of parameters from 4 ( $x_{mn}, x_s, y_{mn}, y_s$ ) to 2 ( $\varphi_{AE}^{mn}$  and  $D_{mn}$ ) which will produce a simpler equation as in 3.28.

$$x_{mn} = \cos(\varphi_{AE}^{mn}) \times D_{mn} \quad (3.26)$$

$$y_{mn} = \sin(\varphi_{AE}^{mn}) \times D_{mn} \quad (3.27)$$

$$\vec{k} \cdot \overrightarrow{O_{mn}\hat{O}} = \frac{2\pi}{\lambda} \sin \theta \times D_{mn} \{ \cos(\varphi_{AE}^{mn}) \cos \varphi + \sin(\varphi_{AE}^{mn}) \sin \varphi \} \quad (3.28)$$

3.28 can be simplified using cos trigonometric identity which is  $\cos(a - b) = \cos(a) \cos(b) + \sin(a) \sin(b)$ , which will give new equation as in 3.29.

$$\vec{k} \cdot \overrightarrow{O_{mn}\hat{O}} = \frac{2\pi}{\lambda} \sin \theta \times D_{mn} \times \cos(\varphi - \varphi_{AE}^{mn}) \quad (3.29)$$

The final equation for  $\vec{k} \cdot \overrightarrow{O_{mn}\hat{M}}$  is the combination of 3.23 and 3.29. The equation is written in 3.30. This can be replaced in 3.21 and will give complete equation 3.31 which depends on the position of the elementary cell on the reflecting panel.

$$\vec{k} \cdot \overrightarrow{O_{mn}\hat{M}} = \frac{2\pi}{\lambda} r + \frac{2\pi}{\lambda} \sin \theta \times D_{mn} \times \cos(\varphi - \varphi_{AE}^{mn}) \quad (3.30)$$



$$E_T(\vec{u}) = \sum_{m=1}^N \sum_{n=1}^N E_r^{mn} \times \sqrt{D_C^{mn}} \times \exp j \frac{2\pi}{\lambda} (\sin \theta \times D_{mn} \times \cos(\varphi - \varphi_{AE}^{mn})) \quad (3.31)$$

As the reflectarray is square,  $N$  is the total number of cells in  $x$  and  $y$  axis.

### 3.3.5. Power density and directivity

After obtaining the total radiated field discussed previously, the power density and the directivity of the reflectarray can be calculated. By definition, the power density or noted as  $S(\theta, \varphi)$  is defined as in 3.32, where  $\eta_0 = 120\pi \Omega$ .

$$S(\theta, \varphi) = \frac{1}{2\eta_0} \vec{E}_T \times \vec{E}_T^* = \frac{1}{4\pi r^2} |E_T|^2 \quad (3.32)$$

By replacing  $|E_T|$  with its proper expression in 3.32, the power density  $S(\theta, \varphi)$  can be expressed as in 3.33.

$$S(\theta, \varphi) = \frac{1}{2\eta_0} \left| \sum_m \sum_n \sqrt{D_C^{mn}} \times E_r^{mn} \exp j \frac{2\pi}{\lambda} (\sin \theta \times D_{mn} \times \cos(\varphi - \varphi_{AE}^{mn})) \right|^2 \quad (3.33)$$

By definition, the directivity is the power density divided by the radiated power of the isotropic antenna as written in 3.34.  $P_{C2}$  is the power radiated by the elementary cells and it is equals to  $\sum_m \sum_n |E_r^{mn}|^2$ .

$$D(\theta, \varphi) = \frac{S(\theta, \varphi)}{S_i(\theta, \varphi)} = 4\pi r^2 \frac{S(\theta, \varphi)}{P_{C2}} \quad (3.34)$$

Using the definition, the directivity for the reflectarray is equal to the equation written in 3.35.

$$D(\theta, \varphi) = \frac{\left| \sum_m \sum_n \sqrt{D_C^{mn}} \times E_r^{mn} \exp j \frac{2\pi}{\lambda} (\sin \theta \times D_{mn} \times \cos(\varphi - \varphi_{AE}^{mn})) \right|^2}{\sum_m \sum_n |E_r^{mn}|^2} \quad (3.35)$$

Equation 3.35 is used to calculate the directivity in the simulator. The calculation is not a straight forward process but requires multiples steps and intermediate calculations as demonstrated in this section. Many large calculations are divided into sub calculations in order to ease the translation process between mathematic model and computer programming model.

### 3.4. Simulation program

In previous section sec. 3.3, the theory and the calculations behind this simulator program are discussed. This section will discuss about the simulator itself in term of its functionalities and its running environment especially the process to use the reflection coefficient simulated by Ansoft HFSS.

The simulation program is called “Hybrid Reflectarray Simulator” or HRS, because the calculations to obtain the radiation pattern are realized with the combination of Matlab and Ansoft HFSS. HRS is considered as a collection of libraries which groups all mathematic functions related to the reflectarray calculation instead of a standalone program.

Using these libraries, many type of program can be coded such as the directivity simulator and the program to automate the process to draw the elementary cell patch motif. Fig. 3.6 shows the simulator functionalities overview.

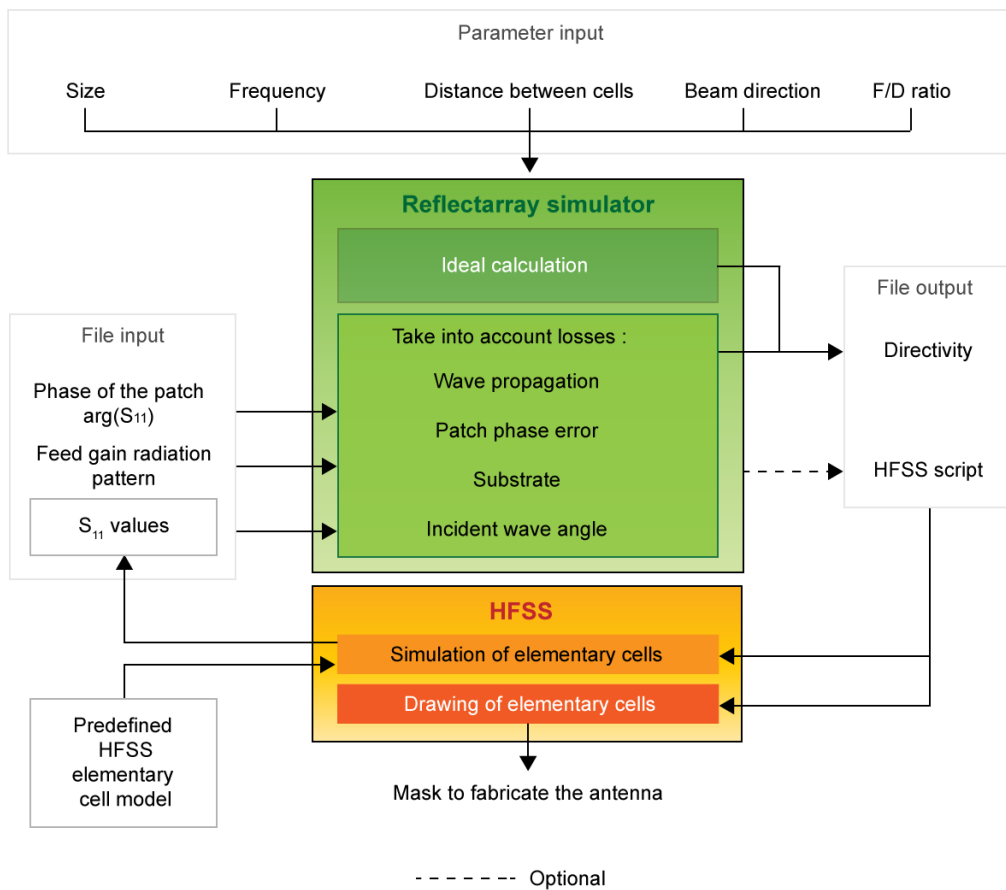


Figure 3.6.: HRS functionalities overview

### 3.4.1. Functionalities

In Fig. 3.6, HRS is represented by the green rectangle and Ansoft HFSS is represented by the orange rectangle. HRS is capable to produce 2 types of radiation patterns. The first one is the ideal directivity radiation pattern which assumes that the incident wave delay is perfectly compensated by the reflection coefficient phase  $Arg(S_{11})$  of the elementary cell and no loss is encountered at the elementary cell level ( $|S_{11}| = 1$ ) as discussed in sec. 3.3.3.

In this case, HRS requires only the parameter's inputs to complete the calculation. These parameter's inputs are compulsory and they are; the size of the reflectarray, the working frequency, the distance which separates the elementary cells, the focused beam direction and the focal length to diameter ratio. The description for these parameters is shown in Tab. 3.4.

Parameter	Description
Size	The size indicates the number of elementary cells in the reflecting panel and for practical reason, it is an odd number
Frequency	Working frequency of the antenna
Distance between cells	This parameter is expressed in multiple of lambda. Example, for an elementary cell with size of $0.5 \times \lambda$ , the parameter value is equal to 0.5
Beam direction	The desired focused beam direction $\theta_b, \varphi_b$ in degrees
F/D ratio	The ratio will determine the focal distance which is defined here as the distance between the feed and the center of the reflectarray

**Table 3.4.:** HRS Parameter input description

The second type of radiation pattern is calculated by taking into account 4 types of losses which are the loss due to wave propagation, the compensated phase errors, the loss in the substrate material and the loss due to the simplification of incident wave angle. By including these losses into the calculation, the expected simulation result is considered to approach the one obtained from full-wave simulators.

In the second case, HRS requires both parameters and file inputs to function correctly. There are 2 types of file input. The first file contains the feed gain radiation pattern which is used to simulate the loss due to the wave propagation. The  $\cos^n$  function approximation can be used as an alternative to replace this file. The second file contains the  $S_{11}$  coefficients for each elementary cell.  $S_{11}$  data inside it will be used to approximate the losses due to the phase error's compensation and the loss in the dielectric material especially due to the  $\tan(\delta)$  factor.

### 3.4.1.1. Feed gain radiation pattern file

The feed gain radiation pattern file can be obtained by simulating feed design at the working frequency in Ansoft HFSS. The obtained radiation pattern can be exported into text file to be read by HRS. Usually, this process is done once at the beginning and can be reused to do the other simulations at the same frequency.

### 3.4.1.2. Reflection coefficient ( $S_{11}$ ) file for passive reflectarray

For passive reflectarray, the elementary cell is designed to produce reflected phase which is able to compensate the incident wave delay. Taking for example a single layer elementary cell that uses rectangular patch as the radiating element. Depending on the position of this cell and the distance from the feed, the size of the patch will be different thus will produce different reflected phase values. This shows that the process to generate the  $S_{11}$  values for each elementary cell is not a simple task and needs multiple sub tasks to generate the complete file. Fig. 3.7 shows the different tasks to generate this file.

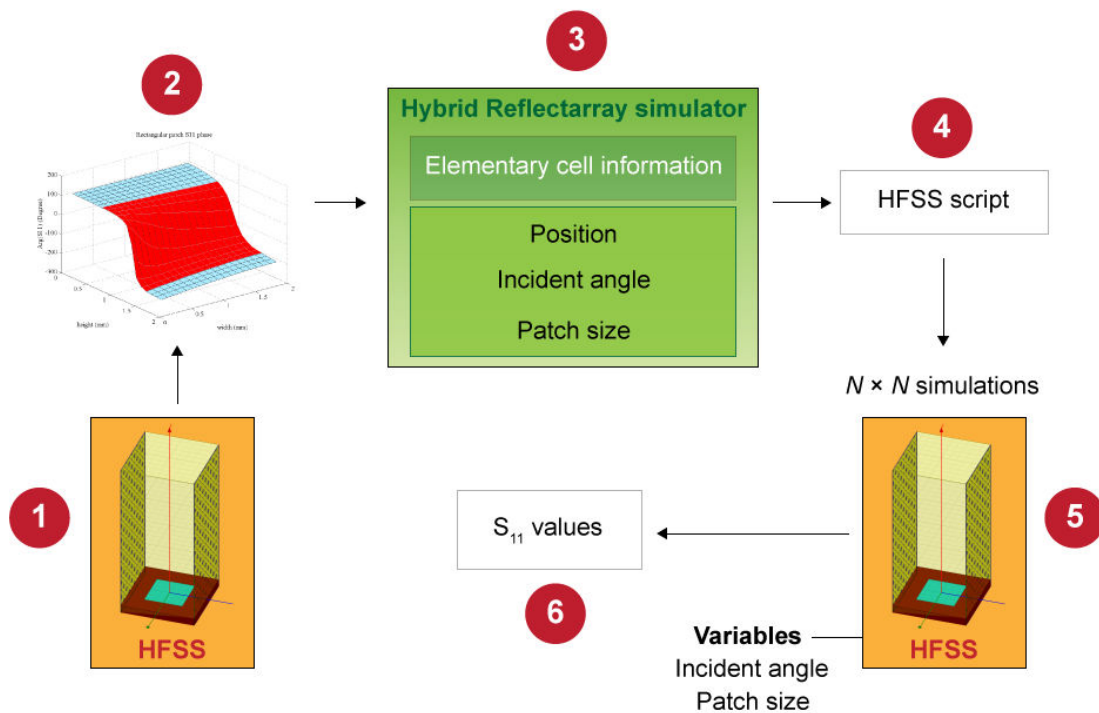


**Figure 3.7.:** Different tasks to generate  $S_{11}$  values for a reflectarray with  $N \times N$  elements

The first task is to prepare the elementary cell model in HFSS with the correct substrate thickness, material and elementary cell size. This model will be used to calculate the reflected phase variations when varying the radiating element geometry size. In case for rectangular patch, this will be the height and the width of the patch. More detail on the elementary cell HFSS simulation model will be discussed in sec. 3.4.2.

Secondly, the obtained phase variations will be inserted to HRS as the file input. With the combination of the phase variations data and the specified parameter input, HRS will be able to calculate for each elementary cell, the position within reflecting panel, the incident angle and the required patch size to obtain the nearest value of  $\varphi_R^{mn}$  (discussed in sec. 3.3.3). Because it is impossible to match exactly the  $\varphi_R^{mn}$  value, some tolerances are required and can be adjusted until all elementary cells patch size can be found.

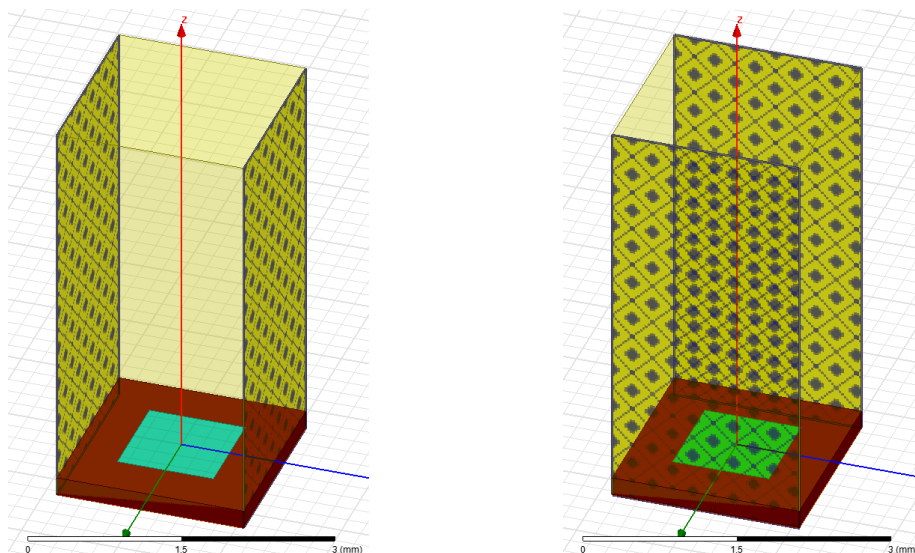
In the third task, using the collected and calculated data, HRS will generate a HFSS script which contains the patch size (width and height) and the incident angle information for each elementary cell. In total there will be  $N \times N$  elementary cells. The script will be useful to automate the simulation process especially when the size of the reflectarray is large.

For the fourth task, the script written in Visual Basic, will be executed to run the  $N \times N$  elementary cell simulations. For each simulation, the script will automatically change the specified variables with their proper values stored in the script file and at the end of each simulation, the obtained  $S_{11}$  value will be saved in the specified text file. In case of rectangular patch, the variables are the incident angle and the patch size. Finally, after finishing all simulations, all the values of  $S_{11}$  can be found in the text file and this file corresponds to the “ $S_{11}$  values” label in task 6 in Fig. 3.7. This file can be used with HRS to calculate the directivity radiation pattern which takes into account different losses discussed previously.

### 3.4.2. Ansoft HFSS elementary cell simulation model

Using HRS,  $S_{11}$  values have significant impact on the calculated radiation pattern. To obtain these values, electromagnetic simulation software or technique such as waveguide simulator (WGS) measurement [73] can be used. However the measurement techniques are only suitable for reconfigurable elementary cell with fixed geometry because less number of elementary cell design is required. In case of passive elementary cell, many design variations are required to compensate the incident wave delay and plus the setup for the measurement is costly. In this project,  $S_{11}$  values are simulated using Ansoft HFSS and to approach the real world situation, the phase errors due to the incident wave's angle is taken into account in the simulation.

Using this software, there are 2 available configurations. The first one is by assuming the wall boundaries around the cell are magnetic and electric field walls as shown in Fig. 3.8. In those circumstances, the cell can be supposed to be periodically infinite. To excite the cell, the plane wave port is used.



a) Elementary cell electrical wall

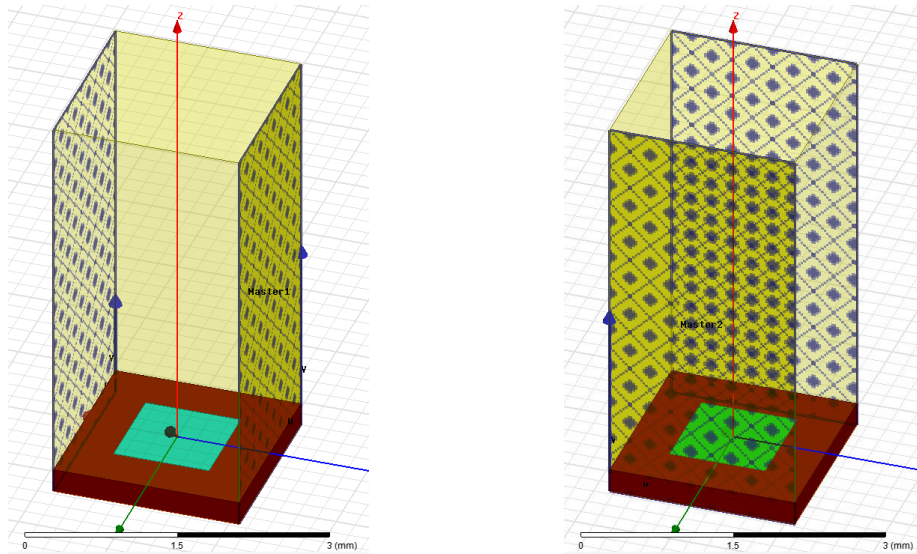
b) Elementary cell magnetic wall

**Figure 3.8.:** Elementary cell model using electrical and magnetic wall boundaries

The configuration shown in Fig. 3.8 works well, but it is only true for normal incident wave. In this case the incident electric field is forced to be perpendicular to the electric walls due to the boundary conditions. Thus to include the phase errors due to the incident wave angle's variation, another configuration is needed.

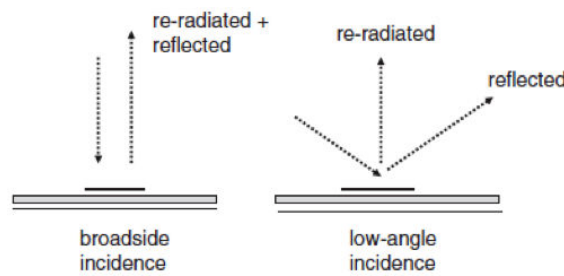
The second configuration is by using “Floquet mode” shown in Fig. 3.9. Using this mode the incident wave's angle can be specified within periodic and infinite elementary cell environments. The configuration looks similar to the configuration using electrical and magnetic wall boundaries, but instead of those boundaries, the master and slave wall boundaries are used.

Another thing to be considered is, the position to measure the  $S_{11}$  value. In magnetic and electric walls configurations, the  $S_{11}$  is measured on the port surface. In “Floquet mode” configuration, the  $S_{11}$  is measured on the elementary cell surface. This is not due to the “Floquet mode” but primarily caused by the incident wave's angle variation. This can be explained by referring Fig. 3.10 [20].



a) Floquet mode Master 1 wall

b) Floquet mode Master 2 wall

**Figure 3.9.:** Elementary cell model using Floquet mode boundaries**Figure 3.10.:** Re-radiated and reflected waves of a elementary cell

For a normal incident wave or referred as broadside incidence, both of reflected and re-radiated waves are turned back in the same direction as the incident wave. In this case, measuring the  $S_{11}$  at the port surface is reasonable. On the other hand, if the incident wave angle (referred to low-angle incidence) is changed, only re-radiated wave is turned back towards the measurement surface. This means that the reflected wave has been ignored. In order to obtain a correct value of  $S_{11}$ , the value needs to be measured on the elementary cell's surface and not on the port surface.

### 3.4.3. Environment and structure

HRS is written in Matlab scripting language. The choice of using Matlab is because it supports a lot of scientific features such as matrix operation, good plotting features and the most important is an excellence and complete documentation. HRS has been tested and executes smoothly on mid-range Windows based computer. The generated Ansoft HFSS script can be executed either on Windows or Linux operating system with the condition that the software is correctly configured and installed.

Matlab scripting language can be programmed using object oriented programming or known as OOP [74]. This advantage makes the programming process becomes easier and the written codes are easy to be maintained. Using this OOP, the process to translate the formulas described in sec. 3.1 becomes a straight forward process as each object illustrated in Fig. 3.3 can be directly translated to objects in Matlab as shown in Fig. 3.11. More detail can be found in Appendix A.

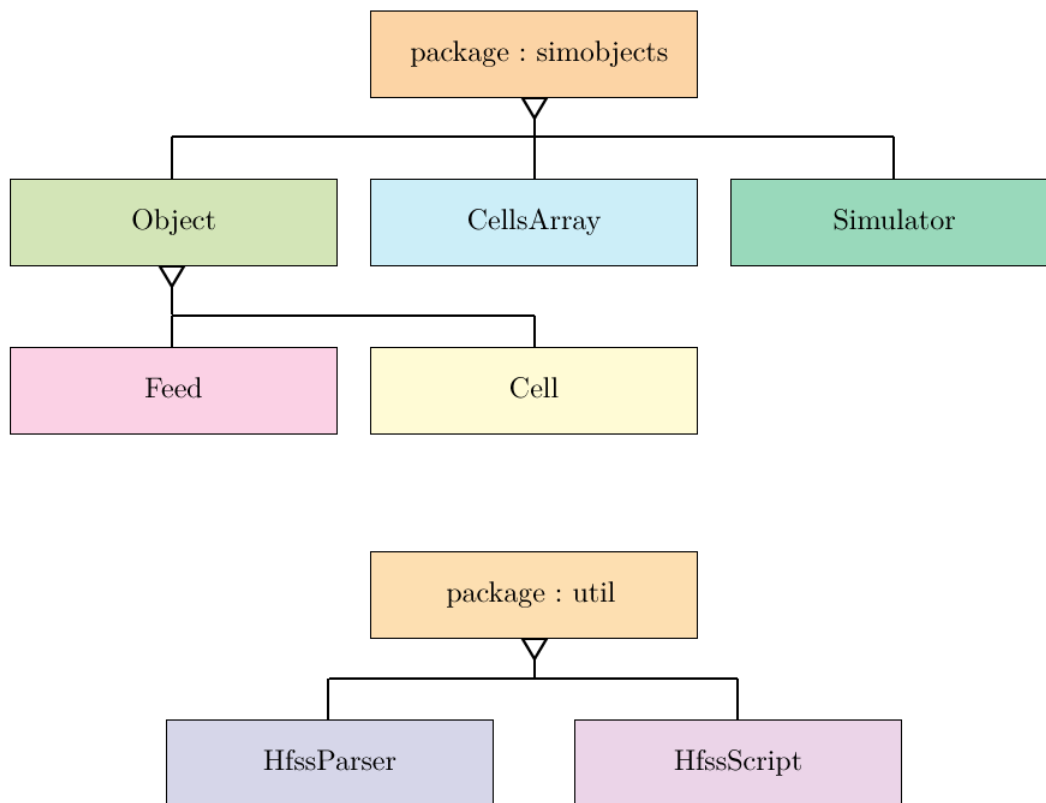


**Figure 3.11.:** HRS Matlab class diagram



### 3.5. Simulation analysis

This section will discuss the simulation results produced by HRS and the comparison of the directivity radiation pattern against results simulated entirely in Ansoft HFSS. Some analysis have been made to investigate the influence of reflectarray's size, focal distance and phase delay correction level to the simulated radiation pattern.

To test and validate the HRS simulation results, the design of 9x9 elementary cells reflectarray is chosen because it is faster to be simulated (full wave simulation with HFSS) compared to a large reflectarray. The chosen working frequency is 76 GHz and the focal to diameter ratio ( $f/D$ ) is 0.5. The elementary cell design is a single layer structure and its dimension is  $\lambda/2$  at 76 GHz. The substrate used is Duroid with the permittivity relative  $\epsilon_r$  equals to 2.23, dielectric loss tangent ( $\tan \delta$ ) equals to 0.005 and the thickness equals to 0.254 mm. Fig. 3.12 shows the HFSS model design and the elementary cell simulation model used by HRS.

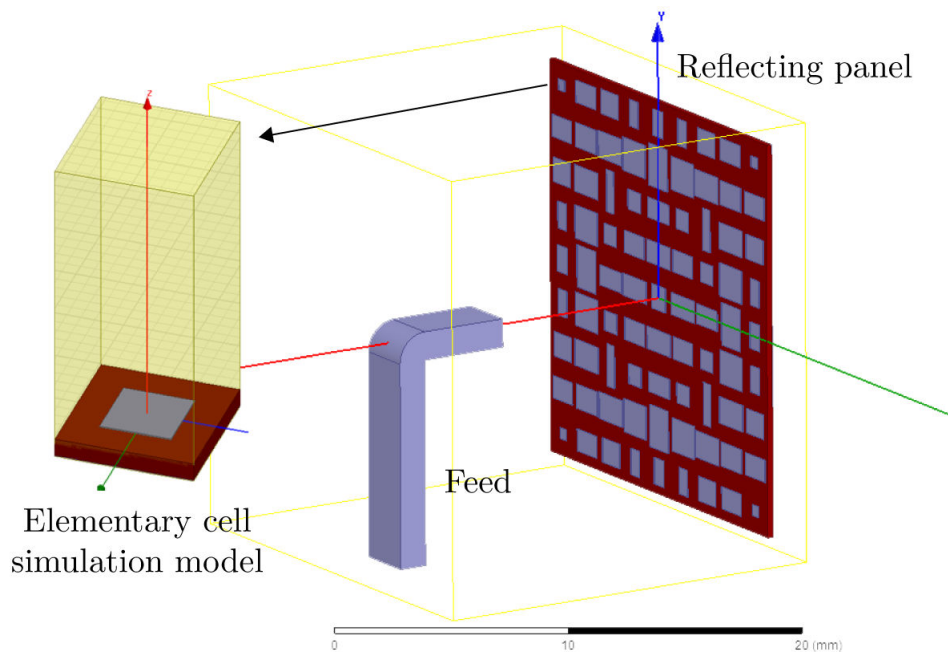


**Figure 3.12.:** 9x9 rectangular reflectarray HFSS simulation design at 76 GHz,  $f/D = 0.5$

For the elementary cell design, there are 2 types of radiating element designs (microstrip patch). The first design is rectangular patch which can be described by its width and height parameters. The second design is based on circle geometry but with hollow rectangle shape at the center. This geometry is named as “No Entry” patch as it resembles the no entry sign which can be seen on the road as shown in Fig. 3.13.

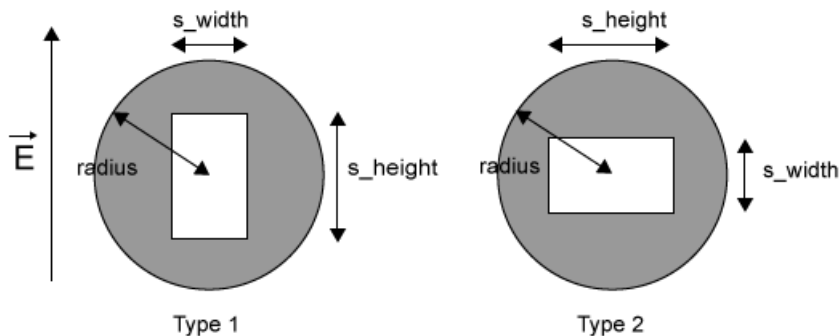


**Figure 3.13.:** No entry patch design as the radiating element

Both reflectarrays are fabricated using rectangular and no entry patches and measured. The dimension of these reflectarrays is  $4\lambda \times 4\lambda$  and there are in total 81 elementary cells with the reflecting panel width and height equals to 8.8 mm. These reflectarray are designed to focus the main beam at  $\varphi = 0^\circ, \theta = 0^\circ$ . The size of these reflectarrays is very small and in case of the measurement setup, it is difficult to align the feed to the center of reflecting panel as shown in Fig. 3.14.

Small size is chosen because it is well-known that small size reflectarray works worse than large size reflectarray, thus the comparison between HRS and the measurement is more difficult. Therefore if HRS works properly for small reflectarray, the simulation results for all sizes of reflectarray are confident to be correct.

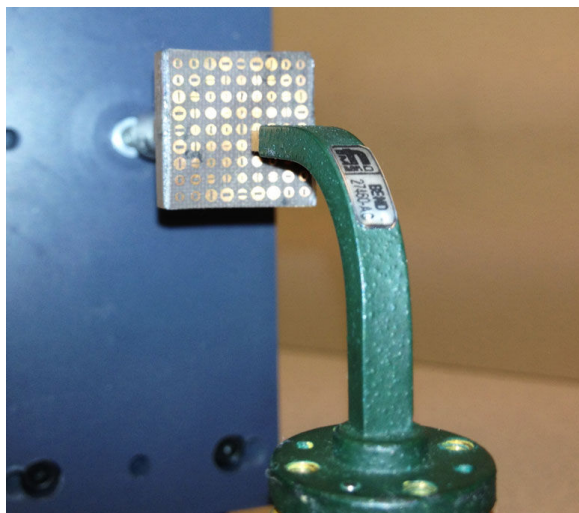


**Figure 3.14.:** 9x9 no entry patch reflectarray at 76 GHz,  $f/D = 0.5$

The results comparison will compare the gain radiation pattern between the result produced by HRS, Ansoft HFSS and the measurements of the fabricated reflectarray.

### 3.5.1. Results comparison

Fig. 3.15 and Fig. 3.17 show respectively the H-plane gain radiation pattern for rectangular reflectarray and H-plane gain radiation pattern for no entry reflectarray. For each reflectarray, there are 3 lines. The red dots represents the simulation results calculated by HRS and the purple dashed line represents the results calculated by HFSS, while the measurements are represented by straight blue line. In this case the directivity for each elementary cell  $D_C^{mn}$  is approximate using  $\cos^n$  with  $n = 3$ . This means that only the elementary cells in the center become the major contributor in the calculation.

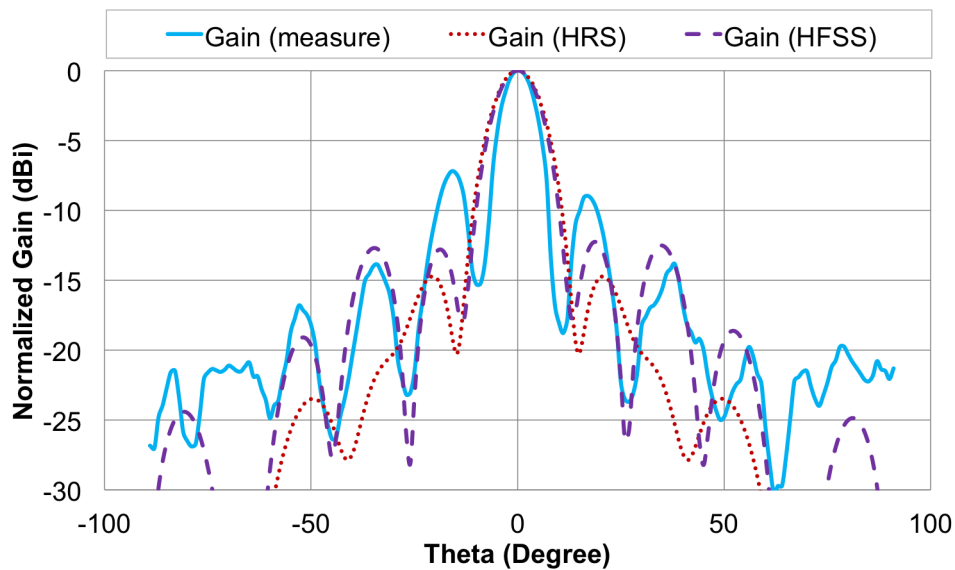


**Figure 3.15.:** H-plane rectangular reflectarray gain pattern radiation at 76GHz

Comparing the radiation pattern in Fig. 3.15, the radiation pattern produced by HFSS has higher side lobes compared to the one calculated using HRS. The main lobe beam width for both HFSS and HRS has small different with HRS having larger beam width. This can be explained by the ignorance of the mutual coupling effects between elementary cells in HRS calculation, while in HFSS, the coupling effect is taken into account which contributes to produce higher side lobes and narrower main lobe.

Looking at Fig. 3.16, the majorities of the rectangular patches on the reflecting panel are large and approach one to another. This can produce the strong mutual coupling between each cells, as can be noticed in the simulation and measurement results. The measured radiation pattern approaches the result simulated by HFSS better than the radiation pattern calculated by HRS.

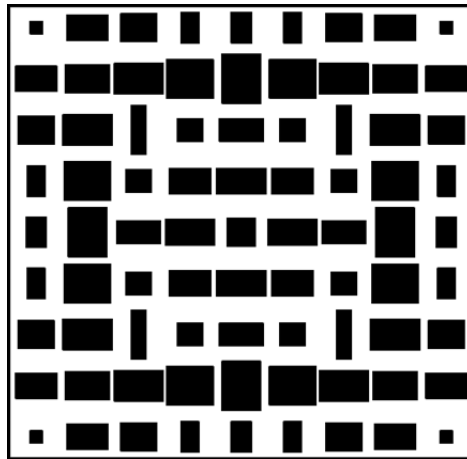


**Figure 3.16.:** 9x9 rectangular reflectarray elementary cell radiating elements geometry

For no entry reflectarray, the radiation patterns can be seen in Fig. 3.17. In this case, both radiation patterns calculated by HRS and HFSS seem to approach each other better than the radiation pattern for rectangular reflectarray. The first 3 side lobes for both patterns share the same oscillations pattern with slightly higher side lobes and wider main lobe produced by HRS. The patterns are almost identical in the main lobe area. This indicates that the no entry patch has low mutual coupling effect because HRS ignores this effect in the calculation.

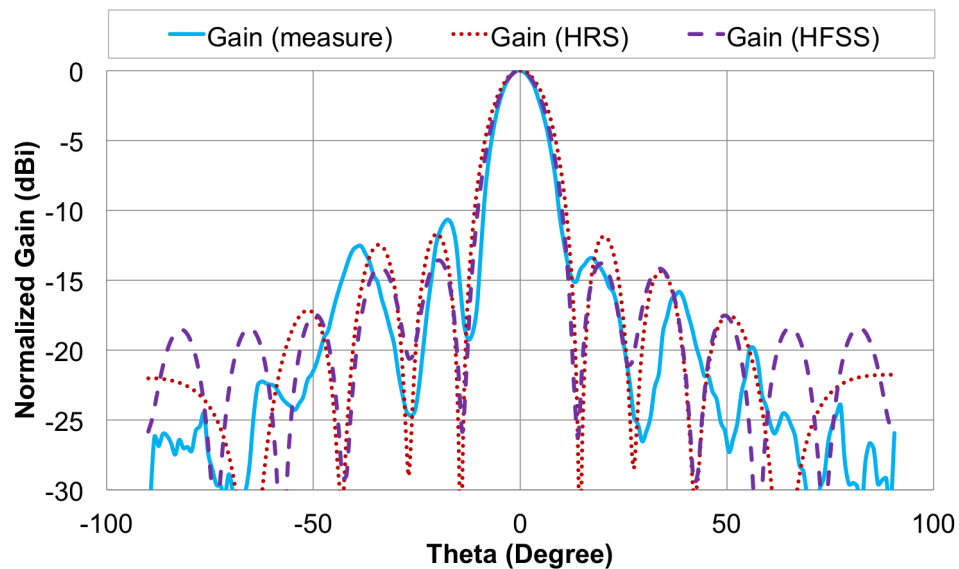


**Figure 3.17.:** H-plane no entry reflectarray gain pattern radiation at 76GHz

The radiating element shapes as shown in Fig. 3.18 on the no entry reflecting panel occupy less space than the shapes on the rectangular reflecting panel, this will reduce the mutual coupling between cells. In this case, the higher side lobes level is caused by the spillover and aperture blockage effects. These two effects are ignored in the HRS calculation.

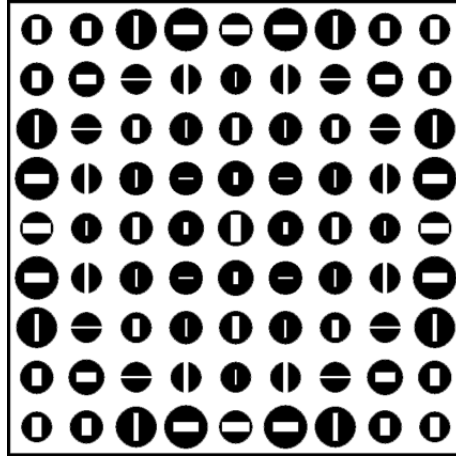


**Figure 3.18.:** 9x9 no entry reflectarray elementary cell radiating elements geometry

In addition to the radiation patterns, the maximum gain values are also simulated, as shown in Fig. 3.19. The maximum gain values comparisons are able to indicate whether HRS is capable to do acceptable and correct calculation results outside of the reflectarray working frequency.

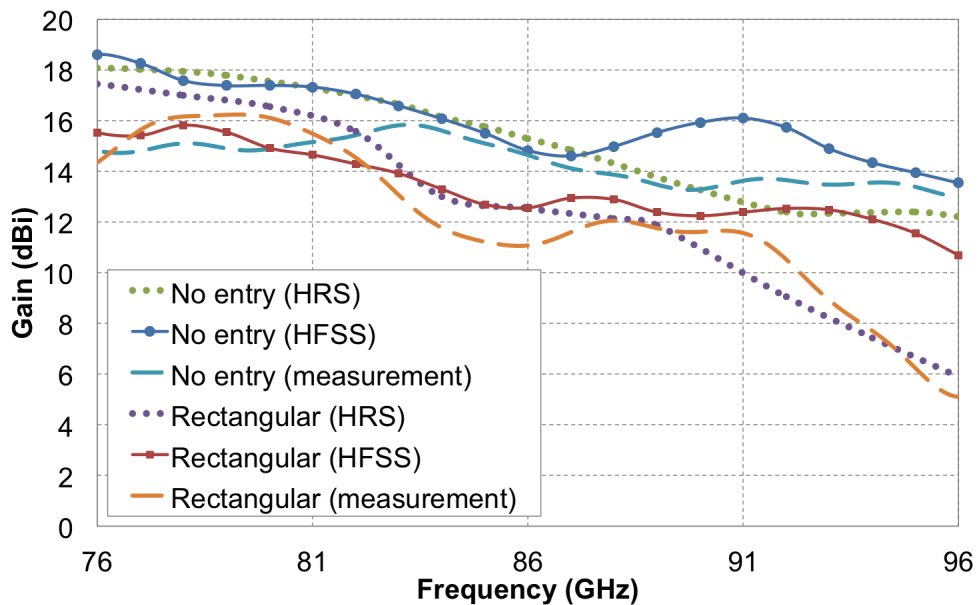


**Figure 3.19.:** Maximum gain for rectangular and no entry reflectarrays

In Fig. 3.19, for each reflectarray, there are 3 lines. The dots represents the simulation results calculated by HRS and the dot lines represents the results calculated by HFSS, while the measurements are represented by dashed lines. For the gain values calculated with HRS and HFSS, the lines in range between 76 GHz and 86 GHz show some similarities such as the ascending pattern for both lines. However, the HRS gain values for no entry reflectarray approach better the values obtained by using HFSS.

Outside 86 GHz, the gain values for both HRS and HFSS are not exactly identical although their values decrease. This shows the elementary cell with linear phase behavior works well with HRS. In fact the no entry elementary cell has been designed to provide linear phase response over certain limited frequency [75]. This explains the similarities for HRS and HFSS lines for no entry reflectarray from 76 GHz to 86 GHz. Larger than 86 GHz, the no entry elementary cell is expected to behave non-linearly.

For the rectangular reflectarray, the rectangular elementary cell has been know to have narrow bandwidth and behaves with non linear phase response over frequency as discussed previously in sec.2.3. Because of this, HRS is incapable to produce gain values that 90% of them approach the values simulated using HFSS.

The measurement results for the maximum gain values are unavailable due to the measurement devices limitation at the frequency higher than 81 GHz. In addition, small reflectarray is very sensitive to displacement error especially the displacement of the feed where it is difficult to perfectly aligned the feed to the center of the reflecting panel. Contrary to the simulation using HFSS where the simulations are perfectly setup and the feed is perfectly aligned.

HRS is not a mean to replace Ansoft HFSS but rather as an alternative to quickly simulate the reflectarray by using only the simulated  $S_{11}$  value of the elementary cell. This will be an advantage in case there are only a few elementary cells used when designing reflectarray because the same  $S_{11}$  values can be reused for this purpose and less simulation using HFSS is needed. For example when working with active reflectarray, the phase variation is limited to  $P$  number of phase variations which is usually less than 4 variations. This means, to simulate active reflectarray using HRS, only  $P$  number of  $S_{11}$  values are required.

Some comprises need to be made when choosing the phase variation number because it will degrade the reflectarray performance especially in term of the radiation pattern maximum value and side lobes level. In the next section, some comparisons using HRS are made to see the influence of the  $P$  value on the reflectarray radiation pattern.

### 3.5.2. Order of the phase correction

As being discussed previously and in sec. 2.5, the order of correction desired or noted as  $P$  has effect on the reflectarray radiation pattern performance. For active elementary cell, the high value of  $P$  means the design of the elementary cell will be more complex and costly to be fabricated.

In this section, the comparison between 3 value of correction order ( $P = 2, 4, 8$ ) will be discussed using the results calculated by HRS. Using the equation 2.6 written in sec. 2.5, the phase variations for all 3 values of  $P$  are calculated and indicated in Tab. 3.5.

$n$	Order of correction ( $P$ )		
	2 (1-bit)	4 (2-bits)	8 (3-bits)
1	$0^\circ$	$0^\circ$	$0^\circ$
2	$180^\circ$	$90^\circ$	$45^\circ$
3		$180^\circ$	$90^\circ$
4		$270^\circ$	$135^\circ$
5			$180^\circ$
6			$225^\circ$
7			$270^\circ$
8			$315^\circ$

**Table 3.5.:** Phase variations for 3 correction's order number

For this purpose, 4 reflectarrays are simulated using HRS. The first reflectarray is assumed to compensate perfectly the incident wave's delay. This is the ideal case where each incident wave's phase delay is corrected using the opposite value of the delay which results the perfect correction as demonstrated in equation 3.20. The radiation pattern calculated using this reflectarray will be used as the reference for the comparison.

The second reflectarray is assumed to have perfect elementary cell where  $|S_{11}^{mn}| = 1$  and is able to compensate delays using 3-bits elementary cell with 8 phase variations as listed in Tab. 3.5. The third and the fourth one have the same perfect elementary cell as the second one, but with less phase variation for the compensation using 2-bits and 1-bit elementary cell respectively.

The chosen focal to diameter ratio is  $F/D = 0.5$  and the working frequency is 20 GHz. The reflectarray has  $21 \times 21$  elementary cells with dimension of the elementary cell equals to  $\lambda/2$ . In this simulation, the value of the elementary cell directivity  $D_C^{mn}$  is approximate using  $\cos(n)$  with  $n = 3$ . The main beam direction is focused at  $\varphi_b = 0, \theta_b = 0$ . The maximum gain radiation patterns are shown in Fig. 3.20 and the gain values are normalized to the maximum value of the perfect reflectarray.

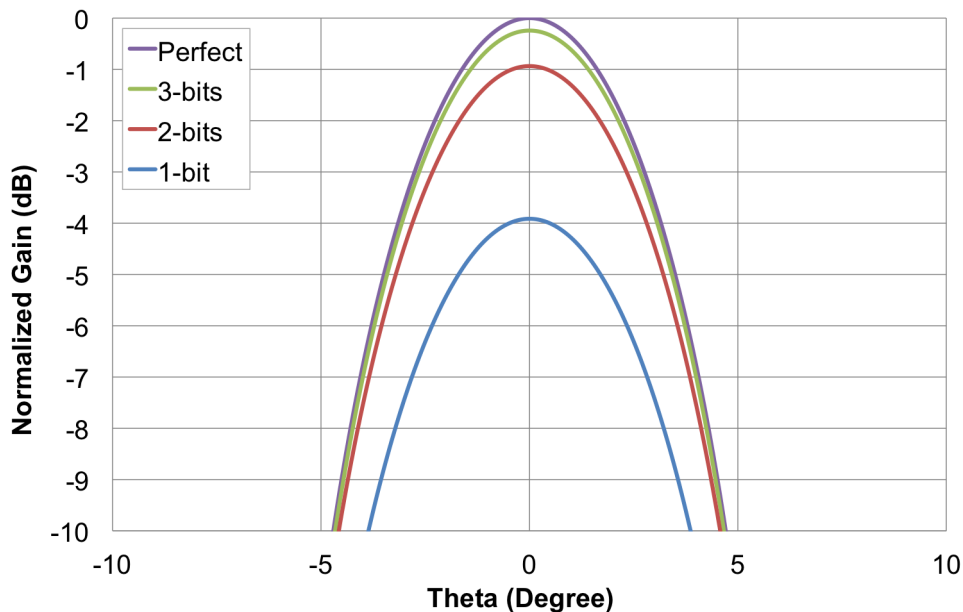


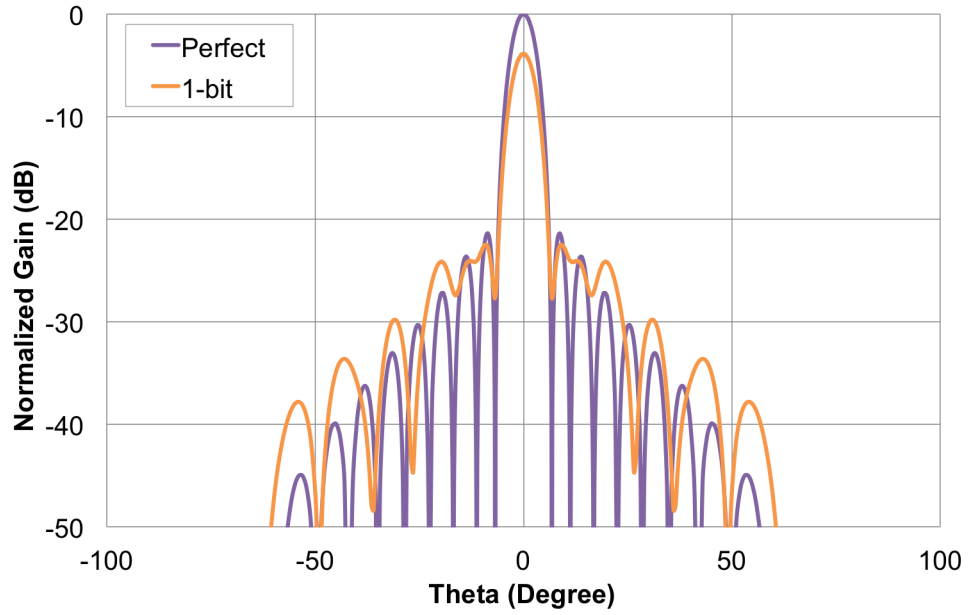
**Figure 3.20.:** Normalized gain radiation patterns for perfect reflectarray and the Fresnel reflectarray using 3-bits, 2-bits and 1-bit elementary cell

The 3-bits elementary cell configuration has the highest phase variations number which is equals to 8. This means that the reflectarray with such elementary cell capability is able to compensate better the phase delay than the reflectarray which uses 2-bits and 1-bit configuration. In this case, the difference between the maximum gain using perfect reflectarray and 3-bits elementary cell is small, with the difference equals to 0.24 dB.

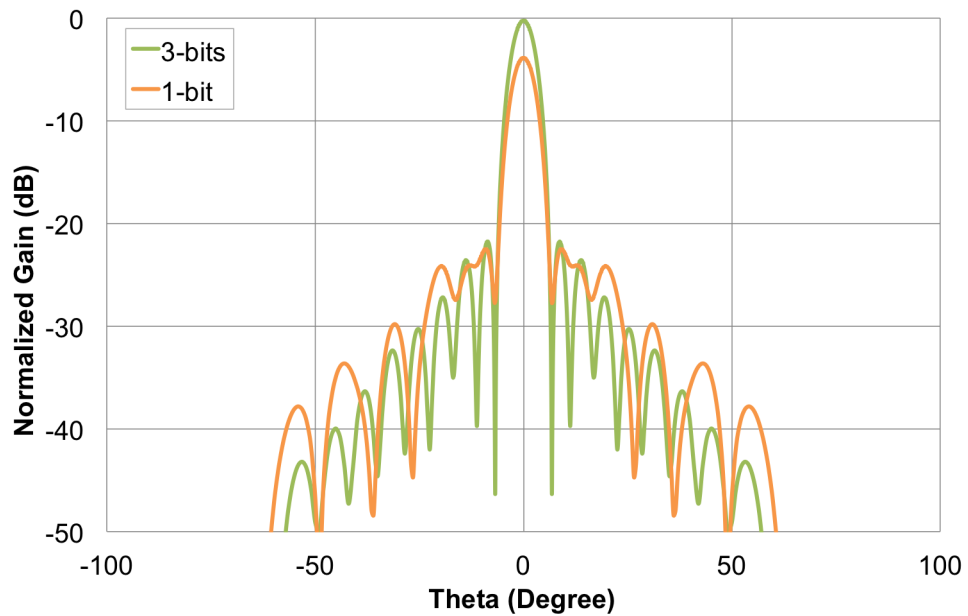
For 2-bits elementary cell configuration, there are 4 possible values of phase and they are as indicated in Tab. 3.5 in column 2-bits. Using 4 phase variations instead of 8 phase variations has dropped the maximum gain with 1 dB of decrement. Among these cases, the 1-bit elementary cell configuration has the largest phase error compensation because there are uniquely 2 phase variations which are  $0^\circ$  and  $180^\circ$ . With 2 states of elementary cell, the maximum gain is significantly reduced by 4 dB which is considerably large.

Fig. 3.21 shows the comparison of radiation patterns between perfect reflectarray and 1-bit Fresnel reflectarray. The purple line represents radiation pattern for perfect reflectarray and the orange line represents the radiation pattern for reflectarray using 1-bit elementary cell. In term of radiation pattern, the side lobes for 1-bit reflectarray becomes higher compared to the perfect reflectarray side lobes. Comparing 1-bit radiation patterns with 3-bits and 2-bits reflectarray (Fig. 3.22 and Fig. 3.23), the overall patterns are identical except lower value of maximum gain and some reductions of side lobes oscillations.





**Figure 3.21.:** Normalized gain radiation patterns for perfect reflectarray and 1-bit Fresnel reflectarray



**Figure 3.22.:** Normalized gain radiation patterns for 3-bits and 1-bit Fresnel reflectarray

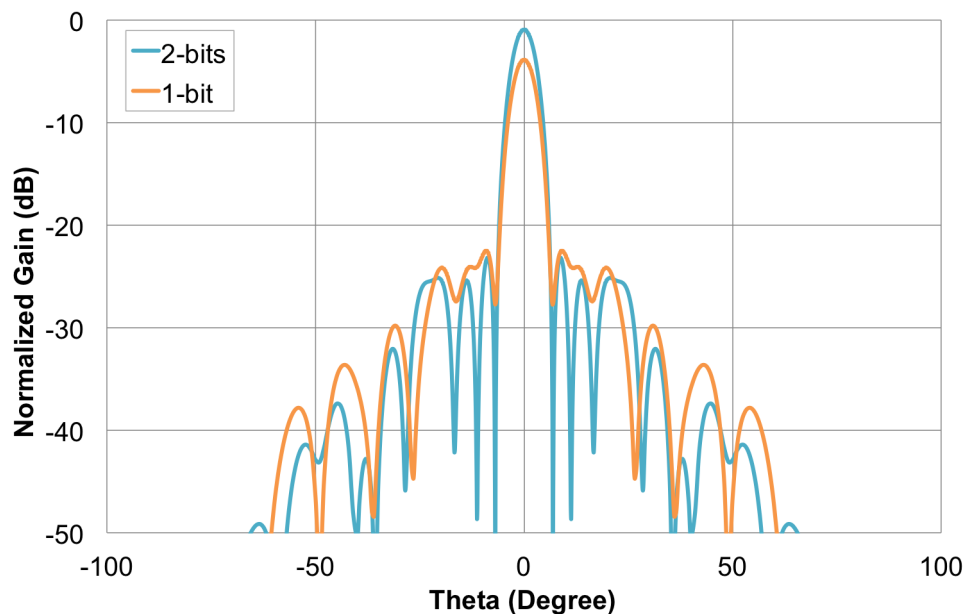


**Figure 3.23.:** Normalized gain radiation patterns for 2-bits and 1-bit Fresnel reflectarray

The 1-bit case can be considered as the worst case scenario because  $180^\circ$  of phase error is intentionally applied to the reflectarray. With this large value of error, the reflectarray is able to tolerate with other source of phase errors such as error due to the fabrication which can slightly change the reflected phase. Using 1-bit elementary cell with 2 phase variations degrades the reflectarray performance, but from the simulations results discussed previously, the produced radiation pattern is still acceptable because the half power beam width (HPBW) is about  $6^\circ$  and the difference between the main beam and side lobes level is greater than 15 dB.

Using 3-bits and 2-bits elementary cell is better for the phase compensation because it will give better reflectarray performance, but in term of the fabrication and elementary cell design, the process will be extremely difficult and challenging especially when working with small dimension of elementary cell at high frequencies. This means that more active components such as RF MEMS and p-i-n diode are needed in the small space area. Moreover, each of the active components used need to be polarized or biased to achieve elementary cell reconfigurability and this constraint needs to be considered. In addition, losses from active devices have to be considered and the overall gain is decreased [76].

Compromises need to be made between the performance and the complexity of the design process. 1-bit elementary cell configuration is able to satisfy both performance and design complexity which includes the fabrication process.

## 3.6. Conclusion

This chapter discusses the theory and the concept behind the Hybrid Reflectarray Simulator (HRS) developed specifically to aid and accelerate the design process of the active elementary cell. HRS is not a simulator to replace real 3D electromagnetic simulator but rather as an alternative tool to quickly validate the reflectarray design according to pre-determined performance.

For more accurate results, the same reflectarray can be simulated entirely in real simulator. This will reduce the time consumption because it takes a lot of time and computer resource to simulate large reflectarray using real simulator.

The formula and equations used in the HRS are also discussed and demonstrated especially in the reflected wave and phase delay compensation part where it shows how HRS and Ansoft HFSS works. HRS is developed using object oriented programming (OOP) language. Some general knowledge on the OOP has been introduced including the example to model feed object in Matlab using feed file class definition in Appendix A.

Some discussions on the simulation results are made, this includes the comparison between results calculated using HRS and Ansoft HFSS. Using HRS, the influence of the order of the phase correction is analyzed and compared. Correction order equals to 2 (1-bit) degrades the reflectarray performance but in term of design complexity and the fabrications challenge, 1-bit elementary cell is considered as the less risky solution to achieve elementary cell reconfigurability.

The next chapter will discuss the process to design 1-bit active Fresnel reflectarray especially the difference steps required in order to design and validate the 1-bit elementary cell.

## 4. Active fresnel reflectarray (AFR)

This chapter will discuss the process to design the active fresnel reflectarray (AFR) especially the active elementary cell for the application of the unmanned aerial system (UAS) communication antenna. The chosen working frequency is 20 GHz with focal to diameter ratio ( $f/D$ ) equals to 0.5. The distance between each elementary cell is  $\lambda/2$  and at 20 GHz,  $\lambda = 15$  mm, which makes the distance equals to 7.5 mm. The reflectarray has  $21 \times 21$  elementary cells with total dimension equals to  $157.5 \text{ mm} \times 157.5 \text{ mm}$ .

Active reflectarray uses the same components as passive reflectarray, but in addition, there are new components added to the passive's structure. These new components are the active element in the elementary cell with the combination of the circuit to control the active element states. In the elementary cell, an active element is added to control the reflected phase. In the context of this project, the active element added is a p-i-n diode. This extends the passive elementary cell capability to produce 2 reflected phase values. Thanks to the extended capability, it is possible to change the phase distribution electronically using the same elementary cell design, which finally results in the change of the radiation pattern.

The integrated p-i-n diodes are not able to operate correctly on their own. A diode control circuit is needed to monitor and control the integrated diode states. This control circuit will decide the state for each diode either ON or OFF, which depends on the desired phase distribution. The phase distribution is controlled by the computer and it is the control circuit who acts as the intermediate connection between the reflectarray and the computer.

The next section will discuss the active elementary cell design process starting from the passive cell design to the active cell design optimized for fabrication purpose.

### 4.1. Elementary cell design

This section discusses the design process of the active elementary cell starting from the base design until the final design which is optimized for fabrication purpose. This section also highlights the encountered difficulties when designing the reconfigurable 1-bit elementary cell. The main requirement for this reconfigurable elementary cell is the capability to reflect 2 phase values with a phase difference

equals to  $180^\circ$ . Ansoft HFSS is used as the main simulation software in the elementary cell design process. HRS and CST are used when doing simulation for the entire reflectarray because previous experiments simulating active reflectarray with integrated diode showed that HFSS is not capable to handle lumped elements correctly when the complexity of the problem is too large compared to the size of the lumped element (diode).

#### 4.1.1. Passive cell

The elementary cell design is inspired from passive cell [31] which is a multi-layer based elementary cell as shown in Fig. 4.1. The cell is designed to work in the frequency range of 9.40 GHz and 9.90 GHz. Fig. 4.1(a) shows the exploded view of the different dielectric and metal layers. There are 4 dielectrics layers and 4 metal layers in the structure.

The square patch acts as the radiating element. It is printed on substrate d(2) with slotted metal as the ground plane. The patch is covered by substrate d(1) which is located on the top surface. A bent U-shaped microstrip line is added below the slotted ground metal with d(3) substrate in-between. Below the microstrip line, there is another substrate d(4) with metal layer printed at the bottom of it. Tab. 4.1 shows the properties of the substrates used in the elementary cell.

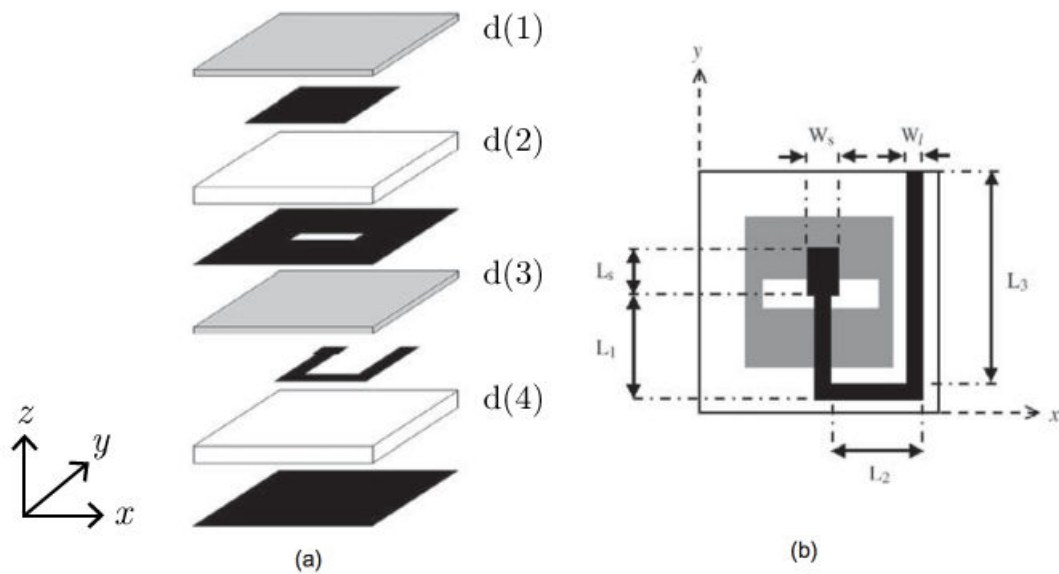


**Figure 4.1.:** Elementary cell based on a U-shaped aperture-coupled delay line (a) Expanded view, (b) top view (From [31], © 2006 IEEE.)

Fig. 4.1(b) shows the elementary cell view in  $xy$  plane. In this view, the U-shaped microstrip line is represented by multiple segments of black color rectangle.

Dielectric layer	Thickness (mm)	$\epsilon_r$	$\tan\delta$
d(1)	0.790	3.200	0.0030
d(2)	2.000	1.067	0.0002
d(3)	0.790	3.200	0.0030
d(4)	7.770	1.000	0.0000

**Table 4.1.:** Dielectric materials used in the aperture-coupled elementary cell at 20 GHz

The microstrip line has 2 segments. The first segment is noted as  $W_s$  and  $L_s$  is the matching stub with a fixed length which is aligned to the center of the aperture in the  $x$  axis and also to the center of the slotted metal ground. The second segment is the open-ended line which is the combination of  $L_1$ ,  $L_2$  and  $L_3$ . This second segment is used to control the phase of the reflection coefficient and it is proportional to twice the length of this segment. Tab.4.2 shows the metal layers dimensions for the elementary cell.

Metal layer	X (mm)		Y (mm)	
Line	$W_s$	4.00	$L_s$	5.00
			$L_1$	14.00
	$W_l$	1.85	$L_2$	13.00
			$L_3$	17.00
Slot	6.00		1.00	
Patch	10.00		10.00	
Unit cell	20.00		20.00	

**Table 4.2.:** Metal layers dimensions

The amplitude and phase of the reflection coefficient for the elementary cell are shown in Fig.4.2. The phase delay of the elementary cell is directly proportional to the length of the U-shaped stub with some nonlinear behavior at the resonance of the microstrip line. The phase range produced by this elementary cell is greater than four times of  $360^\circ$  which gives a maximum value of around  $1500^\circ$ . In this case, the losses are increased with the length of the stub with the average losses in the order of 0.1 dB/cm.

This passive cell structure has some advantages and suitable characteristics to be converted to a reconfigurable elementary cell. The quasi linear reflected phase behavior is important to ensure good performance of the reflectarray and can increase the bandwidth. This also makes the elementary cell more robust to fabrication errors especially at high frequencies where the size of the elementary cell becomes smaller and more sensitive to fabrication error. This passive elementary cell encounters only small dissipative losses and this will reduce the total losses when integrating p-i-n diode because the losses in the diode itself is already large.

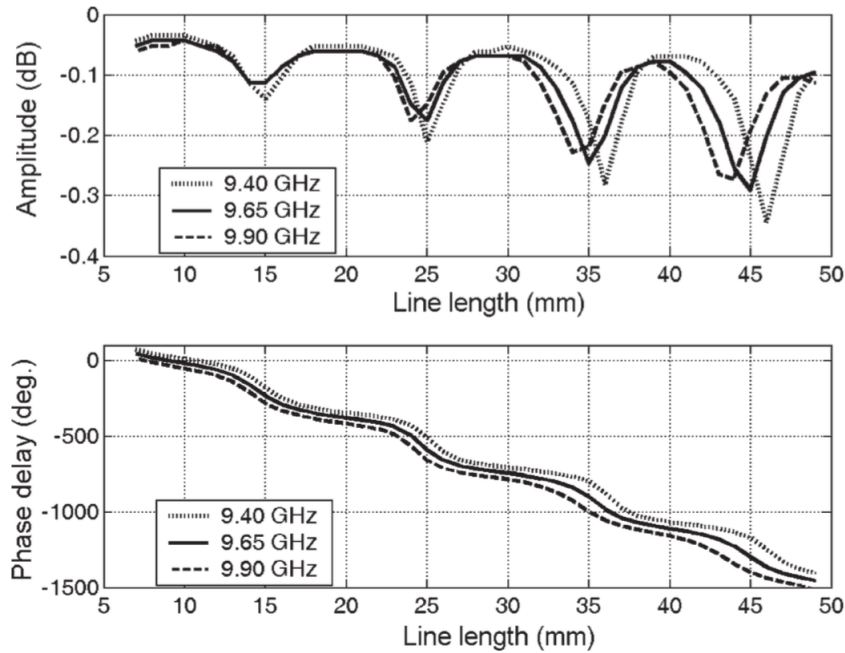


**Figure 4.2.:** Amplitude and phase of reflection coefficient for U-shaped reflectarray unit cell with ground plane (From [31], © 2006 IEEE.)

One of the interesting characteristics is the element's separations in the form of layers. This allows an integration of the phase control system to the stub without modifying the radiation layer on the top which is sensitive to any unwanted materials such as solder joint especially at high frequency. In addition, the phase tuning stub layer occupies its own layer and this gives flexibility and extra space to integrate the diode. This is obvious at the high frequency because the size of the elementary cell becomes smaller and less space is left to add active component such as diode.

The operating frequency band for the passive elementary cell is 9.40–9.90 GHz and in this project, the chosen working frequency is 20 GHz which is twice higher than the original operating frequency. Thus, the elementary cell has to be redesigned (dimensions of the patch, slot and the stub) to function at 20 GHz.

#### 4.1.2. Frequency adaptation

Changing the working frequency of the original elementary cell is not a straightforward process and difficult task as it involves multiple design parameters which influences the  $S_{11}$  coefficients as shown in Fig. 4.3. As the starting point, all dimensions of the original cell except the unit cell are decreased by the factor of 2. The unit size parameter is fixed to 7.5 mm and the substrate thicknesses are unchanged. In this process, the delay line segment  $L_2$  and  $L_3$  are excluded from the simulation

to reduce the parameter complexity.  $L_1$  and  $W_l$  are equal to 3 mm and 0.40 mm respectively because the scaled down size is too large to be fitted in the new unit cell. Tab. 4.3 shows the resized metal dimensions. This process will change the resonance of the elementary cell to be around 20 GHz by shifting up or down the resonance towards 20 GHz. The resized elementary cell is simulated starting from 10 GHz to 30 GHz in order to determine its resonant zones.

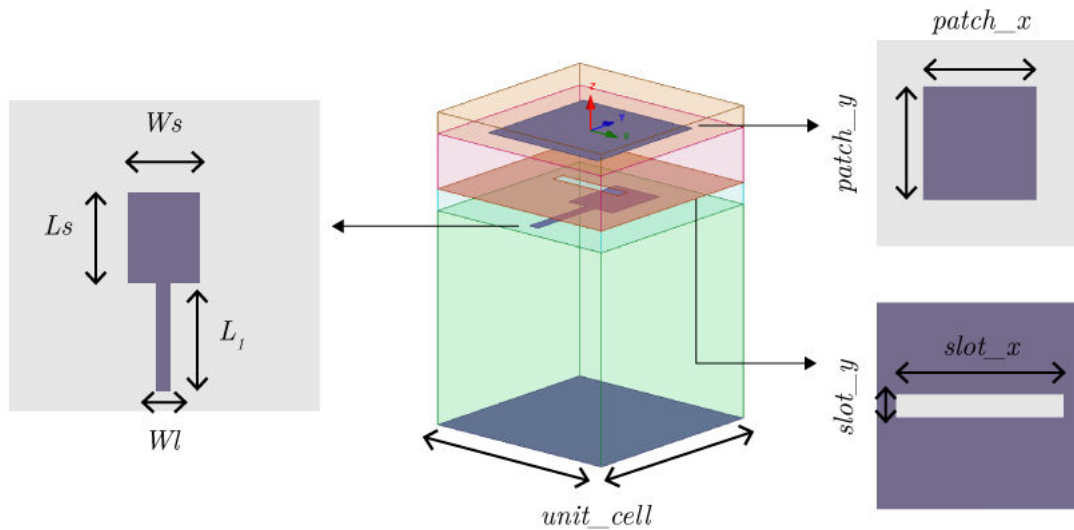


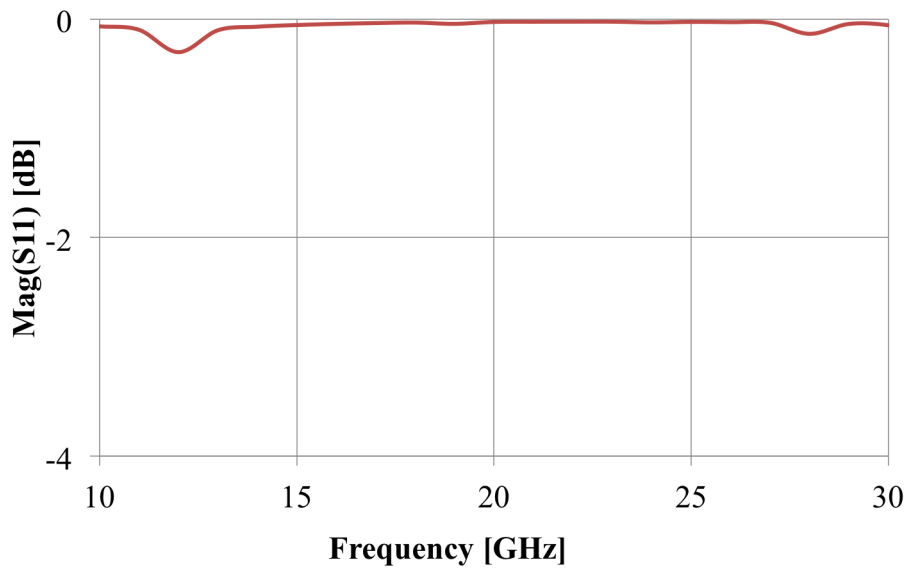
**Figure 4.3.:** Resized elementary cell HFSS simulation model and parameters

Metal layer	X (mm)		Y (mm)	
Line	$W_s$	2.00	$L_s$	2.50
	$W_l$	0.40	$L_1$	3.00
Slot	3.00		0.50	
Patch	5.00		5.00	
Unit cell	7.50		7.50	

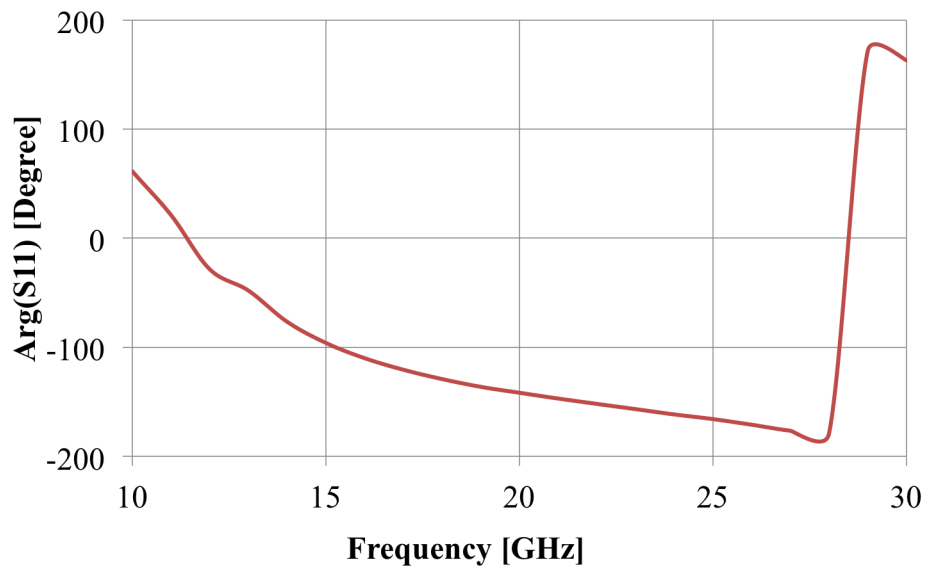
**Table 4.3.:** Resized metal layers dimensions

Fig. 4.4 and Fig. 4.5 show the magnitude and phase of the resized elementary cell respectively. From the simulation results, no resonance zone can be found around 20 GHz. Above 25 GHz, there is a resonance at 27.9 GHz.





**Figure 4.4.:** Resized elementary cell  $S_{11}$  magnitude



**Figure 4.5.:** Resized elementary cell  $S_{11}$  phase

Fig. 4.6 shows the surface current distribution for the resized elementary cell. From the simulation, the current is primarily distributed on the patch and follows by the slot and small amount of current on the stub. Based on this observation, the rectangle patch has major influence on the cell reflected coefficient. The adaptations is started by firstly changing the patch parameters, secondly the slot parameters and finally the stub parameters. The process requires trial and error approach where

only one parameter is changed at one time and the results are evaluated before changing the next parameters.

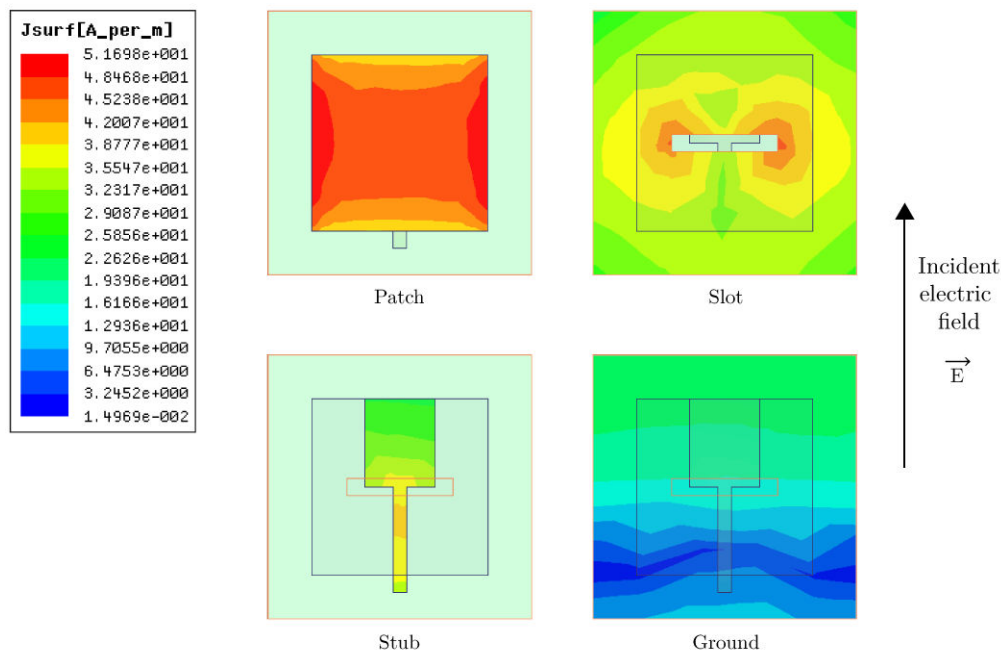


**Figure 4.6.:** Surface current distributions for the resized elementary cell at 20 GHz

The patch geometry is described only by one parameter as its shape is square. In this case  $patch\_x = patch\_y$ . The initial size of the patch is 5 mm and after a parameter tuning, the size chosen is 1.5 mm. If the size is too large, only a small amount wave will be coupled to the stub via slotted metal surface because the majority of the wave will be reflected by the patch. On the contrary, if the patch is too small, the majority of the wave will be coupled to the stub and insufficient wave will be reflected back.

The slotted metal surface parameters are  $slot\_x$  and  $slot\_y$  (Fig. 4.3). The  $slot\_x$  parameter either shifts up or down the resonance frequency but this parameter is limited to the  $unit\_cell$  size that also imposes the limit to shift the resonance frequency. In this case  $slot\_x$  value is fixed to 6.5 mm. On the other hand, the  $slot\_y$  parameter influences both the phase variation steepness and the resonance frequency. The phase variation steepness decreases when the  $slot\_y$  is increased. The  $slot\_y$  parameter value is set to 0.2 mm to satisfy both the phase variation steepness and the resonance frequency approaching 20 GHz.

The stub consists of 2 segments. The first segment is the matching stub indexed by  $W_s$  and  $L_s$ . The second segment is the phase delay line. It is defined by  $W_l$  and  $L_l$ . In this case,  $W_s = L_s = 2.5$  mm. The value of  $W_s$  is increased from 2.0 mm

to 2.5 mm because the width of the phase delay line,  $W_l$ , is decreased to 0.2 mm to reduce the space consumption especially when adding the additional segments of line  $L_2$  and  $L_3$ . Tab. 4.4 shows the parameters for the elementary cell working at 20 GHz.

Metal layer	X (mm)		Y (mm)	
Line	$W_s$	2.50	$L_s$	2.50
	$W_l$	0.20	$L_1$	3.00
Slot	6.50		0.20	
Patch	1.50		1.50	
Unit cell	7.50		7.50	

**Table 4.4.:** Resized metal layers dimensions for 20 GHz

Fig. 4.7 and Fig. 4.8 show the  $S_{11}$  magnitude and phase coefficients after adapting the elementary cell design parameters with the resonance zone can be found around 20 GHz. In this case, the length's variation of the phase delay line will result in the changes of the reflected phase values.

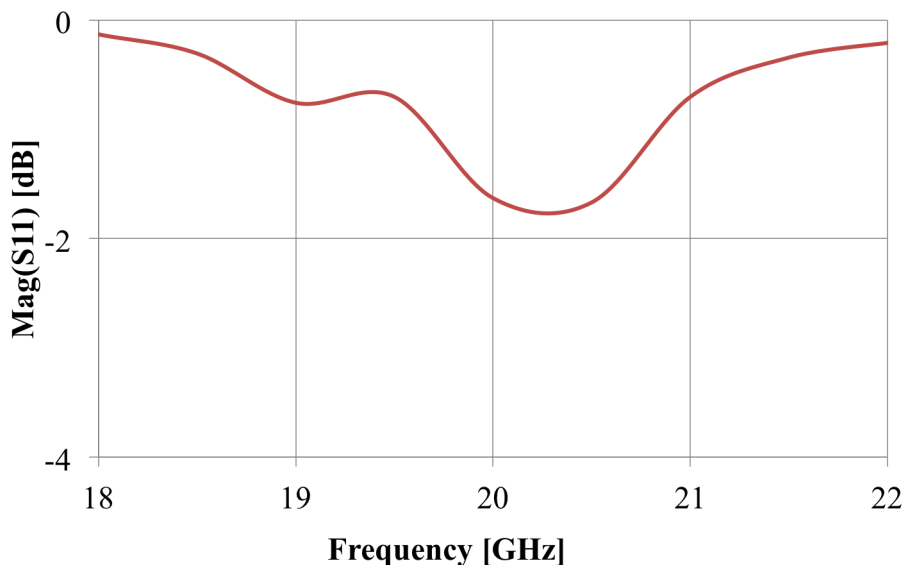


**Figure 4.7.:**  $S_{11}$  magnitude after parameters adaptation for 20 GHz

Fig. 4.9 shows the current distributions for the metal layers. In this case, the currents are well distributed among the metal surfaces with maximum current that can be found on the slotted rectangle and on the phase delay line. This shows that the phase delay line is capable to function correctly when its length varies. The next section will discuss the p-i-n diode integration within the phase delay line in order to achieve reconfigurable  $S_{11}$  coefficient.

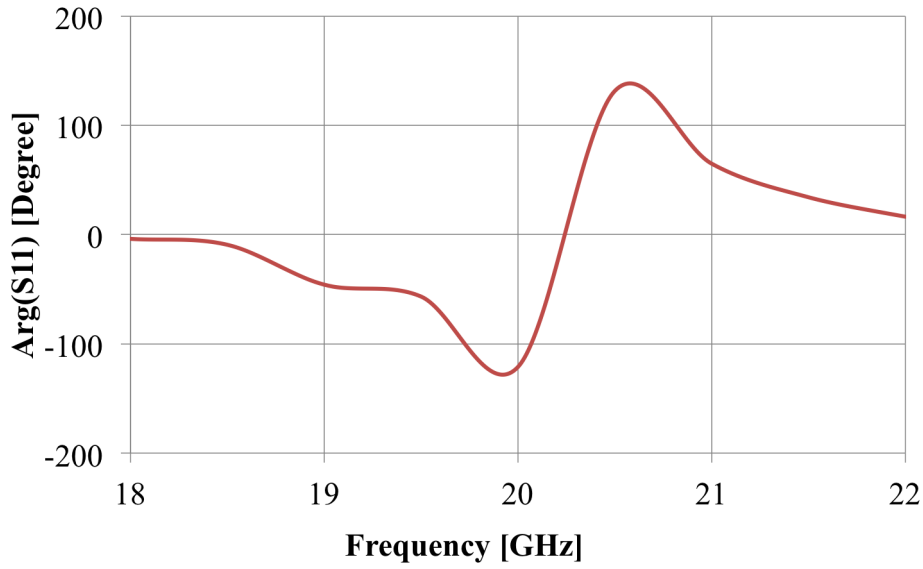


Figure 4.8.:  $S_{11}$  phase after parameters adaptation for 20 GHz

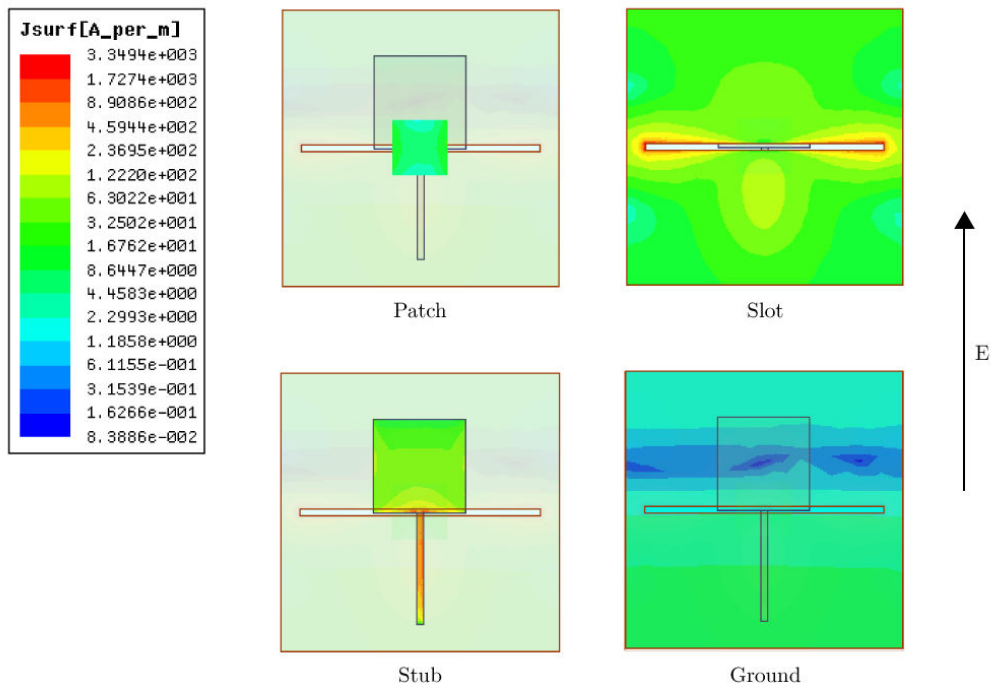
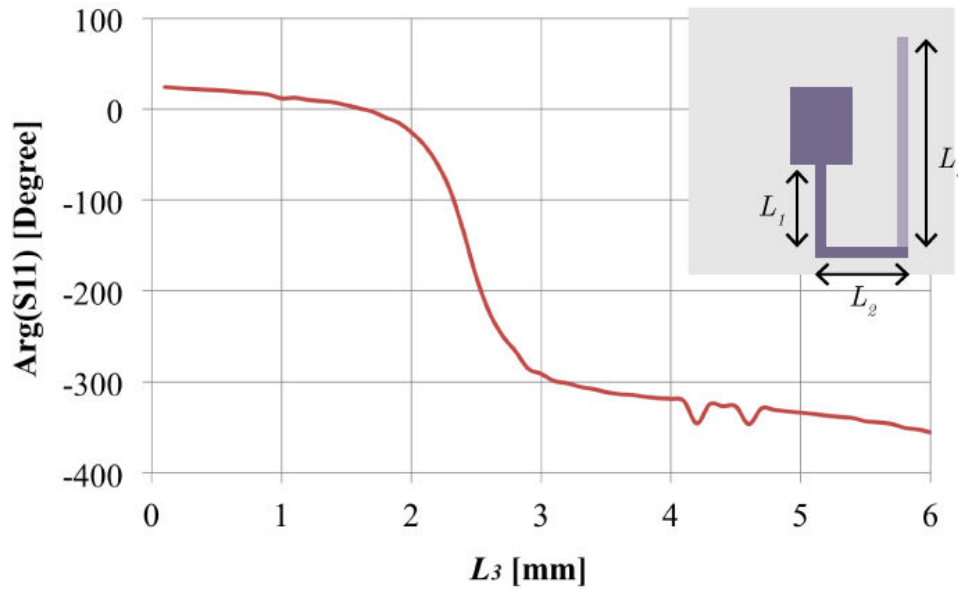


Figure 4.9.: Surface current distributions for the adapted elementary cell at 20 GHz

### 4.1.3. Diode integration

Before integrating the p-i-n diode,  $L_2$  and  $L_3$  segments are added to  $L_1$  in order to increase the delay line length as shown in Fig. 4.10. The value of  $L_2$  equals to 3 mm while the length of  $L_3$  varies between 0.1 mm to 6 mm to obtain the reflected phase value based on the length of the delay line. The result is shown in Fig. 4.10.



**Figure 4.10.:** Phase variation as function of  $L_3$  length

This phase variation versus length is used as reference curve within  $L_3$  segment. By using diode, this segment can be electronically separated into 2 sub segments noted as  $L_{31}$  and  $L_{32}$  as shown in Fig. 4.11. This produces 2 effective phase delay lines variations which correspond to 2 values of the reflected phase. In this case, the desired difference between them is  $180^\circ$ . The p-i-n diode is integrated within  $L_3$  segment because this segment has more space and sufficient length variation to obtain the desired phase difference.

To determine the lengths of  $L_{31}$  and  $L_{32}$  segments, the graph of reflected phase versus  $L_3$  segment shown in Fig. 4.12 is used. One of the possible combinations is by fixing the length of  $L_{31}$  to 1.6 mm. At this length, the reflected phase value is  $0^\circ$ . The length of  $L_{32}$  is fixed to 0.9 mm. This will produce the total length of 2.5 mm when diode is in ON state which corresponds to the reflected phase of  $184^\circ$ .

By using this length combination, the desired phase difference between OFF and ON state can be achieved. In the simulation, p-i-n diode is modeled using lumped boundary surface. This surface width noted as  $W_d$  equals to  $W_l$  and its height equals to  $L_d$  as shown in Fig. 4.12. In this case  $L_d$  equals 0.1 mm. Because of this, the length of the segment  $L_{32}$  needs to be subtracted with  $L_d$  for obtaining the correct result.

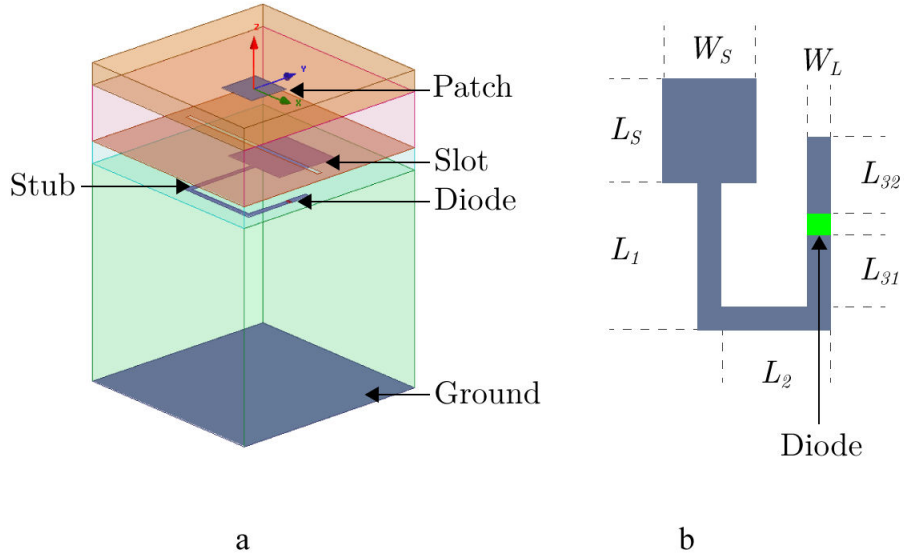


**Figure 4.11.:** Aperture-coupled passive elementary cell with the integrated p-i-n diode within the phase tuning stub on the right

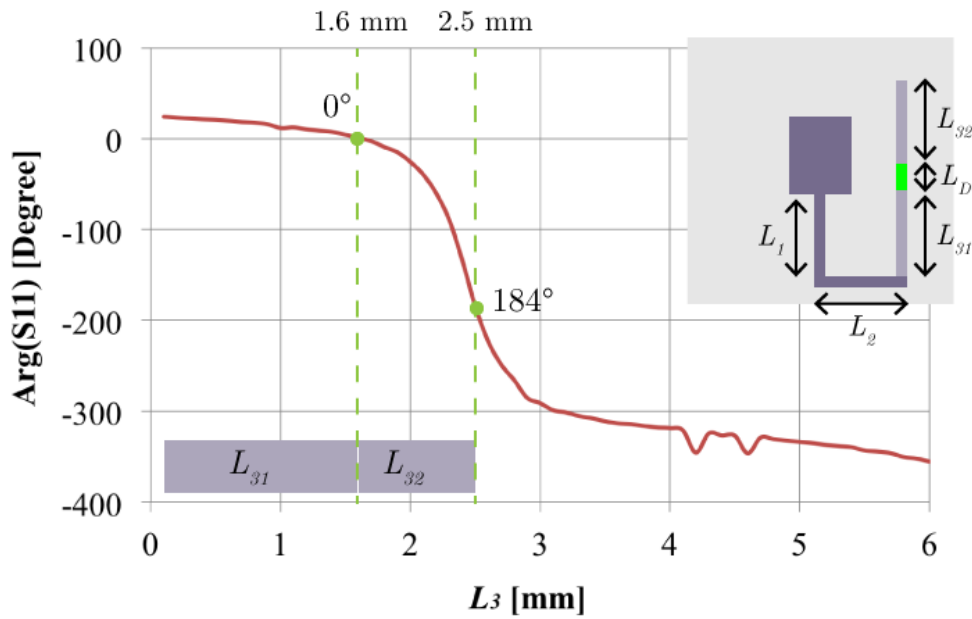


**Figure 4.12.:** Phase variation in the function of  $L_3$  length with  $L_{31}$  and  $L_{32}$  segments length

Tab. 4.5 shows all metal dimensions after integrating the p-i-n diode lumped boundary surface. The p-i-n diode is modeled as  $RL$  circuit for ON state and  $CL$

circuit for OFF state as shown in Fig. 4.13. In these models,  $R = 8 \Omega$ ,  $C = 27\text{fF}$  and  $L = 30 \text{ pH}$  [23].  $R$  corresponds to different types of losses and this value depends on the current flowing through the diode. Higher current intensity will decrease the  $R$  value. The inductance value  $L$  depends on the diode packaging size. These values are measured based on beam-lead type p-i-n diode (M/A-COM MA4AGBLP912) at 60.25 GHz. For full-wave analysis of the elementary cell, these values are considered as the worst scenario because they are measured at 60.25 GHz which is approximately three times higher than 20 GHz (the chosen working frequency of the AFR). In reality, the  $R$  value will be lower at 20 GHz which results in smaller loss when diode is in ON state.

Metal layer	X (mm)		Y (mm)	
Line	$W_s$	2.50	$L_s$	2.50
	$W_l$	0.20	$L_1$	3.00
			$L_2$	3.00
			$L_{31}$	1.60
			$L_{32}$	0.80
Diode	$W_d$	0.20	$L_d$	0.10
Slot	6.50		0.20	
Patch	1.50		1.50	
Unit cell	7.50		7.50	

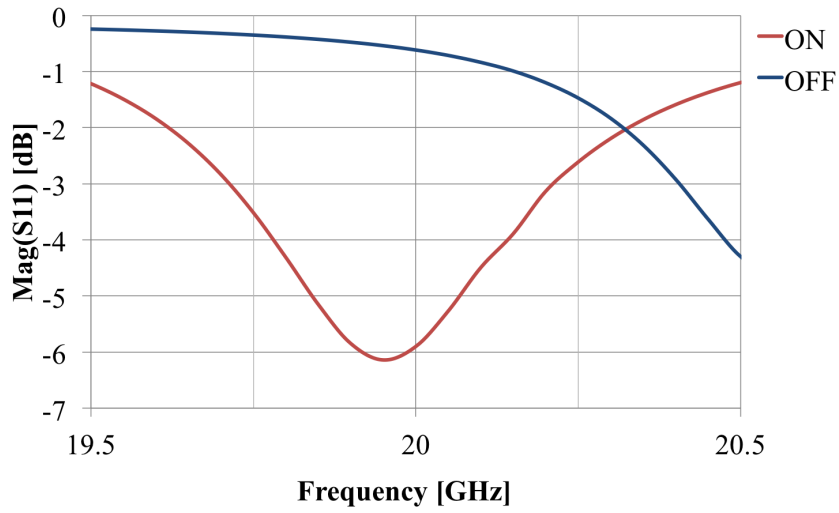
**Table 4.5.:** Metal dimensions with diode integration



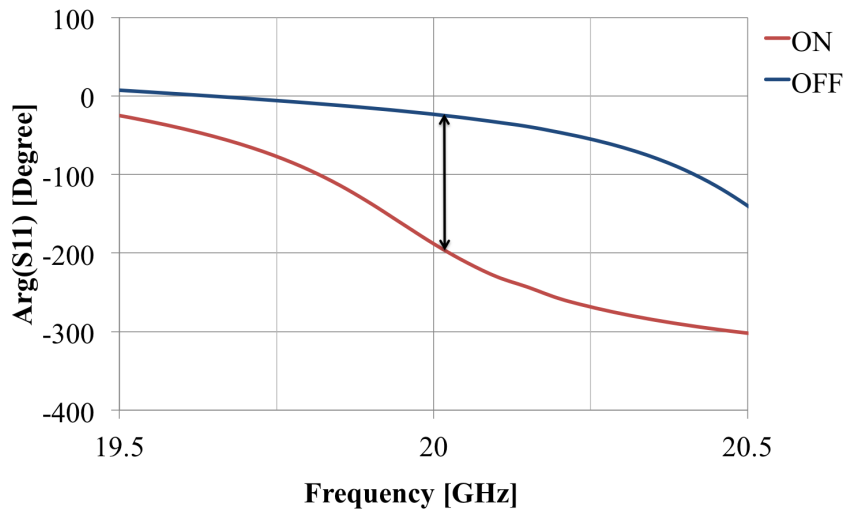
**Figure 4.13.:** p-i-n diode circuits equivalent

Fig. 4.14 and Fig. 4.15 show the simulation results when diode are in ON and OFF states respectively. At 20 GHz, the phase difference between ON and OFF states is  $183^\circ$ . The magnitude for OFF state is  $-0.71 \text{ dB}$  and  $-5.27 \text{ dB}$  when diode is biased. Fig. 4.16 and Fig. 4.17 show the surface current distributions on metal layers when diode are ON and OFF. When diode is ON, most of the currents concentrate around slotted rectangle and phase delay line. When diode is in OFF state, the current is primarily distributed on the patch and less current can be observed around the slotted rectangle. These simulation results demonstrate that the modified passive elementary cell is able to change the reflected phase value electronically with the help of p-i-n diode. In this first phase of the elementary cell design, the loss for the ON state is not considered as the immediate priority but will be optimized later to reduce the loss. The concept of phase switching has been proven to work but in

real world application, the diode needs to be DC polarized and the next section will discuss the diode polarization circuit.



**Figure 4.14.:**  $S_{11}$  magnitude when diode is in ON and OFF state



**Figure 4.15.:**  $S_{11}$  phase when diode is in ON and OFF state



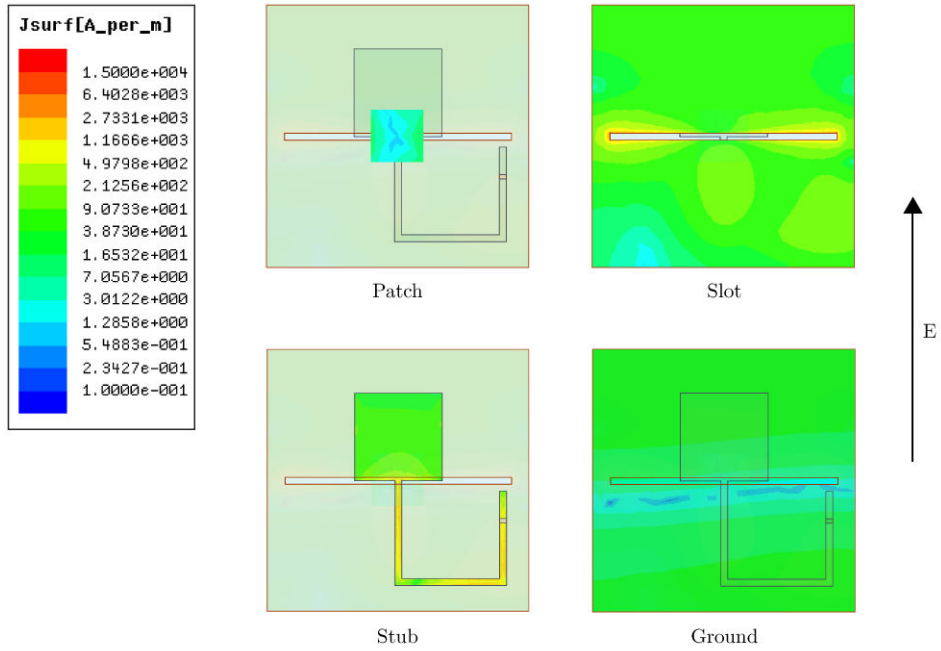


Figure 4.16.: Surface current distributions when diode is ON at 20 GHz

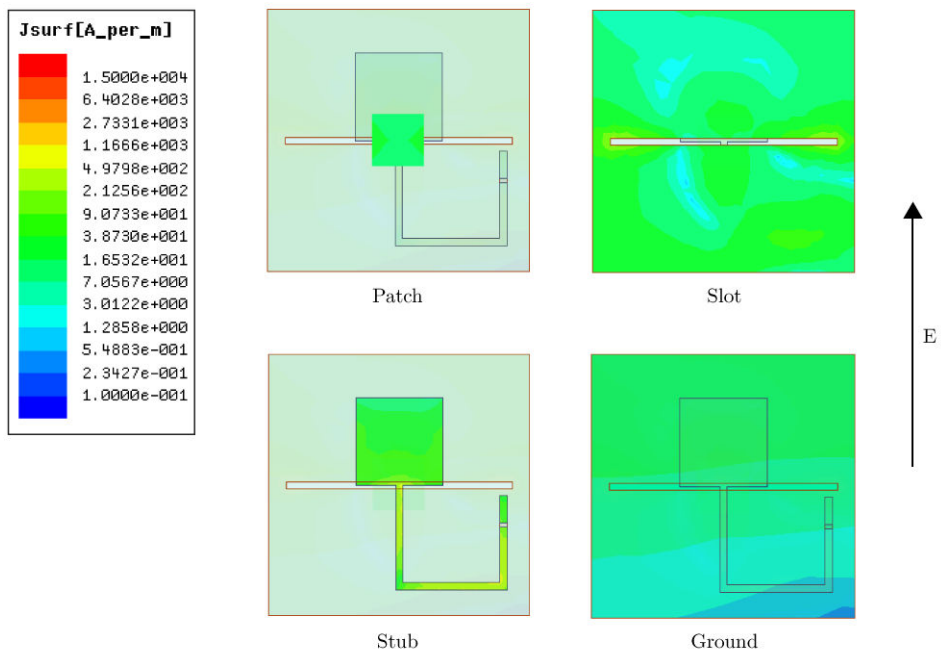
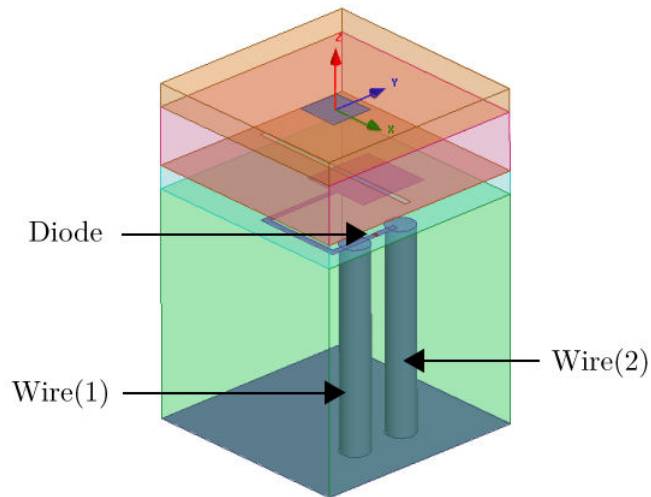


Figure 4.17.: Surface current distributions when diode is OFF at 20 GHz

#### 4.1.4. The diode DC polarization circuit

The first attempt to polarize the diode is by connecting 2 wires directly to the phase delay line as shown in Fig. 4.18. One of the wire will be connected to the positive voltage and the other one will be connected to the ground. However this technique changes completely the reflected phase for both ON and OFF states as shown in Fig. 4.19.



**Figure 4.18.:** Diode polarization with 2 wires connected to the phase delay line

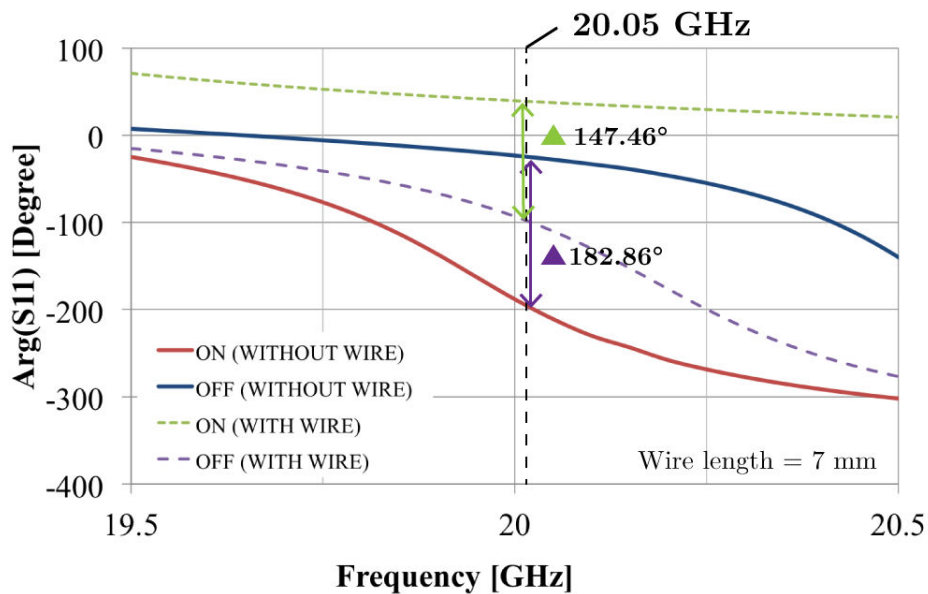


**Figure 4.19.:** Reflected phase differences before and after connecting polarization wires

In Fig. 4.19, the phase difference becomes  $147.46^\circ$  instead  $180^\circ$  at 20 GHz. In addition, the cell's resonance frequency is shifted. In order to ensure independent characteristics of the elementary cell with respect to the wire, a disc coupled structure inspired from [23] is added to the elementary cell structure as shown in Fig. 4.20. The disc coupled acts as a RF choke to make the wire metal becomes invisible from the point view of RF. The connection from the wire to the phase delay line is handled by Via(2) and the Via(1) connects the phase delay line to the slot level that acts as the ground plane as can be seen in the side view of Fig. 4.20. By using common ground, the diode polarization line can be simplified as only one connection is required for each cell to control the diode's states.

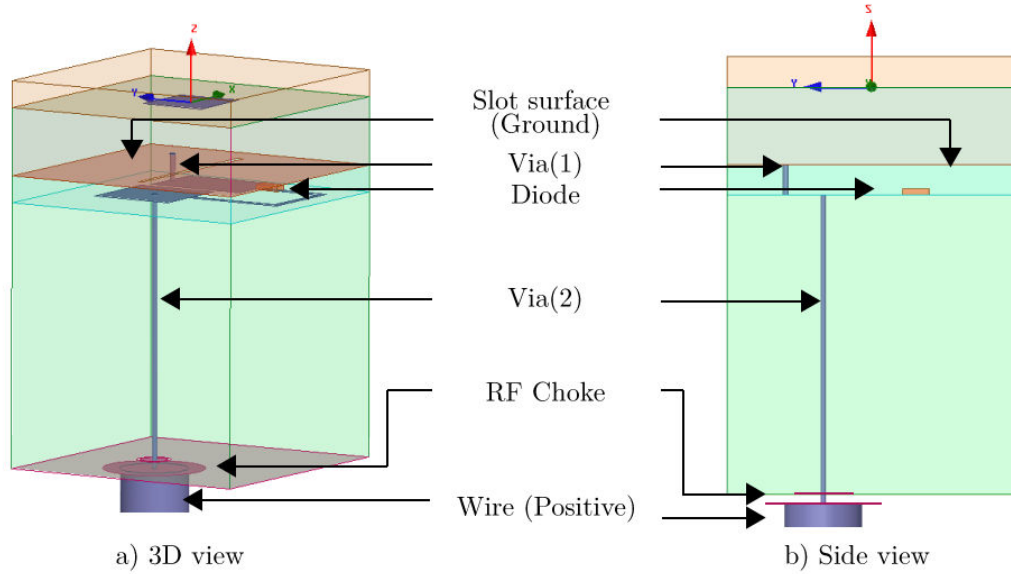


**Figure 4.20.:** Elementary cell with RF choke added to the bottom

The phase delay line is modified to accommodate the via connection to the slot surface. The modification consists of adding rectangle patch to the end of segment  $L_{s2}$  as shown in Fig. 4.21. The size of the added rectangle patch is described by  $W_{s2} = 2$  mm and  $L_{s2} = 3$  mm. Via(2) is connected to the center of matching stub ( $W_s$  and  $L_s$ ) and the Via(1) is connected to the end of new added rectangle patch. The diameter for these vias is 0.15 mm.

The ground surface is also modified to add the RF choke structure. The ground is divided into 2 parts, the first part is known as upper surface and the second part is known as lower surface as shown in Fig. 4.22. On the upper ground surface, a disc circle noted as Disc(1) with diameter equals 0.8 mm is added. The Disc(1) is separated by the ground surface with empty gap noted as  $D_{GD} = 0.1$  mm. On the lower surface, a second disc noted as Disc(2) with diameter equals to 3 mm is added and it is aligned center to the Disc(1). These upper and lower ground surfaces are separated by air layer with the thickness of 0.254 mm.

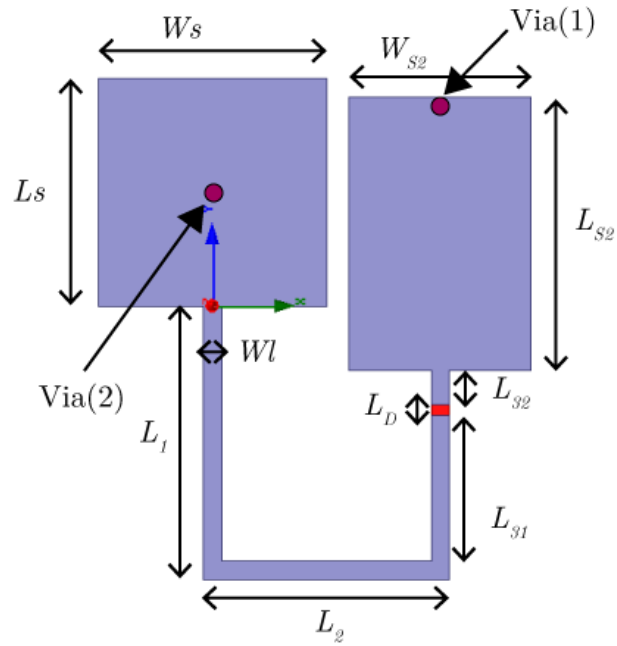


Figure 4.21.: Phase delay line modification

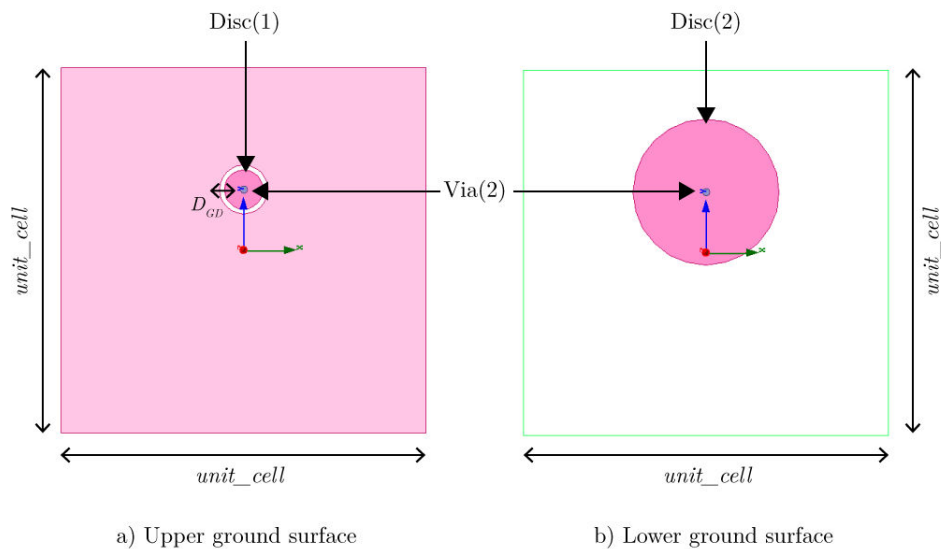


Figure 4.22.: Ground surface modification with disc coupled structure

The disc coupled structure changes the cell geometry, therefore the dimensions of the patch, slot and stubs need to be readjusted. Tab. 4.6 shows the updated metal and ground layers dimensions. By using the RF choke structure, the wires influence on the  $S_{11}$  coefficient especially the reflected phase is significantly reduced.

Metal layer	X (mm)		Y (mm)	
Line	$W_s$	2.50	$L_s$	2.50
	$W_{s2}$	2.00	$L_{s2}$	3.00
	$W_l$	0.20	$L_1$	3.00
			$L_2$	2.50
			$L_{31}$	1.60
			$L_{32}$	0.38
Diode	$W_d$	0.20	$L_d$	0.10
Slot	5.40		0.20	
Patch	2.00		2.00	
Unit cell	7.50		7.50	

Ground layer	Diameter (mm)	Distance (mm)
Disc(1)	0.80	-
Disc(2)	3.00	-
$D_{GD}$	-	0.10

**Table 4.6.:** Metal dimensions with diode integration and RF choke

Fig. 4.23 and Fig. 4.24 show the reflected magnitude and phase of the elementary cell after the integration of the RF choke. From the results, the wires presence shows minor influence on the  $S_{11}$  coefficient. At 20 GHz, the phase difference between ON and OFF states is retrieved at  $180^\circ$  and the loss is approximately around 5 dB.

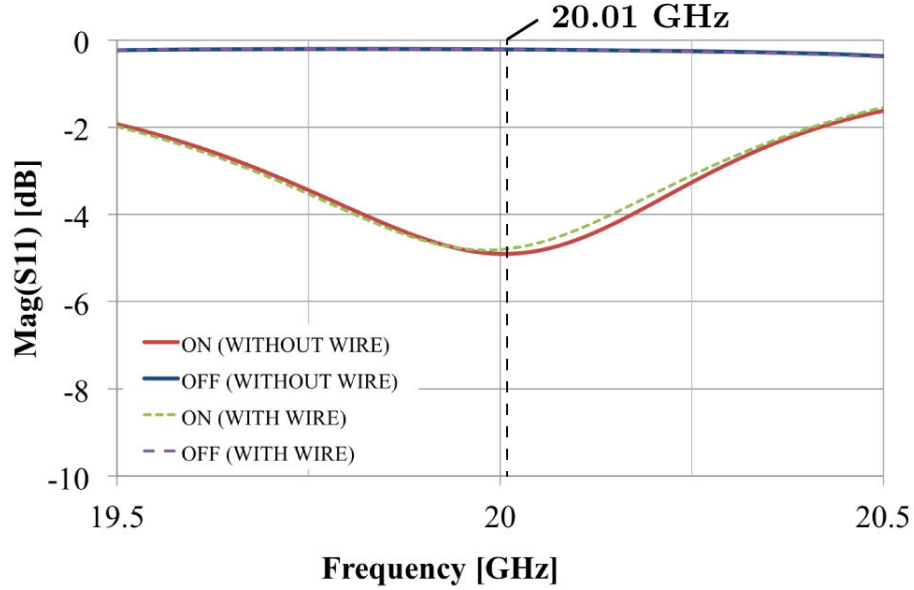


**Figure 4.23.:** Reflected magnitude of 2 states p-i-n diodes with polarization line

Fig. 4.25 and Fig. 4.26 show the surface current distributions after adding RF choke layers. When diode is in ON state, most of the currents are distributed around slotted surface and on the phase delay line. In the opposite case, most of the currents are concentrated on the patch and the phase delay line.

The integration of the polarization line has enabled the elementary cell to be

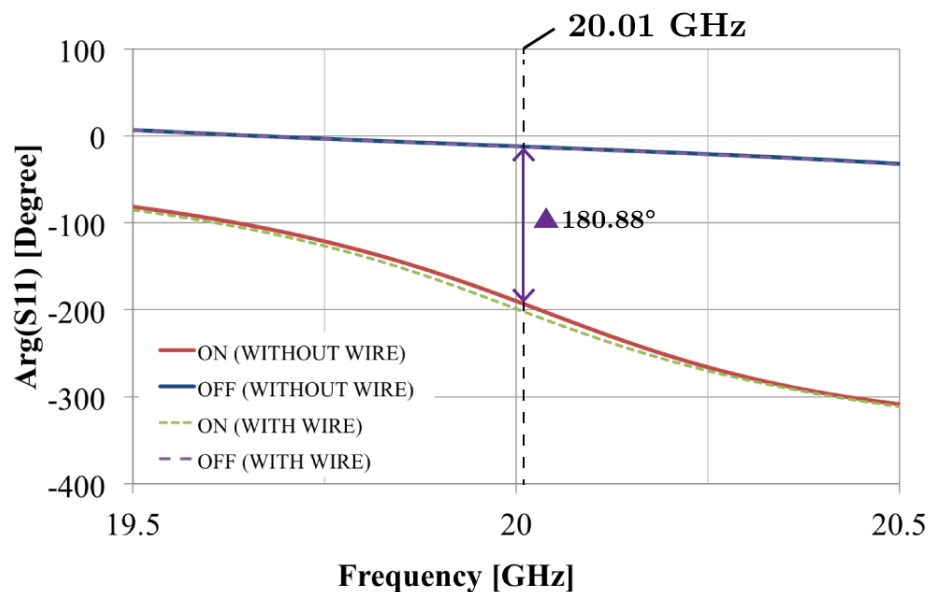


**Figure 4.24.:** Reflected phase of 2 states p-i-n diodes with polarization line

fabricated for real world application. However at this stage, the design is not completely ready for fabrication purpose especially in terms of the dielectrics used in the elementary cell. The thickness of the dielectric layers need to be standardized. Moreover, the actual design includes an air layer that contains the Via(2) and the RF choke. This layer has to be replaced by a solid dielectric for fabrication purpose.

The challenge to fabricate the prototype requires more adaptations in order to meet the fabrication requirements and to reduce errors due to the fabrication processes. In fabrication, the antenna thickness must not exceed the thickness limit imposed by the manufacturer and via diameter must respects the substrate's thickness ratio.

For this purpose 2 types of dielectrics are used and investigated. The first dielectric is RT/duroid® 6002 ( $\epsilon_r = 2.94$ ,  $\tan\delta = 0.0012$ ). This material is chosen because of its low dielectric loss tangent which makes it is an ideal material for millimeter wave application.

The second dielectric is Meteorwave™ 2000 ( $\epsilon_r = 3.40$ ,  $\tan\delta = 0.0040$ ). The dielectric loss tangent for this material is approximately three times higher than the first material but it is still in the acceptable range. The advantage of this material is that its cost is much lower than RT/duroid® 6002. The next section will discuss the design process to use the uniform dielectric material and thickness standardization for all dielectric layers.

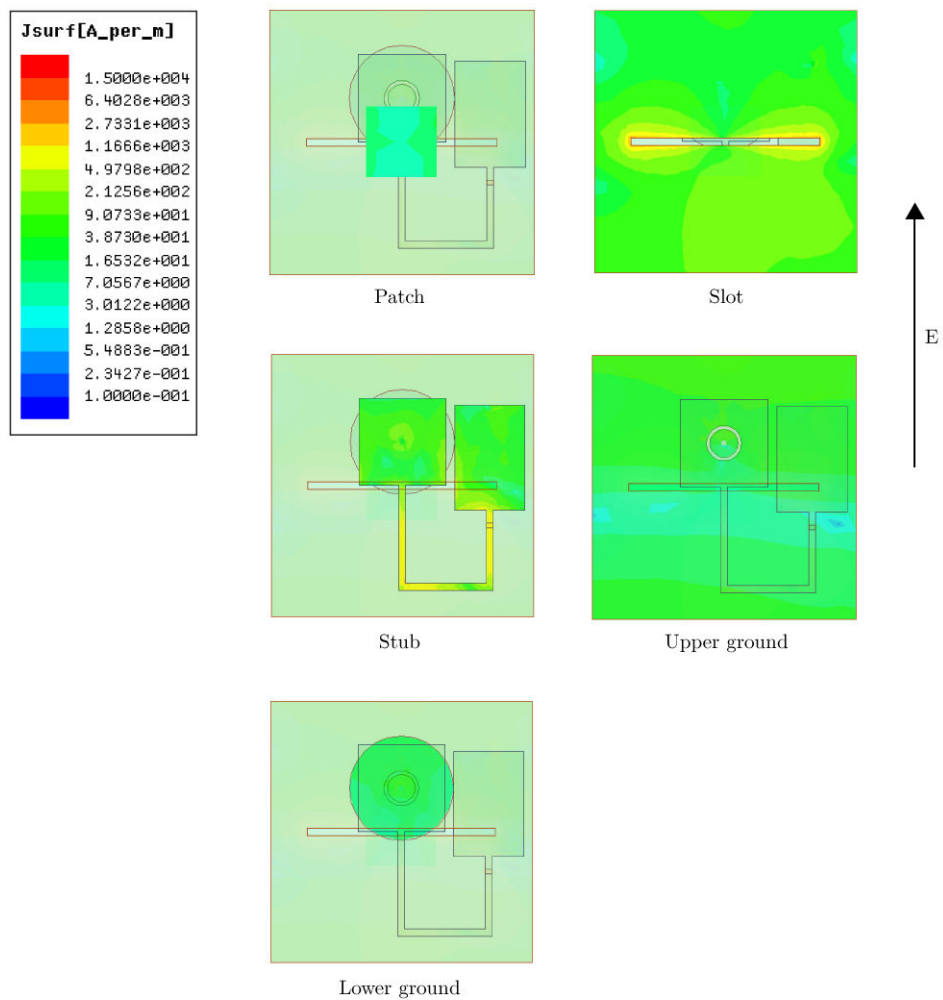


**Figure 4.25.:** Surface current distributions with additional lower ground when diode is ON at 20 GHz

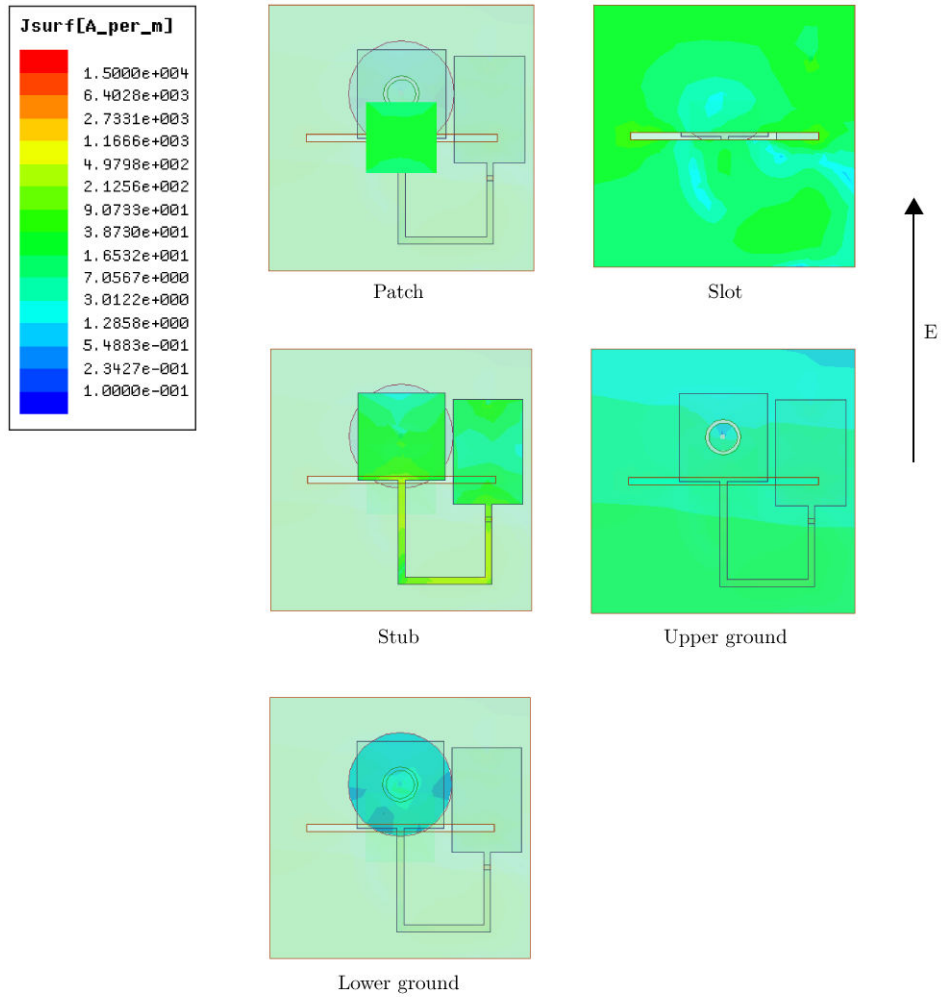


**Figure 4.26.:** Surface current distributions with additional lower ground when diode is OFF at 20 GHz



### 4.1.5. Dielectric standardization using RT/duroid® 6002

The RT/duroid® 6002 can be characterized by having  $\epsilon_r = 2.94$  and low dielectric loss tangent ( $\tan\delta$ ) which equals 0.0012. Because the permittivity and the thickness of the dielectric substrates are modified, the metal layers geometries need to be readapted to make the elementary cell works at 20 GHz. Fig. 4.27 shows the structure adjustment in order to standardize the dielectric material and thickness.

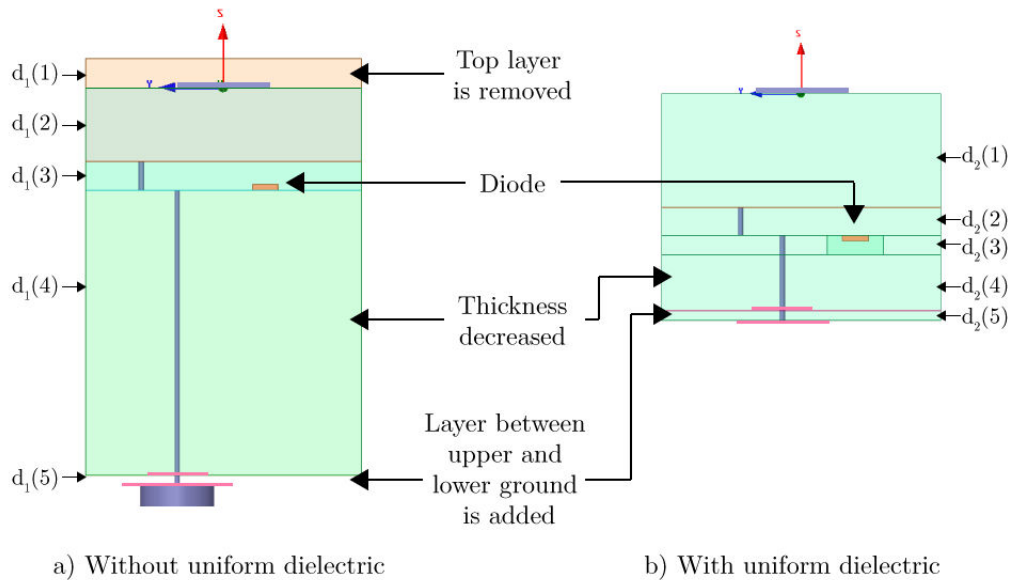


**Figure 4.27.:** Dielectrics adaptations for RT/duroid® 6002

Fig. 4.27(a) shows the elementary cell design discussed in the previous section which has been integrated with RF choke and diode polarization line. Fig. 4.27(b) shows the new design which uses common dielectric material and standard thickness.

The top dielectric  $d_1(1)$  is removed to simplify the fabrication process. Previously, the long Via(2) and the RF choke structure were wrapped in air layers of  $d_1(4)$  and  $d_1(5)$  but in the new design, these layers are switched to standardized dielectric material.

In the new design, the dielectric  $d_1(4)$  is split into 2 layers noted as  $d_2(3)$  and  $d_2(4)$  because an empty space is required in layer  $d_2(3)$  to place the physical p-i-n diode. The total thickness of substrate  $d_1(4)$  is decreased and  $d_2(4)$  is chosen to be as small possible, as it is difficult and expensive to fabricate long via.

Tab. 4.7 and Tab. 4.8 shows the dielectric characteristics from the original passive cell and the new one after using the same dielectric material for all layers with standard thickness. The layer  $d_1(4)$  thickness has been significantly reduced from 7.770 mm to 2.032 mm which is the combination of layers  $d_2(3)$  and  $d_2(4)$ .

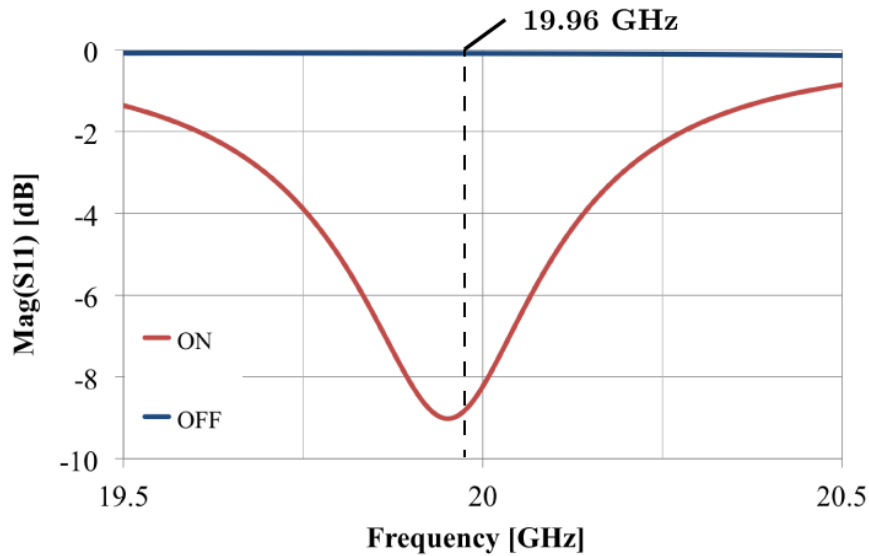


Metal layer	X (mm)		Y (mm)	
Line	$W_s$	1.00	$L_s$	1.00
	$W_{s2}$	2.00	$L_{s2}$	2.00
	$W_l$	0.20	$L_1$	3.00
			$L_2$	2.50
			$L_{31}$	1.00
			$L_{32}$	0.80
Diode	$W_d$	0.20	$L_d$	0.70
Slot	3.90		0.20	
Patch	1.50		1.50	
Unit cell	7.50		7.50	

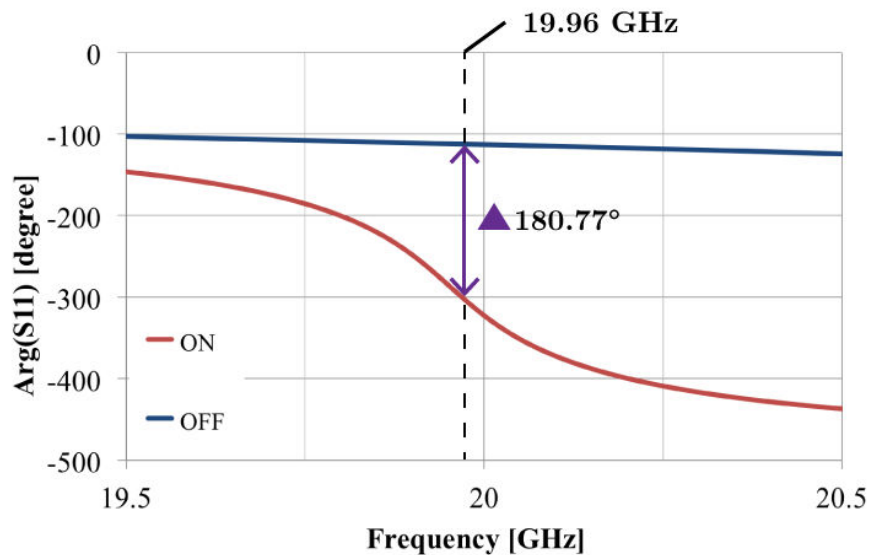
Ground layer	Diameter (mm)	Distance (mm)
Disc(1)	0.80	-
Disc(2)	3.00	-
$D_{GD}$	-	0.10

**Table 4.9.:** Metal dimensions for the standard material and thickness using RT/duroid® 6002

Fig. 4.29 and Fig. 4.30 show the magnitude and phase for the elementary cell using RT/duroid® 6002 substrate. The phase difference is obtained at 20 GHz with reflection loss equals -8.98 dB. The large loss is influenced by multiple factors such as the loss in the diode. It is also due to the surface wave effect at the level of  $d_2(1)$  substrate. Some optimizations are needed to reduce the loss and this will be discussed in the next section.

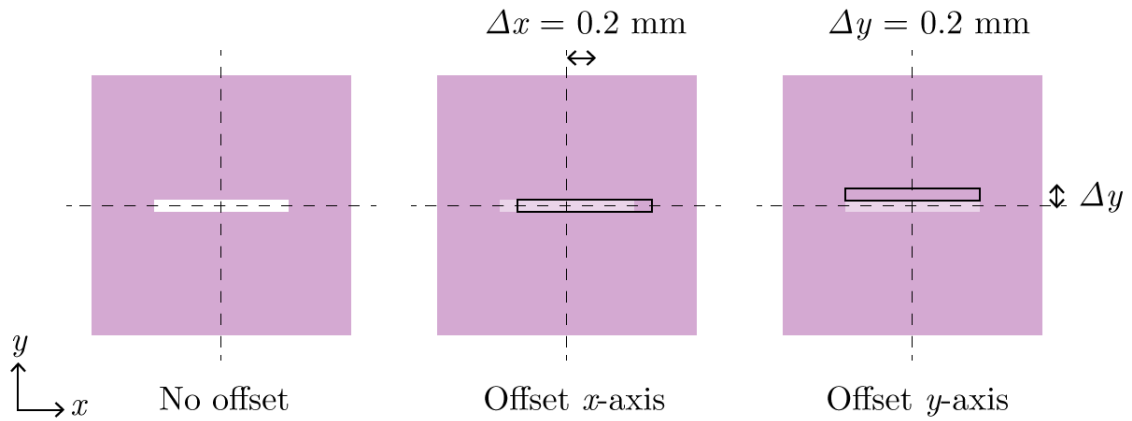


**Figure 4.29.:**  $S_{11}$  magnitude for ON and OFF state using RT/duroid® 6002 substrate

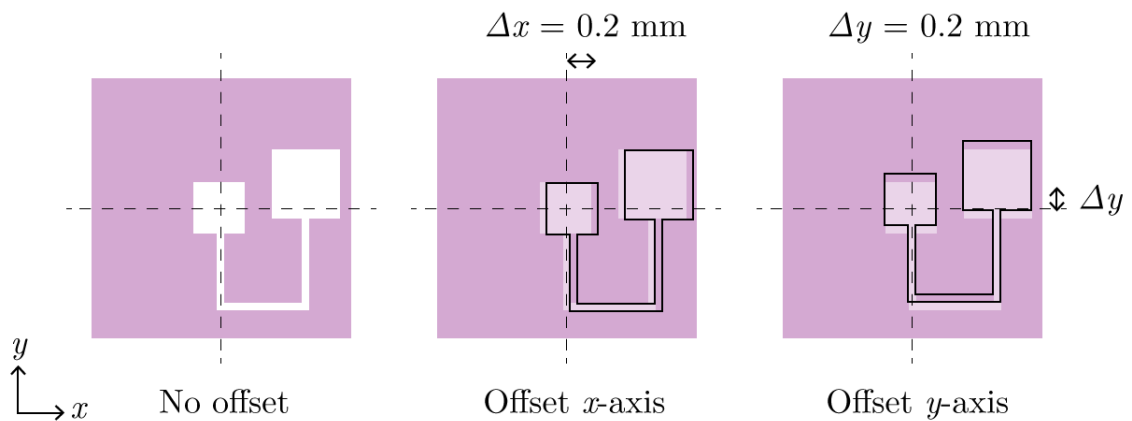


**Figure 4.30.:**  $S_{11}$  phase for ON and OFF state using RT/duroid® 6002 substrate

Before going into fabrication, it is good to estimate the error due to fabrication imperfection and its influence on the reflected phase value. When working with multi layer structure such as this cell, it is impossible to perfectly align the layers as in simulation design, so there will be some misalignment when these layers are stacked together. Fig. 4.31 and Fig. 4.32 show the offset configuration for slot layer and stub layer respectively. The offset distance for  $x$  and  $y$  axis directions equal 0.2 mm and this misalignment value is larger than the typical fabrication tolerance.



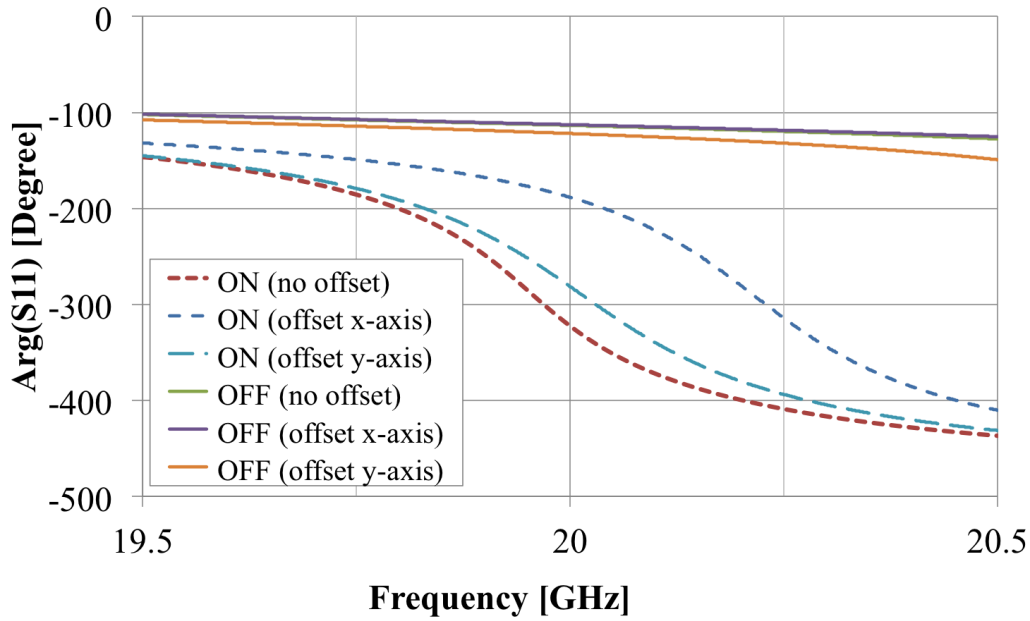
**Figure 4.31.:** Offset configuration for slot layer



**Figure 4.32.:** Offset configuration for stub layer

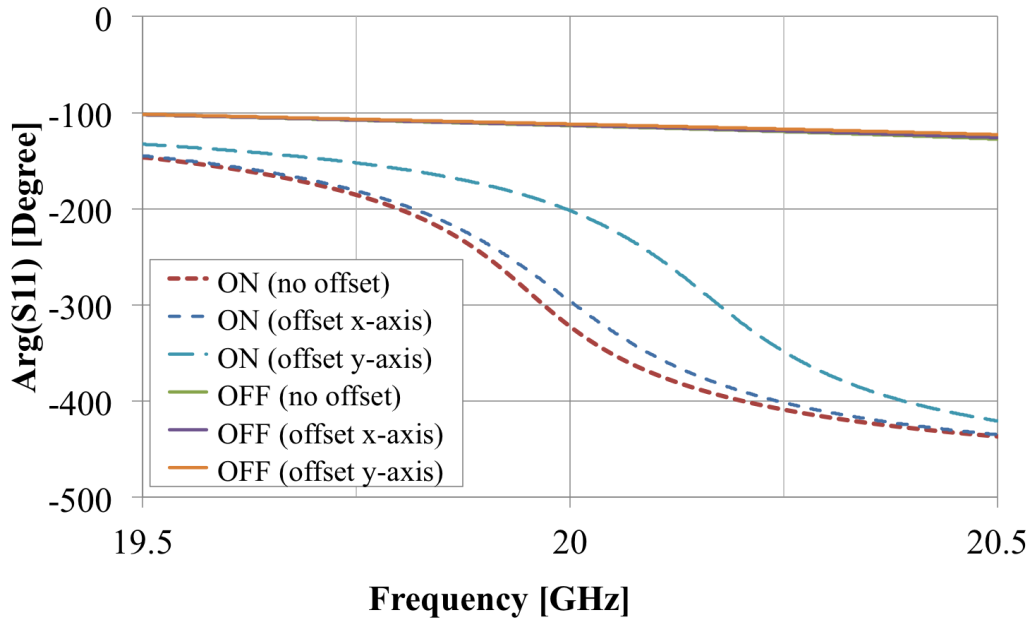
Fig. 4.33 shows the phase variations when slot position is offset by 0.2 mm in  $x$  and  $y$  axis directions. The offset in  $y$  direction has less influence on the reflected phase while an offset of the slot layer in  $x$  direction shifts the reflected phase by 0.2 GHz when the diode's state is ON. The reflected phase when diode is off is not significantly influenced by the slot layer offset.

Fig. 4.34 shows the phase variations for the offset of the stub layer as shown in Fig. 4.32. From the results, a phase shift of 0.2 GHz is observed when the stub layer



**Figure 4.33.:** Reflected phase variations due to the slot layer offset (0.2 mm) in x-axis and y-axis

is offset by 0.2 mm in  $y$  direction (diode is on). The offset of the stub in  $x$  direction has small influence on the phase variations either when diode is ON and OFF.



**Figure 4.34.:** Reflected phase variations due to the stub layer offset (0.2 mm) in x-axis and y-axis

In general the reflected phase is not influenced by the layers offsets when diode is off. In both cases, the phase shift observed due to the offset is around 0.2 GHz. This means that the errors due to the layers misalignment are acceptable as the frequency shifts are small relative to elementary cell designed frequency (20 GHz). One of the advantages of Fresnel reflectarray is that it is less sensitive to the elementary cell's reflected phase error due to the correction in zones instead of per elementary cell.

Fig. 4.35 and Fig. 4.36 show the surface current distributions for ON and OFF diodes states using standard thickness and RT/duroid® 6002 substrate. These current distributions are used and analyzed in order to understand the influence of the square metal patch on the cell's reflected wave ( $S_{11}$ ). The cell simulation shows that the current is mainly concentrated on the slotted metal surface and the phase tuning stub and is weak on the patch on the top of the cell. Therefore, the presence of this patch has a negligible influence on the surface currents.

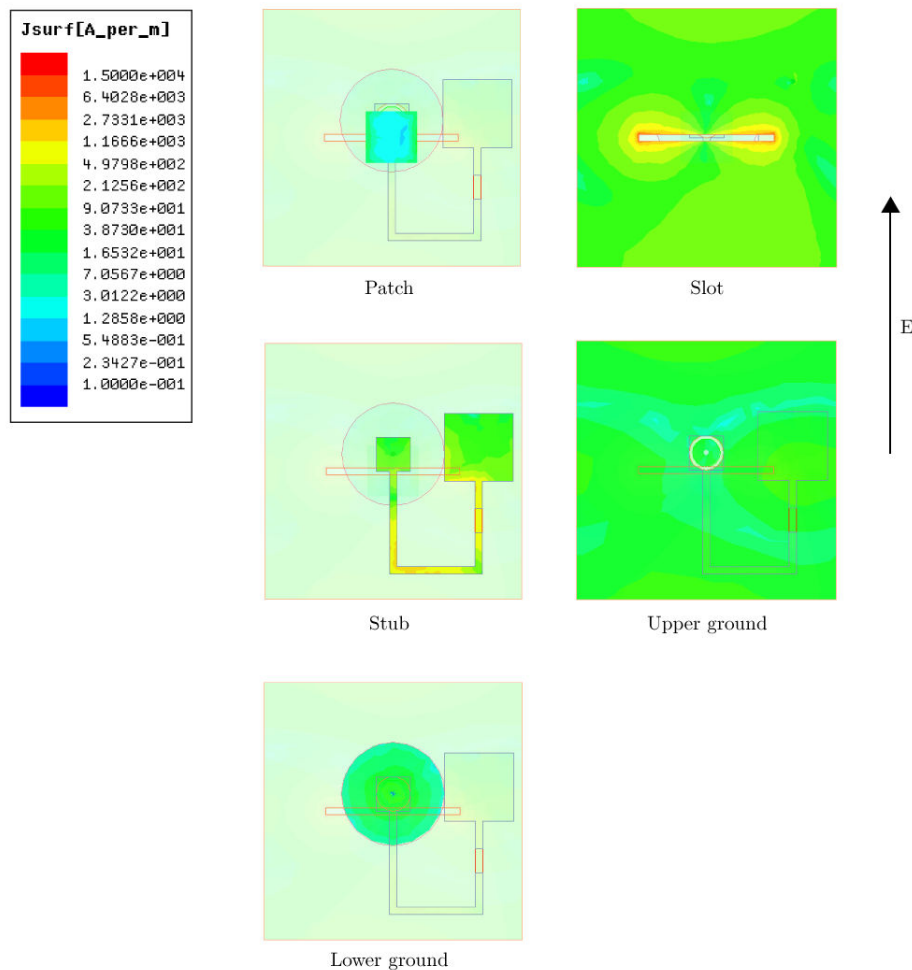


**Figure 4.35.:** Surface current distributions using RT/duroid® 6002 substrate when diode is ON at 20 GHz

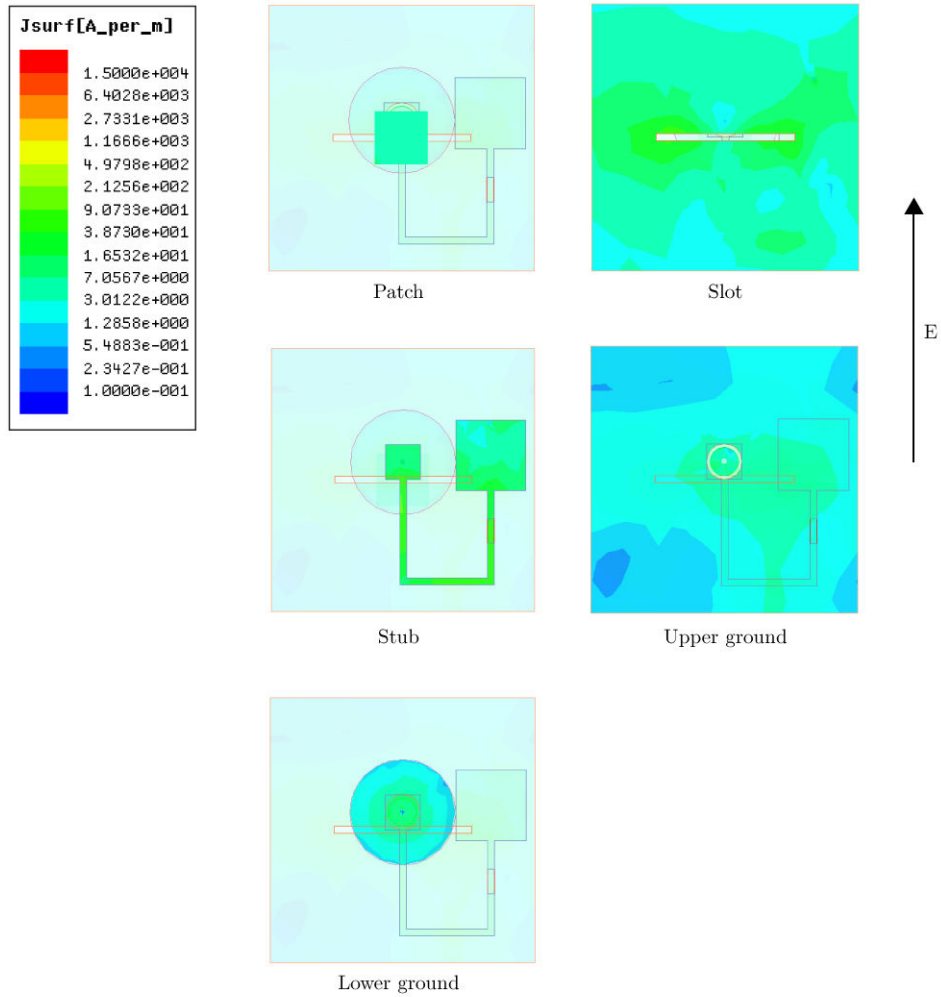


**Figure 4.36.:** Surface current distributions using RT/duroid® 6002 substrate when diode is OFF at 20 GHz



Fig. 4.37 shows the surface current intensities with (a) and without (b) the patch on the top of the cell. The surface current analysis shows that higher current intensity is present on the slotted surface in ON state and this explains why the patch has less influence on the cell's reflected wave. Moreover, the absence of the patch has small effect to the cell's reflected wave variation.

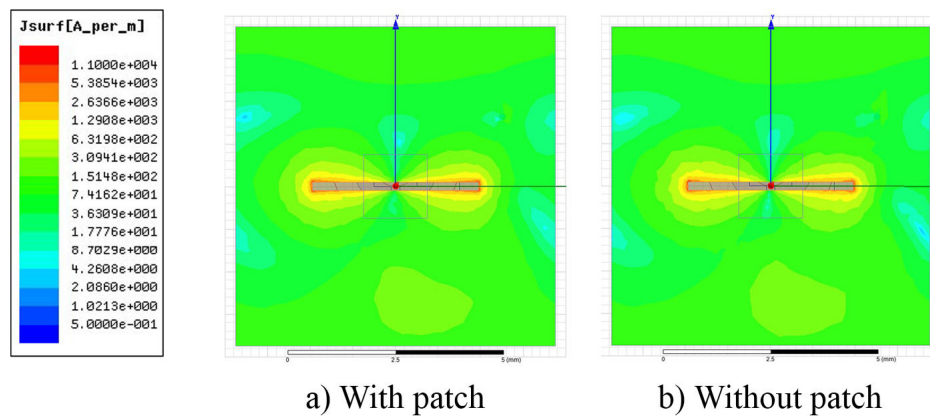


**Figure 4.37.:** Slotted surface current comparison with and without square patch as radiating element

Fig. 4.38 shows the cell's reflected wave magnitude comparison. The cell's reflected wave magnitudes for OFF state in both cases are identical. For ON state, the loss value is higher when the patch is removed which is - 9.5dB and with the presence of the patch, the loss value is - 9dB. In Fig. 4.39, the phase variation for the 2 cases is small. With the presence of the patch, the phase variation between ON and OFF state at 20GHz is  $181^\circ$ , while the phase variation without the patch is  $184^\circ$ . This indicates that  $180^\circ$  phase variation is still be obtained despite of the absence of the patch on the top of the cell's surface. This means that the slot layer is the major contributor to the radiation.

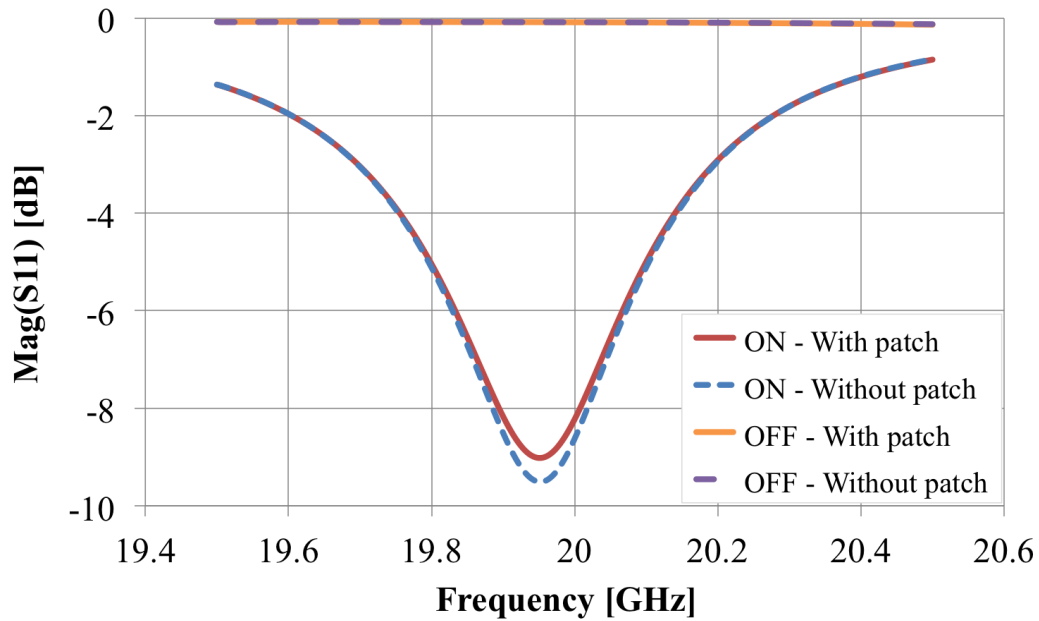


Figure 4.38.: Cell's reflected magnitude comparison when patch is removed

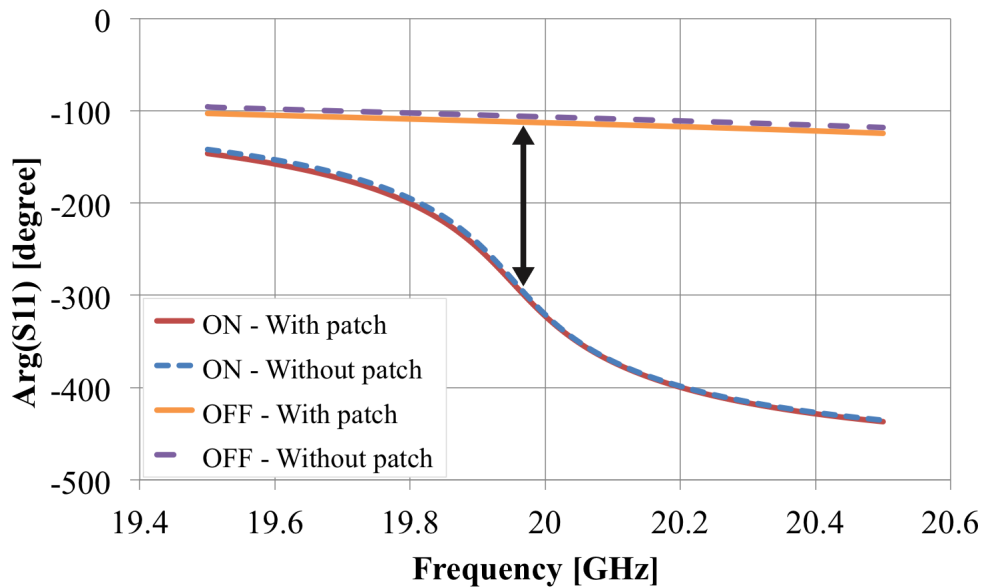


Figure 4.39.: Cell's reflected phase comparison when patch is removed

One of the factors which contributes to the major loss of the reflected wave is due to the surface wave effect. The elementary cell shown in Fig. 4.27(b) has 5 substrates with the total thickness equals to 6.096 mm. The thickness of substrate labeled  $d_2(1)$  is 3.048 mm and it is the thickest in the structure. The calculated

cutoff frequency for  $d_2(1)$  thickness is 17.7 GHz (first mode cutoff frequency), this thick value will introduce the surface wave effect and contributes to the large value of reflected wave loss ( $S_{11}$ ).

In order to ensure this cutoff frequency is greater than 20 GHz, the maximum thickness for  $d_2(1)$  cannot exceed 2.69 mm. The cutoff frequency and maximum thickness values are calculated by using equation 4.1 [77]. In the equation,  $n$  is the surface wave mode ( $n = 0, 2, 4, \dots$  for TM modes,  $n = 1, 3, 5, \dots$  for TE modes),  $c$  refers to the speed of light,  $h$  is the substrate's thickness and  $\varepsilon_r$  is the relative substrate's dielectric constant. In order to avoid surface waves, the thickness of  $d_2(1)$  is changed to 2.286 mm that is the closest standardized thickness value.

$$f_{cutoff} = n \times \frac{c}{4 \times h \times \sqrt{\varepsilon_r - 1}} \quad (4.1)$$

Fig. 4.40 shows the comparison between the original (same dielectric material) and standardized thickness elementary cell and the one optimized for reducing the reflected wave loss. In Fig. 4.41 and Fig. 4.42, original refers to the unmodified elementary cell Fig. 4.40(a) while optimized refers to elementary cell Fig. 4.40(b) that does not have any patch on the top surface and  $d_2(1)$  equals to 2.286 mm. For the cell's magnitude, the loss value decreases from -9 dB to -5.4 dB. For the reflected phase, there is an offset that changes the phase values but the phase variation between ON and OFF states is maintained ( $180.2^\circ$  at 19.93 GHz). Moreover, the phase variation for ON state is smoother at the center frequency of 20 GHz.

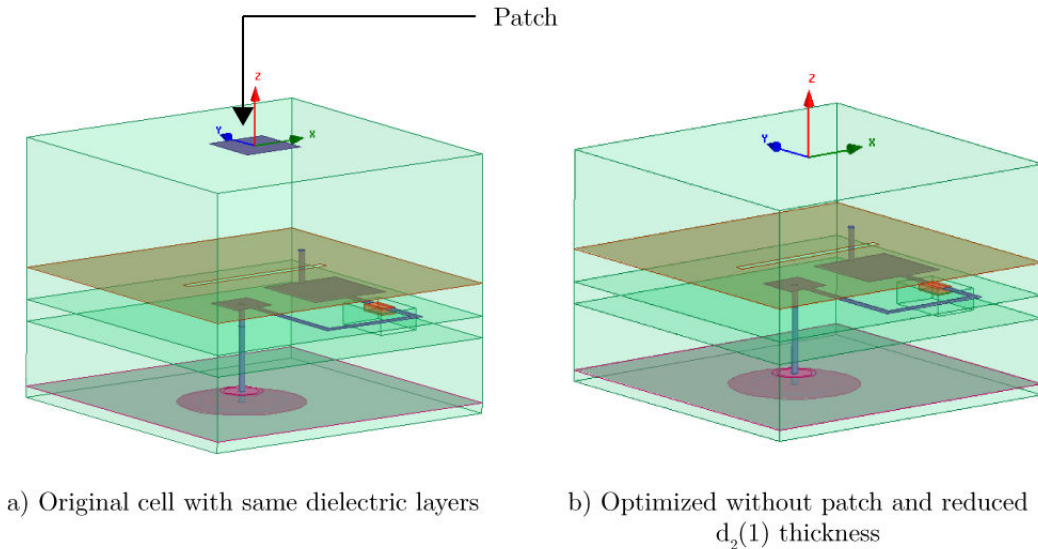


**Figure 4.40.:** Elementary cell comparison between original and optimized design

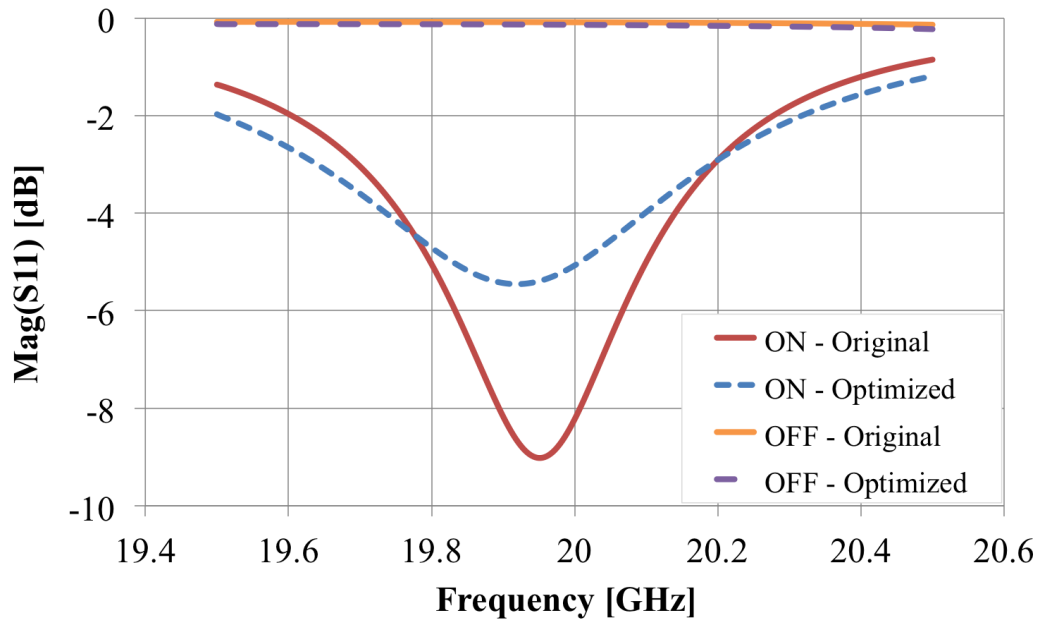


**Figure 4.41.:** Cell's reflected magnitude comparison with reduced  $d_2(1)$  thickness and patch removed

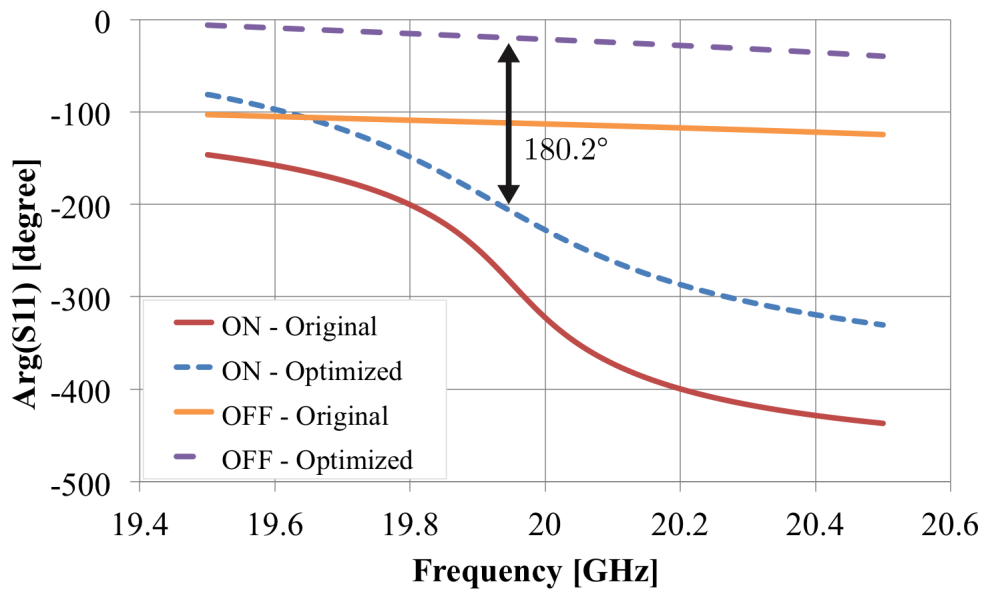


**Figure 4.42.:** Cell's reflected phase comparison with reduced  $d_2(1)$  thickness and patch removed

From these simulation results, new thickness value helps to reduce the magnitude of  $S_{11}$  loss and the phase variation error, as the consequence the reflectarray performance can be improved. By removing the radiating layer, one of the possible fabrication errors for the elementary cell is also reduced. The elementary cell structure without patch on the top has created new possibility of reflectarray design. Using the optimized elementary cell design, it is possible to create active slotted reflectarray that integrates radome directly on top of it.

This can be done either by using the top substrate  $d_2(1)$  as it is or by replacing it with a more robust radome material such as Rohacell ( $\varepsilon_r = 1.04$ ,  $\tan\delta = 0.01$ ). In this case, the slotted rectangle size needs to be adjusted to take into account the new material dielectric constant. The advantage of this concept is that it will simplify the whole antenna structure and less space is required for the antenna protection. The next section will discuss the standardization using second material which is Meteorwave™ 2000.

### 4.1.6. Dielectric standardization using Meteorwave™ 2000

Meteorwave™ 2000 substrate ( $\epsilon_r = 3.40$ ,  $\tan\delta = 0.004$ ) has been proposed by manufacturer as alternative to RT/duroid® 6002 because it is less expensive. Changing dielectric material requires elementary cell geometries to be readapted. It can be seen that this material has shifted down the working frequency to 19 GHz instead of 20 GHz in Fig. 4.43. In addition, more loss is encountered which makes the reflected magnitude value equals to -7.6 dB.

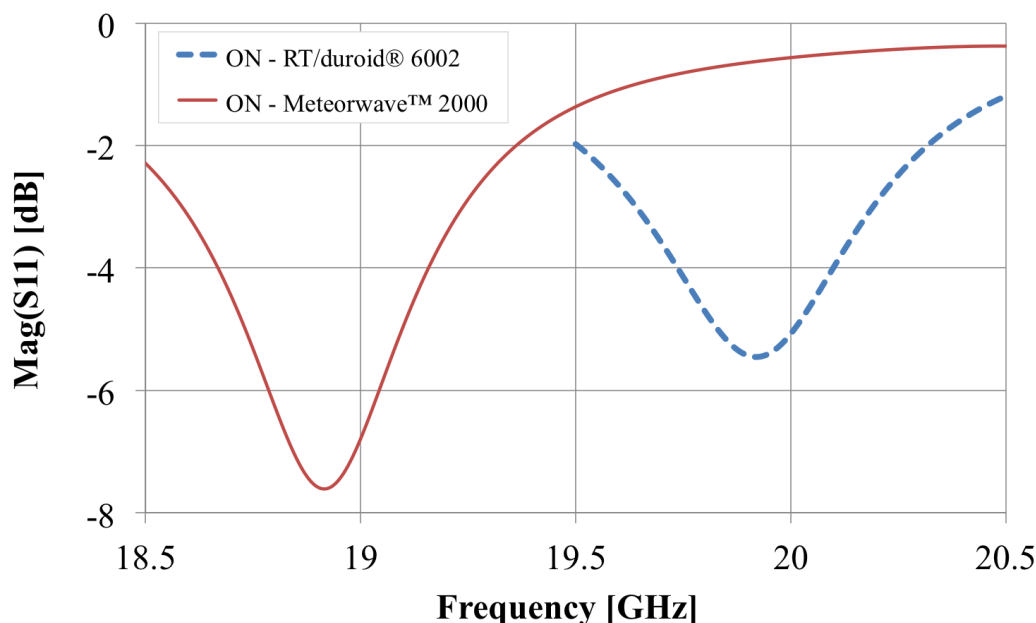


**Figure 4.43.:**  $S_{11}$  magnitude for ON state using 2 different substrates

One of the possible solutions to readapt the working frequency is to modify the dimension of slotted rectangle surface defined by  $slot_x$  and  $slot_y$ . Setting these 2 parameters respectively to 2.8 mm and 2.2 mm makes the elementary cell working at 20 GHz. This is the simplest solution because the rest of the parameters for phase tuning stub, upper and lower ground are unchanged. In addition, the manufacturer imposes via diameter constraint based on the substrate thickness as shown in Fig. 4.44.

Via(1) diameter is increased from 0.15 mm to 0.6 mm. Based on manufacturer requirement, Via(1) diameter to  $d_2(2)$  substrate thickness ratio is 8:10 and the diameter for Via(2) must be 0.3 mm. There is also an additional length of 0.15 mm that needs to be added to Via(2) as shown in Fig. 4.44(b). The thicknesses of  $d_2(1)$  and  $d_2(5)$  are reduced to 1.524 mm and 0.127 mm respectively in order to reduce the total thickness of the structure. Tab. 4.10 and Tab. 4.11 summarize the dielectric thickness and metal layers dimensions for adapting the elementary cell with Meteorwave™ 2000 substrate.

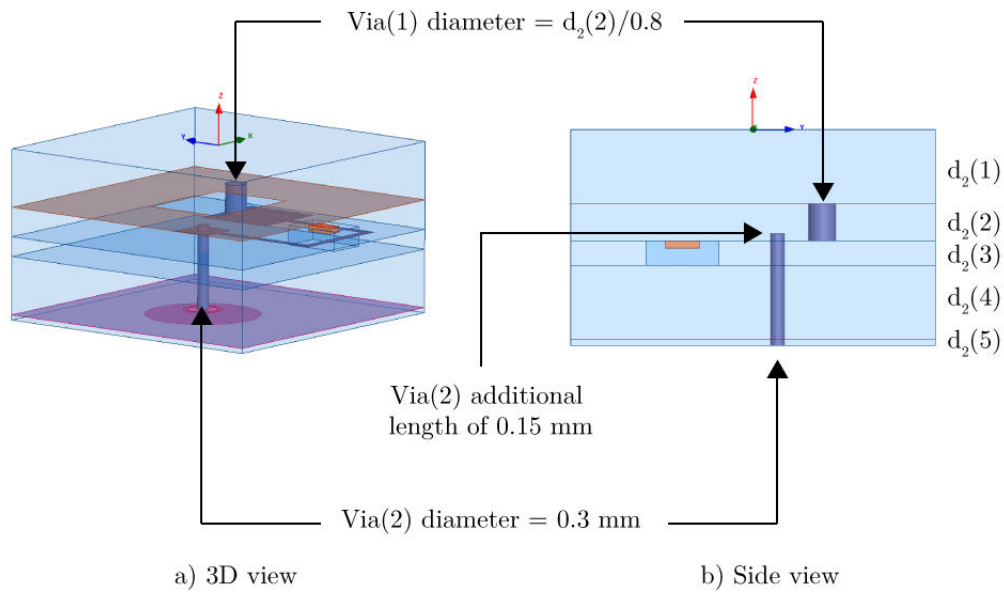


**Figure 4.44.:** Via diameter modification based on substrate's thickness

Dielectric layer	Thickness (mm)	$\epsilon_r$	$\tan\delta$
$d_2(1)$	1.524	3.400	0.004
$d_2(2)$	0.762		
$d_2(3)$	0.508		
$d_2(4)$	1.524		
$d_2(5)$	0.127		

**Table 4.10.:** Dielectric characteristic using Meteorwave™ 2000

Metal layer	X (mm)	Y (mm)	
Line	$W_s$	1.00	
	$W_{s2}$	2.00	
	$W_l$	0.20	$L_1$
			$L_2$
			$L_{31}$
			$L_{32}$
Diode	$W_d$	0.20	
Slot	2.80	2.20	
Unit cell	7.50	7.50	

Ground layer	Diameter (mm)	Distance (mm)
Disc(1)	0.80	-
Disc(2)	3.00	-
$D_{GD}$	-	0.10

**Table 4.11.:** Metal layers dimension for elementary cell using Meteorwave™ 2000 substrate at 20 GHz

Fig. 4.45 and Fig. 4.46 show the reflection coefficient magnitude and phase for the elementary cell using Meteorwave™ 2000 substrate. For each diode states ON and OFF, there are 2 cases. The first case represents normal Via(1) and Via(2) diameters which equal 0.15 mm. The second case noted as “Via changes” is the via height and diameter modifications as shown in Fig. 4.44.

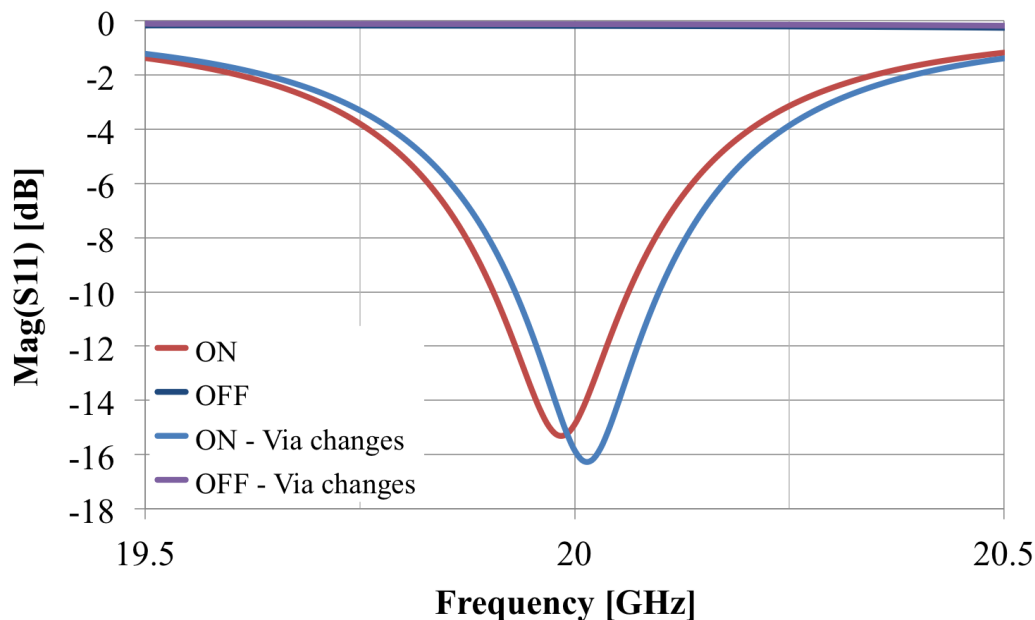


**Figure 4.45.:** S<sub>11</sub> magnitude for elementary cell using Meteorwave™ 2000 substrate at 20 GHz with small and large diameter via

In both cases, the loss encountered in this design is large. For normal via diameter, the loss is -14.4 dB at 20 GHz and for large via the loss value is -16.2 dB. The changes in via diameter and height have increased the loss about 2 dB with small frequency shift. Despite the via changes, the phase difference of 180° is still obtained at 20 GHz. There is a phase offset introduced with the large via diameter.

The via modifications in the elementary cell add 2 dB to the reflected wave loss which is already large compared to the one using RT/duroid® 6002 substrate. Multiple combinations of slotted rectangle surface *slot\_x* and *slot\_y* parameters are tested to obtain the combination that gives minimum loss of -10 dB but none combination is found at 20 GHz.

This shows that to improve the performance of the elementary cell, modifications on the other parameters and geometries are required. Relying only on the slotted rectangle parameters is inadequate. One of the possible solutions to reduce the loss is to minimize the matching stub connected to the phase delay line. This will maximize the reflected wave as only small effect of matching stub is taken into account. In addition, rather than making the cell functioning in the middle of the



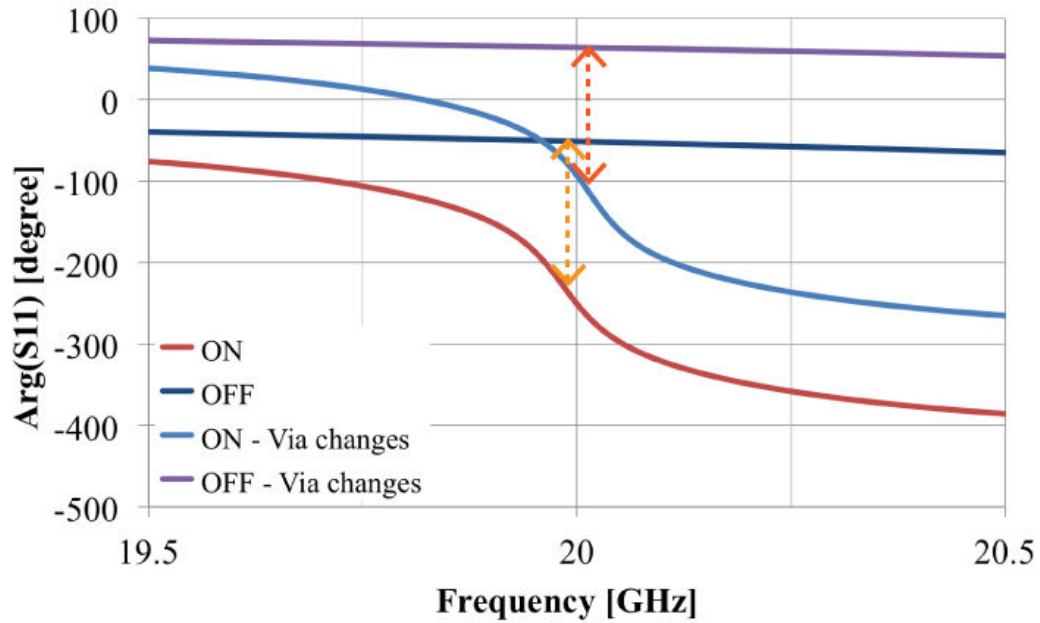


**Figure 4.46.:**  $S_{11}$  phase for elementary cell using Meteorwave™ 2000 substrate at 20 GHz with small and large diameter vias

resonance zone which has the maximum loss, functioning a little outside of the resonance zone will help to reduce the loss.

Using the same design optimized for RT/duroid® 6002 and replacing the dielectrics with Meteorwave™ 2000 is used as the base design. The  $S_{11}$  magnitude for this design is shown in Fig. 4.43 with resonance at 19 GHz with  $S_{11}$  magnitude equals -7.6 dB. The matching stub is described by  $W_s$  and  $L_s$  parameters. Setting these values both ( $W_s$ ,  $L_s$ ) to 0.2 mm transforms the matching stub to behave like a phase delay line as shown in Fig. 4.47.

Fig. 4.48 shows the  $S_{11}$  magnitude comparison using large and small matching stubs. Decreasing the size of the matching stub has increased the reflected wave without significantly changing the resonance frequency. Using large matching stub gives a loss of -7.6 dB while using small matching stub results a loss value of -4.7 dB. In this case, the loss is reduced by 3 dB. Small matching stub size will help to reduce the loss and improve the elementary cell performance. Based on this observation, the phase tuning stub geometry is adjusted by reducing the length of the matching stub and the total electrical length of the phase delay line is increased in order to obtain phase difference of  $180^\circ$  outside resonance zone. The changes are shown in Fig. 4.49.

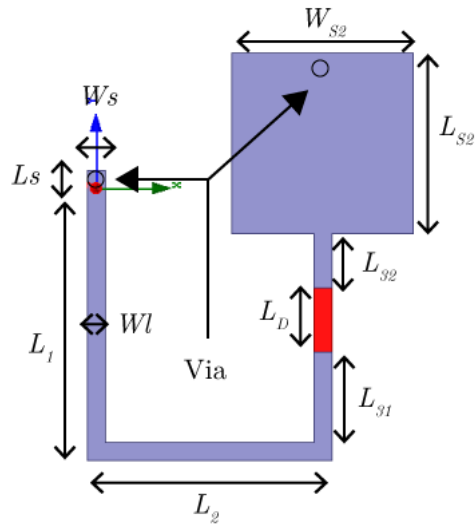


Figure 4.47.: Matching stub modification

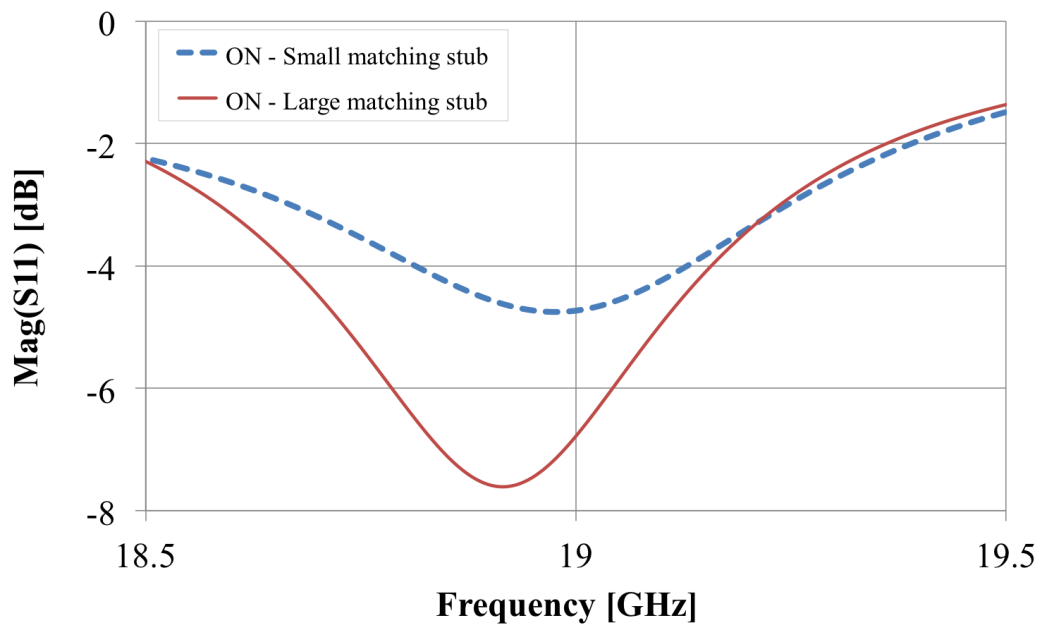
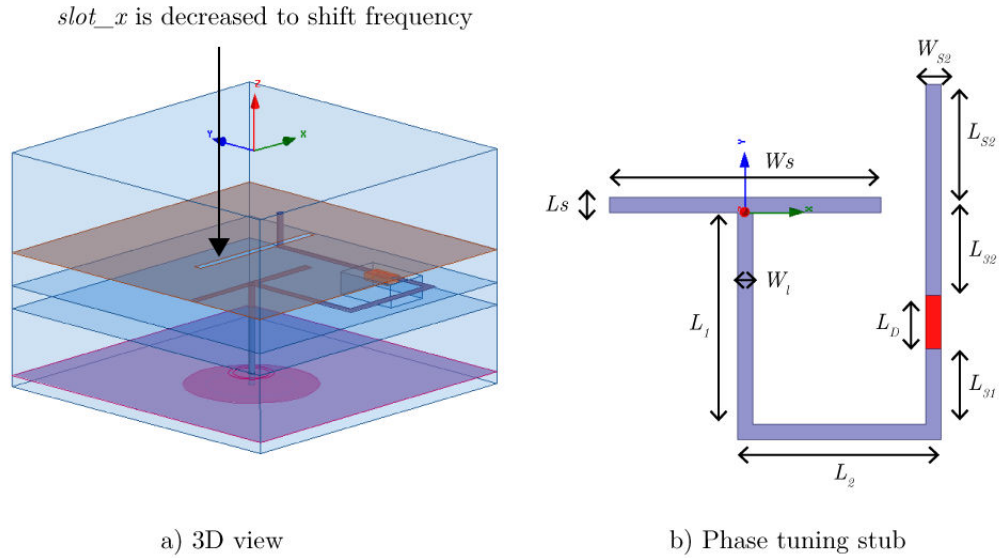


Figure 4.48.:  $S_{11}$  magnitude comparison for large and small matching stub size



**Figure 4.49.:** Phase tuning stub modifications to adapt and optimize elementary cell for Meteorwave™ 2000

In Fig. 4.49(b) the  $W_{s2}$  parameter is changed to 0.2 mm in order to have more space for increasing the width of matching stub which is noted as  $W_s$ . To increase the total length of the stub,  $W_s$  is set to 3.6 mm and its height  $L_s$  is decreased to 0.2 mm. To shift the working frequency upwards to 20 GHz, the *slot\_x* parameter is decreased to 3.6 mm from 3.9 mm as shown in Fig. 4.49(a).

Fig. 4.50 and Fig. 4.51 show the  $S_{11}$  magnitude and phase for the elementary cell using the modified phase tuning stub (Fig. 4.49(b)). The phase difference of  $180^\circ$  is retrieved at 19.87 GHz. At this frequency, the  $S_{11}$  loss values are -4.9 dB for ON state and -1.8 dB for OFF state. From these simulations results, the elementary cell shows its capability to work near to the resonance zone but not at the center of the resonance where the loss is maximum.

Fig. 4.52 and Fig. 4.53 show the current distributions on metal layers for diode states ON and OFF. The current distributions are quite identical for both states as the elementary cell works outside resonance zone at 20 GHz.

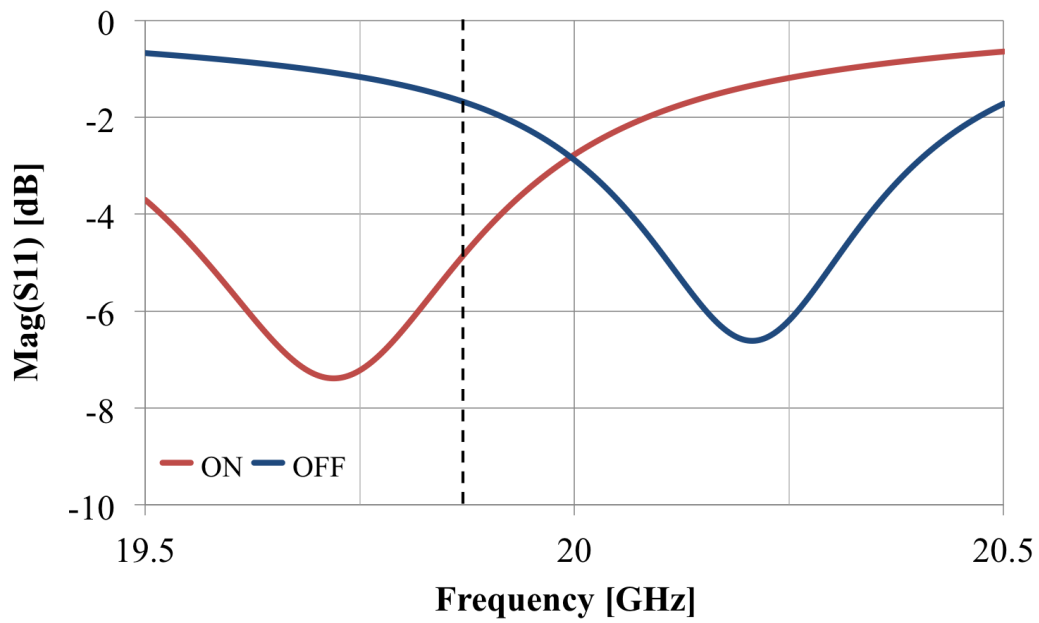


Figure 4.50.:  $S_{11}$  magnitude for the elementary cell shown in Fig. 4.49

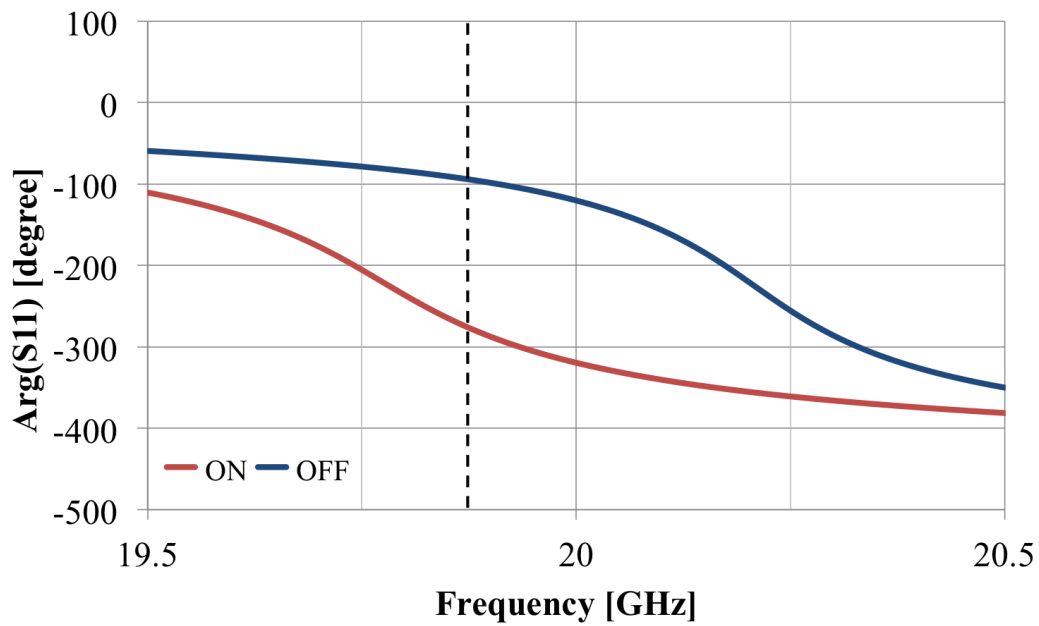
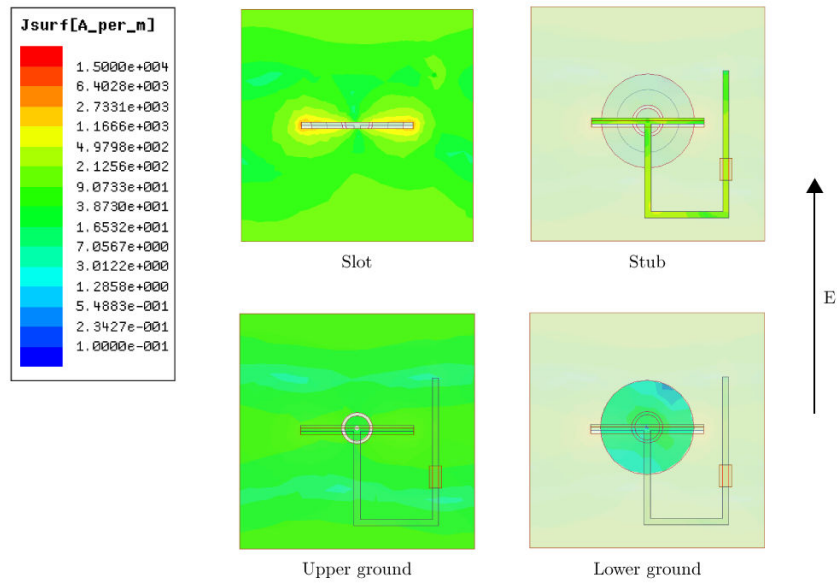
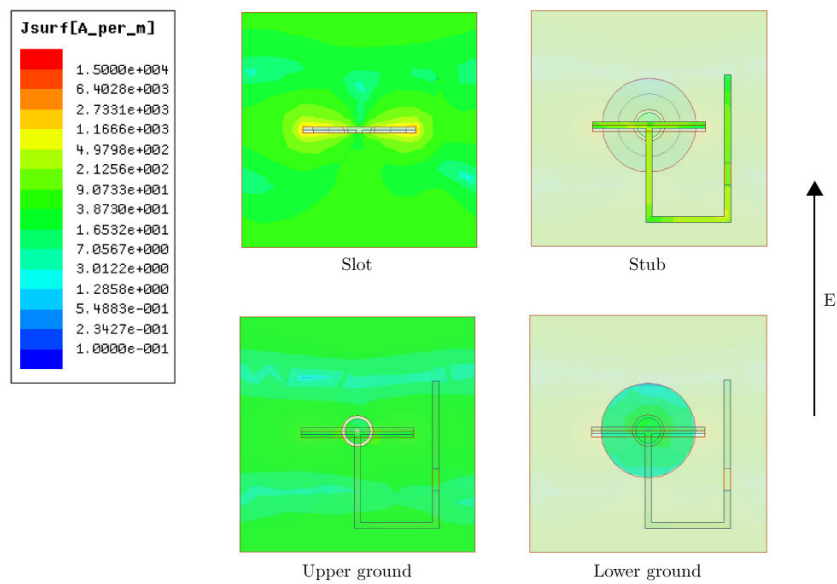


Figure 4.51.:  $S_{11}$  phase for the elementary cell shown in Fig. 4.49



**Figure 4.52.:** Surface current distributions when diode is ON at 20 GHz using Meteorwave™ 2000



**Figure 4.53.:** Surface current distributions when diode is OFF at 20 GHz using Meteorwave™ 2000

The constraints on the via diameter and height as discussed previously and shown in Fig. 4.44, are applied to the new elementary cell design. Phase tuning stub geometry is slightly adjusted to take into account the change in the via diameter as illustrated in Fig. 4.54. Two discs are added to the phase tuning stub for connection with Via(1) and Via(2). The first disc specified by diameter  $\varnothing_2$  is positioned at the middle of Via(2) with  $\varnothing_2 = 0.5$  mm and the hole for the disc has diameter of Via(2) which is 0.3 mm. The second disc is added at the end of the delay line and it is described by  $\varnothing_{12}$  with hole diameter  $\varnothing_{11}$ . The diameter  $\varnothing_{12} = 1.2$  mm and the hole inside it has diameter  $\varnothing_{11} = 0.8$  mm. Tab. 4.12 summarizes the metal layers dimensions for the design which takes into account the changes in via diameter.

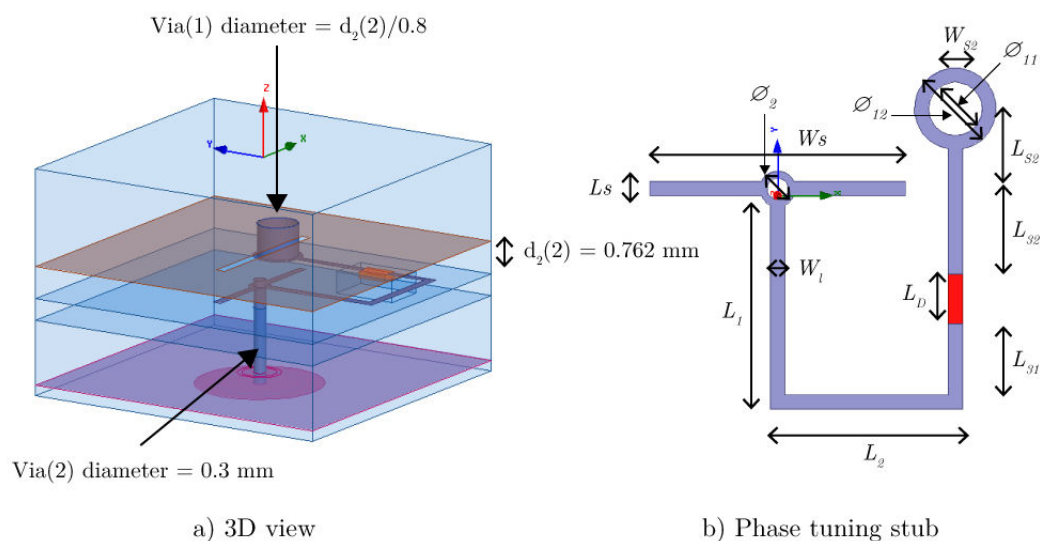


**Figure 4.54.:** Phase tuning stub geometry modification for large via

Metal layer	X (mm)		Y (mm)	
Line	$W_s$	3.60	$L_s$	0.20
	$W_{s2}$	0.20	$L_{s2}$	2.00
	$W_l$	0.20	$L_1$	3.00
			$L_2$	2.50
			$L_{31}$	1.00
		$L_{32}$	0.80	
Diode	$W_d$	0.20	$L_d$	0.70
Slot	3.60		0.20	
Unit cell	7.50		7.50	

Ground layer	Diameter (mm)	Distance (mm)
Disc(1)	0.80	-
Disc(2)	3.00	-
$D_{GD}$	-	0.10

Via disc	Diameter (mm)
$\varnothing_{12}$	1.2
$\varnothing_{11}$	0.8
$\varnothing_2$	0.5

**Table 4.12.:** Metal layers dimensions with via discs

Fig. 4.55 and Fig. 4.56 show the  $S_{11}$  magnitude and phase after applying the via changes. The changes in via diameter and height have modified the  $S_{11}$  magnitude and phase for ON state. The phase difference of  $180^\circ$  is retrieved at 19.61 GHz with the  $S_{11}$  magnitude equals -9.3 dB. The Via(2) diameter's modification shifts the elementary cell working frequency towards resonance zone which results in large value of loss.

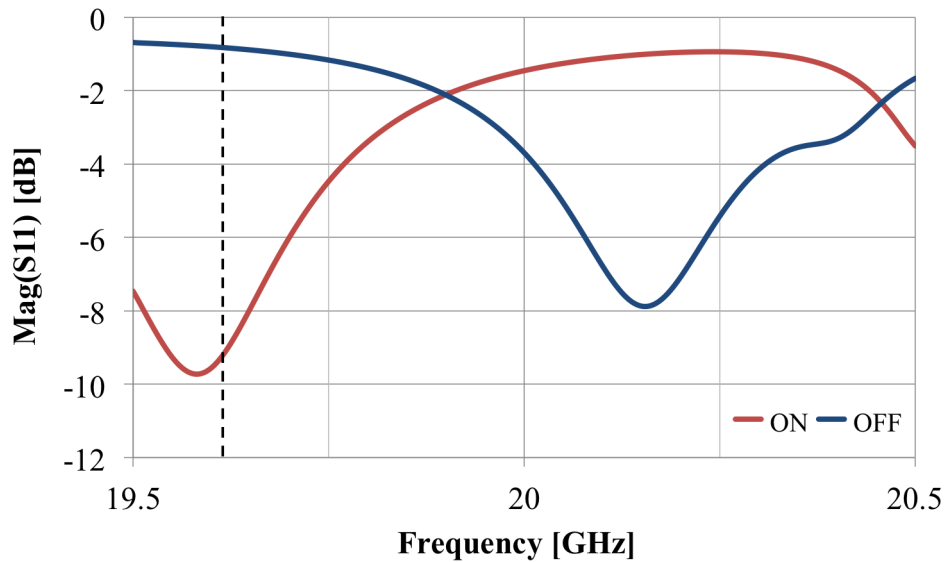


**Figure 4.55.:**  $S_{11}$  magnitude for the elementary cell after applying the via changes

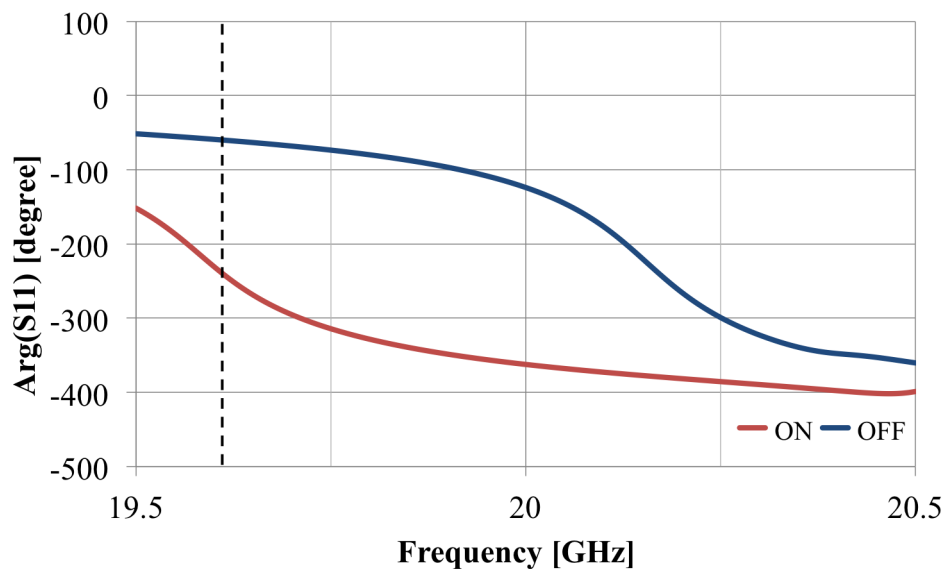


**Figure 4.56.:**  $S_{11}$  phase for the elementary cell after applying the via changes

One possible solution to overcome the phase shift is by increasing and adjusting the phase delay line length. Additional segment is added to the phase tuning stub as shown in Fig. 4.57. The segment added is labeled as  $L_4$  and its value is 2.6 mm. In addition, the value of  $L_{s2}$  is increased by 0.4 mm which makes the total length equals 2.4 mm. To decrease the Via(2) diameter, the thickness of  $d_2(2)$  is decreased to 0.635 mm from 0.762 mm. The  $slot\_x$  parameter is increased by 0.1 mm to adjust the working frequency to approach closer 20 GHz. Tab. 4.13 and Tab. 4.14 show the updated dielectric characteristics and metal layers dimensions.

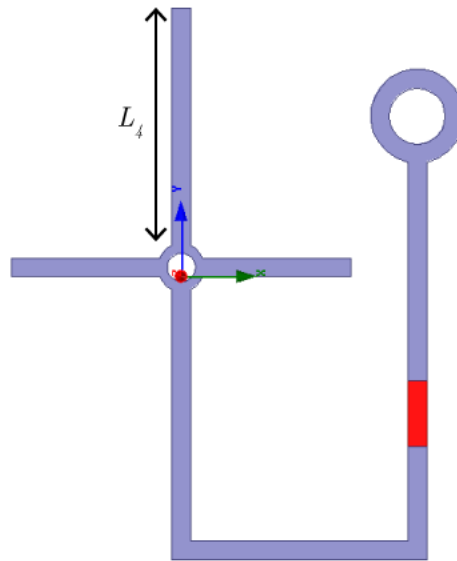


**Figure 4.57.:** Additional stub segment added to compensate the phase shift

Dielectric layer	Thickness (mm)	$\epsilon_r$	$\tan\delta$
$d_2(1)$	2.286	3.400	0.004
$d_2(2)$	0.635		
$d_2(3)$	0.508		
$d_2(4)$	1.524		
$d_2(5)$	0.254		

**Table 4.13.:** Dielectric characteristic using Meteorwave™ 2000 adapted for new phase delay line design shown in Fig. 4.57



Metal layer	X (mm)		Y (mm)	
Line	$W_s$	3.60	$L_s$	0.20
	$W_{s2}$	0.20	$L_{s2}$	2.40
	$W_l$	0.20	$L_1$	3.00
			$L_2$	2.50
			$L_{31}$	1.00
			$L_{32}$	0.80
			$L_4$	2.60
Diode	$W_d$	0.20	$L_d$	0.70
Slot	3.70		0.20	
Unit cell	7.50		7.50	

Ground layer	Diameter (mm)	Distance (mm)
Disc(1)	0.80	-
Disc(2)	3.00	-
$D_{GD}$	-	0.10

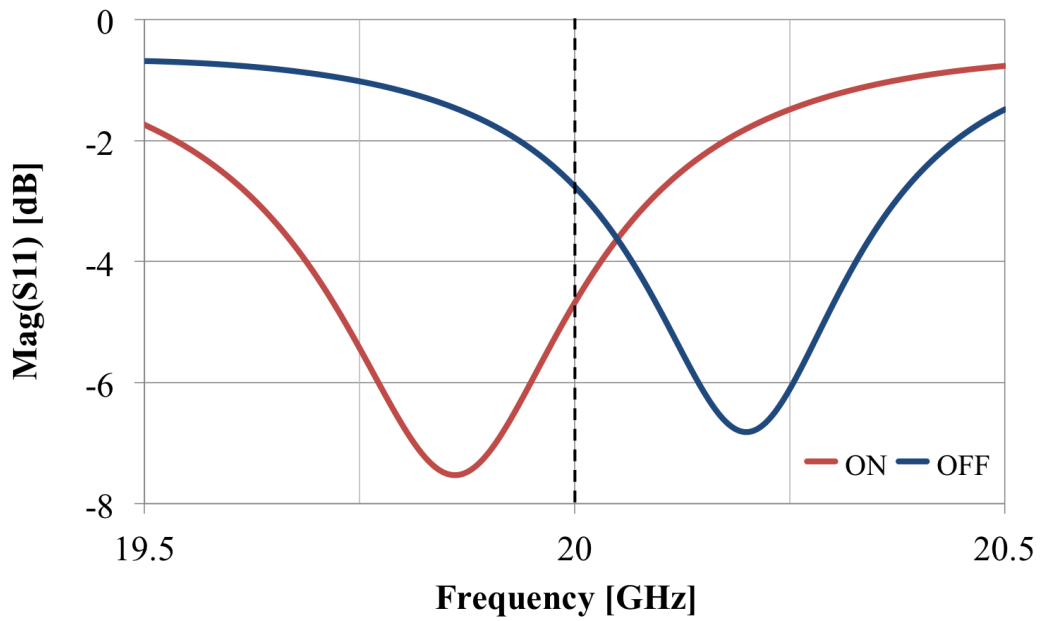
Via disc	Diameter (mm)
$\varnothing_{12}$	1.2
$\varnothing_{11}$	0.8
$\varnothing_2$	0.5

**Table 4.14.:** Updated metal layers dimensions with additional stub segment of  $L_4$

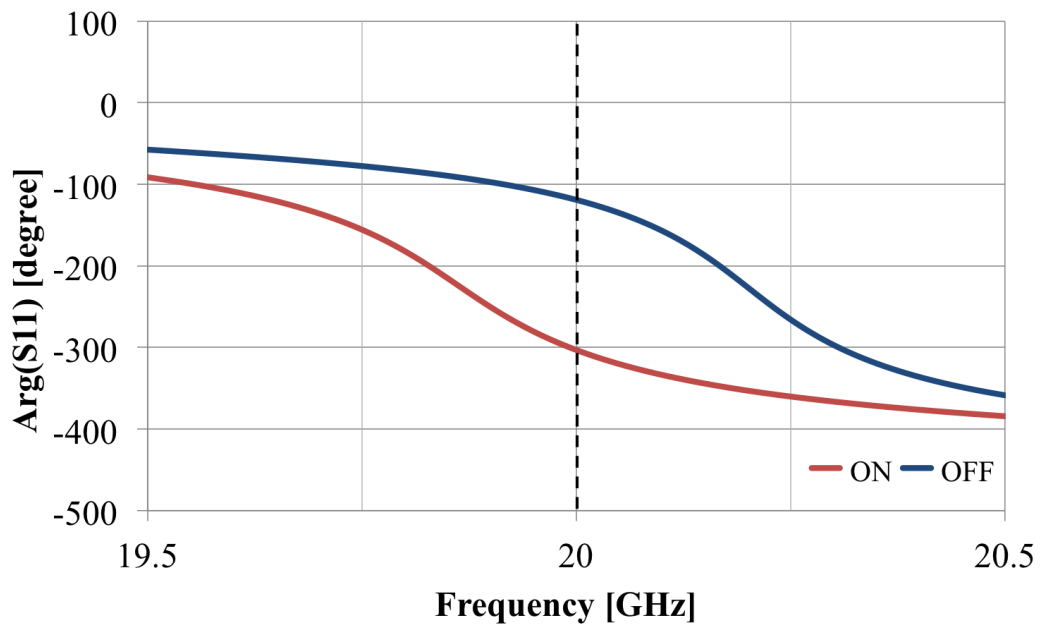
The simulation results for the optimized elementary cell design are shown in Fig. 4.58 and Fig. 4.59. The loss for ON and OFF states are -4.7 dB and -2.8 dB respectively. The loss is reduced by 4.6 dB and the phase difference desired is obtained at the center frequency of 20 GHz. The optimized design improves significantly the performance of the elementary cell which takes into account the fabrication constraints and requirements imposed by the manufacturer.

Fig. 4.60 and Fig. 4.61 show the current distributions on metal layers using the optimized design. In both cases, the current distributions are almost identical with less current intensity at the end of the stub which connects the large via. Current intensity is stronger in ON state on the slotted rectangle surface compared to OFF state.

The optimized design using Meteorwave<sup>TM</sup> 2000 substrate shows some performance improvement in term of S11 magnitude loss. The design has been altered to take into account fabrication constraints especially the constraints for the substrate thickness and via diameter. The material chosen is less expensive compared to the high performance RT/duroid<sup>®</sup> 6002 with the same performance delivered. This is achieved by optimizing the elementary cell geometries such as the phase tuning stub design. Tab. 4.15 summarizes the elementary cell designs discussed in this section. Each of these designs will be used in the reflectarray simulations discussion in the next section.



**Figure 4.58.:**  $S_{11}$  magnitude for ON and OFF state using Meteorwave™ 2000 substrate with optimized design



**Figure 4.59.:**  $S_{11}$  phase for ON and OFF state using Meteorwave™ 2000 substrate with optimized design

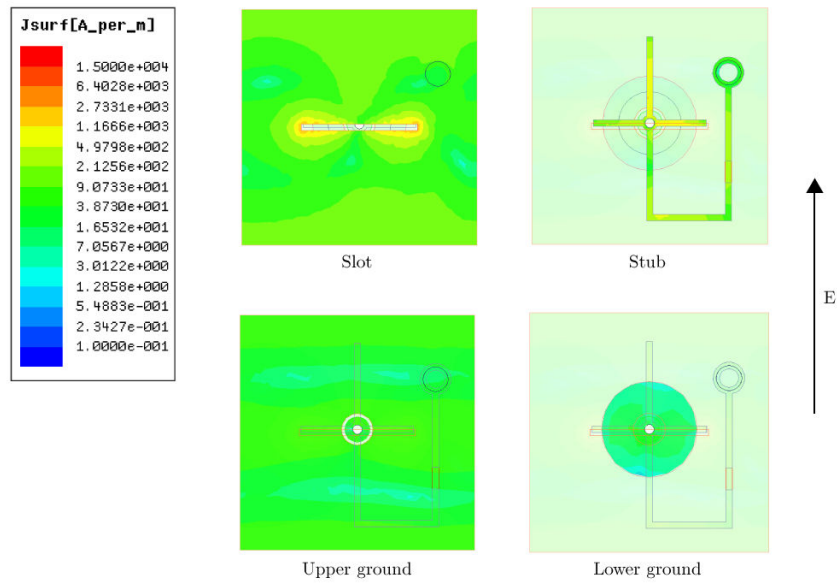


**Figure 4.60.:** Surface current distributions when diode is ON at 20 GHz using Meteorwave™ 2000 with optimized design

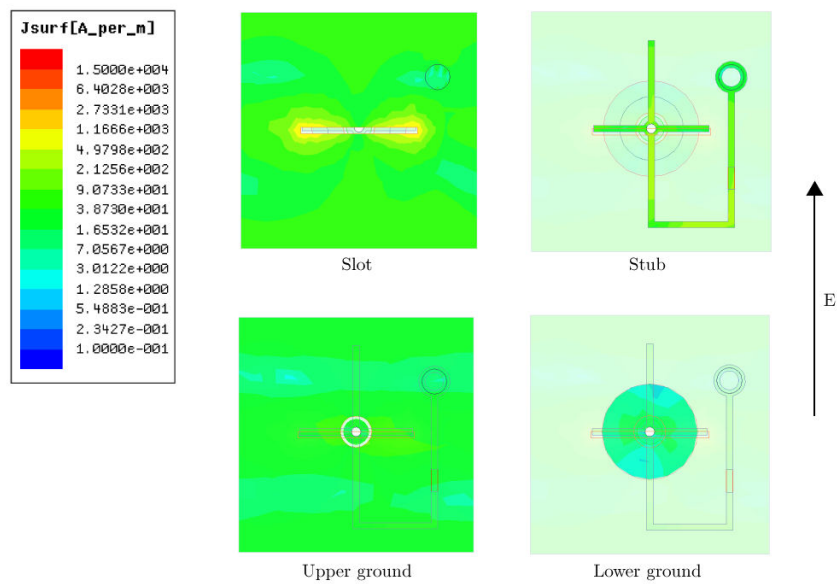


**Figure 4.61.:** Surface current distributions when diode is OFF at 20 GHz using Meteorwave™ 2000 with optimized design

Design	Dielectric	Variation	Diode state	Mag( $S_{11}$ ) [dB]	Arg( $S_{11}$ ) [Degree]
1	RT/duroid® 6002	1) Standard thickness	ON	-9.0	-293.0
			OFF	-0.1	-112.2
2	RT/duroid® 6002	1) Standard thickness 2) Without patch	ON	-5.4	-199.5
			OFF	-0.1	-19.3
3	Meteorwave™ 2000	1) Standard thickness 2) Without patch 3) Large via diameter 4) Small matching stub ( $W_s = 3.6$ mm, $L_s = 0.2$ mm) 5) Additional stub segment $L_4 = 2.6$ mm	ON	-4.7	-303.1
			OFF	-2.8	-119.1

Table 4.15.: Elementary cell designs

## 4.2. Reflectarray simulations

This section will discuss the reflectarray simulations using the elementary cell design shown earlier in the previous section. In this project, the size of the AFR chosen is  $21 \times 21$  elements and the working frequency is 20 GHz. The focal to diameter ratio ( $f/D$ ) equals to 0.5. The distance between each elementary cell is  $\lambda/2$ . AFR designs are simulated by full electromagnetic software simulator (CST) and using in house simulator (HRS).

Using CST, it takes in average about 21 days or 3 weeks to complete the AFR simulation for one given focused beam direction and assuming the simulation runs for non stop 24 hours. The simulation runs on standard workstation which has Intel i7 Quad cores processor (3.4 GHz), 24 GB of RAM and using solid state hard disk (SSD) for the best performance. The SSD accelerates the calculation by one week compared to the use of normal hard disk which has mechanical part.

From the number above, it takes 21 weeks to have a complete radiation pattern that ranges from theta  $-30^\circ$  to  $30^\circ$  for every  $10^\circ$ . The phase shift distributions for these ranges are shown in Fig. 4.62. Because of the limited computer resource and long simulation time, not all AFR simulations are simulated by CST especially in testing the beam scanning capability. For each elementary cell designs, the beam scanning is tested using HRS because the results are obtained much faster (10 minutes) than using CST.

### 4.2.1. Optimal frequency of the AFR

Initial simulations at the working frequency (20 GHz) using CST show that the AFR does not work correctly despite of using the working elementary cell at the same frequency. Fig. 4.63 and Fig. 4.64 show the directivity obtained using CST at 20 GHz. In both cases, the maximum directivity is not retrieved at the center of the feed but around  $\theta = 30^\circ$  for Fig. 4.63 and  $\theta = 20^\circ$  for Fig. 4.64. To better understand the AFR behavior, the maximum normalized directivity for frequencies range from 19.8 GHz to 20.8 GHz is plotted. Fig. 4.65 and Fig. 4.66 show the maximum normalized directivity for the AFR which uses “Design 1” and “Design 2” (Tab. 4.15) as unit cell respectively.

In Fig. 4.65, the maximum directivity for all directions is obtained around 20.4 GHz. For theta  $0^\circ$  and  $10^\circ$ , the directivity curve shows quasi-linear behavior from 20 GHz to 20.5 GHz but not for theta  $20^\circ$  and  $30^\circ$ . Fig. 4.66 shows the maximum normalized directivity for the AFR which uses the improved version of “Design 1” elementary cell noted as “Design 2”. The same linear pattern can be seen in Fig. 4.66 for theta  $0^\circ$  and  $10^\circ$ . In this case, the maximum directivity for theta  $0^\circ$ ,  $10^\circ$  and  $20^\circ$  is found at 20.5 GHz a little bit higher than shown in Fig. 4.65.

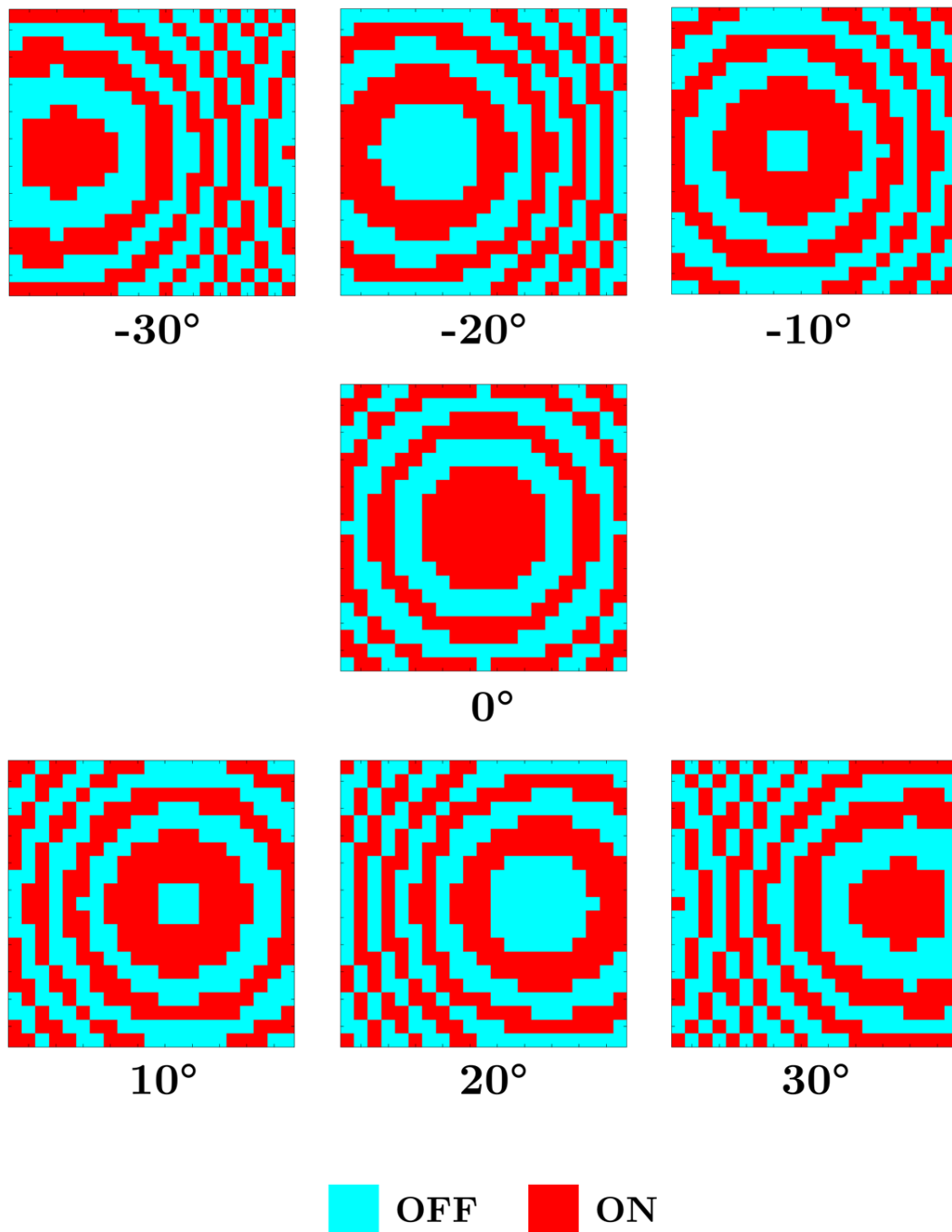


**Figure 4.62.:** Phase shift distributions for beam scanning between  $-30^\circ$  and  $30^\circ$  with step of  $10^\circ$  at 20 GHz

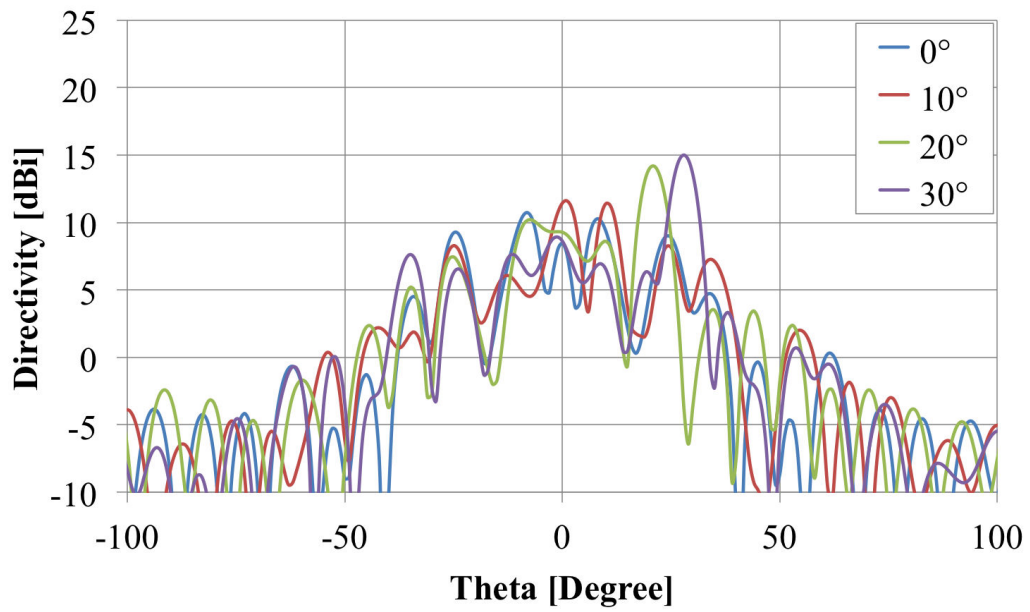


**Figure 4.63.:** 21×21 AFR directivity radiation pattern simulated using CST at 20 GHz with “Design 1” elementary cell as unit cell

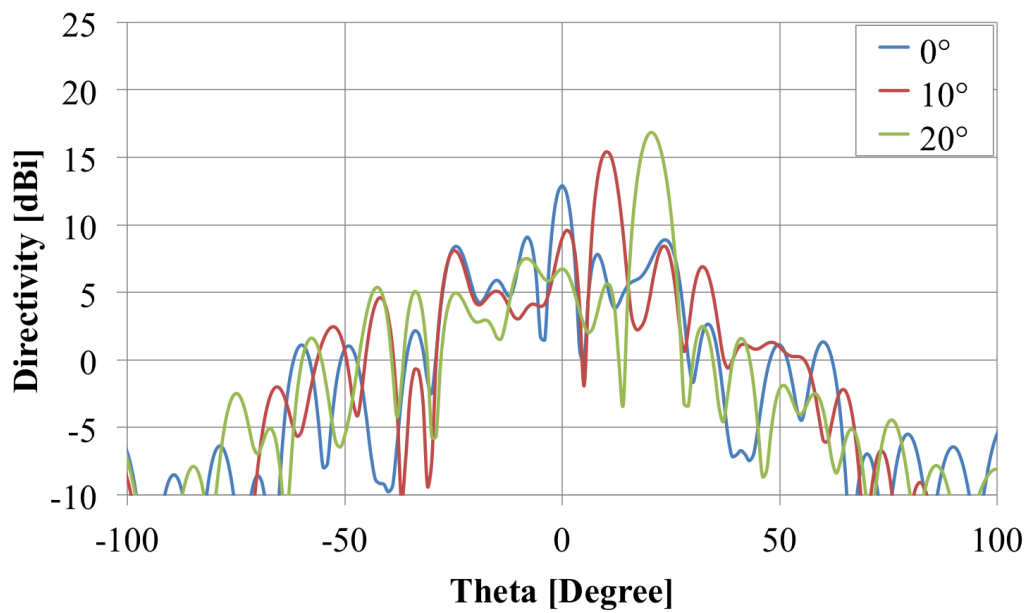


**Figure 4.64.:** 21×21 AFR directivity radiation pattern simulated using CST at 20 GHz with “Design 2” elementary cell as unit cell

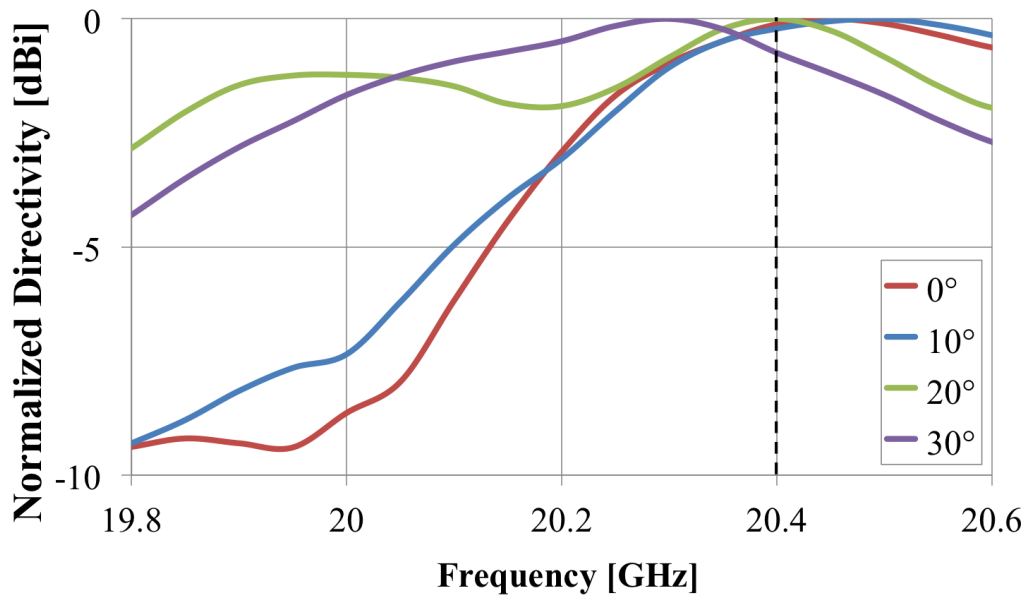


**Figure 4.65.:**  $21 \times 21$  AFR maximum normalized directivity simulated using CST with “Design 1” elementary cell as unit cell

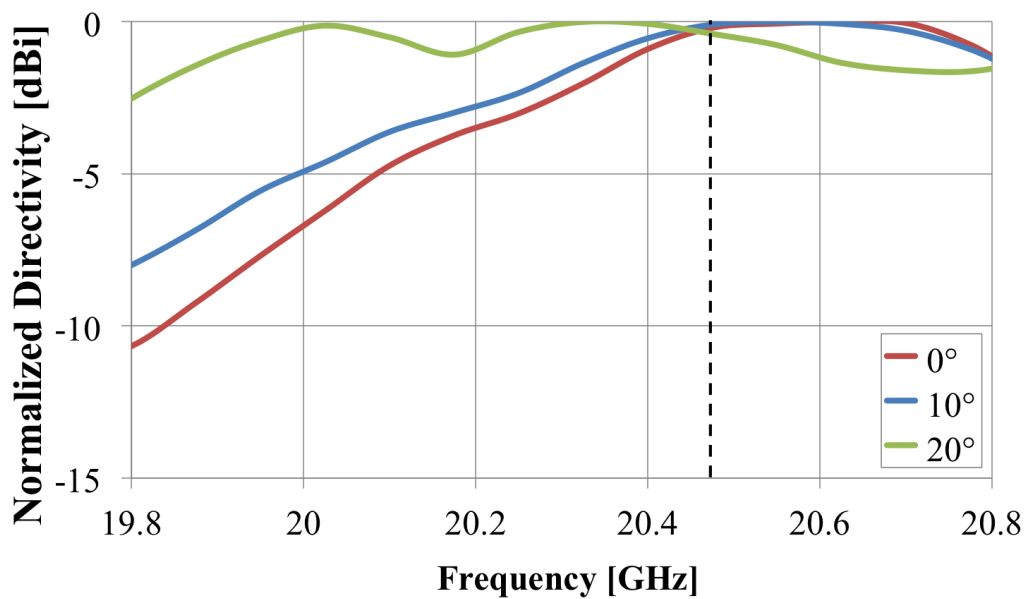
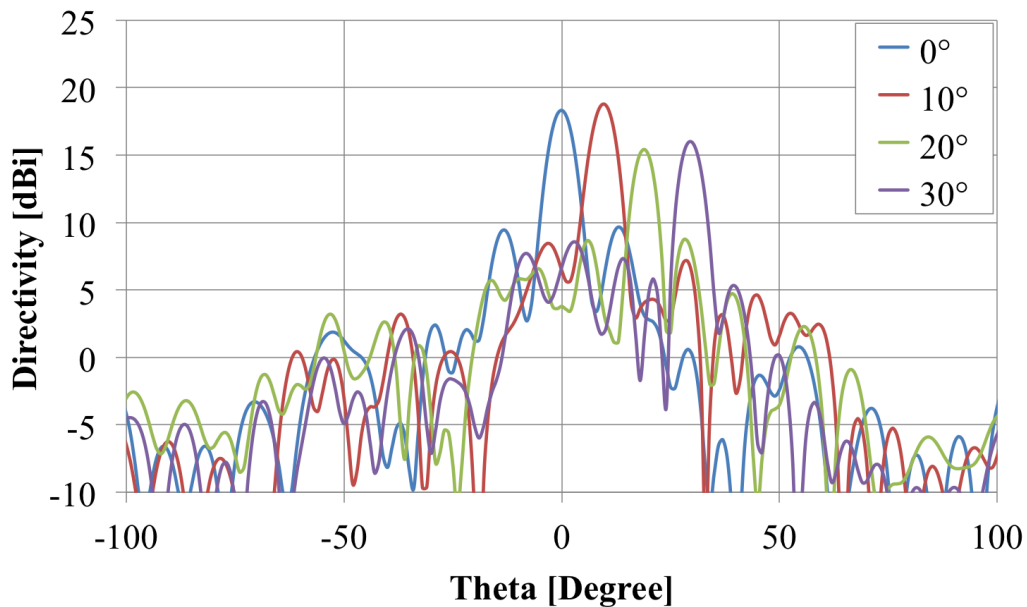


**Figure 4.66.:**  $21 \times 21$  AFR maximum normalized directivity simulated using CST with “Design 2” elementary cell as unit cell



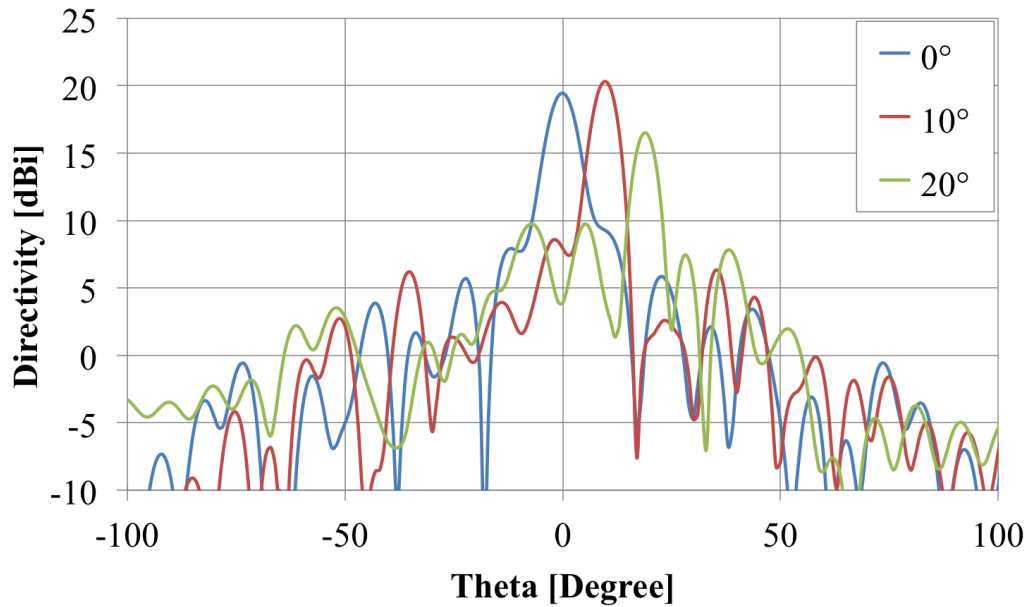
Based on the simulation results, the working frequency of the AFR is shifted to higher working frequency of the elementary cell (20 GHz). This explains the directivity radiation pattern obtained in Fig. 4.63 and Fig. 4.64 where maximum directivity values are not obtained at the desired focus beam directions because the radiation patterns are taken at 20 GHz.

Fig. 4.67 and Fig. 4.68 show the radiation pattern for “Design 1” and “Design 2” taken at 20.4 GHz and 20.5 GHz respectively. From the results, maximum directivity is observed at the desired focus beam direction ( $0^\circ$ ,  $10^\circ$ ,  $20^\circ$  and  $30^\circ$ ). This shows that the AFR works correctly around 20.5 GHz with 0.5 GHz of frequency shift from the working elementary cell frequency (20 GHz).



**Figure 4.67.:**  $21 \times 21$  AFR directivity radiation pattern simulated using CST at 20.4 GHz with “Design 1” elementary cell as unit cell

The frequency shift only can be observed when simulations are obtained with CST while in HRS the working frequency is unchanged at 20 GHz. The simulation results using HRS are discussed in the next section where beam scanning capability of the AFR is tested using HRS at 20 GHz.



**Figure 4.68.:**  $21 \times 21$  AFR directivity radiation pattern simulated using CST at 20.5 GHz with “Design 2” elementary cell as unit cell

The elementary cell designs simulations discussed previously are designed with normal incidence wave. Once the design is confirmed and finalized (dimensions and materials are fixed), new simulations using HFSS are conducted with oblique incidence to obtain the  $S_{11}$  elementary cell coefficients in the function of incident wave angles as shown in Fig. 4.69, Fig. 4.70 for “Design 1” and in Fig. 4.71, Fig. 4.72 for “Design 2” respectively. In Fig. 4.69, the maximum values are above 0 dB due to the simulations artifacts. These coefficients are used in HRS in order to obtain the radiation pattern shown in sec. 4.2.3.

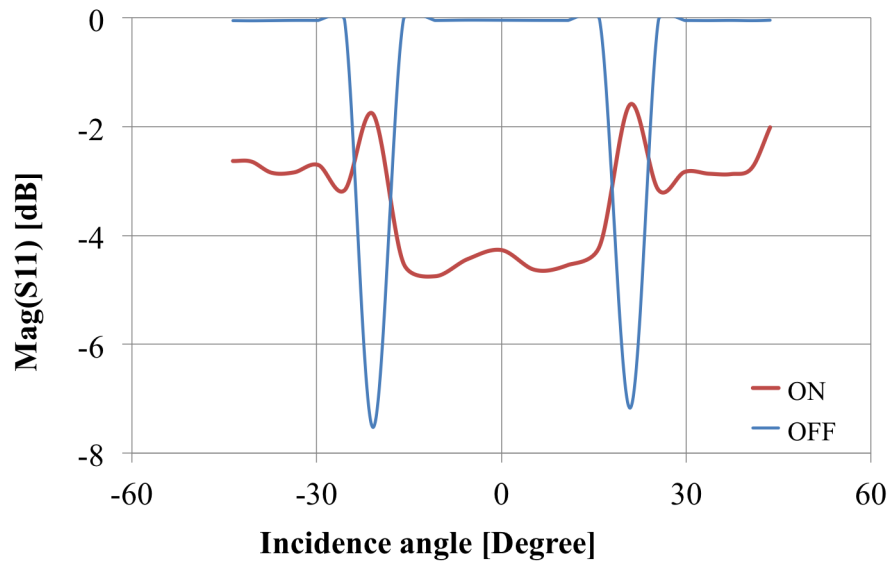


**Figure 4.69.:** Magnitude of  $S_{11}$  coefficient in the function of incident angle for “Design 1” at 20 GHz

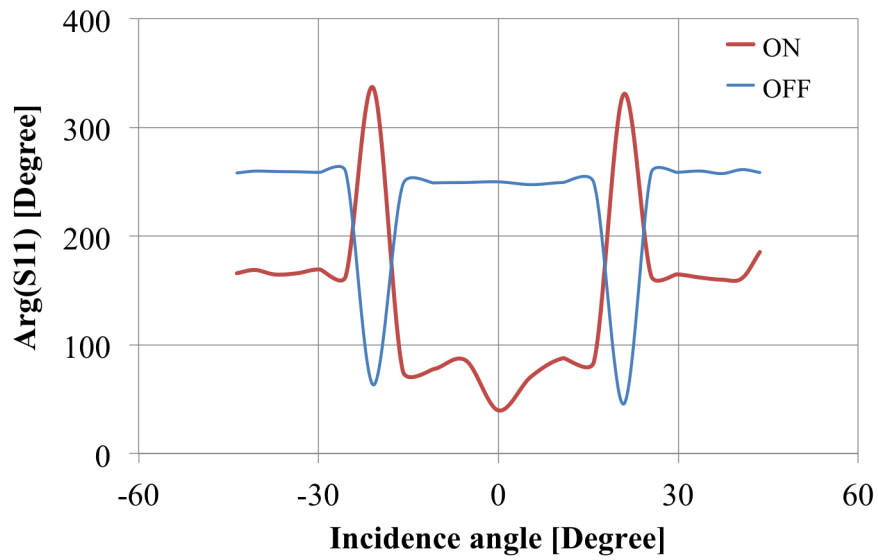


**Figure 4.70.:** Argument of  $S_{11}$  coefficient in the function of incident angle for “Design 1” at 20 GHz

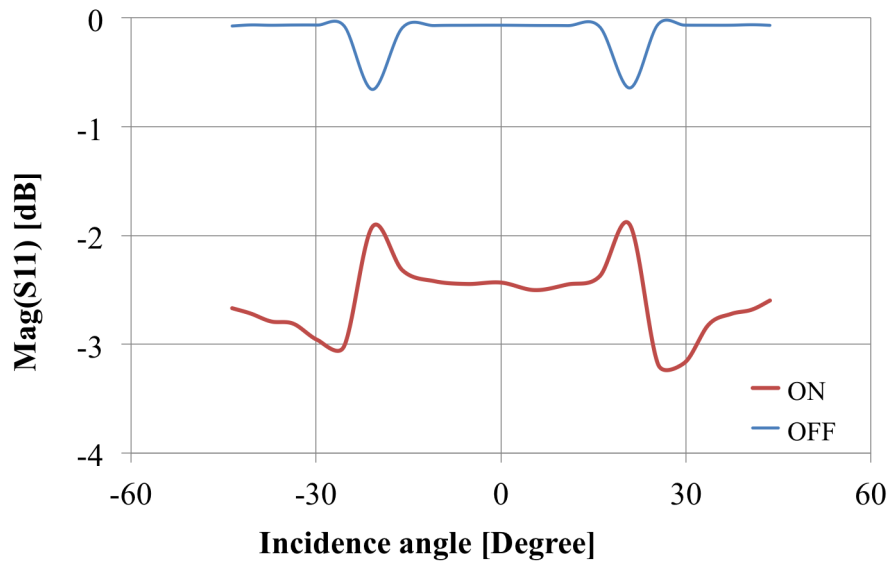


**Figure 4.71.:** Magnitude of  $S_{11}$  coefficient in the function of incident angle for “Design 2” at 20 GHz

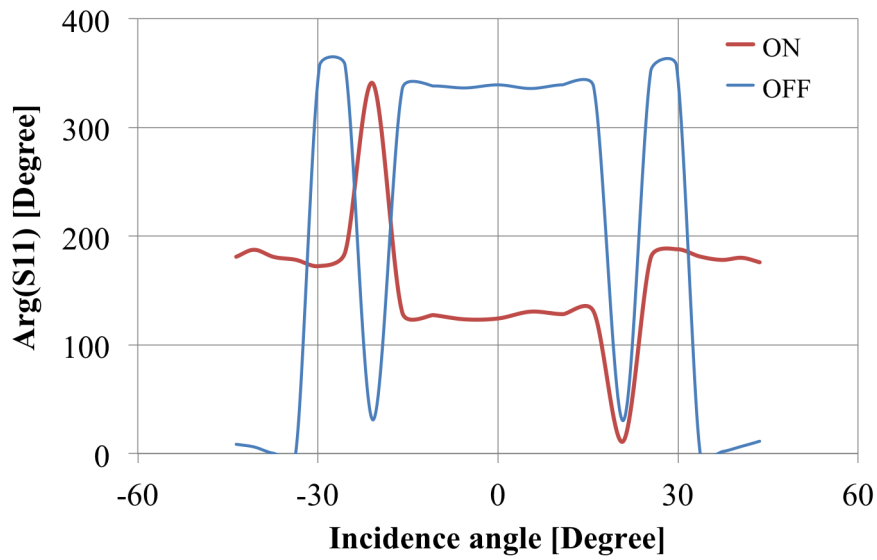


**Figure 4.72.:** Argument of  $S_{11}$  coefficient in the function of incident angle for “Design 2” at 20 GHz

## 4.2.2. Beam scanning capability

To test the beam scanning capability, the AFR is simulated using HRS where angle of wave incident is taken into account when calculating the corresponding  $S_{11}$  values. Each elementary cell design described in Tab.4.15 is tested. Fig.4.73 shows the radiation pattern for AFR that uses elementary cell labeled “Design 1” as unit cell.

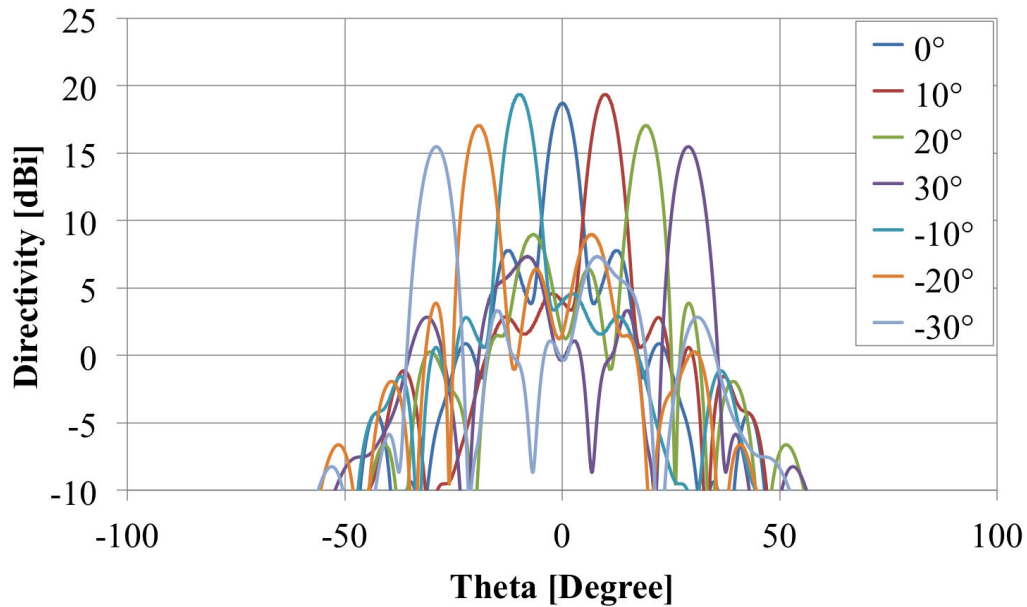


**Figure 4.73.:** 21×21 AFR directivity radiation pattern at 20 GHz using “Design 1” elementary cell as unit cell (HRS)

The maximum values are obtained for  $\theta = 10^\circ$  and  $\theta = -10^\circ$  with maximum directivity equals 19.4 dBi. At  $\theta = 0^\circ$ , the directivity value is 18.7 dBi, lower by 0.7 dB than the direction for  $\theta = 10^\circ$  and  $\theta = -10^\circ$ . At  $\theta = 20^\circ$ , the directivity value is 16.7 dBi. The same value is obtained for  $\theta = -20^\circ$ . The lowest value is obtained as  $\theta = 30^\circ$  and  $\theta = -30^\circ$  with value equals 15.2 dBi. Fig.4.74 shows the radiation pattern for the AFR which integrates the optimized version of “Design 1” known as “Design 2” as the unit cell.

The directivity values in the case shown in Fig.4.74 are higher than the values in Fig.4.73 because the unit cell itself has been improved to reduce the loss. At  $\theta = 0^\circ$ , the directivity is 19.6 dBi which is higher by 1 dB from the previous case. At  $\theta = 10^\circ$ , the directivity calculated is 19.9 dBi. The maximum directivity values are obtained at  $-10^\circ$ ,  $0^\circ$  and  $10^\circ$ . For theta equals  $20^\circ$ , the directivity is decreased by 1.6 dB which makes the value equals 18.3 dBi. The lowest directivity is shown at  $30^\circ$  with the directivity value equals 17 dBi. Fig.4.75 shows the directivity radiation pattern for the AFR which uses “Design 3” as the unit cell.

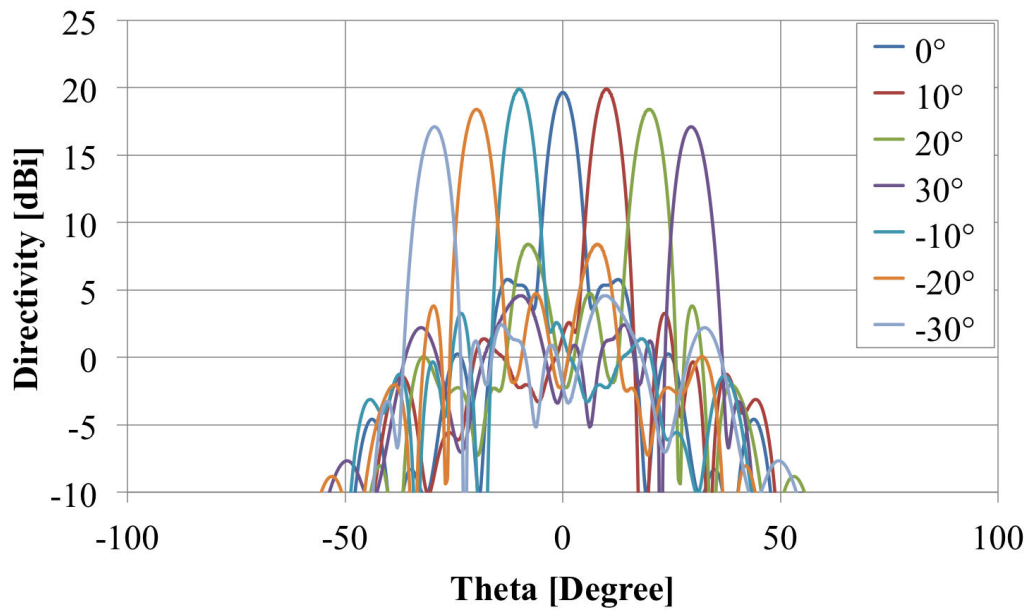


**Figure 4.74.:**  $21 \times 21$  AFR directivity radiation pattern at 20 GHz using “Design 2” elementary cell as unit cell (HRS)

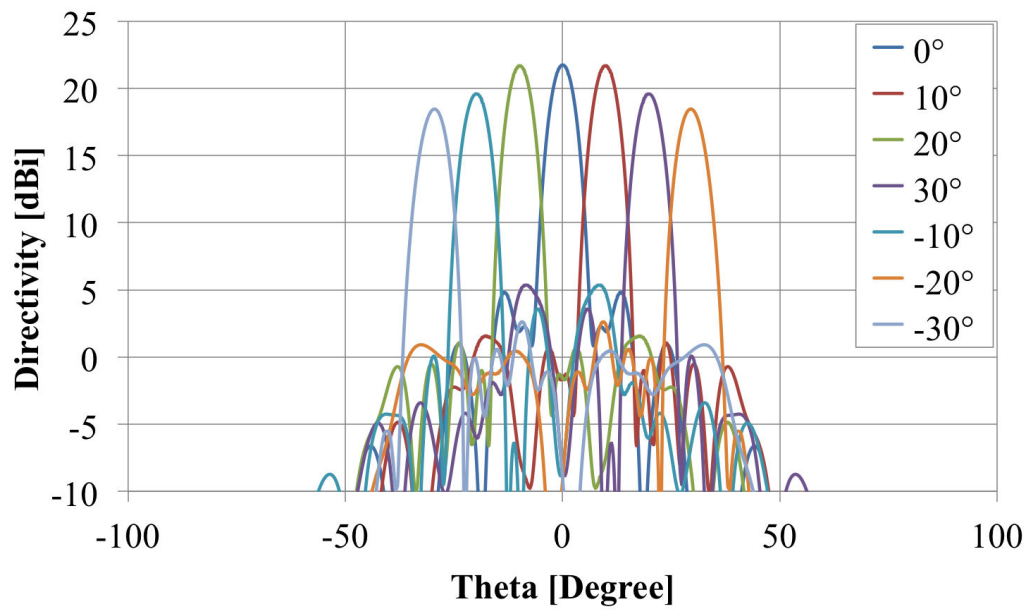


**Figure 4.75.:**  $21 \times 21$  AFR directivity radiation pattern at 20 GHz using “Design 3” elementary cell as unit cell (HRS)

The maximum directivity is obtained at  $\theta = 0^\circ$ ,  $\theta = 10^\circ$  and  $\theta = -10^\circ$  with maximum value equals to 21.7 dBi. At  $\theta = 20^\circ$  and  $\theta = 30^\circ$ , the directivity values are 19.6 dBi and 18.3 dBi respectively. For all elementary cell designs, the beam scanning capability is demonstrated to be working with good performance. The pattern radiation reconfigurability is achieved based on the simulations results shown in Fig. 4.73, Fig. 4.74 and Fig. 4.75.

The results show that higher directivity is obtained with AFR that uses elementary cell labeled “Design 3” compared to AFR with “Design 1” or “Design 2”. “Design 3” is considered to be ready and complete for fabrication because all the changes and modifications applied are based on the feedback and comments from the manufacturer.

### 4.2.3. Result comparison against CST

To compare the performance of the AFR simulated with HRS, simulations using CST are conducted for AFR which uses “Design 1” and “Design 2” as the elementary cell. Fig. 4.76 shows the directivity radiation pattern comparison between the radiation pattern simulated with CST at 20.4 GHz against the one calculated using HRS at 20 GHz. At  $\theta = 0^\circ$ , the difference between the 2 maximum values is 0.38 dB. The maximum value simulated with CST is 18.32 dBi and the maximum value calculated using HRS is 18.7 dBi. At  $\theta = 10^\circ$ , the small difference of 0.66 dB is also observed between CST maximum directivity value which equals 18.74 dBi and HRS maximum directivity value which is 19.4 dBi.

At  $\theta = 20^\circ$ , the value calculated using HRS (16.85 dBi) is much higher than the one obtained with CST (14.94 dBi) with the difference equals to 1.9 dB. Using CST,  $\theta = 20^\circ$  gives the lowest directivity value compared to HRS which gives the lowest directivity at  $30^\circ$  (15.2 dBi). The difference at  $30^\circ$  is 0.73 dB with CST maximum value equals 15.93 dBi. In Fig. 4.76, the maximum HRS values approach the ones obtained with CST but the side lobes levels between these 2 calculations are different with lower side lobes is observed for HRS.

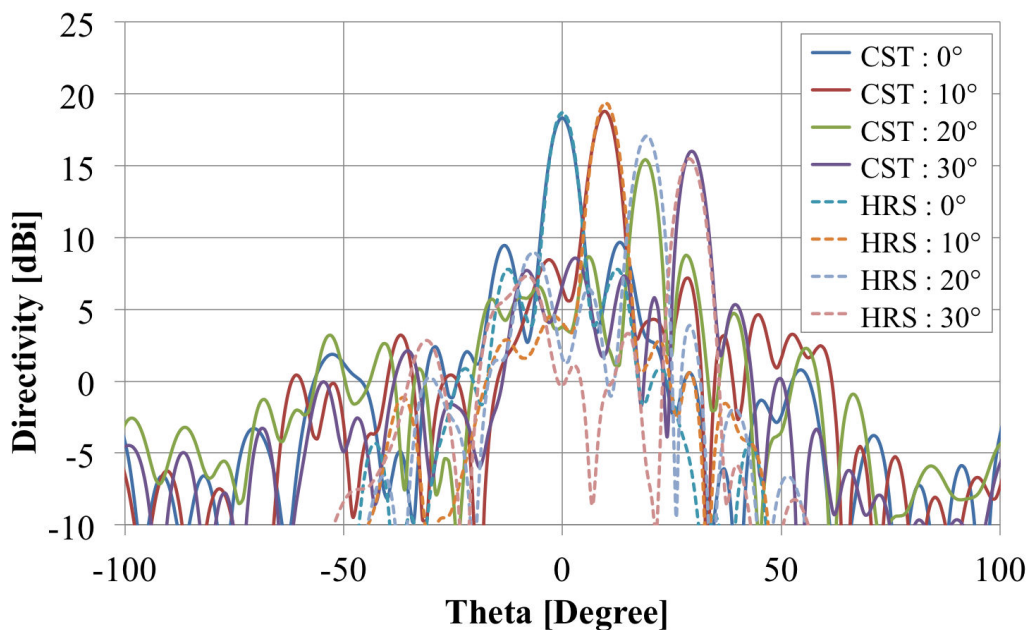


**Figure 4.76.:**  $21 \times 21$  AFR directivity radiation pattern simulated using CST at 20.4 GHz and using HRS at 20 GHz with “Design 1” elementary cell as unit cell

Fig. 4.77 shows the same comparison between results calculated using HRS and results obtained with CST. In this case, the CST radiation pattern is taken at 20.5 GHz where the majority of directivity values are maximum. At  $0^\circ$ , the CST



maximum directivity is 19.4 dBi and the HRS value is 19.6 dBi. This makes the difference between these 2 maximum values equals 0.2 dB. At  $10^\circ$ , the maximum directivity difference is 0.4 dB. At this direction, the CST value obtained is 20.3 dBi and the HRS directivity value is 19.9 dBi. At  $20^\circ$ , the significant different is spotted where the difference value is 2.3 dB. The maximum directivity calculated using HRS is much higher with the value equals 18.4 dBi while the CST directivity value is 16.1 dBi.

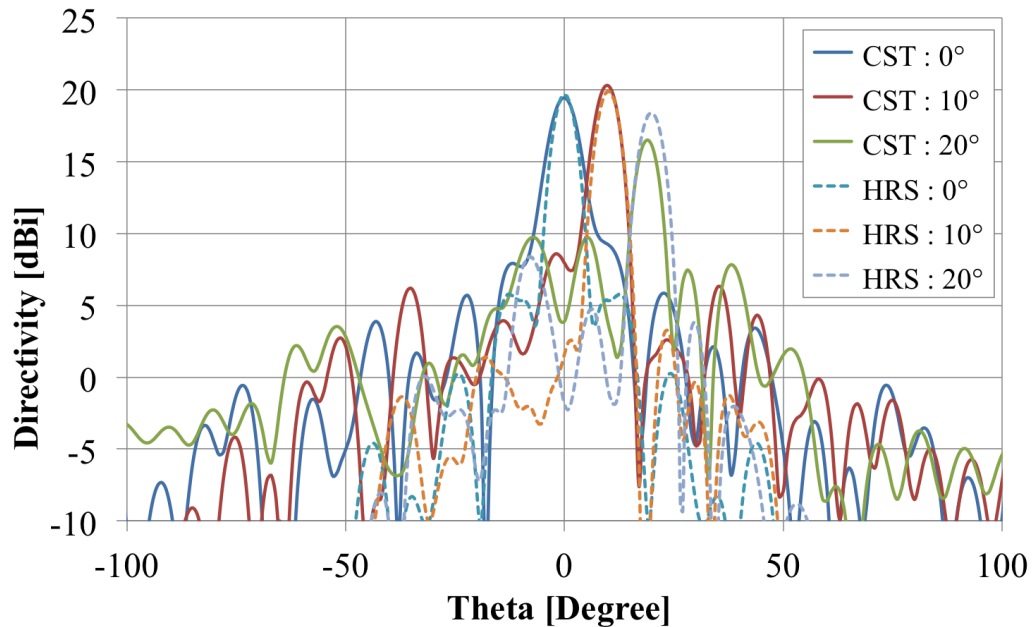


**Figure 4.77.:**  $21 \times 21$  AFR directivity radiation pattern simulated using CST at 20.5 GHz and using HRS at 20 GHz with “Design 2” elementary cell as unit cell

In general, HRS is able to approximate the maximum directivity values with correct directions as can be seen in Fig. 4.76 and Fig. 4.77. Using CST, the shift of the working frequency at 20 GHz is observed which makes the AFR works slightly at the higher frequency but in tolerable range. HRS is not able to approximate the frequency shift and the non linear behavior because it requires true electromagnetic calculation to correctly take into account these behaviors. Obtaining the result 100 times faster than CST with acceptable directivity level and direction is already an advantage for HRS because it helps to accelerate the AFR design process.

#### 4.2.4. Improvement using optimized elementary cell design

In sec. 4.1.5, two major elementary cell designs are discussed and in Tab. 4.15 they are noted as Design 1 and Design 2. These 2 designs are differentiated by the thickness of the most top substrate noted as  $d_2(1)$  and in Design 2, the metal patch on the top radiating layer is removed. Both of these designs use the same dielectric material. Based on the unit cell simulation result, Design 2 has better performance because the loss of the reflected wave is -5.4 dB for ON state compared to Design 1 which encounters -9.0 dB of loss.

To test the improvements made by the optimized elementary cell (Design 2) against unoptimized design (Design 1), the AFR is simulated for 2 focused beam directions using CST. The first direction is  $\varphi = 0^\circ$  and  $\theta = 0^\circ$ . The second direction is  $\varphi = 0^\circ$  and  $\theta = 10^\circ$ . For each direction, the directivity patterns are compared against directivity pattern produced by the unoptimized design.

Simulation results show the improvements achieved in terms of the maximum directivity value and side lobes levels. In Fig. 4.78, the maximum directivity for Design 1 is 18.3 dBi and for optimized design (Design 2), the value increases by 1.2 dB and reaches 19.5 dBi. The optimized design also produces lower side lobes compared to the original one, especially the first side lobes.

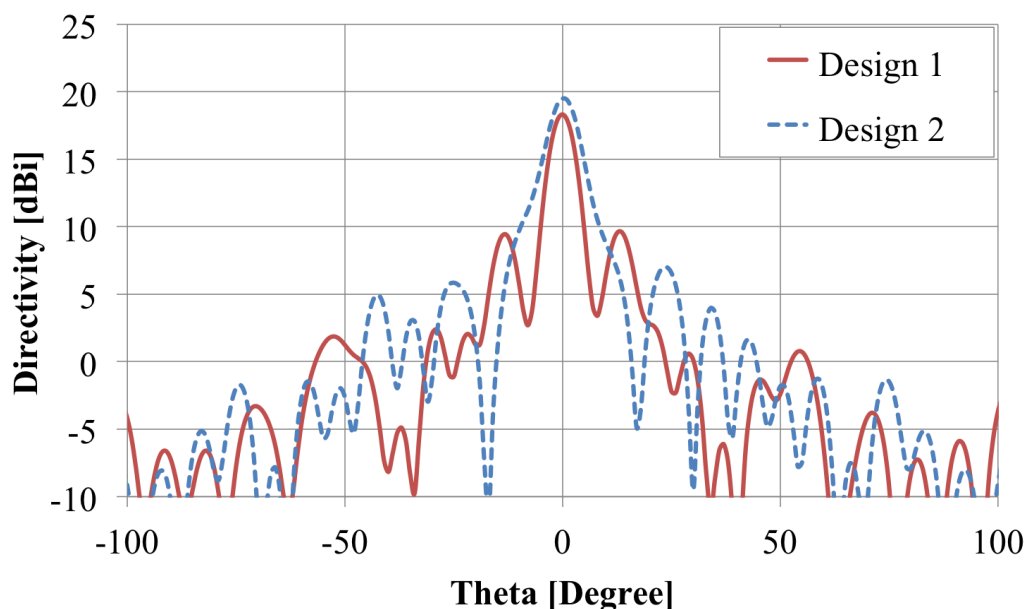


**Figure 4.78.:**  $21 \times 21$  AFR directivity radiation pattern comparison for  $\theta = 0^\circ$  using Design 1 and Design 2 (CST)

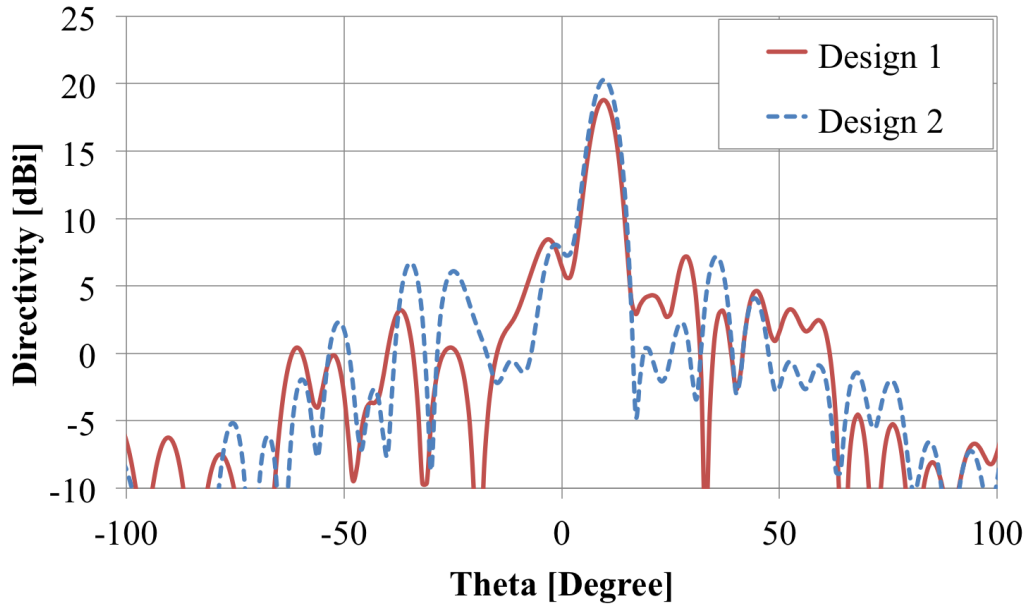


**Figure 4.79.:**  $21 \times 21$  AFR directivity radiation pattern comparison for  $\theta = 10^\circ$  using Design 1 and Design 2 (CST)

In Fig. 4.79, the radiation pattern shows that beam-scanning capabilities work well for both designs. In this case, the main beam is focused to  $\theta = 10^\circ$ . Maximum value at this direction is 18.7 dBi for the Design 1 and 20.3 dBi for the optimized design (Design 2). The directivity is increased by 1.6 dB, which is higher than the case when main beam is focused to  $0^\circ$ .

From the simulation results, a reduction of 3.6 dB of elementary cell  $S_{11}$  loss produces in average an increment of 1.4 dB in maximum directivity value. For small reflectarray, the improvement can be easily noticed because for a small reflectarray, the performance of the elementary cell is more important than the influence of the cells network while for a large reflectarray, the influence of the cells network has higher impact on the radiation pattern and antenna performance. The improvement is not really significant but having a low loss elementary cell is better because the small improvement can be used to compensate other losses in real world application such as the loss due to the measurement setup. In this case, the elementary cell performance needs to be maximized in order to be able to handle the unpredictable environment.

In the results produced by HRS and CST, the maximum directivity at  $\theta = 10^\circ$  is observed to be higher than direction focused at  $\theta = 0^\circ$ . This effect is due to the calculation problem when converting the theoretical phase distribution pattern into 1-bit phase distribution pattern (Fresnel zone). This problem slightly changes the AFR performance which results in higher directivity at  $10^\circ$ . After applying correct calculation for the phase conversion, the calculated radiation patterns using HRS

show maximum directivity is obtained at theta  $0^\circ$  instead of theta  $10^\circ$ . Fig. 4.80 and Fig. 4.81 show the radiation pattern simulated using HRS with the phase distribution corrected.

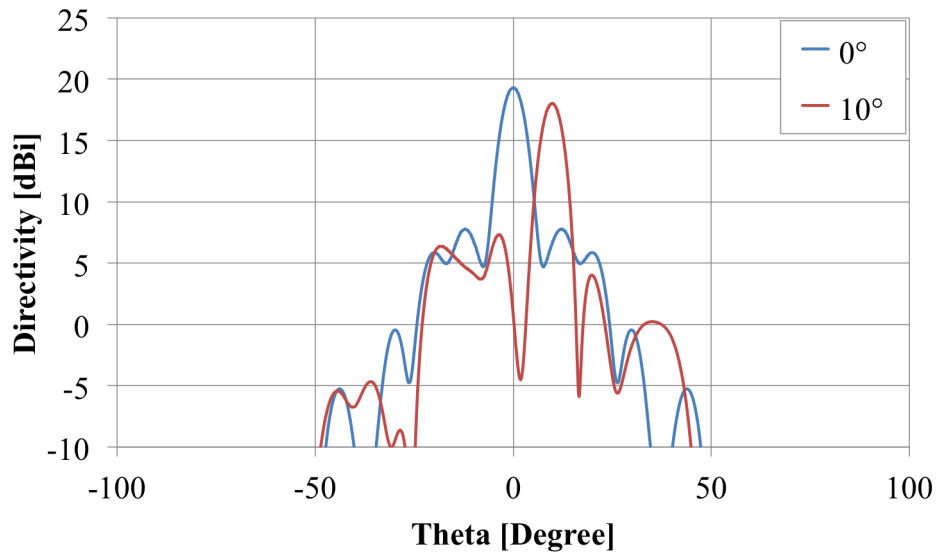


**Figure 4.80.:**  $21 \times 21$  AFR directivity radiation pattern simulated using HRS with phase distribution corrected (Design 1)

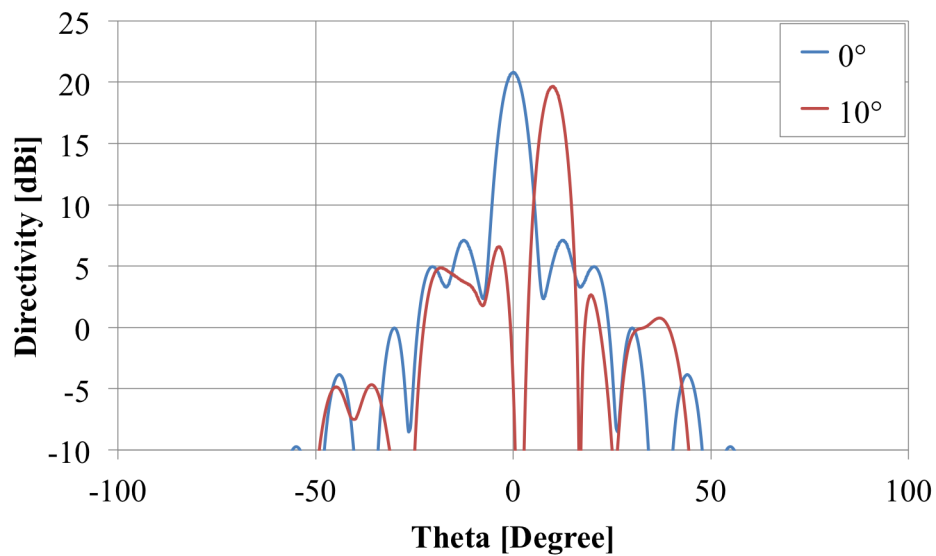


**Figure 4.81.:**  $21 \times 21$  AFR directivity radiation pattern simulated using HRS with phase distribution corrected (Design 2)

For “Design 1”, the maximum directivity at theta  $0^\circ$  is 19.3 dBi and at theta  $10^\circ$ , the maximum directivity value equals to 18.0 dBi. For “Design 2”, the maximum directivity at theta  $0^\circ$  is 20.8 dBi while at theta  $10^\circ$ , the obtained value is 19.6 dBi. In case of “Design 2”, the directivity values are higher because “Design 2” elementary cell is an improved version of “Design 1” elementary cell (refer to Tab.4.15) which results in improvements of the AFR performance.

### 4.3. Conclusion

Multiple elementary cell structures have been designed and simulated in order to obtain the desired steering capability. The design process to correctly adapt the design geometry is a laborious task and requires a lot of trial and error as it involves many design parameters. Integration of p-i-n diode in simulation model is a straight forward process but to complete the diode with physical polarization line is challenging process because the fabrication constraints and elementary cell performance need to be taken into account.

2 types of dielectrics materials which are RT/duroid® 6002 and Meteorwave™ 2000 are tested and the performance between these 2 materials is compared. RT/duroid® 6002 is considered better than Meteorwave™ 2000 due to its low dielectric loss tangent value and it is suitable for millimeter wave application. But having high performance material does not guarantee the best performance for the elementary cell because the performance is the combination result of having good material and good physical design. By optimizing the elementary cell design, Meteorwave™ 2000 is also capable to produce the same performance as using RT/duroid® 6002 but at the lower cost.

Simulation results shows that the designed elementary cells are able to produce an active fresnel reflectarray with beam scanning capability. Results comparison is made to evaluate the in house simulator (HRS) against full electromagnetic simulator software CST. HRS is shown to produce reasonable directivity values that approach the CST values at correct directions.

The elementary cell design undergoes multiple modifications and changes based on the feedback and comments from the manufacturer. Despite having all these modifications, the manufacturer has reported to have some difficulties to automatically weld the small p-i-n diode located in the middle of the elementary cell. The current fabrication technology is unable to overcome this problem. Thus the complete antenna can not be manufactured for the moment, at least at national level.

The next section will discuss the diode controller part which is responsible to handle the diodes states for all p-i-n diodes integrated in the AFR. Without this controller, it is difficult to change the AFR phase distribution in order to change the beam direction.

## 5. Diode controller

The diode controller is used to control the p-i-n diode states in the elementary cells in order to obtain the desired reflectarray phase distribution pattern. It is possible to control the diodes manually using switches but for a large size reflectarray that contains hundreds of diodes, using manual switches is inefficient. Thus an automated system is required to ease the control process. For this purpose, computer is used to control the states of the diodes integrated in the elementary cell in order to achieve the desired radiation pattern. The work starts with the conception of the controller with some important issues to be answered such as the total number of diode to be controlled and the power consumption for the total diodes.

### 5.1. Circuit conception

The first thing in the conception stage is to determine the number of diodes to be controlled. This can be considered as the total number of controllable outputs and it depends on the number of the elementary cell in the AFR. In this project, the AFR discussed in the previous chapter has 441 elementary cells distributed in 21 rows and 21 columns. This means, 441 controllable outputs are required to correctly drive each of the diode integrated in the elementary cells. In reality, the fabricated AFR can be in any size or configuration and it is not necessarily to be in square configuration. Because of this, it is more interesting to have a diode controller with flexible number of controllable output rather than a fixed number restricted to only 441 controllable outputs. This provides extra benefit as the same diode controller can be used for multiple AFR sizes such as  $4 \times 4$  elements,  $15 \times 15$  elements and also  $21 \times 21$  elements.

For this purpose, a sub-circuit that contains 32 controllable outputs is used. To extend the number of outputs, multiple sub-circuits can be connected together and this allows the number of controllable output to be adjusted as required. For example a single sub-circuit can used to control AFR that contains a maximum number of 32 elementary cells. To support multiple combinations of elementary cells rows and columns, the connection between the controllable output and the diode in elementary cell is done by using copper wire. Fig. 5.1 shows the application of single sub-circuit for 2 different AFR configurations. On the left side is an AFR with  $3 \times 3$  elements and on the right side is an AFR with  $5 \times 5$  elements.

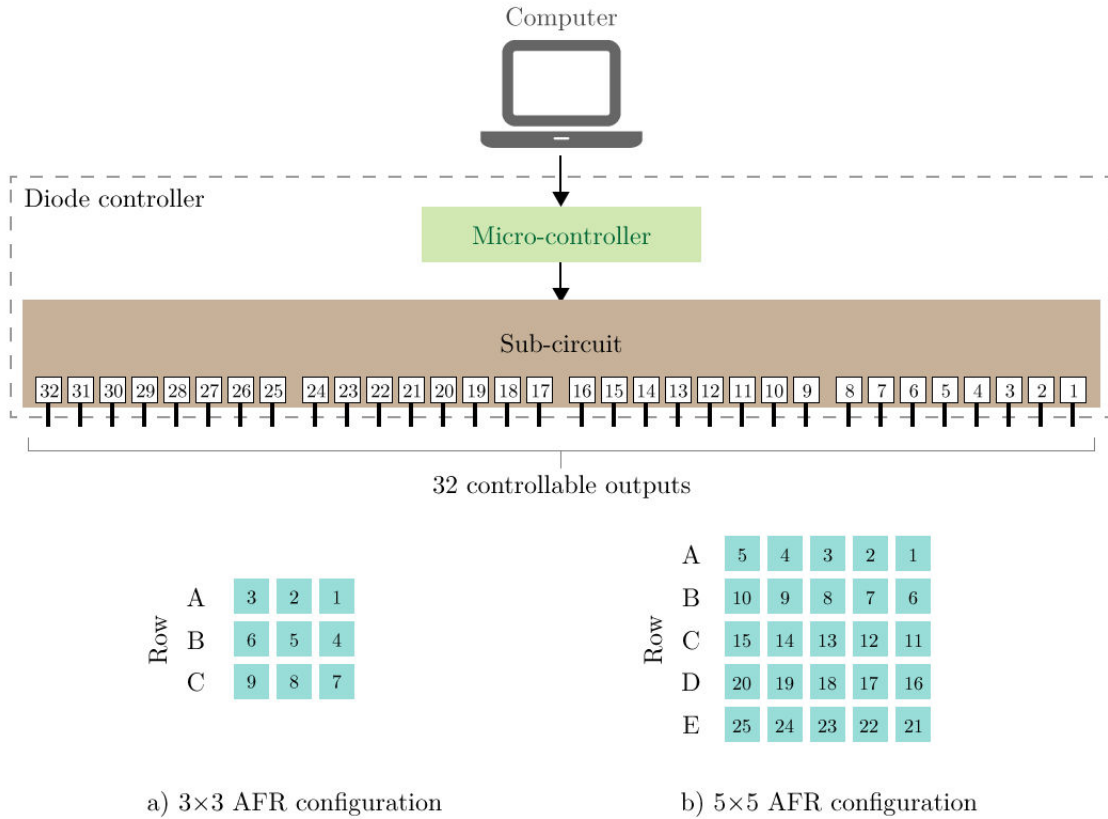


**Figure 5.1.:** Single sub-circuit application for two different AFR configurations

In Fig. 5.1, computer is connected to the diode controller which consists of a micro-controller and sub-circuit. More information on the micro-controller and sub-circuit will be discussed in detail in the next section. The controllable outputs in the sub-circuit are labelled with number 1 until 32. In each AFR configuration, the number label in the elementary cell corresponds to the controllable output connection. This shows that a single sub-circuit is sufficient to control 2 types of AFR configurations because the diodes in these reflectarrays are less than 32 diodes. In case the size of the AFR is larger than 32 elementary cells, for example AFR with  $8 \times 8$  elementary cells, 2 sub-circuits are required to control the diodes.

However the connections shown in Fig. 5.1 pose an inconvenient because the controllable outputs to elementary cell connections associations change with AFR configurations. For example for  $3 \times 3$  AFR, the controllable output numbered 5 is connected to elementary cell in Row B while for  $5 \times 5$  AFR, the same controllable output is connected to the elementary cell in Row A. This means that each time the different size of AFR is used, the controllable outputs connections need to be rearranged.

To overcome this inconvenient, a single sub-circuit controllable outputs are fixed to one row of the AFR. For both AFR configurations in Fig. 5.1, the sub-

circuit controllable outputs will control the elementary cells in Row A. In this case, 3 sub-circuits and 5 sub-circuits are required to control the elementary cells for  $3 \times 3$  AFR and  $5 \times 5$  AFR respectively. In this project, 32 sub-circuits are used and their combinations is referred as “Matrix” circuit. This allows the diode controller to control a maximum number of 1024 diodes in 32 rows and 32 columns as shown in Fig. 5.2.

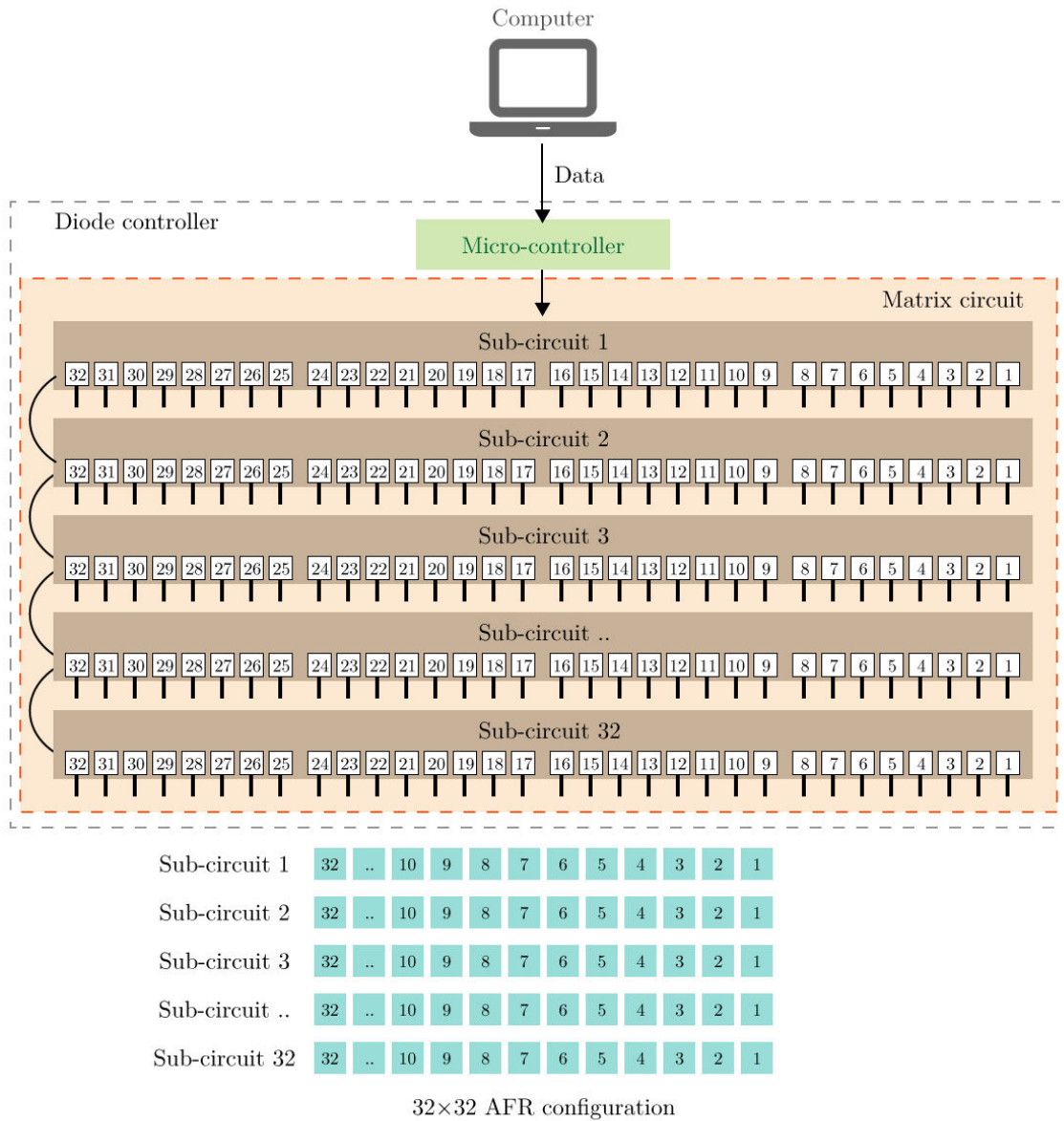


**Figure 5.2.:** 32 cascaded sub-circuits for  $32 \times 32$  AFR configuration

By using the configuration shown in Fig. 5.2, the controllable outputs connections associations are fixed and the adjustment between different AFR sizes can be realized directly from the computer by modifying the data sent to the micro-



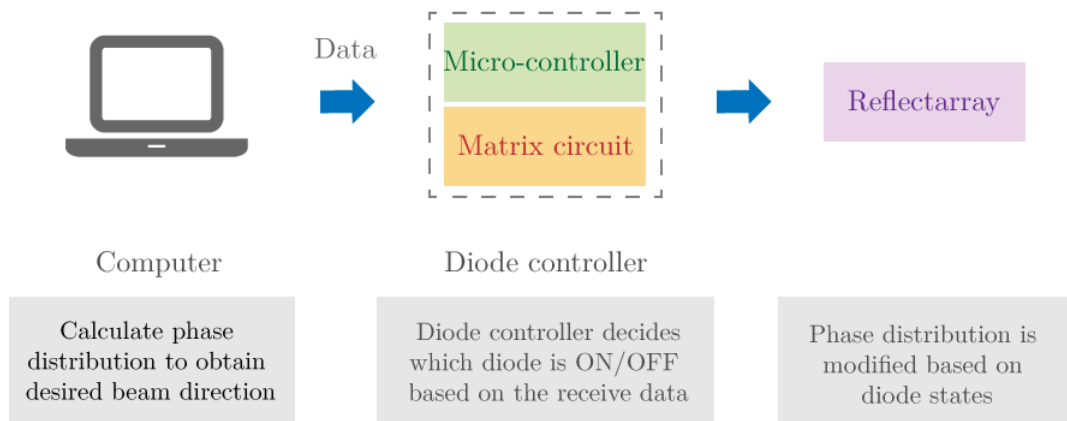
controller. The data transmission and controllable outputs association will be explained in the next sections.

Another important aspect is the power consumption to drive all 1024 diodes at once with the assumption that the antenna used is an AFR with  $32 \times 32$  elements. For a single sub-circuit with 32 controllable outputs, power consumption is less important than 1024 controllable outputs and relying only on the power provided by the micro-controller is not sufficient for a large number of diodes. To handle correctly the large amount of power consumption, an independent power supply will be used to bias the diodes. This power separation allows the possibility to regulate the power consumed by the diodes as needed.

The next section will discuss the diode controller working mechanism and the binary data relationships with the controllable outputs and the diode states.

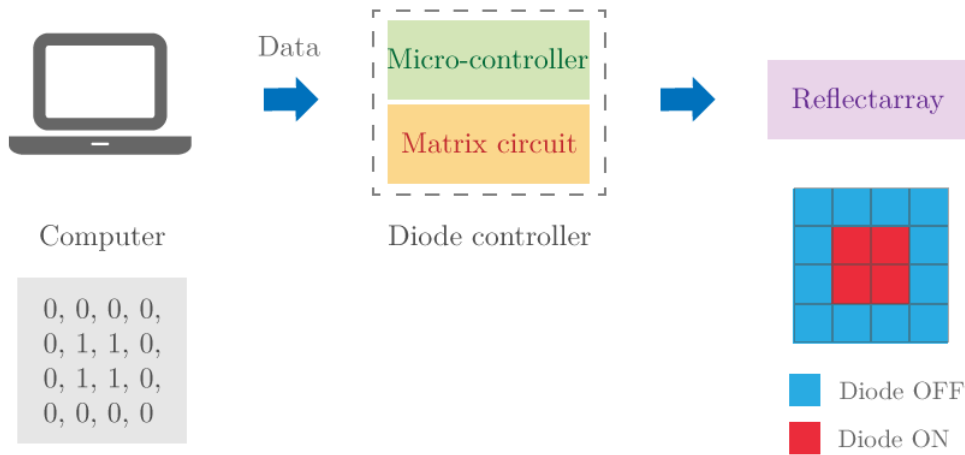
## 5.2. Working mechanism

Fig. 5.3 shows the diode controller system architecture. Diode controller is the communication link between computer and reflectarray.



**Figure 5.3.:** Diode controller system architecture

In Fig. 5.3, the diode controller is represented by the rectangle dashed line box and it is composed of 2 major components. The first component is the micro-controller which communicates with the computer and the second component is the matrix circuit which has direct connections to the p-i-n diodes in the elementary cells. Computer is used to calculate the phase distribution required to focus the main beam to the desired direction, then data is sent to the diode controller circuit via the micro-controller inside it.



**Figure 5.4.:** Computer data and diode state in elementary cell relationship

Data sent from computer will be a binary array where each case (0 or 1) in the array represents diode state in each elementary cell as shown in Fig. 5.4 with an example of controlling small reflectarray with  $4 \times 4$  elementary cells. Data “1” represents an ON state while data “0” represents an OFF state. Sending this data to the diode controller will bias only 4 diodes in the center of the reflectarray whereas the others are in OFF state. This explains the relationship between the binary data from the computer and the diode states in the elementary cells. The next section describes the diode controller components (micro-controller and matrix circuit) in detail.

### 5.3. Components

Fig. 5.5 shows the components that construct the diode controller. The micro-controller component is an Arduino board which communicates with the computer via USB port. The board contains not only a micro-controller but it also comes with complete elements for electronic development purpose such as power supply input, input and output ports both for digital and analog signals. Despite of having complete elements for development, the existing output ports are insufficient to be connected to each p-i-n diode in the elementary cells. For a reflectarray with  $32 \times 32$  elementary cells, 1024 output connections are required. To meet this connection requirement, additional matrix circuit is needed in order to extend the number of ports in the Arduino board output.

The matrix circuit is composed of 32 numbers of sub circuits. Rather than using large circuits that produces directly large number of outputs, using sub circuit is more preferable because of the possibility to extend the additional outputs and

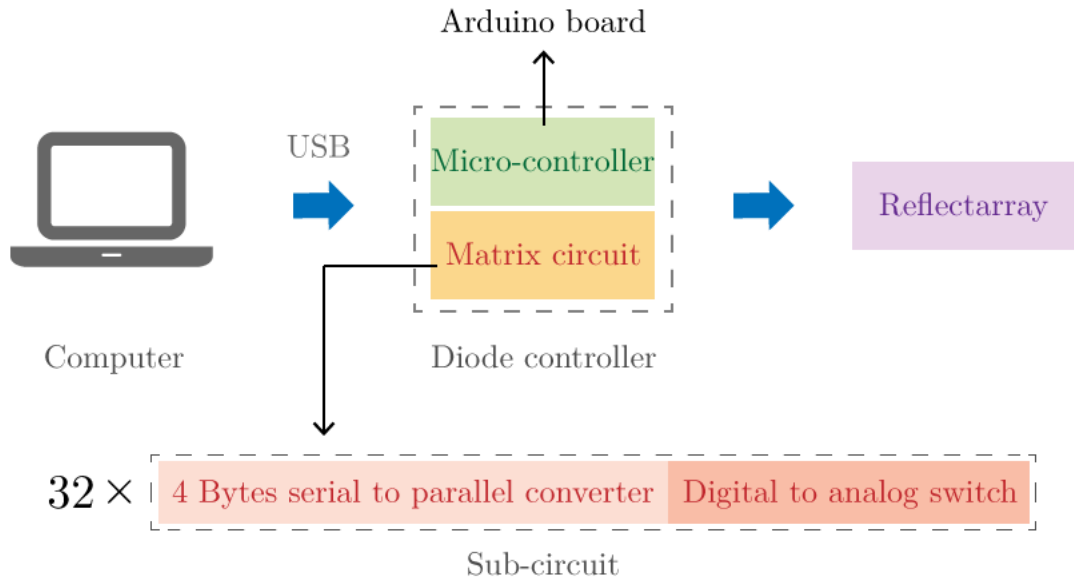


**Figure 5.5.:** Diode controller sub components

the possibility to replace the concerned broken sub circuit without having to replace the entire large circuit.

As shown in Fig. 5.5, the sub circuit consists of a serial to parallel converter circuit and digital to analog switch circuit. The serial to parallel converter circuit is capable to convert 4 Bytes of serial data to 1-bit of 32 parallel outputs. This means that a sub circuit is capable to produce 32 connections to the elementary cells. The digital to analog switch is used to provide an alternative power supply for biasing the diodes because depending uniquely on the power provided by the Arduino board is not enough if the total number of diodes are high.

To test the functionality of the diode controller, a green LED matrix panel will be used as LED shares the same characteristic as p-i-n diode. Green light indicates the diode is on, while no light indicates that the diode is off. By comparing the LED matrix panel light pattern with the provided data array from the computer, the functionality of the diode controller can be verified. The components discussion in the next section focuses more in the sub-circuit level that is the base element for the large matrix circuit.

### 5.3.1. Micro-controller (Arduino board)

Arduino board is chosen because it can be obtained inexpensively and this board has a large collection of good technical documentations which can be referred online. Fig. 5.6 shows the board with its components.

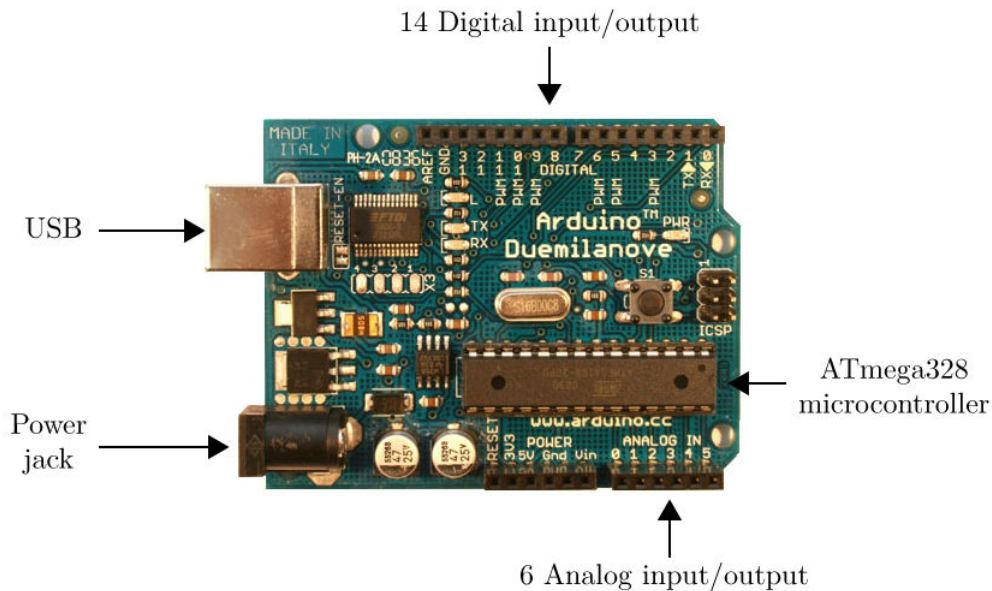


**Figure 5.6.:** Arduino Duemilanove (ATmega328) board

The micro-controller for this board is ATmega328 which runs at 16MHz. The clock speed is sufficient enough for switching diodes because in this project the switching time is not critical. The main objective is to demonstrate the beam scanning capability and radiation pattern reconfigurability. The micro-controller has 32KB of flash memory which is used to store the program and the data array of the diodes states to obtain the desired radiation pattern.

It has 14 digital and 6 analog inputs or outputs. These ports can be configured to be either input or output. It also provides 2 output powers of 5 V and 3.3 V respectively. The 5 V power output will be used as VCC for the shift registers located on the sub-circuit board. USB port will be used as the main connection to the computer and also as the power supply for the Arduino.

Another important reason for choosing this board is because its setup environment is very simple and straight forward process. To enable the computer to communicate with this board, a special software which can found on its website ([www.arduino.cc](http://www.arduino.cc)) must be installed. It is free and available on many major computing platform such as Windows, Mac OS and Linux.

The software has the complete features for the communication. It allows user to put the code to program the board and at the same time performs code validation for errors or incompatibility for the board. The coding language for Arduino is similar to C style language. With good documentations, references and easy setup environment, less time is required for new user to start working with this diode controller in the future.

### 5.3.2. Matrix sub-circuit

The matrix sub-circuit is composed of 2 components which are serial to parallel output circuit and digital to analog switch circuit for independent power supply to bias the diodes. Each of the Arduino input/output pin can provide or receive a maximum of 40 mA current. This amount of current is sufficient to control a small amount of diode but not for 1024 diodes. This can be shown with LEDs panel where the LED used (Kingbright subminiature LED) has a forward voltage of 2 V and it consumes 5 mA with low light intensity emission that is sufficient to notice whether the LED is biased or not. This is taken from the manufacturer datasheet and it is shown in Fig.5.7. For a 4×4 LEDs panel, 40 mA is sufficient because statistically only half from the total diodes will be biased according to the phase distribution pattern. In this case, only 8 LEDs are biased with the total current consumption around 40 mA.

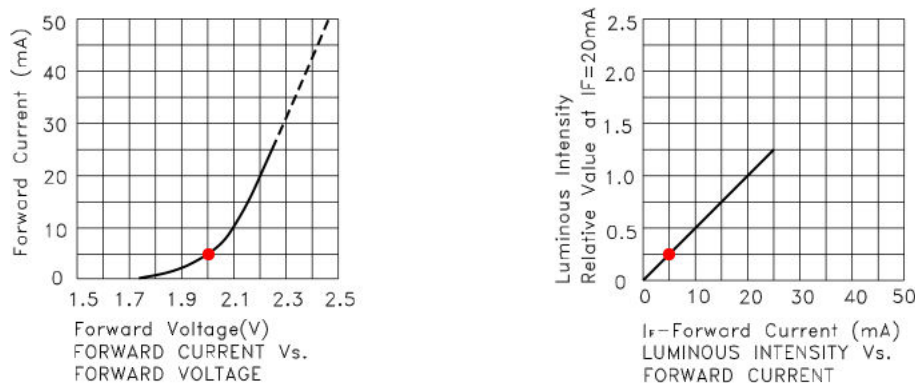


**Figure 5.7.:** Kingbright subminiature LED forward current and luminous intensity graphs (KM2520SGD01)

However for a large LEDs panel that contains 32×32 elements, the average current consumption is estimated to be around 2.6 A. It is the same case for the p-i-n diode integrated in the elementary cells. The p-i-n diode needs at least 5 mA to function correctly. By increasing the current intensity to 15 mA, the p-i-n diode resistance value ( $R$ ) can be decreased. This helps to increase the reflection coefficient magnitude as the loss within the p-i-n diode is reduced. The consumption is very high either for large LEDs panel or AFR. At this level, it is obvious that an

external power supply is needed because the default current provided by Arduino is not enough. It also gives the flexibility to regulate the current runs through the diodes especially in case where high current intensities are needed to improve the AFR performance.

Fig. 5.8 shows the printed circuit board (PCB) drawing for the diode controller. The top part of the circuit represents the digital to analog switch circuit and the bottom part is the serial to parallel output circuit. In total there are 16 analog switches because 2 switches are required to handle 8 outputs.

For the serial to parallel conversion part, there are 4 shift registers and each of them is capable to convert 8-bits of output. The pink box represents input data from Arduino and they are serial data which contains diode states array, latch and clock signal to control the shift registers. The serial data output is used to cascade the diode controller circuit to another diode controller circuit for additional outputs.

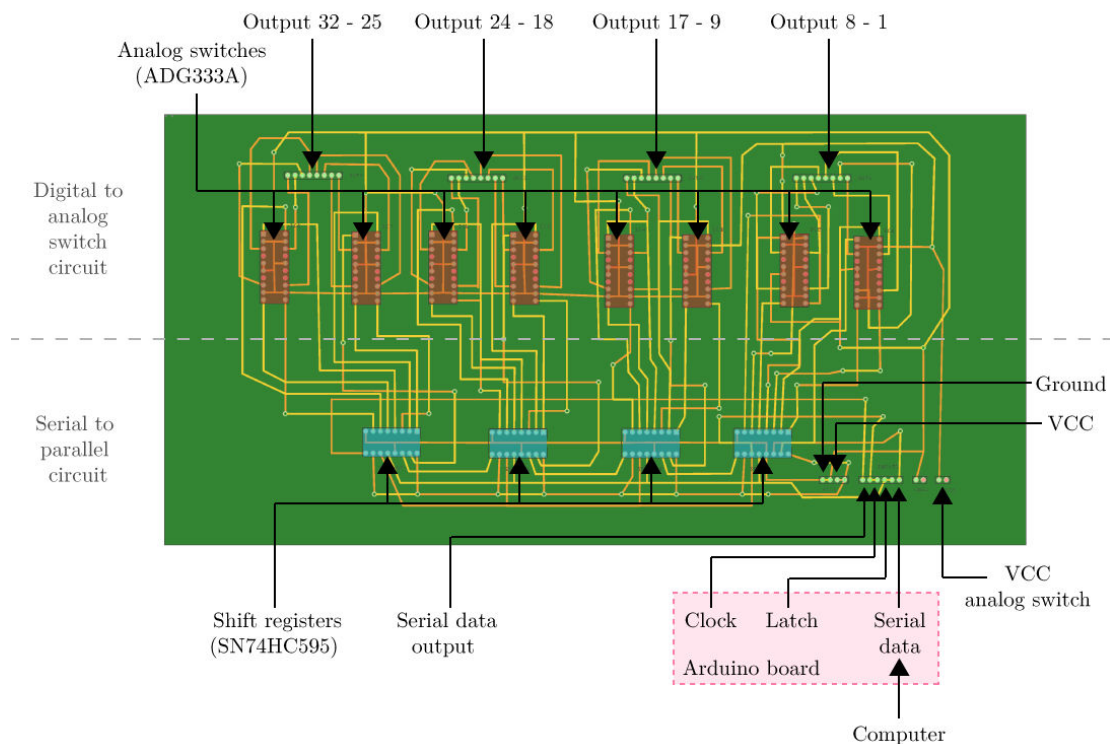


**Figure 5.8.:** PCB drawing for matrix sub circuit

Fig. 5.9 shows the fabricated diode controller PCB which is drawn using Fritzing software. The board uses top and bottom layers for metal interconnections. For the output and input connections, break away male headers (right angle) are used as the connection to the wires.

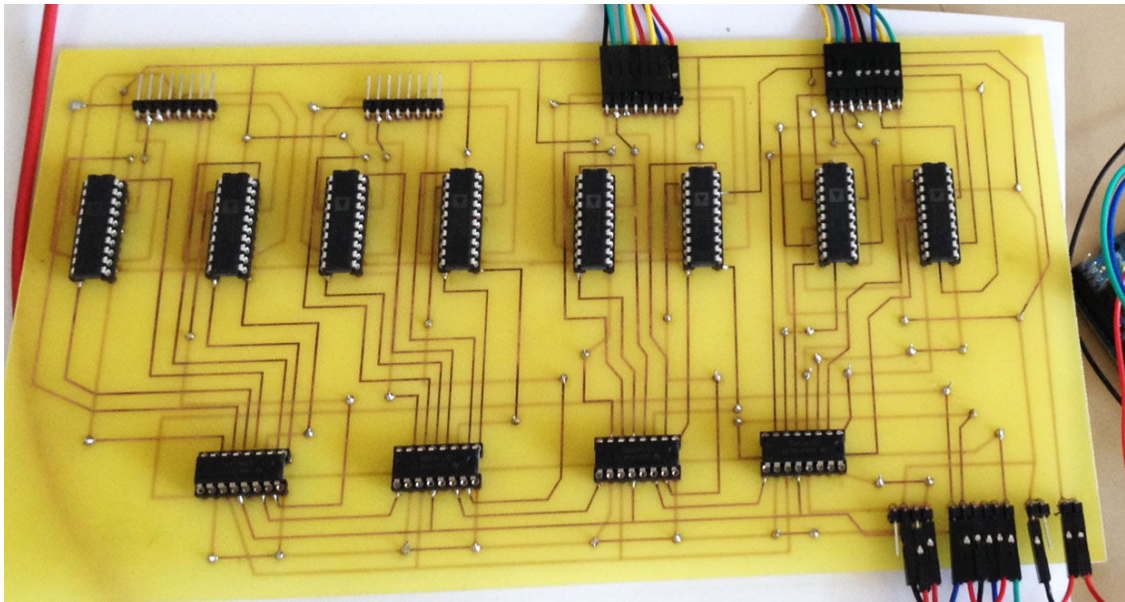


**Figure 5.9.:** Fabricated matrix sub circuit PCB

### 5.3.2.1. Serial to parallel output circuit

To convert the serial data to become 1-bit of parallel output, shift register IC is used. In this project, the chosen shift register has the reference number of 74HC595 and is manufactured by Texas Instrument. In the datasheet, it is known as “8-bit shift registers with 3-state output registers”. Fig. 5.10 shows the package top view for the shift register. It has 16 pins which 7 of them are reserved for inputs and the rest are the outputs. Tab. 5.1 shows the pins mnemonics and their description taken from the manufacturer datasheet.

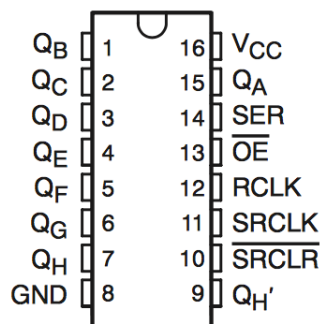


**Figure 5.10.:** 74HC595 package top view

Pin	Mnemonic	Description
15, 1-7	$Q_A$ - $Q_H$	1-bit output pin
8	GND	Ground, $V_{SS}$
9	$Q_H'$	Serial out
10	SRCLR	Master clear, active low
11	SRCLK	Shift register clock
12	RCLK	Storage register clock (Latch)
13	OE	Output enable, active low
14	SER	Serial data input
16	$V_{CC}$	Positive supply voltage

**Table 5.1.:** Shift register pins description

Based on the datasheet provided, the pin SRCLR needs to be connected to the  $V_{CC}$  for high state in order to disable the clear function while OE pin needs to be connected to the ground (GND) for low state in order to enable all the output pins. The pin storage register clock (RCLK) plays an important role to ensure the correct functionality of the conversion. It needs to be set as high state while sending the serial data into the shift register and at the end of serial data. This pin needs to be in low state. This makes the registers memorize the last values inside them and retain the values as long as  $V_{CC}$  is supplied.



The shift register is simulated using Quartus II simulator to verify the pin connections and the expected behavior. Fig. 5.11 shows the pin connections setup for the simulation where inputs are arranged on the left side and outputs are arranged on the right side. Fig. 5.12 shows the simulation results for the shift register.

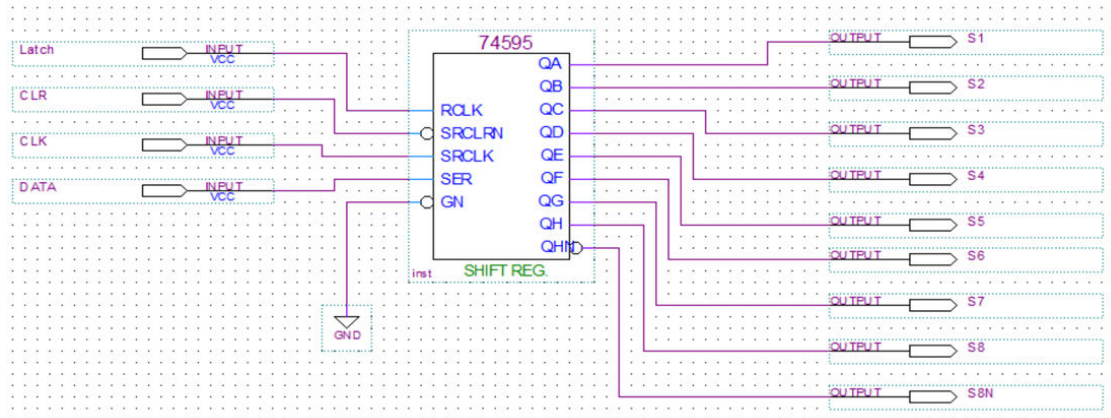


Figure 5.11.: Pin connection setup in Quartus II simulator

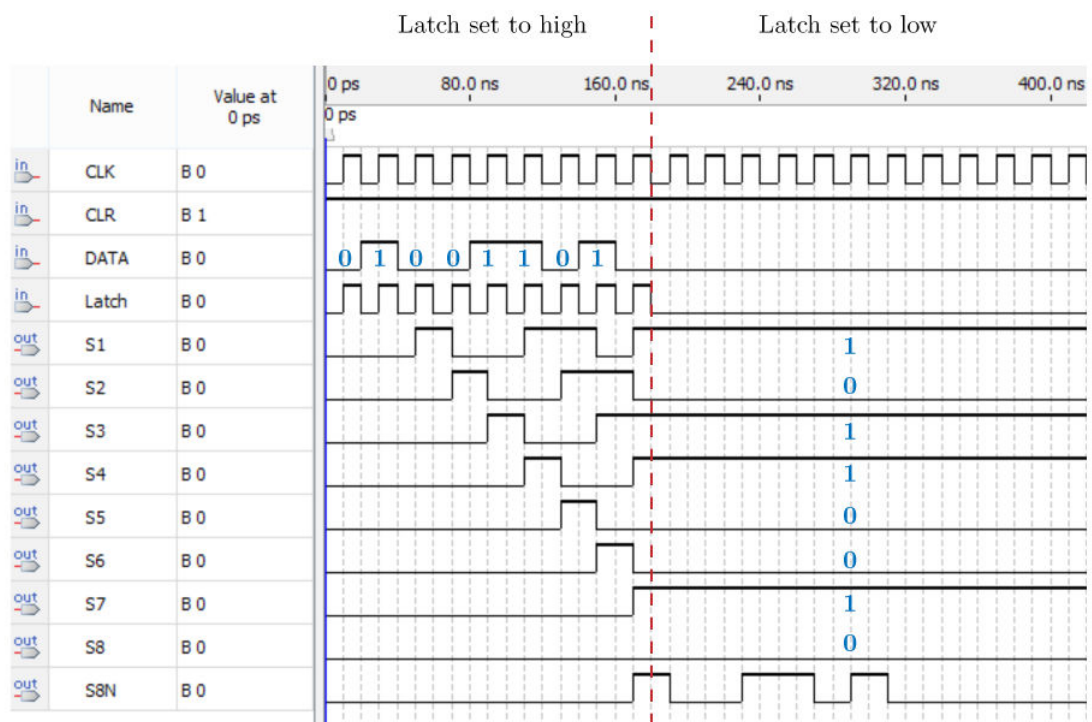


Figure 5.12.: Simulation timetable for 8-bit shift register

In this simulation the clock signal (CLK) frequency is set to 50 MHz. CLR is always set to high to disable the clear value function. The serial data (DATA) is a series of values 0,1,0,0,1,1,0,1. At the beginning of the conversion, the latch (SRCLK) is set to high. In each clock cycle, the data series will be shifted by one clock cycle. In this case, to correctly shift the data series to their proper pin output, 8 clock cycles are required. However to ensure that all data series are correctly shifted, an additional cycle is taken into account and this increases the required clock cycles to 9. After the ninth cycle, the latch pin is set to low. This makes the shift register retains the last value outputted by each pin as long as the  $V_{CC}$  is presence (memory state).

In general, the number of cycles is determined by the number of element in data series. The result shows that the data series has been properly converted to 1-bit of data and outputted to pin 1 until pin 8 according to their position in the data series. The first element in the data series will be outputted to pin 8 while the last element will be outputted to the pin 1.

By cascading the multiple shift registers, the number of outputs is increased and more cycles are needed to do the conversion. Fig. 5.13 shows the pin connections for cascading 2 shift registers in order to obtain 16 outputs where 16 clock cycles are required to complete the conversion. The sub matrix circuit is designed to do the conversion for 32 outputs which is equivalent to 4 Bytes of serial data. In this case, 4 shift registers are cascaded to obtain 32 outputs. Fig. 5.14 shows the fabricated sub circuit for 32 outputs using 4 cascaded shift registers.

The fabricated circuit shown in Fig. 5.14 has been tested and it works well to do the conversion for small number of diodes. For a large number of diodes, the current output provided on each output pin is not stable and can not be regulated to meet voltage and current requirements. To overcome these problems, an additional circuit is required to be attached to the output pin of this serial to parallel circuit. The circuit uses the digital to analog switch IC as the main component.

Serial output of the first shift register is connected to the serial input of second shift register

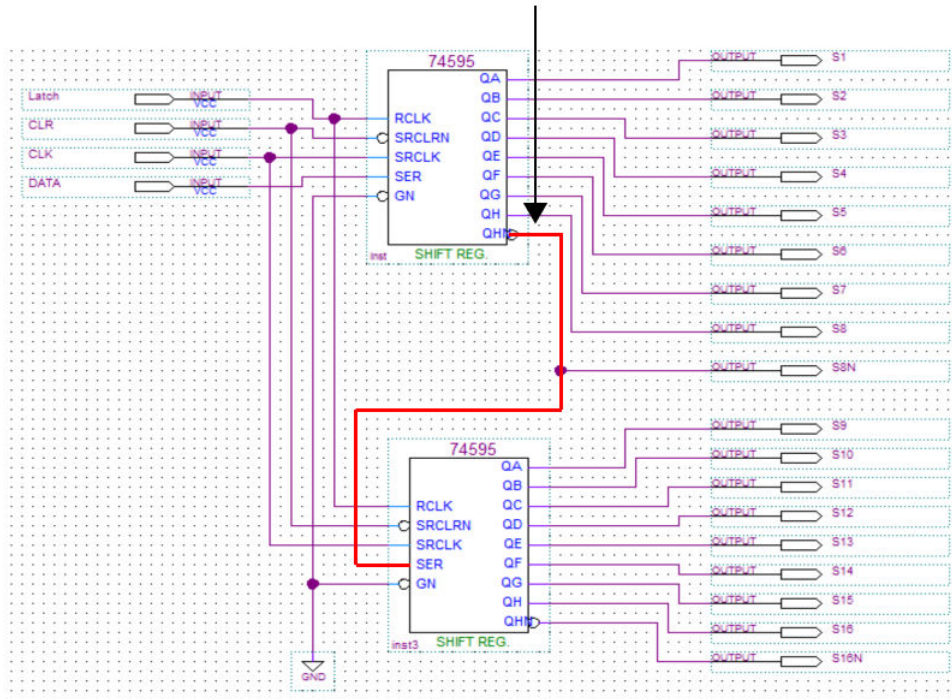


Figure 5.13.: Cascading 2 shift registers to obtain 16 outputs

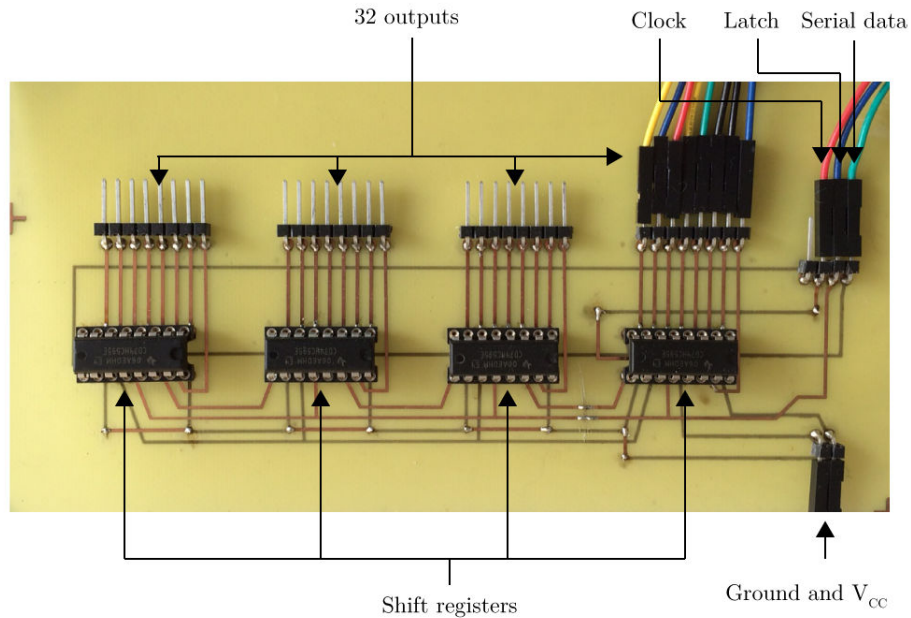
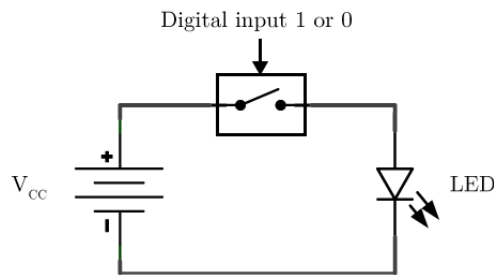


Figure 5.14.: Fabricated serial to parallel conversion circuit for 8 Bytes of data using 4 shift registers

### 5.3.2.2. Digital to analog switch circuit

The basic concept for this circuit is similar to normal switch but the control mechanism is managed by digital input as shown in Fig. 5.15. In this case, if the digital input is 1, the circuit is connected and the LED emits light and in the contrary case where digital input is 0, the circuit is opened and no current flows through the LED.



**Figure 5.15.:** Digital to analog switch circuit

The switch used in this project is single pole double throw (SPDT) based switch that uses CMOS technology for faster switching speed and low power dissipation. Its model is ADG333A and it is manufactured by Analog Devices. Fig. 5.16 shows the functional block diagram of the switch. The switch package contains 4 independent SPDT switches which are controlled by digital input noted as IN1, IN2, IN3 and IN4.

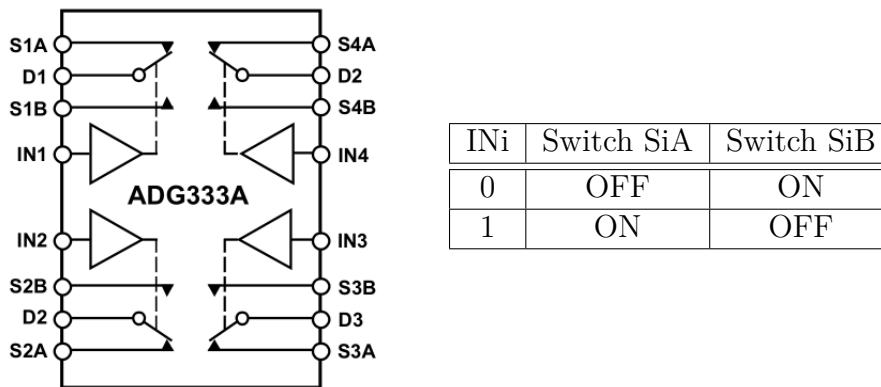


**Figure 5.16.:** ADG333A functional block diagram and truth table (right side)

Based on the truth table, the switch will be either connected to switch A or switch B. The “A” and “B” switches are referred as SiA, SiB and “i” is the switch number. In total there are 4 switches. If the digital IN<sub>i</sub> input is 0, the switch is connected to switch B. If the digital input is 1, the switch is connected to switch A.

To have a better synchronization with the binary matrix from the computer (1 = diode is ON, 0 = diode is OFF), switch A is chosen. This will directly translate the binary matrix data to the correct switch states that is similar to the diode states. Because of that, the “B” switches are unused and are not connected. Fig. 5.17 and Tab. 5.2 show the switch pin configurations and descriptions respectively.

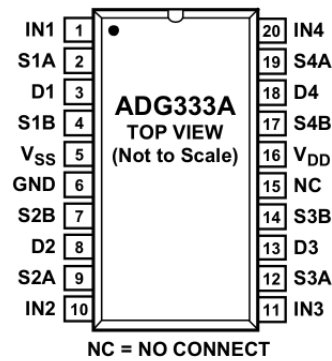


**Figure 5.17.:** ADG333A pin configurations

Pin	Mnemonic	Description
1, 10, 11, 20	IN1, IN2, IN3, IN4	Logic Control Input
2, 4, 7, 9, 12, 14, 17, 19	S1A, S1B, S2B, S2A, S3A, S3B, S4B, S4A	Source Terminal. Can be an input or output.
3, 8, 13, 18	D1, D2, D3, D4	Drain Terminal. Can be an input or output.
5	V <sub>SS</sub>	Most Negative Power Supply Potential in Dual Supplies. In single-supply applications, it can be connected to ground.
6	GND	Ground (0 V) Reference.
15	NC	No connect.
16	V <sub>DD</sub>	Most Positive Power Supply Potential.

**Table 5.2.:** ADG333A pin descriptions

The pins IN1, IN2, IN3 and IN4 are connected to the output connection of serial to parallel circuit. 5 pins are connected to the ground (GND) and they are S1B, S2B, S3B, S4B and V<sub>SS</sub>. The power supply connection is connected to the pins S1A, S2A, S3A, S4A and V<sub>DD</sub>. The pins D1, D2, D3 and D4 are considered as output pins as they are connected to the p-i-n diodes in the elementary cell via wires. Fig. 5.18

shows the pin connection configurations using the fourth switch (S4A, IN4, D4) to control the diode.

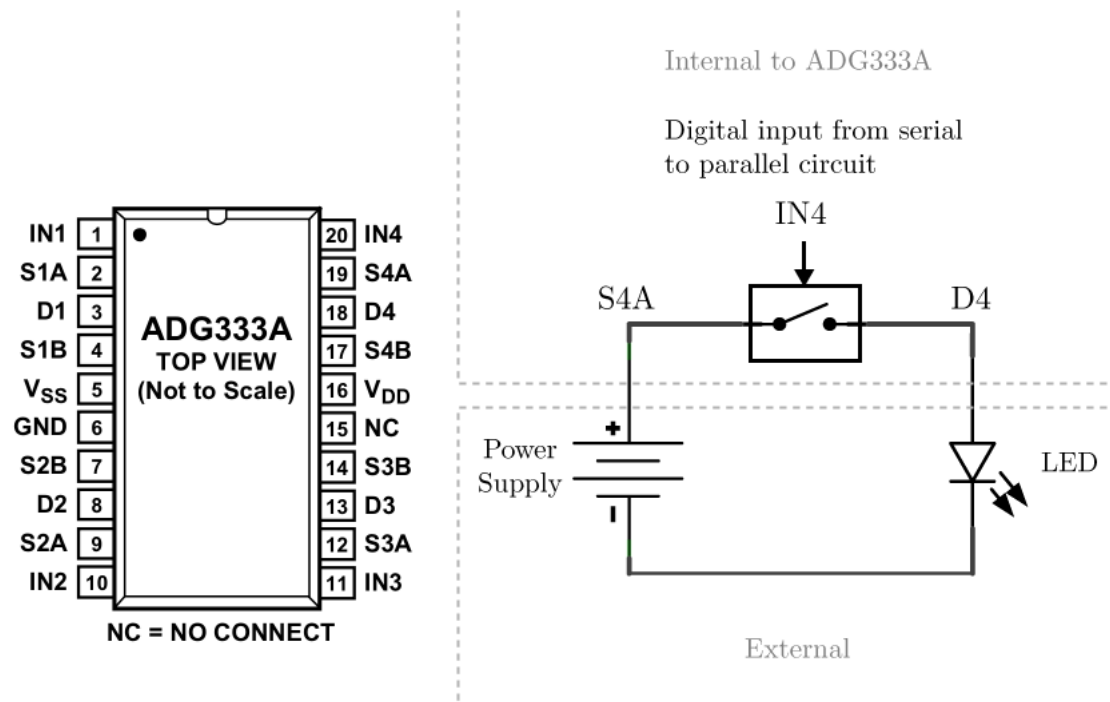


**Figure 5.18.:** Pin connection using fourth switch as an example

In Fig. 5.18, the digital input IN4 is connected to one of the outputs from serial to parallel circuit. The positive power supply is connected to the source number 4 (S4A) and the positive pin of the LED diode is connected to the drain number 4 (D4). The negative pin of the LED is connected directly to the negative terminal of the power supply.

This configuration shows that the LED diode uses the separate power supply as the main power instead of relying on the power coming from the serial to parallel circuit. In addition, it is possible to regulate the power supply connected to the LED as needed. This example uses only one switch output, but in reality, all 4 switches of the circuit ADG333A are used for driving 4 diodes. In this case, to produce 32 outputs of connections, 8 digital to analog switches are needed for each sub matrix circuit.

## 5.4. Test and validation

To validate the diode controller functionality, the sub-circuit is tested with series of LEDs aligned together to form 32 outputs. By comparing the LED light pattern with the configured data array in the computer, the function of the sub-circuit can be validated. Fig. 5.19 shows the diode controller connections with the computer, power supply and a series of LED.

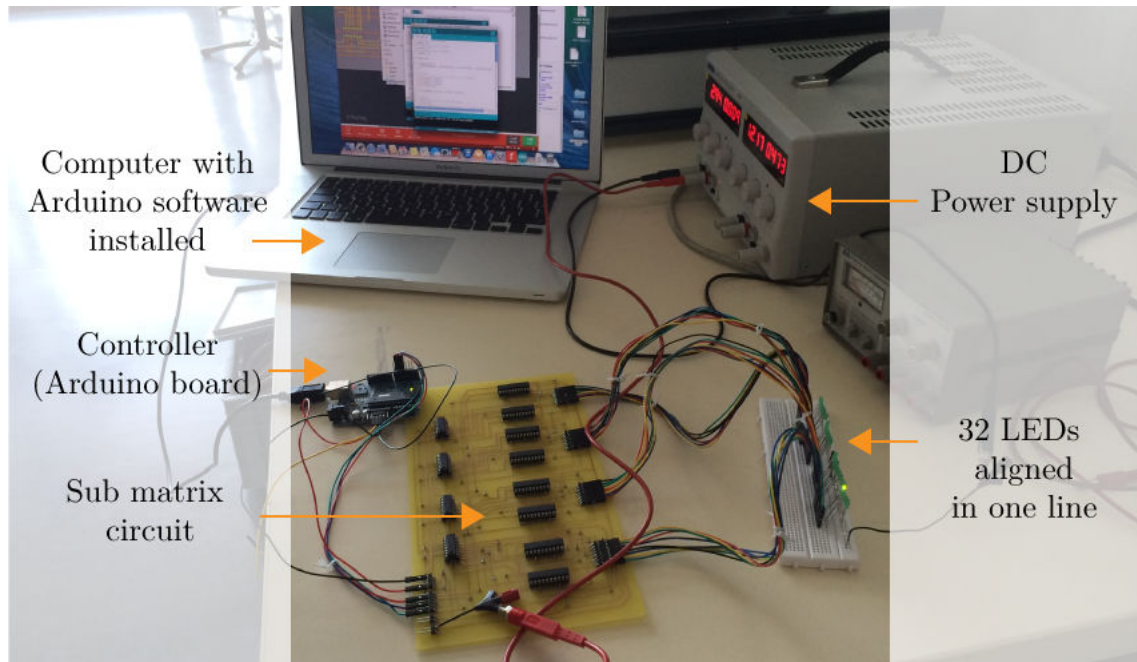


**Figure 5.19.:** Diode controller connections configurations

After validating the function of a single sub-circuit, 2 sub-circuits are cascaded to form a matrix circuit that is capable to handle 64 outputs. A  $8 \times 8$  LED matrix panel is fabricated for this purpose. For the test purpose, all controllable outputs of the sub-circuit are used for all 64 LEDs. In this test case, a sub-circuit is not configured to match matrix panel rows, but for the final design, each sub-circuit corresponds to a single row in the LED matrix panel. The geometry of the LED panel is designed to approach the active reflectarray design. This gives better test environment because the physical connection using wires and antenna placement are able to be evaluated. Fig. 5.20 shows the fabricated LED matrix panel. The size of this panel is similar to a  $8 \times 8$  elements reflectarray at 20 GHz. The LED package is subminiature type which can be fitted into the small elementary cell size.

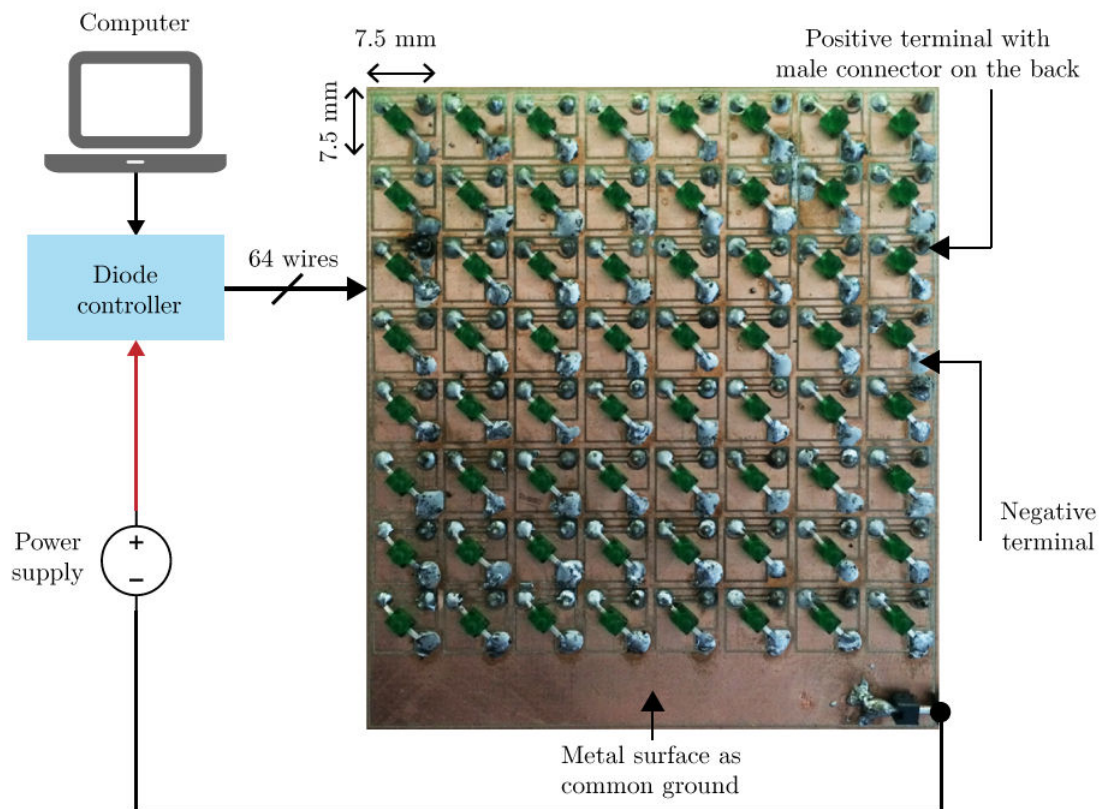


**Figure 5.20.:**  $8 \times 8$  LED matrix panel

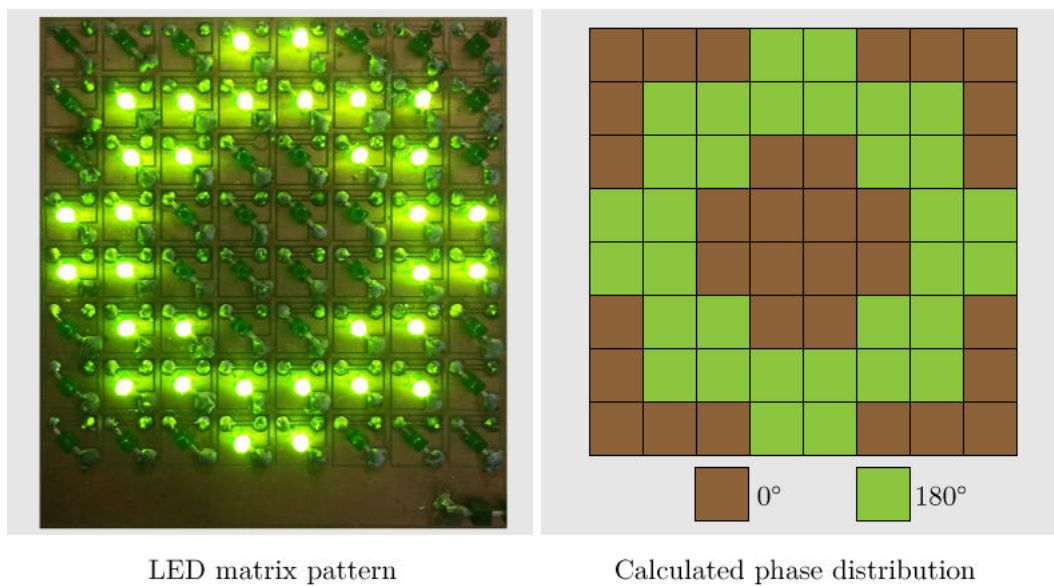
The size of each element in the panel is  $7.5 \text{ mm} \times 7.5 \text{ mm}$ . This is the same size of the active elementary cell at 20 GHz. The positive terminal for the LED is connected to the male connector at the back side of the panel. The connector is used to connect the LED to the output of the diode controller which controls the state of the diode. The negative terminal is connected to the common metal surface and it is connected to the ground terminal of the power supply.

Fig. 5.21, Fig. 5.22, Fig. 5.23 and Fig. 5.24 show the LED matrix pattern and calculated phase distribution comparison for beam focused at  $\theta = 0^\circ$ ,  $\theta = 10^\circ$ ,  $\theta = 20^\circ$  and  $\theta = 30^\circ$  respectively. In these figures, the left side shows the LED matrix pattern produced by diode controller and on the right side it shows the calculated phase distribution for AFR with 64 elementary cells at 20 GHz. The phase value of  $0^\circ$  corresponds to diode in OFF state while the value of  $180^\circ$  is obtained when diode is in ON state. Each figure shows the same pattern configuration for LED matrix pattern and calculated phase distribution. This indicates that the diode controller circuit design is correct.



From these comparisons, the diode controller works well as it is capable to generate the desired diode states pattern corresponding to the desired phase distribution pattern. As discussed in the beginning of the chapter, the final diode controller design will be able to support  $32 \times 32$  diodes. A lot of wires are used as each LED positive terminal on the LED matrix panel requires one wire per connection. This can be an inconvenient as the number of wire is increased with the number of elements. For a large LED panel or reflectarray, the wires need to be labelled in order to reduce the wires management complexity.

This approach has the advantage to be compatible with any size of LED panel or real active reflectarray that is limited to  $32 \times 32$  elements even when using a non square LED panel, for example a  $15 \times 32$  LED panel. Currently, the  $32 \times 32$  LED panel and the diode controller that supports  $32 \times 32$  elements are still in fabrication process.



**Figure 5.21.:** LED matrix pattern and phase distribution comparison for beam focused at  $\theta = 0^\circ$

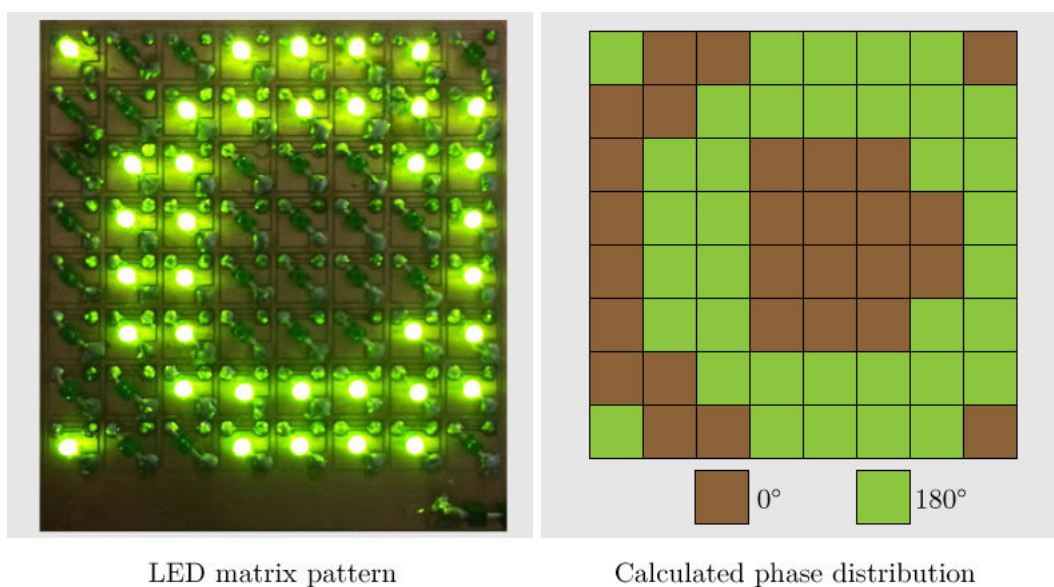


**Figure 5.22.:** LED matrix pattern and phase distribution comparison for beam focused at  $\theta = 10^\circ$

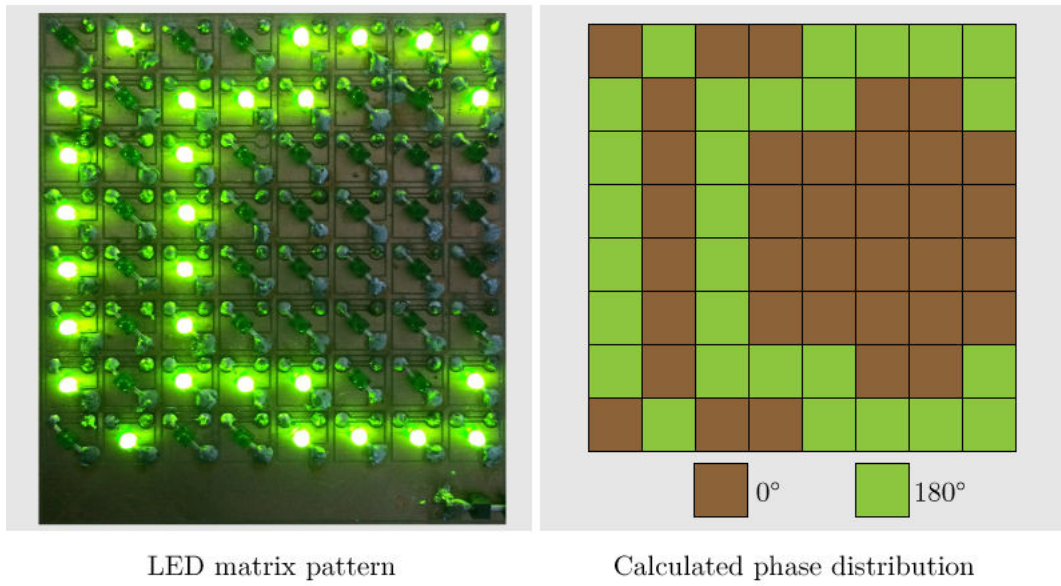


**Figure 5.23.:** LED matrix pattern and phase distribution comparison for beam focused at  $\theta = 20^\circ$

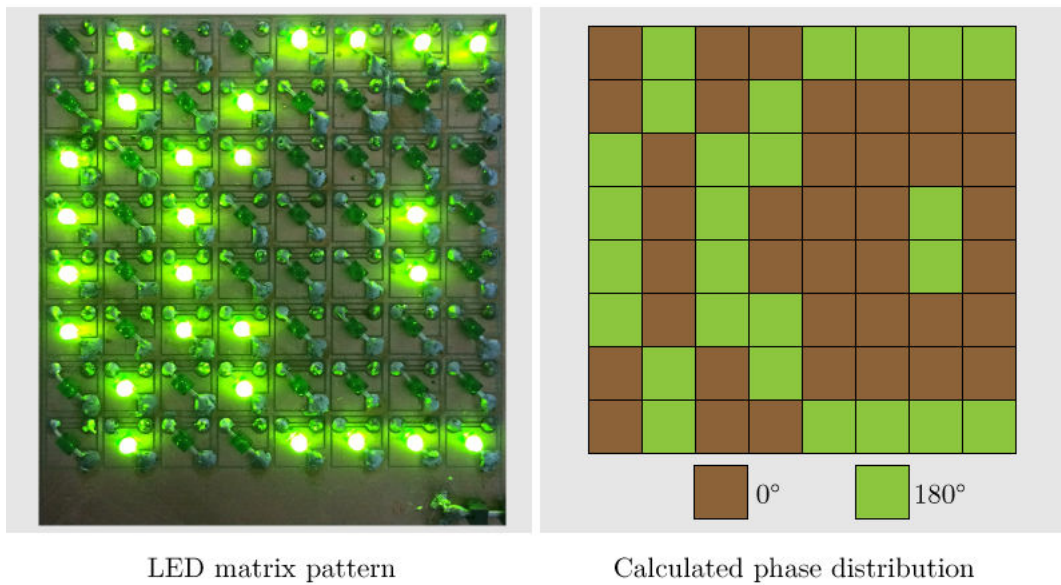


**Figure 5.24.:** LED matrix pattern and phase distribution comparison for beam focused at  $\theta = 30^\circ$

## 5.5. Conclusion

The concept and the architecture of the diode controller were discussed in this chapter. This includes the main components used in the controller and the problem linked to the power supply for biasing the large amount of diodes. For the controller part, Arduino board is used and its advantages for this project are highlighted especially for meeting the required specifications at the low cost.

The matrix circuit used to convert the serial data to parallel is divided into small sub-circuit which is capable to convert 4 Bytes of data. By using sub-circuit, it is easier to extend the number of outputs and at the same time it simplifies the process to handle the circuit malfunctions due to broken parts.

The diode controller is fabricated and tested. Its functionality is validated by using LED matrix panel which represents the active reflectarray. The LED matrix panel pattern produced by the diode controller is compared to the desired phase distribution. The results show that the diode controller works well and is ready to be used with the active reflectarray. The final design of the diode controller will be able to support  $32 \times 32$  diodes and currently, it is in the fabrication process.



## 6. General conclusion

In this project, the study and the conception of active reflectarray for UAV link communication application at 20 GHz is conducted. The project is divided into 4 phases. The first phase is the study of the existing technologies to accomplish reconfigurable antenna. The second phase is the theoretical and mathematical study for developing reflectarray simulator in order to accelerate the design process. The third phase is the conception and simulation of active reflectarray where most of the work consists of designing the reconfigurable elementary cell. The final phase is the work related to the p-i-n diodes controller which manages the diodes states in each elementary cells based on the given phase distribution.

The study of the existing technologies to achieve reconfigurable antenna leads to multiple possible solutions. Those solutions are based on RF MEMS switch, varicap diode, liquid crystal, ferroelectric material and PIN diode. These solutions have different level of complexities especially in terms of fabrication and integration with the antenna. RF MEMS and PIN diodes are considered to be the best options and in this project PIN diode is selected because of the cost and because they have already proven to be suitable in industrial application. In the future work, RF MEMS solution can be used as the replacement of PIN diode because it will help to increase the performance of the reflectarray.

The purpose of the theoretical and mathematical study in the second phase is to develop a reflectarray simulator that is capable to calculate quickly the radiation pattern for any given phase distribution. The simulator uses Matlab environment and it is called Hybrid Reflectarray Simulator. This simulator helps a lot in the reflectarray design process by decreasing significantly the amount of simulation time compared to the simulation using full electromagnetic software. Study on the correction order number is also observed in this phase. Having high correction order will not necessarily improve the performance because the loss inside in active element must also be considered.

A Reconfigurable elementary cell design has been proposed. The design is optimized for fabrication purpose and it uses inexpensive material in order to reduce the total fabrication cost. Simulations at the elementary cell and reflectarray levels show that the design works well and beam scanning capability is achieved. Despite applying all the modifications imposed by the manufacturer, the reflectarray is still unable to be fabricated due the other fabrication constraints. The design could be improved by moving the p-i-n diode to the outside of the substrate. This eliminates the diode soldering problem. However the diode polarization line needs to be

modified to adapt the new diode placement.

The diode controller is designed and fabricated independently from the reflectarray and it can be used to control other types of antenna that integrates p-i-n diode as switching element. The functionality of this controller is validated using a LED matrix panel. By cascading multiple sub circuit together, the number of the controlled elements can be increased as needed. In addition, the voltage and the current flowing through the diode can be controlled because the power supply is made independently from the control circuit. This increase the controller flexibility as it can be adapted to fit the type of application required. In terms of switching performance, using faster micro-controller will be able to increase the speed.

In the short term period, the modification on the elementary cell diode polarization line will enable the reflectarray to be fabricated and measured because the current design can not be fabricated by the manufacturer contrary to their first statement due to position of the diode in the middle of substrates. The modification requires the p-i-n diode to be moved at the back side of the elementary cell and some geometry adjustments are needed for the phase delay line and the via. Once the reflectarray is fabricated, it can be tested directly with the diode controller that is already validated and shown to be working well.

In the future, reconfigurable antenna will be available widely and accessible to many types of applications because of the advancement in the fabrication that will reduce the cost and the price. Reconfigurable antennas or also smart antennas will play major role in the next decades as communications devices such as mobile phones are designed to be more power efficient and intelligent in terms of handling the wireless signal. This will also benefit the manufacturer as the same antenna can be used for multiple frequencies and multiple radiation patterns.

For reflectarray, advancement in fabrication will enable more sophisticated reconfigurable reflectarray to be fabricated at much smaller size and compact especially at the high frequencies. In terms of conception at the elementary cell level, one of the interesting concepts to be discovered and researched is by using optical based material to achieve reconfigurability as discussed in [78]. Nowadays, modern houses are changing towards smart houses where everything is connected and the presence of the smart antenna is essential. This will allow the integration of smart antenna in optical appliances that behave like antenna and at the same time serve as lighting purpose.

## 7. Resume (French)

Cette thèse a été effectuée au sein du Laboratoire d'Electronique, Antennes et Télécommunications (LEAT) à Sophia Antipolis et le projet est financé par l'Université Malaysia Pahang (UMP) grâce au programme de bourse de doctorat financé par le ministre de l'éducation nationale de la Malaisie. Le directeur de thèse est Claire Migliaccio, professeur à l'Université Nice Sophia Antipolis en codirection avec Jérôme Lanteri (maitre de conférences à l'Université Nice Sophia Antipolis).

L'objectif de cette thèse est de concevoir un réseau réflecteur à dépointage électronique à 20 GHz pour des applications de communication avec des drones (Unmanned Aerial System). Le principe de fonctionnement des réseaux réflecteurs est similaire à celui d'une antenne parabolique. La principale différence concerne la forme du réflecteur. En effet les panneaux des réseaux réflecteurs sont plans contrairement à la parabole. Le panneau réflecteur se compose de cellules élémentaires qui sont utilisées pour contrôler la phase réfléchiée de l'onde d'incidente. Le contrôle de la phase au niveau de la cellule élémentaire nous permet de focaliser le diagramme de rayonnement dans la direction souhaitée.

De nombreux exemples de cellules élémentaires sont présentés et notamment les différentes technologies utilisées pour réaliser une cellule reconfigurable. Les technologies mentionnées sont l'interrupteur RF MEMS, la diode varicap, les cristaux liquides, les matériaux ferroélectriques et la diode PIN. Il est nécessaire faire des compromis au moment de faire le choix parce qu'il faut considérer le coût de fabrication, la complexité de la conception tout en conservant des performances acceptables. Dans cette thèse, la solution retenue est l'utilisation de diodes PIN. Cette dernière a fait l'objet de nombreuses études que ce soit au niveau laboratoire mais également industriel et possède des atouts intéressants en terme de performance et de coût.

Un programme de simulation « maison » a été développé pour calculer rapidement le diagramme de rayonnement pour tous types de distribution de phase. Ce programme est écrit sous l'environnement Matlab et s'appelle « Hybrid Reflectarray simulator » ou HRS. Il nous a été très utile dans le processus de design des réseaux réflecteurs, notamment du fait d'un temps de simulation très fortement réduit par rapport aux logiciels de simulation électromagnétique. Nous avons aussi utilisé cet outil pour faire l'étude sur le niveau de la correction de zones de Fresnel des réseaux réflecteurs actifs. L'étude montre que d'avoir un niveau de correction élevée ne garantit pas la meilleure performance parce qu'il faut aussi considérer les



perdes dans l'élément actif lui-même ( dans notre cas, il s'agit des pertes dans les diodes PIN).

Plusieurs structures de cellules élémentaires sont simulées pour tester la capacité de dépointage du faisceau. L'intégration de la diode PIN dans la simulation est assez facile mais l'intégration dans le design des lignes de polarisation est plus délicat car il faut tenir compte des contraintes de fabrication ainsi que les performances de la cellule. Finalement, nous avons proposé un design qui est prêt et optimisé pour fabrication. Ce design utilise le matériel de type Meteorwave <sup>TM</sup> 2000 qui est moins cher que les substrats de type Rogers, ce qui permet de réduire le cout de fabrication.

Les simulations au niveau de la cellule élémentaire et du réseau réflecteur montrent que le design fonctionne bien et qu'il est possible de dépointer électroniquement le faisceau de l'antenne. Malgré les changements effectués sur le design, le fabricant éprouve toujours des difficultés pour souder de façon automatique les diodes PIN qui sont positionnées sur une des couches intérieures du réseau réflecteur. La technologie actuelle de fabrication ne peut pas encore résoudre ce problème et pour l'instant nos réseaux réflecteurs actifs ne peuvent pas encore être fabriqués.

Les diodes intégrées dans les cellules ont besoin d'un système de contrôle automatique pour bien contrôler l'état de chacune de diode (ON/OFF) à partir de la distribution de phase donnée. Pour cette raison, le contrôleur de diode est fabriqué indépendamment de l'antenne de réseaux réflecteurs. Il pourra ainsi être réutilisé pour d'autres réseaux réflecteurs utilisant des diodes PIN comme composants électroniques pour la reconfiguration de diagramme. Un démonstrateur à base de LEDs a été réalisé permettant ainsi de vérifier le bon fonctionnement de ce contrôleur. Il est de plus possible de régler la tension et les courants consommés par les diodes indépendamment du contrôleur du fait de l'utilisation d'une source d'alimentation externe. Cela nous permet d'avoir plus de flexibilité en terme de puissance d'alimentation et nous pouvons régler les sources comme il faut pour les différents types d'application.

Dans l'avenir, il serait nécessaire de modifier la position de la diode afin de rendre la fabrication plus aisée. Dans ce cas il faudra retravailler sur les lignes de polarisation et aussi les géométries du stub et des vias. Il sera peut-être nécessaire de déplacer la diode à l'extérieur du substrat en face l'arrière de la cellule par exemple. Quand les réseaux réflecteurs seront fabriqués, ils pourront être directement testés avec le contrôleur de diode qui est déjà fonctionnel.

# A. Object oriented programming in Matlab

To understand the concept of OOP and its advantages, consider the following example in describing the feed mathematic model (Fig. A.1) in Matlab. An object is created from a class definition. A class definition is a text file that contains codes, denoted by keywords and end statements which describe different elements of the class. In case of the feed model, the feed object will be created using feed class definition. In the class definition, there are parts of code that describes the properties of an object.

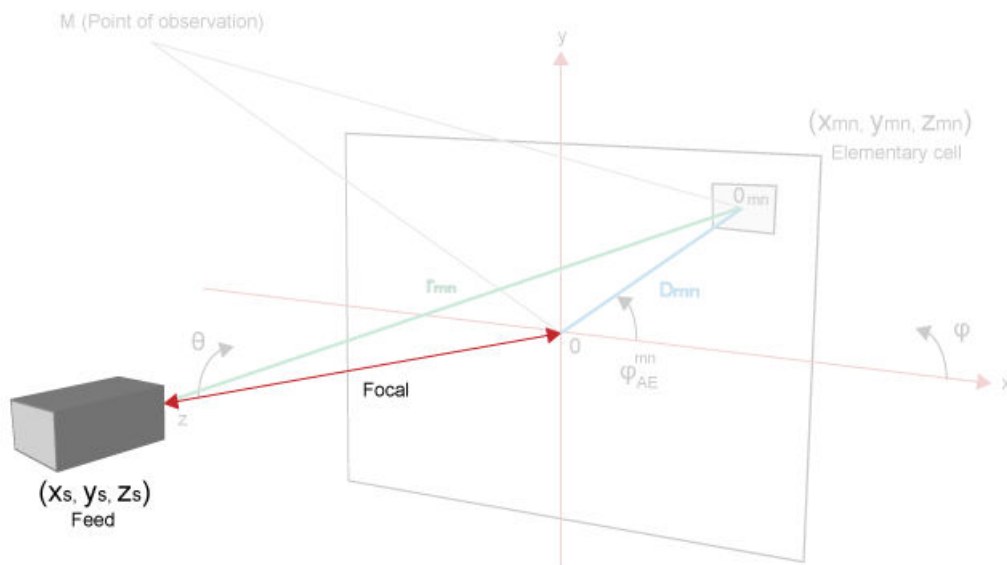


**Figure A.1.:** Feed object properties

Fig. A.2 shows the class definition for the feed model. The properties code block contains variables that describe the properties of the feed model. The feed can be described by its position in 3D coordinates  $(posX, posY, posZ)$  and also its focal distance and information on the focal to diameter ratio. In Matlab, feed object created using the shown class definition will have these properties stored inside the object. To create a feed object using feed class definition, the Algorithm A.1 is used.

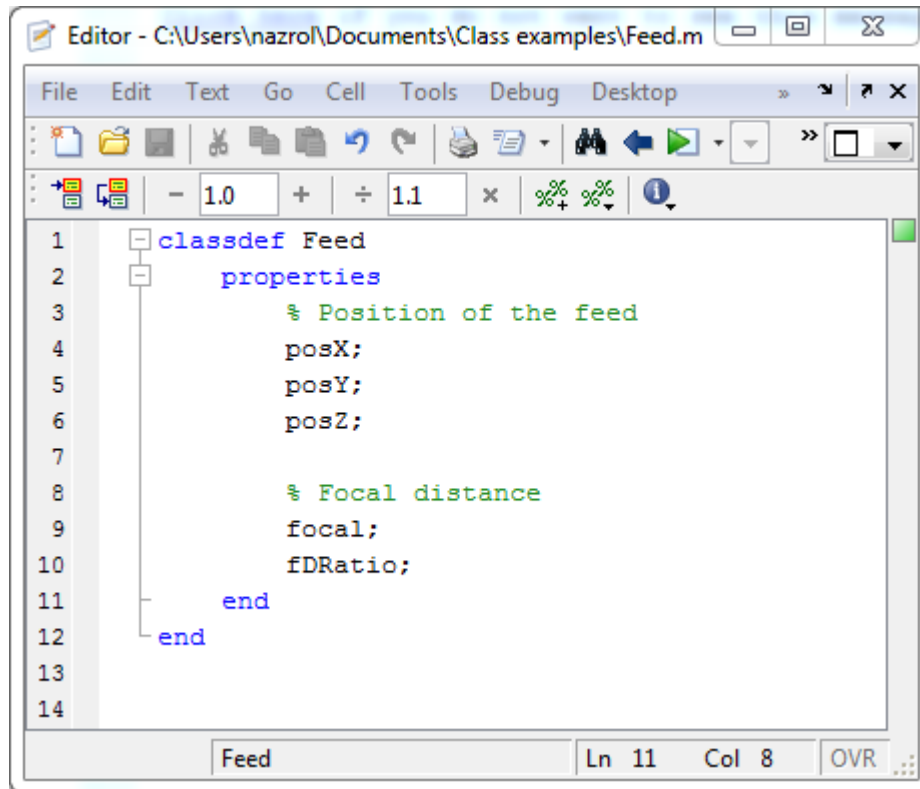


**Figure A.2.:** Feed class definition file Feed.m with properties

---

**Algorithm A.1** Feed object creation using feed class definition

---

```
primaryFeedObject = Feed;
```

---

The created feed object can be accessed using “primaryFeedObject” variable, but its properties values are still undefined and the created feed object is unusable. The properties values need to be defined after the object creation. This can be done by accessing the properties in the object of “primaryFeedObject” as shown in Algorithm A.2.

---

**Algorithm A.2** Setting the primaryFeedObject properties values

---

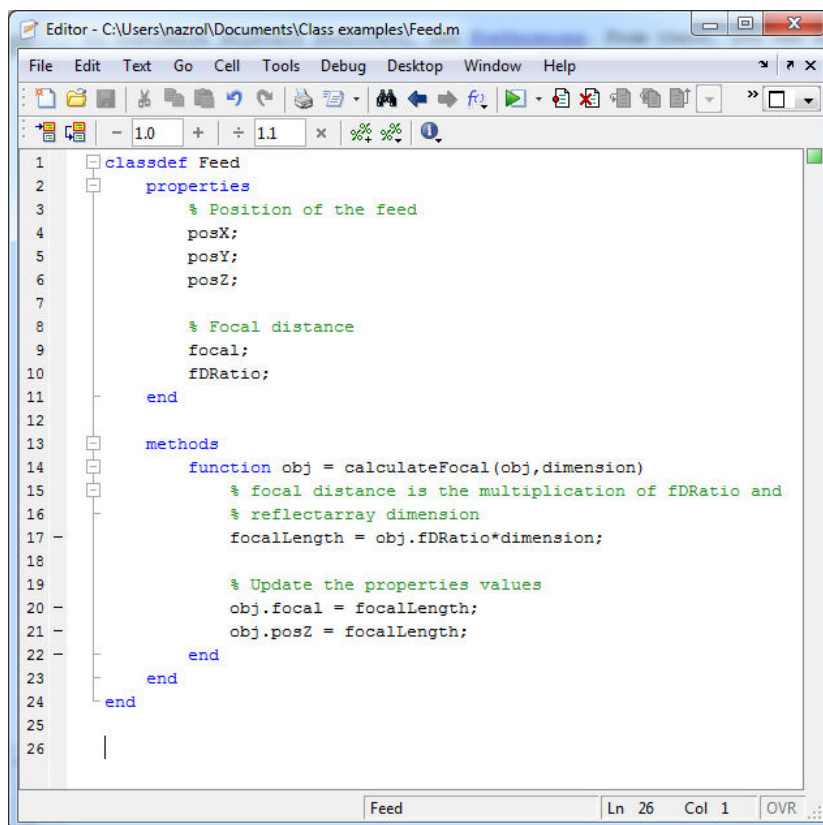
```
primaryFeedObject.posX = 0;
primaryFeedObject.posY = 0;
primaryFeedObject.fDRatio = 0.5;
```

---

The position properties ( $posX$ ,  $posY$ ,  $posZ$ ) of the feed are set to 0 and the focal to diameter ratio ( $fDRatio$ ) is set to 0.5. For  $posX$  and  $posY$  positions, the values are correct because the feed is positioned on the center of the reflectarray. But for the  $posZ$  value, the value is not 0 as there are some distances between the feed and

the reflecting panel. This value depends on the  $fDRatio$  value and the size of the reflecting panel.

Some calculations are needed to assign the proper  $posZ$ . To do this, a method named “calculateFocal” will be added to the feed class definition. Method is considered as function or operation that can be performed on the object especially when modifying the properties values. Fig. A.3 shows the new codes added to define the “calculateFocal” method.



```

1 classdef Feed
2     properties
3         % Position of the feed
4         posX;
5         posY;
6         posZ;
7
8         % Focal distance
9         focal;
10        fDRatio;
11    end
12
13    methods
14        function obj = calculateFocal(obj,dimension)
15            % focal distance is the multiplication of fDRatio and
16            % reflectarray dimension
17            focalLength = obj.fDRatio*dimension;
18
19            % Update the properties values
20            obj.focal = focalLength;
21            obj.posZ = focalLength;
22        end
23    end
24 end
25
26

```

**Figure A.3.:** Added new “calculateFocal” method in feed class definition

To calculate the focal distance value for the “primaryFeedObject”, the new added method “calculateFocal” will be used. After executing the Algorithm A.3, the value of the focal distance will be determined based on the specified reflecting panel size. In this case, the size of the elementary cell is 7.5 mm.

---

**Algorithm A.3** Calculation of focal distance value for primaryFeedObject

---

```

elementaryCellSize = 7.5E-3;
primaryFeedObject.calculateFocal(21*elementaryCellSize);

```

---

One of the OOP advantage is the code reusability. In this example, the second feed object can be created in the similar way as the first feed object without conflicting between each other properties values because the properties are well encapsulated in their own domain. This is shown in Algorithm A.4.

---

**Algorithm A.4** Primary and secondary feed objects creations using one feed class definition

---

```
// Global value
elementaryCellSize = 7.5E-3;

// Object creations
primaryFeedObject = Feed;
secondaryFeedObject = Feed;

// Assigning the properties values
primaryFeedObject.posX = 0;
primaryFeedObject.posY = 0;
primaryFeedObject.fDRatio = 0.5;
primaryFeedObject.calculateFocal(21*elementaryCellSize);

secondaryFeedObject.posX = -2*elementaryCellSize;
secondaryFeedObject.posY = 0;
secondaryFeedObject.fDRatio = 0.7;
secondaryFeedObject.calculateFocal(21*elementaryCellSize);
```

---

Algorithm A.4, two feed objects are created by using the same class definition. This can avoid codes duplications such as multiples properties definition for each feed. In the example, the secondary feed position is offset to the left by 2 unit cells and the focal distance is farther than the primary feed. Both feeds are defined in the same context and can coexist with less code definition which reflects the real life conditions. In HRS, all objects illustrated Fig. 3.3 are considered as objects and they are defined in Matlab as class definitions. There are in total 7 classes and they are grouped in 2 types of packages. Package is used to group the classes into their functionalities. There are two packages. The first one is “simobjects” package and the second one is “util” package. The classes descriptions are shown in Tab. A.1.

Package	Class	Description
simobjects	Object	A basic class which represents an object. This class contains coordinates properties (position X, position Y and position Z)
	Feed	This class represents the feed for the reflectarray. The main properties for this class are : <ul style="list-style-type: none"> <li>• Gain values</li> <li>• Focal to diameter ratio</li> </ul>
	Cell	This class represents the elementary cell. Most of the main formulas are being written in this class. The properties for this class are : <ul style="list-style-type: none"> <li>• Gain and directivity value</li> <li>• Phase to compensate the wave travel's distance</li> <li>• Patch type and dimension</li> <li>• <math>S_{11}</math> value</li> </ul> The main methods in this class are : <ul style="list-style-type: none"> <li>• Calculation of incident and reflected wave</li> <li>• Patch size and phase calculation</li> </ul>
	CellsArray	This class represents the entire cells objects which are constructed using "Cell" class. The main formula to calculate the directivity is defined in this class.
	Simulator	Simulator is the main class which uses "Feed" and "CellsArray" classes. This class instructs and coordinates the calculations so that each formula is being executed in the right order.
util	HfssParser	This class is used when we are dealing with the importation of data from HFSS. The methods inside this class can convert data from HFSS to a Matlab data structure.
	HfssScript	This class deals with the creation of HFSS script either to simulate the elementary cell or to draw the complete reflectarray.

Table A.1.: HRS class definition descriptions



# References

- [1] A. Tamminen, S. Makela, J. Ala-Laurinaho, J. Hakli, P. Koivisto, P. Rantakari, J. Saily, A. Luukanen, and A. Raisanen, "Reflectarray design for 120-GHz radar application: Measurement results," *Antennas and Propagation, IEEE Transactions on*, vol. 61, no. 10, pp. 5036–5047, Oct 2013.
- [2] P. Siegel, "Terahertz technology," *Microwave Theory and Techniques, IEEE Transactions on*, vol. 50, no. 3, pp. 910–928, Mar 2002.
- [3] P. de Maagt and G. Crone, "(Sub)millimetre wave antenna technology for upcoming ESA missions," in *Proc. P2000, Millennium Conf. Antennas Propag., Davos, Switzerland*, April 2000.
- [4] N.A.Salmon, "Scene simulation for passive and active millimeter and submillimetre-wave imaging for security scanning and medical applications," in *Proc. SPIE 8th Int. Symp. Remote Sens.*, vol. 5619, December 2004, pp. 129–135.
- [5] G. M.C.Beard and C.A.Schmuttenmaer, "Terahertz spectroscopy," in *J. Phys. Chem. B*, vol. 106, 2002, pp. 7149–7159.
- [6] A. Raisanen, J. Ala-Laurinaho, D. Chicherin, Z. Du, A. Generalov, A. Karttunen, D. Lioubtchenko, J. Mallat, A. Tamminen, and T. Zvolensky, "Antennas for electronic beam steering and focusing at millimeter wavelengths," in *Electromagnetics in Advanced Applications (ICEAA), 2012 International Conference on*, Sept 2012, pp. 1235–1237.
- [7] S. B. Kang, M. H. Kwak, M. Choi, S. Kim, T. Kim, E. J. Cha, and K.-Y. Kang, "Terahertz dielectric response of ferroelectric Ba(x)Sr(1-x)TiO<sub>3</sub> thin films," *Ultrasonics, Ferroelectrics, and Frequency Control, IEEE Transactions on*, vol. 58, no. 11, pp. 2276–2280, November 2011.
- [8] B. S. M. M. N. Vieweg, M. K. Shakfa and M. Koch, "Thz properties of nematic liquid crystals," in *J. Infr. Millim. Terahertz Waves*, vol. 31, 2010, pp. 1312–1320.
- [9] R. Munson, H. Haddad, and J. Hanlen, "Microstrip reflectarray for satellite communication and radar cross-section enhancement or reduction," Aug. 4 1987, uS Patent 4,684,952.
- [10] D. Chang and M. Huang, "Microstrip reflectarray antenna with offset feed," *Electronics Letters*, vol. 28, no. 16, pp. 1489–1491, July 1992.



- 
- [11] D. M. Pozar, "Microstrip reflectarrays myths and realities," in *JINA 2004, International Symposium on Antennas, Nice, France*, November 2004, pp. 175–179.
- [12] J. Lanteri, C. Migliaccio, J.-Y. Dauvignac, and C. Pichot, "Reflectarray using an offset prolate feed at 94 Ghz," in *Antennas and Propagation Society International Symposium, 2008. AP-S 2008. IEEE*, July 2008, pp. 1–4.
- [13] K. Zhang, J. Li, G. Wei, Y. Fan, J. Xu, and S. Gao, "Design and optimization of broadband single-layer reflectarray," in *Antennas Propagation (ISAP), 2013 Proceedings of the International Symposium on*, vol. 02, Oct 2013, pp. 1226–1229.
- [14] D. M. Pozar, S. D. Targonski, and H. D. Syrigos, "Design of millimeter wave microstrip reflectarrays," *IEEE Trans. Antennas Propagat.*, vol. 45, pp. 287–295, February 1997.
- [15] K. Sze and L. Shafai, "Microstrip patches for a reflectarray," *Antennas and Propagation Society International Symposium, 1999. IEEE*, vol. 3, pp. 1666–1669, August 1999.
- [16] K. Konno, Q. Chen, K. Sawaya, S. Kameda, and N. Suematsu, "Reflectarray design by induced electromotive force method," in *Antennas and Propagation Society International Symposium (APSURSI), 2013 IEEE*, July 2013, pp. 1342–1343.
- [17] L. Guo, P.-K. Tan, and T.-H. Chio, "Design of an x-band reflectarray using double circular ring elements," in *Antennas and Propagation (EuCAP), 2013 7th European Conference on*, April 2013, pp. 2947–2950.
- [18] D. Oloumi, S. Ebadi, A. Kordzadeh, A. Semnani, P. Mousavi, and X. Gong, "Miniaturized reflectarray unit cell using fractal-shaped patch-slot configuration," *Antennas and Wireless Propagation Letters, IEEE*, vol. 11, pp. 10–13, 2012.
- [19] T. Smith, U. Gothelf, O. Kim, and O. Breinbjerg, "An fss-backed 20/30 Ghz circularly polarized reflectarray for a shared aperture l- and ka-band satellite communication antenna," *Antennas and Propagation, IEEE Transactions on*, vol. 62, no. 2, pp. 661–668, Feb 2014.
- [20] J. Huang and J. A. Encinar, *Reflectarray antennas*. Hoboken, New Jersey: John Wiley & Sons, Inc., 2008, ISBN: 978-0-470-08491-5.
- [21] A. Gheethan, M. C. Jo, R. Guldiken, and G. Mumcu, "Microfluidic based ka-band beam-scanning focal plane array," *Antennas and Wireless Propagation Letters, IEEE*, vol. 12, pp. 1638–1641, 2013.
- [22] A. Guntupalli, T. Djerafi, and K. Wu, "Two-dimensional scanning antenna array driven by integrated waveguide phase shifter," *Antennas and Propagation, IEEE Transactions on*, vol. 62, no. 3, pp. 1117–1124, March 2014.

- [23] H. Kamoda, T. Iwasaki, J. Tsumochi, T. Kuki, and O. Hashimoto, "60-GHz electronically reconfigurable large reflectarray using single-bit phase shifters," *Antennas and Propagation, IEEE Transactions on*, vol. 59, no. 7, pp. 2524–2531, July 2011.
- [24] S. Targonski and D. Pozar, "Analysis and design of a microstrip reflectarray using patches of variable size," in *Antennas and Propagation Society International Symposium, 1994. AP-S. Digest*, vol. 3, June 1994, pp. 1820–1823 vol.3.
- [25] D. Pozar and T. Metzler, "Analysis of a reflectarray antenna using microstrip patches of variable size," *Electronics Letters*, vol. 29, no. 8, pp. 657–658, April 1993.
- [26] K. Sze and L. Shafal, "Analysis of phase variation due to varying patch length in a microstrip reflectarray," in *Antennas and Propagation Society International Symposium, 1998. IEEE*, vol. 2, June 1998, pp. 1134–1137 vol.2.
- [27] D.-C. Chang and M.-C. Huang, "Multiple-polarization microstrip reflectarray antenna with high efficiency and low cross-polarization," *Antennas and Propagation, IEEE Transactions on*, vol. 43, no. 8, pp. 829–834, Aug 1995.
- [28] J. Huang and R. Pogorzelski, "A ka-band microstrip reflectarray with elements having variable rotation angles," *Antennas and Propagation, IEEE Transactions on*, vol. 46, no. 5, pp. 650–656, May 1998.
- [29] J. Huang, "Bandwidth study of microstrip reflectarray and a novel phased reflectarray concept," in *Antennas and Propagation Society International Symposium, 1995. AP-S. Digest*, vol. 1, June 1995, pp. 582–585 vol.1.
- [30] J. A. Encinar, "Design of two layer printed reflectarrays using patches of variable size," *IEEE Trans. Antennas Propagat.*, vol. 49, pp. 1403–1410, October 2001.
- [31] M. B. E. Carrasco and J. A. Encinar, "Aperture-coupled reflectarray element with wide range of phase delay," *Electronics Letters*, vol. 42, pp. 667–668, June 2006.
- [32] J. A. Encinar and J. A. Zornoza, "Broadband design of three - layer printed reflectarrays," *IEEE Trans. Antennas Propagat.*, vol. 51, pp. 1662–1664, July 2003.
- [33] E. Carrasco, J. Encinar, and M. Barba, "Dual linear polarized reflectarray element with true-time delay," in *Antennas and Propagation, 2009. EuCAP 2009. 3rd European Conference on*, March 2009, pp. 3733–3737.
- [34] H. H. Meinel, "Automotive millimeterwave radar history and present status," in *Microwave Conference, 1998. 28th European*, vol. 1, Oct 1998, pp. 619–629.
- [35] C.-H. Tsai, L.-H. Kan, H.-H. Chen, and S.-J. Chung, "A co-design of dielectric lens and folded reflectarray antenna with the application to 77 GHz long-range mode forward-looking vehicle collision warning radar system," in *Microwave Conference Proceedings (APMC), 2012 Asia-Pacific*, Dec 2012, pp. 676–678.

- 
- [36] I. Gresham, N. Jain, T. Budka, A. Alexanian, N. Kinayman, B. Ziegner, S. Brown, and P. Staecker, "A compact manufacturable 76-77-GHz radar module for commercial acc applications," *Microwave Theory and Techniques, IEEE Transactions on*, vol. 49, no. 1, pp. 44–58, Jan 2001.
- [37] E. Carrasco, M. Barba, B. Reig, J. Encinar, and P. Charvet, "Demonstration of a gathered element for reconfigurable-beam reflectarrays based on ohmic mems," in *Antennas and Propagation (EUCAP), Proceedings of the 5th European Conference on*, April 2011, pp. 1413–1416.
- [38] R. Sorrentino, R. Gatti, and L. Marcaccioli, "Recent advances on millimetre wave reconfigurable reflectarrays," in *Antennas and Propagation, 2009. EuCAP 2009. 3rd European Conference on*, March 2009, pp. 2527–2531.
- [39] M. Hajian, B. Kuijpers, K. Buisman, A. Akhnoukh, M. Plek, L. C. N. De Vreede, J. Zijdeveld, and L. Ligthart, "Active scan-beam reflectarray antenna loaded with tunable capacitor," in *Antennas and Propagation, 2009. EuCAP 2009. 3rd European Conference on*, March 2009, pp. 1158–1161.
- [40] K. Buisman, L. C. N. De Vreede, L. Larson, M. Spirito, A. Akhnoukh, Y. Lin, X. Liu, and L. Nanver, "Low-distortion, low-loss varactor-based adaptive matching networks, implemented in a silicon-on-glass technology," in *Radio Frequency Integrated Circuits (RFIC) Symposium, 2005. Digest of Papers. 2005 IEEE*, June 2005, pp. 389–392.
- [41] K. Buisman, L. de Vreede, L. Larson, M. Spirito, A. Akhnoukh, T. Scholtes, and L. Nanver, "Distortion-free varactor diode topologies for rf adaptivity," in *Microwave Symposium Digest, 2005 IEEE MTT-S International*, June 2005, pp. 157–160.
- [42] M. Ismail, W. Hu, R. Cahill, V. Fusco, H. Gamble, D. Linton, R. Dickie, S. Rea, and N. Grant, "Phase agile reflectarray cells based on liquid crystals," *Microwaves, Antennas Propagation, IET*, vol. 1, no. 4, pp. 809–814, Aug 2007.
- [43] A. Moessinger, R. Marin, J. Freese, S. Mueller, A. Manabe, and R. Jakoby, "Investigations on 77 GHz tunable reflectarray unit cells with liquid crystal," in *Antennas and Propagation, 2006. EuCAP 2006. First European Conference on*, Nov 2006, pp. 1–4.
- [44] W. Hu, R. Cahill, J. Encinar, R. Dickie, H. Gamble, V. Fusco, and N. Grant, "Design and measurement of reconfigurable millimeter wave reflectarray cells with nematic liquid crystal," *Antennas and Propagation, IEEE Transactions on*, vol. 56, no. 10, pp. 3112–3117, Oct 2008.
- [45] W. Hu, R. Dickie, R. Cahill, H. Gamble, Y. Ismail, V. Fusco, D. Linton, N. Grant, and S. Rea, "Liquid crystal tunable mm wave frequency selective surface," *Microwave and Wireless Components Letters, IEEE*, vol. 17, no. 9, pp. 667–669, Sept 2007.

- [46] W. Hu, M. Ismail, R. Cahill, H. Gamble, R. Dickie, V. Fusco, D. Linton, S. Rea, and N. Grant, "Tunable liquid crystal reflectarray patch element," *Electronics Letters*, vol. 42, no. 9, pp. 509–511, April 2006.
- [47] G. Perez-Palomino, P. Baine, R. Dickie, M. Bain, J. Encinar, R. Cahill, M. Barba, and G. Toso, "Design and experimental validation of liquid crystal-based reconfigurable reflectarray elements with improved bandwidth in f-band," *Antennas and Propagation, IEEE Transactions on*, vol. 61, no. 4, pp. 1704–1713, April 2013.
- [48] F. Seitz and D. Turnbull, *Solid State Physics*. Elsevier Science, 1957, no. v. 4, ISBN: 9780080864686.
- [49] M. Lines and A. Glass, *Principles and Applications of Ferroelectrics and Related Materials*, ser. Oxford classic texts in the physical sciences. Clarendon Press, 2001, ISBN: 2001268331.
- [50] J. Nath, D. Ghosh, J.-P. Maria, A. I. Kingon, W. Fathelbab, P. Franzon, and M. Steer, "An electronically tunable microstrip bandpass filter using thin-film barium-strontium-titanate (bst) varactors," *Microwave Theory and Techniques, IEEE Transactions on*, vol. 53, no. 9, pp. 2707–2712, Sept 2005.
- [51] A. Tombak, J.-P. Maria, F. Ayguavives, Z. Jin, G. T. Stauf, A. I. Kingon, and A. Mortazawi, "Voltage-controlled rf filters employing thin-film barium-strontium-titanate tunable capacitors," *Microwave Theory and Techniques, IEEE Transactions on*, vol. 51, no. 2, pp. 462–467, Feb 2003.
- [52] M. Nikfalazar, M. Sazegar, Y. Zheng, A. Wiens, R. Jakoby, A. Friederich, C. Kohler, and J. Binder, "Compact tunable phase shifter based on inkjet printed bst thick-films for phased-array application," in *Microwave Conference (EuMC), 2013 European*, Oct 2013, pp. 432–435.
- [53] M. Sazegar, A. Giere, Y. Zheng, H. Maune, A. Moessinger, and R. Jakoby, "Reconfigurable unit cell for reflectarray antenna based on barium-strontium-titanate thick-film ceramic," in *Microwave Conference, 2009. EuMC 2009. European*, Sept 2009, pp. 598–601.
- [54] A. Kanareykin, E. Nenasheva, S. Karmanenko, A. Dedyk, and V. Yakovlev, "Low-loss ferroelectric for accelerator applications," in *Particle Accelerator Conference, 2005. PAC 2005. Proceedings of the*, May 2005, pp. 4305–4307.
- [55] B. D. Nguyen, K. T. Pham, V.-S. Tran, L. Mai, N. Yonemoto, A. Kohmura, and S. Futatsumori, "Electronically tunable reflectarray element based on c-patch coupled to delay line," *Electronics Letters*, vol. 50, no. 16, pp. 1114–1116, July 2014.
- [56] M. Inam, M. Ismail, A. Zain, and N. Misran, "Multi-state frequency switchable reflectarray antenna design," in *Space Science and Communication (IconSpace), 2013 IEEE International Conference on*, July 2013, pp. 253–256.

- [57] A. Kohmura, J. Lanteri, F. Ferrero, C. Migliaccio, P. Ratajczak, S. Futatsumori, and N. Yonemoto, “Ka-band dual frequency switchable reflectarray,” in *Antennas and Propagation (EUCAP), 2012 6th European Conference on*, March 2012, pp. 3230–3233.
- [58] C. Menudier and T. Koleck, “Sub-reflectarrays performances for reconfigurable coverages,” *Antennas and Propagation, IEEE Transactions on*, vol. 60, no. 7, pp. 3476–3481, July 2012.
- [59] E. Carrasco, M. Barba, and J. Encinar, “X-band reflectarray antenna with switching-beam using pin diodes and gathered elements,” *Antennas and Propagation, IEEE Transactions on*, vol. 60, no. 12, pp. 5700–5708, Dec 2012.
- [60] B. D. Nguyen, J. Lanteri, J. Dauvignac, C. Pichot, and C. Migliaccio, “94 Ghz folded fresnel reflector using c-patch elements,” *Antennas and Propagation, IEEE Transactions on*, vol. 56, no. 11, pp. 3373–3381, Nov 2008.
- [61] A. Kohmura, J. Lanteri, F. Ferrero, C. Migliaccio, S. Futatsumori, and N. Yonemoto, “Ka-band beam switchable fresnel reflector,” in *Antennas and Propagation (ISAP), 2012 International Symposium on*, Oct 2012, pp. 535–538.
- [62] S. Mener, R. Gillard, R. SAULEAU, C. Cheymol, and P. Potier, “Unit cell for reflectarrays operating with independent dual circular polarizations,” *Antennas and Wireless Propagation Letters, IEEE*, vol. 13, pp. 1176–1179, 2014.
- [63] E. Carrasco, M. Barba, B. Reig, C. Dieppedale, and J. Encinar, “Characterization of a reflectarray gathered element with electronic control using ohmic rf mems and patches aperture-coupled to a delay line,” *Antennas and Propagation, IEEE Transactions on*, vol. 60, no. 9, pp. 4190–4201, Sept 2012.
- [64] S. Ebadi, R. Gatti, and R. Sorrentino, “Linear reflectarray antenna design using 1-bit digital phase shifters,” in *Antennas and Propagation, 2009. EuCAP 2009. 3rd European Conference on*, March 2009, pp. 3729–3732.
- [65] B. Wu, A. Sutinjo, M. Potter, and M. Okoniewski, “On the selection of the number of bits to control a dynamic digital mems reflectarray,” *Antennas and Wireless Propagation Letters, IEEE*, vol. 7, pp. 183–186, 2008.
- [66] C.-C. Cheng and A. Abbaspour-Tamijani, “Study of 2-bit antenna-filter-antenna elements for reconfigurable millimeter-wave lens arrays,” *Microwave Theory and Techniques, IEEE Transactions on*, vol. 54, no. 12, pp. 4498–4506, Dec 2006.
- [67] S. Ebadi, R. Gatti, L. Marcaccioli, and R. Sorrentino, “Near field focusing in large reflectarray antennas using 1-bit digital phase shifters,” in *Microwave Conference, 2009. EuMC 2009. European*, Sept 2009, pp. 1029–1032.
- [68] H. Yang, Y. Mao, S. Xu, F. Yang, and A. Elsherbeni, “Analysis and optimization of the scanning performance of 1-bit reconfigurable reflectarrays,” in *Antennas and Propagation Society International Symposium (APSURSI), 2014 IEEE*, July 2014, pp. 1029–1030.

- [69] E. Plaza, G. Leon, S. Loredó, and F. Las-Heras, "Dual polarized transmitarray lens," in *Antennas and Propagation (EuCAP), 2014 8th European Conference*, The Hague, The Netherlands, April 2014, pp. 2305–2308.
- [70] W. An, S. Xu, and F. Yang, "A two-layer transmitarray antenna," in *Antennas and Propagation Society International Symposium (APSURSI), 2014 IEEE*, Tennessee, USA, July 2014, pp. 864–865.
- [71] H. Kaouach, "Antennes quasi-optiques reconfigurables à grande ouverture aux fréquences millimétriques," Ph.D. dissertation, Université Rennes, 2009.
- [72] H. T. Friis, "Noise figure of radio receivers," in *Proc. IRE*, vol. 3, no. 7, July 1944, pp. 419–422.
- [73] M. Hajian, J. Dickhof, C. Trampuz, and L. Ligthart, "Design of hollow patch microstrip reflectarray and measuring phase of reflection coefficient at ka-band using waveguide simulator," in *Antennas and Propagation (EuCAP), 2010 Proceedings of the Fourth European Conference*, Barcelona, Spain, April 2010, pp. 1–5.
- [74] S. McGarrity. (2009, February) Introduction to object-oriented programming in MATLAB. [Online]. Available: <http://www.mathworks.fr/company/newsletters/articles/introduction-to-object-oriented-programming-in-matlab.html>
- [75] C. Migliaccio, K. Mazouni, A. Breard, A. Zeitler, J. Lanteri, J.-Y. Dauvignac, C. Pichot, N. Yonemoto, A. Kohmura, and S. Futatsumori, "Reflectarrays for mm-wave radar applications," in *Antennas and Propagation (APSURSI), 2011 IEEE International Symposium*, Spokane, USA, July 2011, pp. 105–108.
- [76] A. Clemente, "Conception d'antennes à réseaux transmetteurs à depointage et formation de faisceau," Ph.D. dissertation, Université Rennes, 2012.
- [77] J. Weiner and F. Nunes, *Light-Matter Interaction: Physics and Engineering at the Nanoscale*. OUP Oxford, 2012, ISBN: 9780191650093.
- [78] A. Ahmadi, S. Ghadarghadr, and H. Mosallaei, "An optical reflectarray nanoantenna: The concept and design," *Opt. Express*, vol. 18, no. 1, pp. 123–133, Jan 2010. [Online]. Available: <http://www.opticsexpress.org/abstract.cfm?URI=oe-18-1-123>



# Publications

- [79] M. Bin Zawawi, J. Lanteri, and C. Migliaccio, “20-ghz single-bit active elementary cell,” in *Antennas and Propagation (EuCAP), 2013 7th European Conference*, Gothenburg, Sweden, April 2013, pp. 1304–1307.
- [80] M. Binzawawi, J. Lanteri, and C. Migliaccio, “Réseau réflecteur actif à base de déphaseurs 1-bit à 20GHz,” in *18èmes Journées Nationales Microondes (JNM)*, Paris, France, May 2013, pp. J2–AP–P13.pdf. [Online]. Available: <https://hal.archives-ouvertes.fr/hal-00862583>
- [81] M. Bin Zawawi, J. Lanteri, C. Migliaccio, and C. Pichot, “20 ghz active reflectarray using 1-bit phase shifter,” in *Antennas and Propagation Society (AP-SURSI), 2013 IEEE International Symposium*, Florida, USA, July 2013, pp. 1668–1669.
- [82] M. Bin Zawawi, J. Lanteri, and C. Migliaccio, “20-ghz 1-bit slotted active elementary cell,” in *Antennas and Propagation (EuCAP), 2014 8th European Conference*, The Hague, Netherlands, April 2014, pp. 1944–1947.





# Muhammad Nazrol Bin Zawawi

21 rue Paganini  
06000, Nice  
France

E-mail : nazrol.zawawi@gmail.com

---

## WORKING EXPERIENCE

- April 2011 – September 2011      Internship, reflectarray simulator modeling – Electronics, Antennas & Telecommunications Laboratory (LEAT), Sophia Antipolis, France
- April 2007 – June 2007              Diploma internship, web developer – Trigger Networks, Sophia Antipolis, France
- 

## EDUCATION

- November 2011 – April 2015      **PhD in Electronics**  
*Conception and fabrication of active millimetre wave antenna for radar*  
Sponsored by Universiti Malaysia Pahang (UMP) Electronics, Antennas & Telecommunications Laboratory (LEAT)
- September 2009 – October 2011      **Master of Science in Electronics**  
(Telecommunications, Systems & Microelectronics)  
University Nice Sophia-Antipolis, France
- September 2008 – June 2009      **Bachelor of Science in Electrical, Electronic & Automation (Licence)**  
University Nice Sophia-Antipolis, France
- September 2005 – June 2007      **Diploma in Computer Networking & Telecommunications (DUT)**  
IUT Nice Sophia-Antipolis, France
- 

## SKILLS

- Telecom
- Antenna design & fabrication - millimeter wave antenna, reflectarray
- Programming
- Main language used Java, C, PHP, Javascript & Flash ActionScript
  - Experienced developing programs, interactive contents, user interface & website
  - Conception, simulation of logic circuits, Arduino board
- Computer Networking
- Operating system administration and configuration Windows Server, Mac OS X & Linux
  - Linux system programming & bash scripting
  - Able to setup & install local area network, router and switch

